MOLTEN FLUORIDE SALT-ASSISTED SYNTHESIS OF MXENES AS POTENTIAL MATERIAL FOR NONLINEAR PHOTONIC DEVICES AND APPLICATIONS

AIZUDDIN BIN AHMAD KAMELY

FACULTY OF SCIENCE

UNIVERSITI MALAYA

KUALA LUMPUR

2022

MOLTEN FLUORIDE SALT-ASSISTED SYNTHESIS OF MXENES AS POTENTIAL MATERIAL FOR PHOTONIC DEVICES AND APPLICATIONS

AIZUDDIN BIN AHMAD KAMELY

THESIS SUBMITTED IN FULFILMENT OF THE REQUIREMENTS FOR THE DEGREE OF DOCTOR OF PHILOSOPHY

DEPARTMENT OF PHYSICS

FACULTY OF SCIENCE

UNIVERSITY MALAYA

KUALA LUMPUR

2022

UNIVERSITY MALAYA

ORIGINAL LITERARY WORK DECLARATION

Name of Candidate: **AIZUDDIN BIN AHMAD KAMELY**

Matric No: **17199032/2**

Name of Degree: **DOCTOR OF PHILOSOPHY**

Title of Thesis:
MOLTEN FLUORIDE SALT-ASSISTED SYNTHESIS OF MXENES AS POTENTIAL MATERIAL FOR NONLINEAR PHOTONIC DEVICES AND APPLICATIONS

Field of Study: **PHOTONICS ENGINEERING**

I do solemnly and sincerely declare that:

(1) I am the sole author/writer of this Work;
(2) This Work is original;
(3) Any use of any work in which copyright exists was done by way of fair dealing and for permitted purposes and any excerpt or extract from, or reference to or reproduction of any copyright work has been disclosed expressly and sufficiently and the title of the Work and its authorship have been acknowledged in this Work;
(4) I do not have any actual knowledge nor do I ought reasonably to know that the making of this work constitutes an infringement of any copyright work;
(5) I hereby assign all and every right in the copyright to this Work to the Universiti Malaya ("UM"), who henceforth shall be owner of the copyright in this Work and that any reproduction or use in any form or by any means whatsoever is prohibited without the written consent of UM having been first had and obtained;
(6) I am fully aware that if in the course of making this Work I have infringed any copyright whether intentionally or otherwise, I may be subject to legal action or any other action as may be determined by UM.

Candidate's Signature Date: 9/11/2022

Subscribed and solemnly declared before,

Witness's Signature Date: 9/11/2022

Name:

Designation:

MOLTEN FLUORIDE SALT-ASSISTED SYNTHESIS OF MXENES AS POTENTIAL MATERIAL FOR NONLINEAR PHOTONIC DEVICES AND APPLICATIONS

ABSTRACT

Group 4–6 transition metal carbides and nitrides were explored in the twentieth century as promising materials. Their catalytic behavior were founded in the 1970s that led to the exploration towards energy storage applications. Henceforth, a number of nanostructure designs have been introduced, taking tiny steps to enhance the surface area and performance of transition metal carbides and nitrides. The breakthrough in the area took place in 2011 by the discovery of the first two-dimensional (2D) titanium carbide ($Ti_3C_2T_x$) that give birth to a family of 2D transition metal carbides and nitrides, named MXenes (pronounced “maxines”). MXenes have become a large and quickly growing family of 2D materials ever since. In comparison to the other 2D materials, MXenes is relatively new and has not been extensively studied, especially in photonics field. The aim of this study is to synthesize MXenes from precursor MAX phases in non-standard method due to the harmful properties of hydrofluoric acid (HF) used in the standard method. A mixture of molten fluoride salt and acid (HF-forming etchant) is utilized instead, with different concentration, temperature, time, and procedures depending on the type of MXenes. Three different MXenes are being investigated in this work, titanium carbide (Ti_2C), vanadium carbide (V_2C), and niobium carbide (Nb_2C), all three compounds with similar chemical ratio. Preparations and characterizations of the MXenes are described in detail such as lateral size, elemental composition, linear absorption, and nonlinear absorption. Besides synthesis, the MXenes are integrated in fiber laser systems, comprising of pulsed fiber laser, four wave mixing, and all-optical modulation to explore the performance. The optical response of the three MXenes are recorded with typical measurement according to each configuration. The studies commenced and the findings

obtained in this study can contribute to the advancement of MXenes in photonics application.

Keywords: MXenes, MAX phases, HF-forming etchant, Mode-locked laser, Q-switched laser, Four wave mixing, All-optical modulator

SINTESIS MXENES MENGGUNAKAN BANTUAN GARAM FLUORIDA LEBURAN SEBAGAI BAHAN BERPOTENSI UNTUK PERANTI DAN APLIKASI FOTONIK TAK LINEAR

ABSTRAK

Kumpulan 4-6 logam peralihan karbida dan nitrida telah diteroka pada abad ke dua puluh sebagai bahan yang meyakinkan. Sifat pemangkin bahan ini telah dijumpai pada tahun 1970 an yang telah membawa kepada penerokaan terhadap aplikasi simpanan tenaga. Sejak itu, beberapa reka bentuk nano struktur telah mula diperkenalkan, secara perlahan-lahan mempertingkatkan Kawasan permukaan dan prestasi logam peralihan karbida dan nitrida. Kejayaan cemerlang dalam bidang ini berlaku pada tahun 2011 iaitu dengan penemuan titanium karbida ($Ti_3C_2T_x$) dua dimensi (2D) yang telah melahirkan keluarga baru logam peralihan karbida dan nitrida 2D, dinamakan sebagai MXenes (disebut “maxines”). Sejak itu, MXenes telah berkembang secara laju sebagai keluarga bahan 2D. Berbanding dengan yang lain, MXenes adalah masih baru dan belum lagi dikaji secara mendalam, lebih-lebih lagi dia dalam bidang fotonik. Tujuan kajian ini adalah untuk mensintesis MXenes daripada pendahulu MAX phases melalui kaedah bukan piawai disebabkan oleh sifat memudaratkan asid hidrofluorik (HF) yang digunakan dalam kaedah piawai. Sebaliknya gabungan antara garam fluorida cair dan asid (penggores pembentukan HF) digunakan, dengan berbeza pekatan, suhu, masa dan kaedah bergantung kepada jenis MXenes. Tiga jenis MXenes telah dikaji di dalam kajian ini, titanium karbida (Ti_2C), vanadium karbida (V_2C) dan niobium karbida (Nb_2C), ketiga-tiga kompoun mempunyai nisbah kimia yang sama. Persiapan dan pencirian MXenes ditulis secara terperinci seperti size sisi, komposisi unsur, penyerapan linear dan penyerapan tidak linear. Selain sintesis, MXenes dimasukkan ke dalam sistem laser fiber, terdiri daripada laser fiber denyutan, pencampuran empat gelombang dan modulasi semua optic untuk mengkaji prestasi. Tindak balas optic ketiga-tiga MXenes dicatat berdasarkan

ukuran kebiasaan bagi setiap konfigurasi. Kajian telah dibuat dan penemuan yang didapati dalam kajian ini boleh menyumbang kepada kemajuan MXenes dalam bidang fotonik.

Kata Kunci: MXenes. MAX phases, Penggores pembentukan HF, Laser mod terkunci, Laser suis Q, Pencampuran empat gelombang, Modulator semua optik

ACKNOWLEDGEMENTS

First and foremost, I would like to extend my sincere gratitude to my supervisor, Prof. Ulung Datuk Dr Harith bin Ahmad for his precious advice, continuous support, and patience during my PhD study. His support from every aspect including academic-related advice and supply of research facilities has always been the motivation for me to complete my study.

I would also thank Dr. Muhamad Zharif bin Samion, Dr. Norazriena binti Yusoff, Dr. Nor Najwa binti Ismail, and Dr. Mohamad Faizal bin Ismail for their kind help and advice throughout my academic year. Their cooperation have encouraged me at every stage of my study.

Not to mention, I would also like to express gratitude to my friends, lab mates, colleagues and all the staff in the Photonic Research Centre, University Malaya for all kinds of assistance and support. It is their support and the time we spent together that have made my study life a wonderful time.

Finally, I must convey my gratitude wholeheartedly to my parents and family members for providing me with bottomless support and encouragement throughout my years of study and through the process of researching and writing this thesis. Without their tremendous understanding and encouragement in the past few years, it would be impossible to complete my study.

TABLE OF CONTENTS

LIST OF FIGURES

LIST OF TABLES

LIST OF SYMBOLS AND ABBREVIATIONS

$\sigma_a(\lambda_{p/s})$	:	Absorption cross-sections of pump/signal light
E_n	:	Amplitude at the n^{th} mode
ω_n	:	Angular frequency of the oscillation of the n^{th} mode
ω	:	Angular frequency
β_{ij}	:	Branching ratio of the spontaneous transition
ω_0	:	Beam waist radius
$\Delta\lambda$	:	Bandwidth of the amplified spontaneous emission
k_{ij}	:	Cross relaxation rates
$\Gamma_{p/s}$	:	Confinement factor for pump/signal light
A_{core}	:	Cross-section area of the fiber core
C	:	Cross relaxation
λ_c	:	Center wavelength
n	:	Complex refractive index
N_T	:	Density of Tm^{3+}
D	:	Dispersion parameter

$\psi_k^{C_n}$	:	Empty conduction band levels
n	:	Electron concentration or free carrier
m	:	Effective electron mass
$E\|\|x$	:	Electric field parallel
$E\|\|z$	:	Electric field perpendicular
$\sigma_e(\lambda_{p/s})$	:	Emission cross-sections of pump/signal light
τ_{fall}	:	Fall time
$ASE_{f/b}(z)$	:	Forward and backward amplified spontaneous emission power at position z
P_{fl}	:	Fluorescence light
f_c	:	Fundamental frequency
g	:	Gain
v_g	:	Group velocity
I	:	Intensity of light
$Im\ \chi^{(3)}$	:	Imaginary part third-order nonlinear susceptibilities
$Im\ \varepsilon$	:	Imaginary part dielectric function
$\alpha_{p/s}$	:	Intrinsic absorption at pump/signal wavelength

Γ	:	Loss/damping expression in the Drude model
$\chi^{(1)}$	:	Linear susceptibility
n_0	:	Linear refractive index
α_0	:	Linear absorption coefficient
ΔV	:	Laser linewidth
E_{max}	:	Maximum pulse energy
P_{max}	:	Maximum peak power
n_2	:	Nonlinear refractive index
α_2	:	Nonlinear absorption coefficient
β	:	Nonlinear absorption coefficient
ΔT_{pv}	:	Normalized transmittance between peak and valley
$\Delta\phi_0$	:	Nonlinear phase shift
$\psi_k^{V_n}$	:	Occupied valence band levels
$E_k^{V_n}$	:	Occupied valence band states
v_0	:	Optical frequency
P	:	Optical power
P_{ASE}	:	Output power of ASE

$P_{material}$	:	Output power of the ASE injected through material
P	:	Principal value
ω_p^2	:	Plasma frequency
$N_i(z,t)$	:	Population density of *i*th energy level
w_{pij}	:	Pumping and de-excitation rates
h	:	Planck constant
$P_{p/s}^{\pm}(z)$	:	Pump (corresponding to forward and backward)/signal power at position z
ϕ_n	:	Phase of the n^{th} mode
P_0	:	Peak power
T_0	:	Pulse width
Z	:	Position of the sample relative to the focal point
τ_{AC}	:	Pulse duration autocorrelation trace
V_{pp}	:	Peak-to-peak voltage
$Re\ \varepsilon$	:	Real part dielectric function
$Re\ \chi^{(3)}$	:	Real part third-order nonlinear susceptibilities
τ_{rp}	:	Round trip time

τ_g	:	Relaxation time of gain medium
τ_a	:	Relaxation time of saturable absorber
f	:	Repetition rate
Z_0	:	Rayleigh range
τ_{rise}	:	Rise time
T_x	:	Surface termination
$\chi(\omega)$	:	Susceptibility tensor
$\chi^{(2)}$	:	Second-order nonlinear susceptibilities
I_s	:	Saturation intensity
E_s	:	Saturation fluence
c	:	Speed of light
τ_i	:	Spontaneous lifetime of *i*th energy level
w_{sij}	:	Stimulated emission and absorption rates
w_{ij}	:	Stimulated absorption and emission rates
c	:	Speed of light in vacuum
A_{ij}	:	Spontaneous decay rate for radiative decay rates
A_i^{nr}	:	Spontaneous decay rate for non-radiative decay rates

g_{ss}	:	Small-signal gain
$E_{sat,g}$	:	Saturation energy of the gain medium
$E_{sat,a}$	:	Saturation energy of the saturable absorber
$\chi^{(3)}$	:	Third-order optical nonlinearity
$\chi^{(3)}$	:	Third-order nonlinear susceptibilities
S	:	Transmittance at aperture
$E_k^{C_n}$	:	Unoccupied conduction band
ε_0	:	Vacuum permittivity
$\lambda_{p/s}$	:	Wavelength of the pump/signal light
λ_0	:	Zero-dispersion wavelength
AOM	:	Acoustic-optic modulator
A	:	A group element
ASE	:	Amplified spontaneous emission
BBO	:	Barium borate
BP	:	Black phosphorus
CNT	:	Carbon nanotube
X	:	Carbon or nitrogen

CW	:	Continuous-wave
CA	:	Close-aperture
DFT	:	Density-functional theory
DOS	:	Density of states
DFG	:	Difference-frequency generations
EOM	:	Electro-optic modulator
EMS	:	Electromagnetic spectrum
EDFA	:	Erbium-Doped Fiber Amplifier
ESA	:	Excited state absorption
FWM	:	Four wave mixing
FP-LAPW	:	Full-potential linearized augmented plane wave
FESEM	:	Field emission scanning electron
GO	:	Graphene oxide
GSA	:	Ground state absorption
GVD	:	Group velocity dispersion
HF	:	Hydrofluoric acid
HCl	:	Hydrochloric acid

HER	:	Hydrogen evolution reaction
HRTEM	:	High-resolution transmission electron microscopy
IR	:	Infrared
IUPAC	:	International Union of Pure and Applied Chemist
IPA	:	Isopropyl alcohol
ISO	:	Isolator
LiF	:	Lithium fluoride
LiCl	:	Lithium chloride
LN	:	Lithium niobate
LD	:	Laser diode
MWFL	:	Multiwavelength fiber laser
MOPA	:	Master oscillator power amplifier
NOLM	:	Nonlinear optical loop mirror
NPR	:	Nonlinear polarization rotation
NIR	:	Near infrared region
NLSE	:	Nonlinear Schrödinger equation
Nb_2C	:	Niobium Carbide

Nb_2AlC	:	Niobium aluminium carbide
1D	:	One-dimensional
2M	:	Ordered double transition metal
OA	:	Open-aperture
OSA	:	Optical spectrum analyzer
OSC	:	Oscilloscope
OPM	:	Optical power meter
OC	:	Optical coupler
1A	:	Pure A element
KF	:	Potassium fluoride
PC	:	Polarization controller
RPA	:	Random phase approximation
RSA	:	Reverse saturable absorption
rGO	:	Reduced Graphene Oxide
RFSA	:	Radio frequency spectrum analyzer
SBS	:	Stimulated Brillouin scattering
SBRS	:	Stimulated Brillouin-Raman scattering

SA	:	Saturable absorber
SHG	:	Second-harmonic generation
SESAM	:	Saturable absorber mirror
SS	:	Solid solution
1M	:	Single (pure) transition metal
SOA	:	Semiconductor optical amplifier
SNR	:	Signal-to-noise ratio
NaF	:	Sodium fluoride
SMF	:	Single-mode fiber
2D	:	Two-dimensional
3D	:	Three-dimensional
Ti_2C	:	Titanium Carbide
THG	:	Third harmonic generation
TPA	:	Two-photon absorption
TMD	:	Transition metal dichalcogenide
TI	:	Topological insulator
TM	:	Transition metal

M	:	Transition metal
Ti_2AlC	:	Titanium aluminium carbide
TEM	:	Transmission electron microscopy
TDF	:	Thulium-doped silica fiber
TBP	:	Time-bandwidth product
TDFF	:	Thulium-doped fluoride fiber
UV	:	Ultraviolet
V_2C	:	Vanadium Carbide
V_2AlC	:	Vanadium aluminium carbide
WDM	:	Wavelength division multiplexer
XRD	:	X-ray diffraction
0D	:	Zero-dimensional

CHAPTER 1: INTRODUCTION

1.1 An Overview of Fiber Laser

This year 2022 marks the 62nd anniversary of the invention of laser by Theodore Maiman in 1960. Lasers have become crucial part in the upsurging field of photonics, which allow entirely new as well as revolutionized existing scientific and industrial sectors (Maiman & others, 1960; Willner et al., 2012). The first light signal transmission demonstration over 100 km by using fiber laser surpassing far beyond the conventional bulk laser in 1960s, was discovered by Charles Kuen Kao and George Alfred Hockham; this is a major breakthrough in fiber optic (Kao & Hockham, 1966). Lasers utilize the quantum effect of stimulated emission and share a number of mutual features, such as an active medium or gain medium to provide gain, an optical cavity to build up and control the optical field, pumping source to provide the energy and operation state to yield different output (Siegman, 1990).

Fiber laser has slowly taken over bulk laser in solid-state laser technology arena, quickly infiltrating in all sectors of industrial (Shcherbakov et al., 2013), medical(Popov, 2008), and directed energy application (Sprangle et al., 2015). This overwhelming turnover was because of fiber laser has many benefits to offer compared to bulk laser, which is bigger in size, relatively expensive and require frequent maintenance (J. Lee et al., 2015; J. Lee, Koo, et al., 2014b). On the contrary, fiber laser with equivalent output power can be made into compact size because optical fiber are bendable and can be winded into small space. Due to the flexibility and fine size of gain medium in fiber laser, it is possible to have several kilometers long fiber to reach a high gain of the pumping light. Plus, the heat produced by fiber laser can be efficiently dissipated because of the large surface area to volume ratio of optical fiber. Hence, sophisticated cooling system is

unneeded for the fiber laser to function at kilowatts level (Powell & Kaplan, 2012; Traxer & Keller, 2019).

The laser beam is also less susceptible to external disturbance since the optical path is confined within protective cladding layers. Generally, fiber laser possess outstanding stability in high-temperature (Huang et al., 2019) and vibrational working conditions, makes it reliable and nearly maintenance-free (O'Neill et al., 2004). Futhermore, the best beam performance in fiber laser can be attained by single mode fiber. Laser beam quality is described as a measure of how tightly the beam can be focused, which quantified by an M^2 factor and ideally equal to 1 for high quality beam. Excellent beam quality conceives significant applications, for instance, in laser cutting and welding. A high beam quality will permit for an extensive separation between the workpiece and the focusing object, protecting the optics from debris and fumes. Not only that, but the reduced beam diameter can also provide finer structure manufacturing (Tao et al., 2013). The edges of fiber laser over bulk laser are summarized in Figure 1.1.

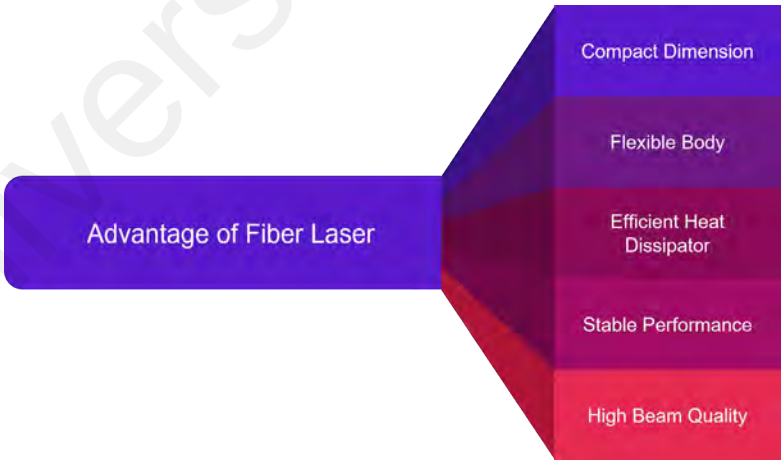

Figure 1.1: Advantages of fiber laser over conventional bulk laser.

1.2 Classification of Fiber Laser

The evolution of optical fiber lasers has perceived various laser output reported in a numerous configuration including multiwavelength, optical modulator and pulsed fiber

laser to feed the ever-growing demands from the laser end-users. This various classification of laser output take part in multitude of applications, such as telecommunications (Kbashi et al., 2021) and microwave photonics (X. Chen et al., 2006) for multiwavelength fiber laser (MWFL). Optical nonlinear effects and intracavity birefringence can be exploited to realize MWFLs, where stimulated Brillouin scattering (SBS) (Al-Mansoori et al., 2018; Shirazi et al., 2008), stimulated Brillouin-Raman scattering (SBRS) (Zhen Wang et al., 2017) and four wave mixing (FWM) (Al-Alimi et al., 2013) are among the nonlinear effects of interest to researchers. Being a by-product of Kerr nonlinear optical effect, FWM has nearly immediate response on the order of femtosecond, which proposes notable potential towards ultrafast all-optical signal processing components in practical realization (B. Jin & Argyropoulos, 2016). Besides, FWM also has a broad range of operating frequency including visible to IR region (Nodop et al., 2009) and low terahertz (THz) (Zhaolu Wang et al., 2012) region. As such, it has been used in numerous applications, those are entangled photon-pair generation (Takesue & Inoue, 2004), nonlinear imaging(Boyer et al., 2008; H. Kim et al., 2009), phase-sensitive amplification (Ho & Wong, 2002), switching (Klonidis et al., 2004), signal generation (Salem et al., 2008) and wavelength conversion (Sekhar et al., 2020).

Apart from multiwavelength fiber laser, all-optical modulator scientific achievements have been accomplished based on Kerr effect (Chow et al., 2009; J. Zheng et al., 2017), saturable absorption (Wei Li et al., 2014; C. Meng et al., 2015), and thermo-optic effect (Gan et al., 2015; Y. Wang et al., 2018) of two-dimensional (2D) materials up to now. Fast response, compact size and broad bandwidth are preferred in all-optical devices for applications in all-optical routing and all-optical logic gates (Yu et al., 2017). All-optical modulators that use thermo-optic effect satisfy the demands of particular fields, including optical routing and switching (Yu et al., 2017). It also possesses a handful of advantages to be applied for phase shifting, intensity switching and modulating when grounded on

interferometers such as easy fabrication, low cost, compact size, and large extinction ratio (Gan et al., 2015; C. Wang et al., 2019). The response time of all-optical modulator is greatly affected by the use of appropriate optical 2D material.

Pulsed fiber lasers have been extensively studied and evolved over the past decades. Pulsed laser can generally be classified into two types, those are Q-switched and mode-locked pulse laser. They have grabbed enormous attention due to its capability to access a wide range of scientific and industrial process including material processing (Salcedo et al., 2012), ultrafast spectroscopy (H.-L. Yang et al., 2014), medical treatment (Fried & Murray, 2005; Popov, 2008), and optical time division multiplex (Y. Dong et al., 2011). Generation of pulsed fiber lasers are based on active and passive approaches, where the former uses external modulator to manipulate the signal intensity by using acoustic-optic modulator (AOM)(Hong et al., 2012) or electro-optic modulator (EOM)(Ji et al., 2007). However, the shortcoming of having external support is the laser cavity becomes bulky (J. Lee, Jung, et al., 2014; J. Lee, Koo, et al., 2014a). Passive technique on the other hand, has the advantage of controlling the intrinsic property of fiber laser, which eliminate the additional size needed in active pulse fiber laser construction. Saturable absorber (SA) plays a crucial role in passive mode-locking technique. Artificial SAs commonly have qualities of high damage threshold and low cost, which initiated based on intracavity nonlinear effects by using nonlinear optical loop mirror (NOLM) (Szczepanek et al., 2015) and nonlinear polarization rotation (NPR) (Yan et al., 2015). On the contrary, unlike artificial SAs, real SAs are made up of 2D materials that exhibit intensity-dependent transmission as well as excellent optical properties. The wide absorption band and ultrafast recovery time are among the attributes that gained interest in the use of 2D materials (Harith Ahmad et al., 2021). Figure 1.2 sums up the classifications of photonics applications with nonlinear devices and phenomena.

Figure 1.2: Photonics applications with nonlinear devices and phenomena.

1.3 2D materials and Its Construction

The knowledge of material structure is the basis of technology, where each application requires specific material properties. The compelling reality is that material behavior is also affected by its size, especially when the dimensions are dialed down to nanoscale for some material. In general, nanomaterials can be grouped by the total number of their nanoscopic dimensions. Quantum dot is an example of zero-dimensional (0D) nanomaterial since all three dimensions of the material are nano sized, while commonly familiar as nanoparticle. If one of the dimensions is larger than nano sized, then it is a one-dimensional (1D) nanomaterial or usually called nanotube. Carbon nanotube is an example of 1D nanomaterial. The group that we engage in our everyday lives that can be perceived by naked eye is three-dimensional (3D) material or referred to bulk material. However, a 3D material with a negligible thickness to the scale of nano in one dimension can be regarded as two-dimensional (2D) nanomaterial which form a planar structure volume or nanosheet. The most recognizable 2D nanomaterial is credited to none other than graphene.

Many materials have 3-dimensions oriented chemical bonds making it unsuitable to cutting these bonds to create 2D materials as it will build a high density of dangling bonds. This state will render it to be chemically and energetically unstable and force it to reposition its structure to lessen its surface energy. However, there are materials with strong chemical bonds along planes but held together by weak van der Waals interaction between these planes such as graphite, an allotrope of carbon. Such material can be separated with no dangling bonds attached; thus, the wide-ranging class of layered materials (van der Waals materials) comprise most of the 2D materials being studied. 2D materials can be constructed mainly by using two methods, top-down and bottom-up. Top-down is when thinning down a bulk material, while bottom-up is when assembling atomic constituent.

These two methods can be subcategorized into several procedures, such as mechanical exfoliation or also known as the Scotch-tape method which was used to make monolayer graphene initially. The surface of layered material is peeled off by applying a piece of sticky tape onto it before stripped down, taking a few layers (flakes) of the material with it. The flakes can then be transferred by pressed onto a substrate. This process has no control over the size and shape, plus it gives little monolayer yield. Still, excellent quality of the monolayer is guaranteed due to the absence of chemical processing, and it produces a reasonable size of monolayer flakes ranging from a few microns up to about 100 μm. Due to this reason, mechanical exfoliation on van der Waals material holds its popularity for lab-based studies but not scalable to incorporate into new technologies. Besides Scotch-tape method, an organic solvent can also be used to carry mechanical force to the layered material in liquid exfoliation method. During the process, layers in material are torn apart due to the tensile stress generated during sonication. There are variations exist to enhance monolayer yield such as introduce reactive ions that propel the layers apart due to the creation of hydrogen bubbles between the material layers or generate additional

shear force on the layers by rapidly mix the solution. Unlike mechanical method, this method is particularly scalable, but it comes with several disadvantages. Not only the flakes are frequently less than 100 nm in size, but it yields low monolayer quantity. The product is incompatible for many optoelectronic applications because it is exposed to high density of defects and residual solvent when extracted from the solution.

Furthermore, a thin layer of the required material can be formed in chemical vapour deposition, where it involves one or more precursor gases that contain the atomic ingredients of the required film, passing through a heated furnace to react together or to react with a substrate. The thickness, quality and composition of the films are influenced by several parameters including temperature, reaction times, and gas pressures and compositions. This technique is highly scalable, and the quality is on par with mechanically exfoliated layers although it appears to be more complex and expensive. Lastly, 2D materials can also be fabricated through solution-based chemical synthesis. An extensive variation of techniques has been developed comprising interface-mediated growth, fusion of nanoparticles into bigger nanosheets, high temperature chemical reactions in solution and many more. Every method is distinctly well-suited to a particular type of 2D material using the appropriate technique. The drawbacks of this method are it has residual solvent problem, and the flakes size is generally less than 100 nm. Nonetheless, it fit for large-scale production for certain applications due to the scalability, economical and versatility.

Graphene as a primordial 2D material has found its outstanding performance in numerous applications ranging from transparent conductor to thermal interface materials, as well as barristor transistor-like devices (K. S. Kim et al., 2009; Stankovich et al., 2006; H. Yang et al., 2012). Yet, there exists an entire periodic table of crystalline solid-state materials each possesses distinct mechanical, electronic, and transport properties. On that note, there are over 1000 papers have been published by scientists since the discovery of

MXenes 11 years ago. This ongoing explosive growth of interest has attracted many researchers from different areas including photonics due to its unique attributes' combination of ceramics and metals. Most of the present MXenes have been created by selective etching of the Al layer from MAX phases up to now, however, there are rooms to be improved to create MXenes safely and effectively.

1.4 Research Objectives

There are lists of MXenes besides primordial Ti_3C_2 that have not being explored yet in photonics application despite its unique physical and chemical properties, since MXenes were relatively new family of 2D materials. Plus, most of the MXenes used in photonics field research are fabricated by using HF, which has its downside mainly to the fabricator. The first attempt to weaken the M-A metallic bonds while preserve the strength of the M-X bonds in MAX phase was by exposing a layered precursor such as Ti_3AlC_2 to concentrated solutions of aqueous HF. HF can easily damage cells and renders it malfunction, while over exposed to the HF can cause death as a consequence of damaged lung tissues. Besides, the leftover of HF in soil environment because of improper chemical waste disposal can negatively affect soil and groundwater quality. The conventional HF etching method is not only harmful but also proven to be inefficient in some cases. Due to the nature of HF being very dangerous to human and environment, however, alternatives were discovered. Hence, the main aim of this research is to use alternative harm-free fabrication method of MXenes (M_2X), and to study the performance of MXenes (M_2X) as nonlinear material in photonics area. Following are the three objectives of this research:

1. To synthesize MXenes from MAX phase by using fluoride salts and acid mixture of lithium fluoride (LiF) and hydrochloric acid (HCl) to replace the conventional harmful hydrofluoric acid (HF).
2. To study the physical and optical properties of synthesized MXenes.

3. To investigate the MXenes performance as nonlinear material in pulsed fiber laser, four wave mixing, and all-optical modulation configurations.

1.5 Thesis Outline

The content of this thesis is organized into six main chapters as Figure 1.3, where a comprehensive discussion about the topic is presented in each chapter. This chapter offers a brief history of fiber laser, different type of fiber laser as well as commonly used methods to construct 2D materials. The objectives of this research are also highlighted in this chapter.

Chapter 2 describes the historical background of nonlinear material, ranging from bulk material to nanomaterial. Then, historical background of MXenes and its current progress. The type of MXenes, its structural composition as well as synthesis method are also presented. Plus, the theoretical prediction of MXenes in electronic and optical properties are described along with the optical nonlinear phenomena. Fundamental concept of fiber lasers including theoretical equation model of thulium in silica and fluoride hosts, Q-switching, mode-locking, four wave mixing and optical modulation are covered in this chapter.

Chapter 3 discusses the fabrication method of MXenes and their characterization comprising of physical and optical sections. The details fabrication method by using HF-forming etchant (LiF + HCl) is described for each MXenes (Ti_2C. Nb_2C, and V_2C), and the experimental setup involves during fabrication process is presented. The chemical safety measure is also included in this chapter. Moreover, the experimental setups for linear and nonlinear optical absorption are described in one of the sections. Finally, the finding from physical characterizations such as FESEM, HRTEM, XRD and Raman

spectroscopy, and optical characterizations such as linear absorption, saturable absorption, and Z-scan analysis on MXenes are addressed.

Chapter 4 addresses the details of mode-locked laser, and Q-switched laser performance by using MXenes. The experimental setup for each configuration are presented early in every section before discussing the experimental findings of each system. A comprehensive performance comparison are presented at the end of every sub-chapter.

Chapter 5 addresses the details of FWM, and all-optical modulator performance by using MXenes. The experimental setup for each configuration are presented early in every section before discussing the experimental findings of each system. A comprehensive performance comparison are presented at the end of every sub-chapter.

Chapter 6 summarizes and concludes the findings of the study that have been carried out in this thesis all-inclusively. Recommendation and possible future work based on the research findings have also been proposed at the end section of this chapter.

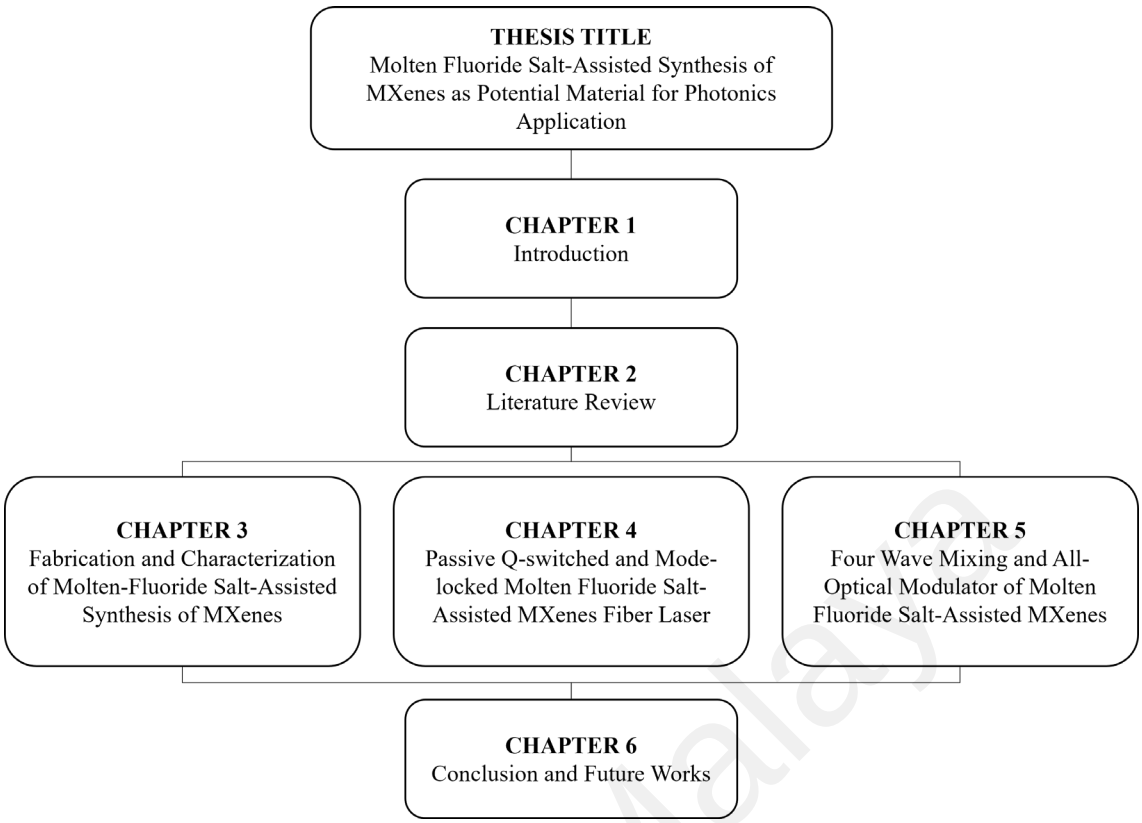

Figure 1.3: Thesis outline.

CHAPTER 2: LITERATURE REVIEW

2.1 Historical Evolution of Nonlinear Optical Material

After the invention of lasers, the first demonstration of second-harmonic generation (SHG) and various other nonlinear optical phenomena were commenced (Boyd, 2008). Nonlinear optical materials in the shape of bulk crystal or semiconductors with average sizes in the order of centimetres by centimetres, like lithium niobate (LN), barium borate (BBO), and semiconductor saturable absorber mirror (SESAM), are usually used in bulk-optic systems (U Keller, 2010). Nonlinear effects of waveguide-based or fiber-based materials are typical nonlinear optical devices utilized in fiber-optic systems that have beam size in tune with that of the systems (Agrawal, 2000). An example of nonlinear optical device that own third-order $\chi^{(3)}$ optical nonlinearity at 2 orders of magnitude greater than silica is silicon waveguide. As much as advantage it possesses, silicon has attenuation at high optical intensities due to the high two-photon absorption (TPA) nonlinearity (Leuthold et al., 2010). Thus, the incorporation of nano-size nonlinear optical materials without TPA would therefore benefit the silicon photonic devices. Potential nano-size 1D or 2D material candidates such as graphene, carbon nanotube (CNT), and transition metal dichalcogenide (TMD) are suitable for the integrated-optic system. These nanomaterials are greatly suitable for application in either fiber or waveguide-optic systems to be significant technology platform (Martinez et al., 2014; Yamashita, 2011a). The development of nonlinear optical devices is shown in Figure 2.1.

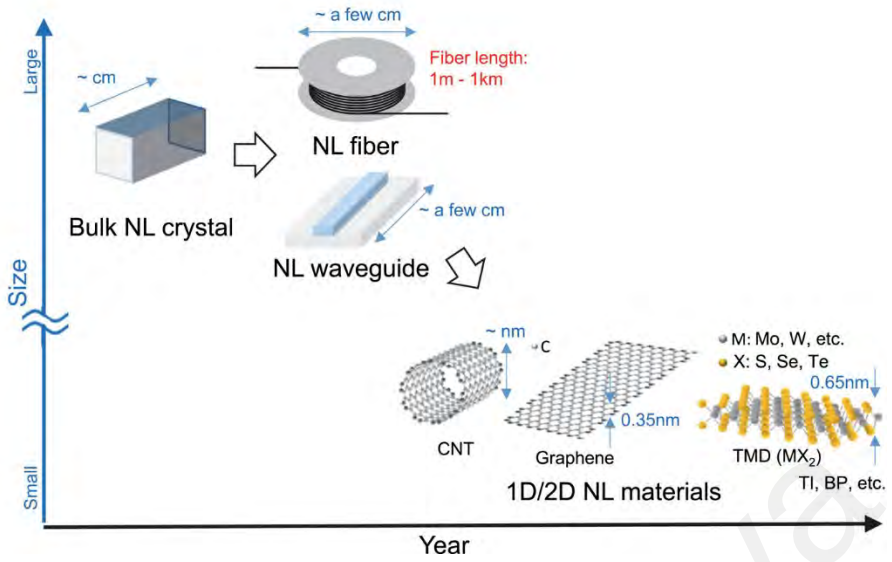

Figure 2.1: Evolution of nonlinear optical devices (Copyright permission from Yamashita, 2019).

The properties of 2D material became a subject of intense study after the discovery of undemanding technique to isolate high quality graphene by A. Geim and K. Novoselov (Novoselov et al., 2004), although the existence of graphene has been reported earlier (Land et al., 1992; Randin, 1981). Graphene, a constituent of the familiar graphite, is a single layer of carbon atoms arranged in a hexagonal honeycomb lattice. Even though graphene is the building block of graphite, but research has revealed that 2D graphene bulk material holds distinct physical, chemical, electronic and optical properties in contrast to its parental material (Ferrari, 2007; Geim, 2009; Partoens & Peeters, 2006). This result has piqued interest in research community to bring this exploration beyond graphene and revealed the potential of various 2D materials over the past decades. TMD (J. Du et al., 2014; Wensong Li et al., 2016), topological insulator (TI) (B. Guo et al., 2016; H. Liu et al., 2014), black phosphorus (BP) (Yu Chen et al., 2015; Sotor et al., 2015), and transition metal carbides or nitrides (MXene) are among the materials that are extensively investigated, which are interesting for many optoelectronics and photonics applications owing to their unique characteristics.

Miniaturized photonics systems can be realized by using 2D materials with natural strong light-material interactions to achieve desired functionalities. Strong light modulations of graphene, graphene oxide (GO), and TMDs have been displayed in nanoscopic scale ultrathin flat lenses down to a monolayer level (J. Yang et al., 2016). On that note, the potential of MXenes have not been fully explored yet, particularly in photonics area. Based on the demonstrated works thus far, MXenes show a great performance in pulse generation (Fu et al., 2021). High performance SAs are enabled by the accomplishment of 2D materials nonlinearity that have manifold of strength higher than the typical semiconductors (Y. Yang et al., 2018; X. Zheng et al., 2014). Plus, the optical instantaneous change characteristics of 2D materials capability make them flexible for various in situ tunable optical instruments by tuning the carrier density or optical bandgap via optical or electrical means. Various function by stacking different 2D material layers into heterostructures are now possible in the development of material family exploration.

2.2 Introduction to 2D Transition Metal Carbides and Nitrides (MXenes)

2.2.1 The Beginning of MXenes

In the twentieth century, group 4 – 6 transition metal carbides and nitrides were explored as hard, high-temperature, chemically stable and wear-resistant materials (Oyama et al., 1988). Several nanostructure configurations have been proposed following the discovery of their catalytic behaviour in the 1970s (Levy & Boudart, 1973) to enhance the surface area and performance in the exploration of energy storage applications (Gogotsi & Andrievski, 2012; Zhong et al., 2016). The study on this topic were taking small steps, until a breakthrough happened in 2011 by the discovery of the first 2D titanium carbide ($Ti_3C_2T_x$) that open on to a new family of 2D transition metal carbides

and nitrides, named MXenes (Naguib et al., 2011b, 2012). It has become a big and rapidly growing family of 2D materials.

MXene has unique physical and chemical properties, which possesses not only outstanding mechanical and chemical stability of ceramic, but also excellent charge accessibility due to its inherent structure (Halim et al., 2014). Among the large family of MXene, Ti_3C_2 is certainly the most dazzling one, involving the systematic experimental studies, and density-functional theory (DFT) theoretical calculations to investigate the electronic structure of many-body systems, in particular atoms, molecules, and the condensed phases. Conversely, only few research on the other MXenes were performed, especially experiment involving photonics field. For example, in passive pulsed laser technology that become a great interest due to its simplicity and compactness. The existing passive pulsed laser system accessible in the market is mainly implemented using SESAM device. SESAM can induce stable pulse operation due to its well-constructed saturable absorption characteristics which is predefined during the fabrication process. Despite its positive performance, the fabrication process of SESAM device requires technologically specific facilities such as molecular beam epitaxy system which is expensive not only for operation but also maintenance. Not only that, the optimization of SESAM device requires additional processes such as structural defects induction and post growth implantation. Overall, the complexity of SESAM's fabrication process leads to high implementation cost of passive pulsed laser system using this technology. Due to the outstanding features of MXenes, it has been used in many applications including hydrogen evolution reaction (HER) (Z. Guo et al., 2016; Ran et al., 2017), electrodes of supercapacitor (Y. Tian et al., 2017; X. Wang et al., 2019) and anode of lithium-ion battery (Y. T. Du et al., 2018). Only few MXenes have been reported in photonics field such as the primordial $Ti_3C_2T_x$ (Y. T. Du et al., 2018), this shows the optical properties of MXenes have yet to be fully explored.

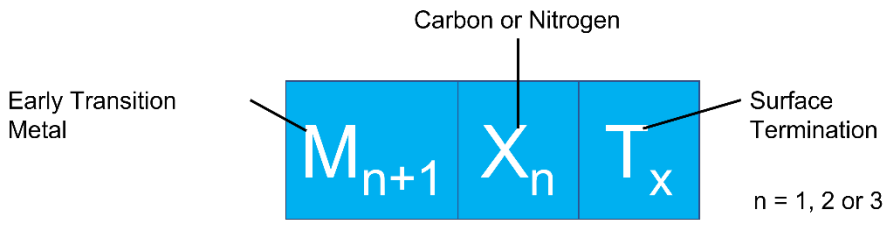

Figure 2.2: Chemical composition of MXenes.

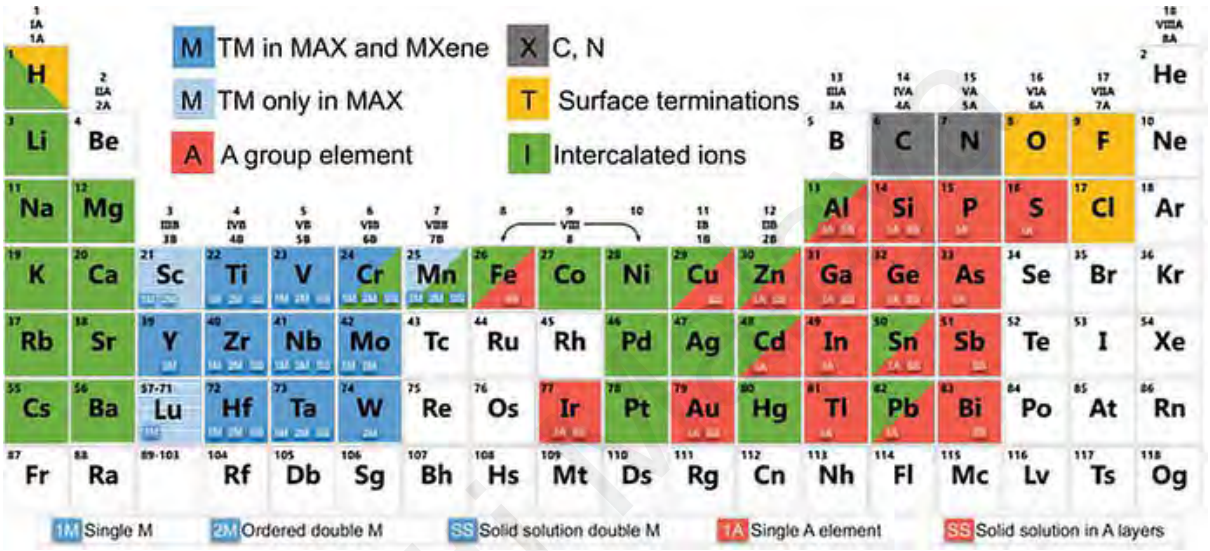

Figure 2.3: Periodic table showing the elements in MAX phases and MXenes, surface terminations, and intercalant cations, based on experimental studies (Copyright permission from Anasori & Gogotsi, 2019).

Inspired by the synthesis of Ti_3C_2, material from similar group has been synthesized such as Ti_2C (Ying et al., 2017), V_2C (Naguib et al., 2013), Mo_2C (Seh et al., 2016) and Nb_2C (Mashtalir et al., 2015). These 2D materials are made by removing an A element from MAX phase, a family of ternary carbide or nitride (Barsoum, 2013), where the A elements are groups 13 – 16 of the periodic table. MXenes have a formula of $M_{n+1}X_nT_x$, where M is an early transition metal, X is carbon or nitrogen, and n is from 1 to 3 as shown in Figure 2.2 (Anasori et al., 2015, 2017). The surface termination groups that are predominantly =O, -F, and -OH are represented by T, and the subscript x in T_x shows the amount of surface functionalities. There are also published reports with surface termination of -Cl on $Ti_3C_2T_x$ MXene on few occasions (W. Sun et al., 2017; S. Yang et

al., 2018). The thickness of the 2D sheets is in the scale of 1 nm and compliant to the n number in MXenes. Thus, the size can be altered by changing the n from M_2XT_x, to $M_3X_2T_x$, and $M_4X_3T_x$.

The selective etching of Al layers from MAX phase have made most of the reported published MXenes so far (25 out of 29). When an A element couples $M_{n+1}X_n$ layers together, it will form layered ternary carbides and nitrides or MAX phase (Barsoum, 2013). However, transition metals of groups 8 – 12 of the periodic table have also shown potential to become the A layer (Fe, Cu, Zn, Cd, Ir, and Au) of MAX phases as proved in recent studies. They can exist either in the form of solid solutions (highlighted with a red "SS" box) or as pure A elements (highlighted with a red "1A" box). SS not only indicates the existence of solid solutions in A-element planes (red), but also in transition metal atomic planes (blue). In the specific elements marked with 1M and 1A suggest the possibility of a single (pure) transition metal and A-element in MAX phase and MXene formation. Figure 2.3 marks all of the experimentally investigated A elements of MAX phases in red and MXenes' surface terminations in yellow. All of the M, X, A, and T of MAX phases and MXenes have also been pointed up in the periodic table. The formation possibility of an ordered double transition metal MAX phase (either in-plane or out-of- plane) is labelled as 2M. Elements that have only been studied through first principle calculations are not included in the periodic table. Transition metals reported for MAX phases and MXenes are shaded in solid blue, and TMs that are only reported in MAX phases are shaded in blue with horizontal stripes (Sc, Lu, and Mn). MAX phases with Mn element have been reported (Ingason et al., 2014; Mockuté et al., 2015), yet there is no pure Mn-containing MXene as M has been synthesized from a MAX phase to date. Lanthanides has the potential ability to be MAX phase components since a lutetium-containing MAX phase (Lu_2SnC) has been synthesized (Kuchida et al., 2013). The recorded intercalated metal cations (Li^+, Na^+, Ca^{2+}, and Al^{3+}) are highlighted in green in

Figure 2.3. Due to the intercalation capability of MXenes, it also has been used to adsorb heavy metal ions such as Pb and Pd. Ions can only enter between the MXene sheets, but not in MXene flakes due to the strong and short M-X bonds. Astoundingly, the intercalated cation sizes and charges can affect the properties of MXenes, comprising electrical, electrochemical, and mechanical, and the interlayer spacing.

2.2.2 Structure, Composition, and Synthesis

Although MAX phases were labeled in the late 1990s, but the first appearance of them were in the 1930s to the 1960s (Barsoum, 2013). The selective etching of the A layers in MAX phases is possible since the M-X bonds are usually stronger than metallic bonding between the M-A layers that holds the $M_{n+1}X_n$ layers together. New subfamilies of MAX phases have been found, specifically in-plane and out-of-plane ordered double transition metal carbides, through the fast development of MXene chemistry and attention given in synthesizing new MXenes. Ordered structures of MAX phases were formed rather than solid solutions in the combination of two transition metals, primarily between a heavy transition metal with a light one. One or two layers of M in the carbide structure are sandwiched by two layers of another transition metal in the out-of-plane ordered structure, such as Mo_2TiAlC_2 and $Mo_2Ti_2AlC_3$. Successfully fabricated ordered double transition metal MXenes through selective etching Al layers are marked in red in Figure 2.4.

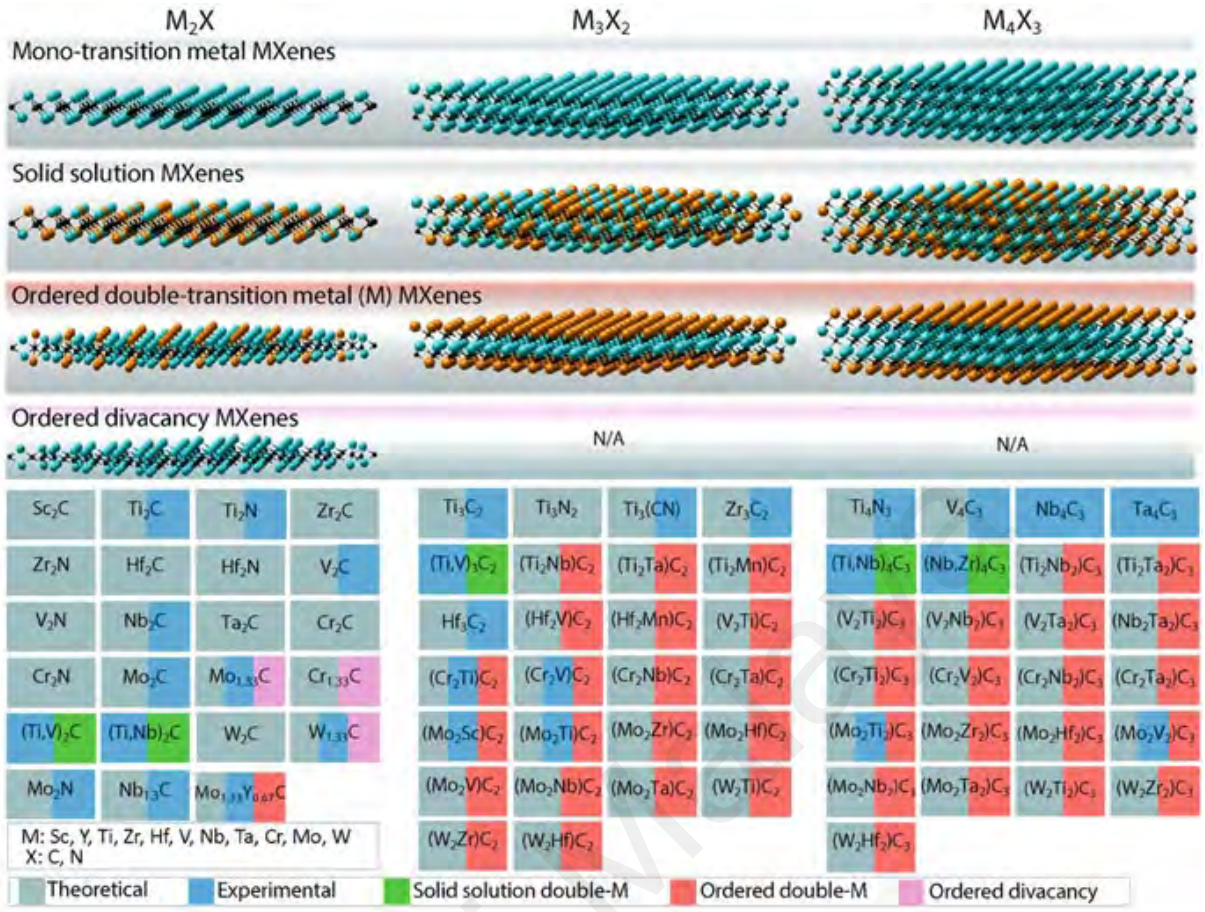

Figure 2.4: Composition of MXene reported until 2019. The table covers both experimentally (shaded in blue) and theoretically (shaded in gray) explored MXenes (Copyright permission from Anasori et al., 2017).

In-plane ordering has been reported in the M_2AC structure comprise of only two layers of M, where the basal planes are made of distinct rows of two types of M elements, such as $(Mo_{2/3}Sc_{1/3})_2AlC$, $(Mo_{2/3}Y_{1/3})_2AlC$, and $(W_{2/3}Y_{1/3})_2AlC$. Selective etching on the in-plane MAX phases yield two different types of MXenes. In-plane ordered double transition metal MXenes can be synthesized by selective etching the Al layers, such as $(Mo_{2/3}Y_{1/3})_2CT_x$ as highlighted in red in Figure 2.4 or ordered divacancy MXenes can be synthesized by selective etching the Al layers with the lighter transition metal, such as $Mo_{1.33}CT_x$ and $W_{1.33}CT_x$ as highlighted in pink in Figure 2.4. Since this MXene phases own about 33% atomic vacancies in the transition metal layers, they obey a $M_{1.33}XT_x$ formula instead of the general formula of $M_{n+1}X_nT_x$. MXenes can also be selective etched from other layered ternary carbides beyond MAX phases, that is a large family of

$(MC)_n[Al(A)]_mC_{m-1}$ with above 30 compounds available. The $M_{n+1}X_n$ layers in such carbides can be isolated from either two layers of an A element (Mo_2Ga_2C) or layers of A element carbides such as Al_3C_3 in $Zr_3Al_3C_5$ and $(Al,Si)_4C_4$ in $Hf_3(Al,Si)_4C_6$. There are beyond 60 possible stoichiometric MXene compositions and a boundless number of solid solutions.

MAX phases and the other 3D layered MXene precursors of ternary carbides and nitrides have primary bonding hold the layers either by the A element or A_mC_{m-1} layers, unlike most of the 2D materials precursors. Subsequently, only chemical exfoliation methods have been utilized to synthesize MXenes. The schematic top-down synthesis of M_2XT_x, $M_3X_2T_x$, and $M_4X_3T_x$ MXenes and MXene precursors are shown in Figure 2.5. So far, fluoride-containing acidic solutions have been utilized for MXene synthesis predominantly, like hydrofluoric acid (HF) or a mix of lithium fluoride (LiF) and hydrochloric acid (HCl). However, electrochemical selective etching makes it possible for fluoride-free etching alternatives, such as etching Ti_2AlC in chloride-containing electrolyte (W. Sun et al., 2017; S. Yang et al., 2018). MXenes have a significant advantage over several other 2D materials in term of feasible large-scale production due to the selective chemical etching. Top-down method has been used by 28 out of 29 MXenes (except for Mo_2N) as shown in Figure 2.5. Surface-termination-free 2D transition metal carbides and nitrides can be made by using bottom-up method, yet it has been the least studied for MXenes since it deals with the formation of bulk and non-2D carbides. Chemical vapor deposition and pulsed laser deposition methods have managed to deposit fine Mo_2C and W_2C film down to $2 – 3$ nm-thick. Another example of bottom-up method is the formation of transition metal oxides and transform them to nitrides and carbides in the salt-templating method.

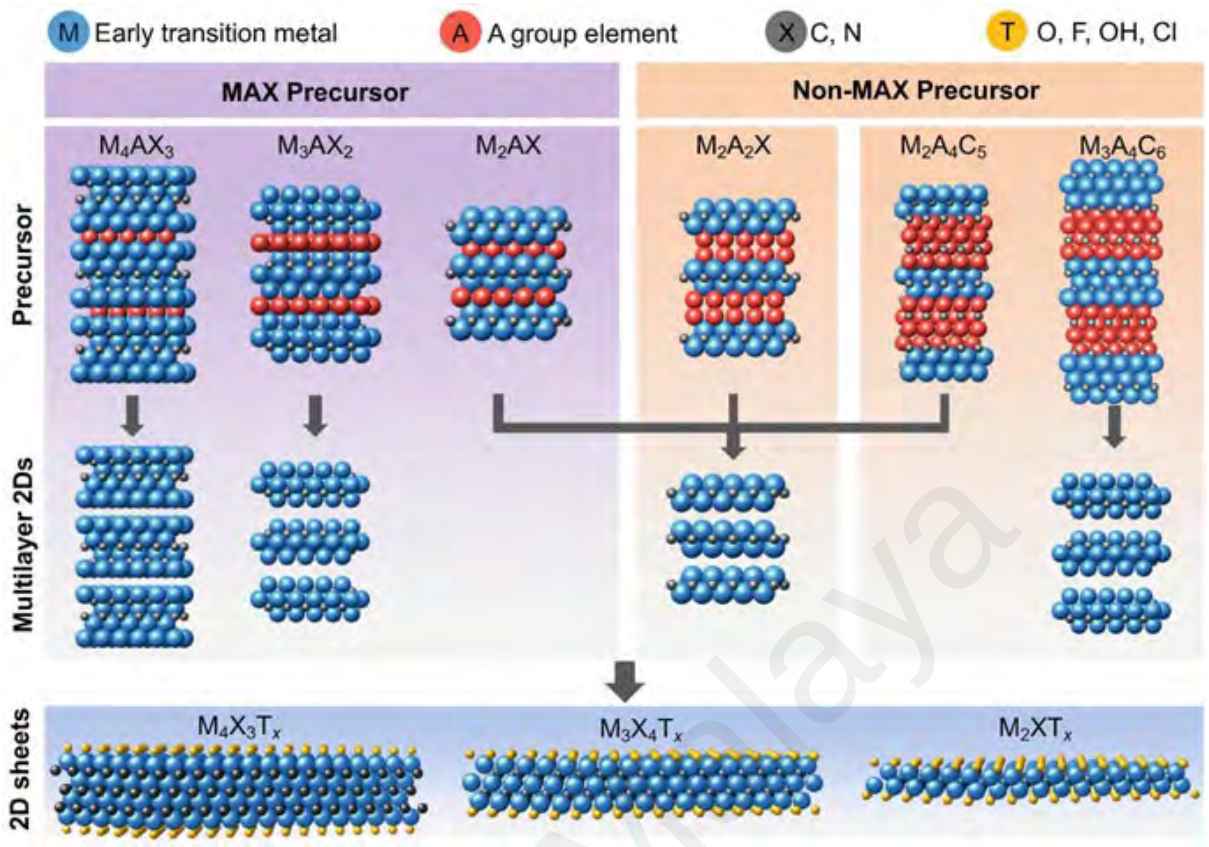

Figure 2.5: Synthesis of MXene from its MAX and non-MAX precursors by selective etching (Top-down) (Copyright permission from Anasori & Gogotsi, 2019).

Synthesis and processing of MXenes through the dominant top-down method selective chemical etching significantly affect its properties (Anasori et al., 2017; Xiao et al., 2018). In the most studied primordial MXene, $Ti_3C_2T_x$, the OH, O and F of surface termination (T_x) come in different ratios depend on the etching process, such as etchant composition and heat, processing conditions, such as rinsing steps and delamination, and post-synthesis steps as well as storage environments. Generally, MXene surfaces has a higher fluorine content if the etchant contains higher concentration of HF. However, the quantity of defects in MXene flakes rises as more aggressive etchant is employed. The morphology of the etched multi-layered powder even disturbed in strong etching conditions, such as accordion-like form of flakes in concentrated HF, which such form is not observed under milder etching conditions. Other than that, the type of transition metals also affects the surface terminations. For instance, despite the requirement of

higher concentration of HF in Mo_2CT_x production (Halim et al., 2016), it has least fluorine terminations in contrast to $Ti_3C_2T_x$.

Delamination to single-layered flakes is an essential step to entirely benefit from the 2D nature of MXenes for applications in adsorption and Li-ion batteries. The separation and delamination of MXene sheets are made through intercalation. Many intercalants have been utilized via chemical or electrochemical reaction that come from distinct metal cations as marked in green in Figure 2.3 and organic molecules. Some heavy metal ions, such as Pb and Pd are adsorbed by using MXenes due to their intercalation capabilities. Ions can only penetrate between the MXene sheets as the M-X bonds are strong and short. As such, the properties, comprising electrochemical, electrical, and mechanical, as well as the interlayer spacing of MXenes can be modified by the intercalant sizes and charges. Numerous cation intercalants can be operated to delaminate MXene, such as a mixture of lithium fluoride (LiF) and hydrochloric acid (HCl) to etch the precursor and raise the pH in the washing step to delaminate MXene, hence, additional intercalant is not required for delamination. In the contrary, organic molecules like tertiary amines (tetrabutyl- and tetramethyl-amonium hydroxides) are used to intercalate and delaminate multilayer MXene when pure hydrofluoric acid (HF) is used during the precursor's etching process. Lately, additional salts, such as lithium chloride (LiCl) has been used to help the intercalation and delamination in a mixed acids solution, such as HF-HCl during the etching process (Sarycheva et al., 2018).

2.2.3 Theoretical Predictions of Electronic and Optical Properties

To realize the integration of MXenes into nanoscale devices, several groups have devoted to grasp the knowledge of its physical behaviour in the last decades (Khazaei et al., 2017), particularly, $Ti_{n+1}X_n$ (X = C, N and n = 1, 2). This MXene compounds were explored substantially in both experiments and theory to understand and predict the properties with substituting elements, lattice structure, and surface termination groups.

Electronic properties and structure of materials intricately affect its optical response, such as enhancement of optical absorption at specific frequencies by band-to-band electronic transitions. An absolute understanding of such possible mechanism underlying material optical response can be gained through theoretical framework, besides predicting behavior of other similar systems, which is crucial for the quickly developing family of synthesized MXenes.

The density of states (DOS) and band structures used to predict optical behavior of single MXene flake are calculated by H. Lashgari et al. through DFT formulation (Lashgari et al., 2014) as laid out by K. Chauduri et al. (Chaudhuri et al., 2019). The overlapping of valence and conduction bands with the Fermi level of electronic properties in most of $Ti_{n+1}X_n$ MXenes verify their metallic class. The 3D orbital of Ti plays significant part to the metallicity near the Fermi level. Furthermore, the optical response (reflection, absorption, complex dielectric function (ε), and electron energy loss function) of 2D $Ti_{n+1}X_n$ MXene compounds, such as Ti_2C, Ti_2N, Ti_3C_2, and Ti_3N_2, are also quantified by H. Lashgari et al. through the full-potential linearized augmented plane wave (FP-LAPW) method (Ambrosch-Draxl & Sofo, 2006) and random phase approximation (RPA) formalism (X. Ren et al., 2012). The imaginary part of the dielectric function, $Im\ \varepsilon$, is evaluated as

$$Im\ \varepsilon_{ij}^{[interband]}(\omega) = \frac{h^2 e^2}{\pi m^2 \omega^2} \sum_n \int dk \langle \psi_k^{C_n} | p^i | \psi_k^{V_n} \rangle \langle \psi_k^{V_n} | p^j | \psi_k^{C_n} \rangle \delta\left(E_k^{C_n} - E_k^{V_n} - \omega\right) \tag{2.1}$$

where the $\psi_k^{C_n}$ and $\psi_k^{V_n}$ correspond to the empty conduction band levels and the occupied valence band levels, respectively, over k points of the first Brillouin zone. $E_k^{C_n}$ corresponds to the unoccupied conduction band and $E_k^{V_n}$ represents the occupied valence

band states, while ω is the frequency of the interacting electromagnetic wave. The corresponding real part, $Re\ \varepsilon$, can be acquired by using inverse transformation

$$Re\ \varepsilon_{ij}^{[interband]}(\omega) = \delta_{ij} + \frac{2}{\pi} P \int_0^{\infty} \frac{\omega' Im\ \varepsilon_{ij}(\omega)}{(\omega')^2 - \omega^2} \tag{2.2}$$

where the principal value of the integral is denoted as P.

The calculation of the effect from the intraband transitions are done separately

$$Im\ \varepsilon_{ij}^{\{intraband\}}(\omega) = \frac{\Gamma \omega_{pl,ij}^2}{\omega(\omega^2 + \Gamma^2)} \tag{2.3}$$

$$Re\ \varepsilon_{ij}^{\{intraband\}}(\omega) = 1 - \frac{\omega_{pl,ij}^2}{\omega(\omega^2 + \Gamma^2)} \tag{2.4}$$

$$\text{where } \omega_p^2 = \frac{ne^2}{\varepsilon_0 m} \tag{2.5}$$

ω_p^2 represents the plasma frequency, n is the electron concentration or the free carrier, m corresponds to the effective electron mass, ε_0 is the vacuum permittivity, and Γ represents the loss/damping expression in the Drude model. The summation of inter- and intraband electronic transitions gives the complete dielectric function as

$$\varepsilon(\omega) = \varepsilon^{\{intraband\}}(\omega) + \varepsilon^{[interband]}(\omega) \tag{2.6}$$

The complex dielectric function, ε tensor has only three nonzero components $\varepsilon^{xx}(\omega) = \varepsilon^{yy}(\omega)$ and $\varepsilon^{zz}(\omega)$ under the excitation of an electric field parallel, $E||x$ and perpendicular, $E||z$ to the c-axis, due to the hexagonal structure group symmetry from monolayers of $Ti_{n+1}X_n$ (X = C, N and n = 1, 2) with three atoms for Ti_2X and five for

Ti_3X_2. Figure 2.6(a) represents the corresponding dielectric tensors of Ti_3C_2. The distinct inter- and intraband electronic transitions contribute straight to the peaks in the $Im\ \varepsilon$, where the Figure 2.6(a)- inset shows the diametric part of the ε, $Re\ \varepsilon$ acquired using the Kramers-Kronig relations (Fox, 2002; Wooten, 1973). Additional significant optical parameters such as the reflection and absorption can be extracted from the frequency-dependent complex dielectric function. The entire contribution of interband transitions from charged valence band states to empty conduction band states is proportional to the absorption spectrum, A as shown in Figure 2.6(b).

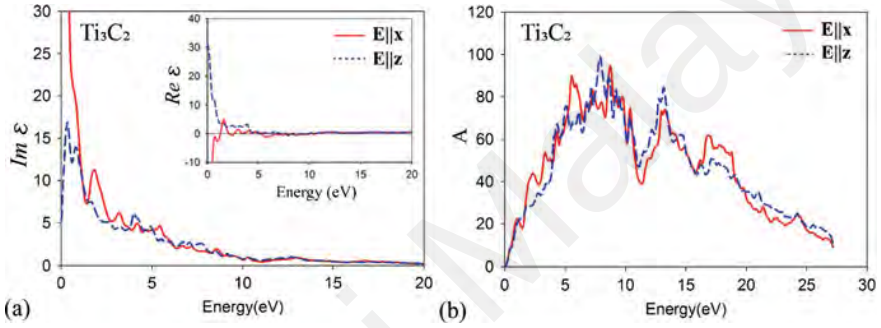

Figure 2.6: Computed (a) imaginary and real part of the dielectric function and (b) absorption coefficient for Ti_3C_2 MXene. The solid red and dashed blue lines represent the two nonzero dielectric tensor components $\boldsymbol{\varepsilon^{xx}(\omega)}$ and $\boldsymbol{\varepsilon^{zz}(\omega)}$ for electric field perpendicular $\boldsymbol{E||x}$ and parallel $\boldsymbol{E||z}$ (Copyright permission from Lashgari et al., 2014).

The functional groups, such as -F, -O, and -OH, during the synthesis activity passivate the outermost transition metal atoms of a single layer of MXene (Naguib et al., 2011a, 2012; X. Zhang et al., 2015). Both structural and electronic properties can be greatly affected by the surface functionalization as appeared in recent studies. Adjustment on the surface functional group can also tailor particular attributes of the MXene properties, such as electron transport and capacitance. The consequence of the functionalization on the optical properties of $Ti_3C_2T_2$ MXene has been discussed by G. Berdiyorov by using computational methods, where 'T' corresponds to a surface functional group, either -F, -O, or -OH (Berdiyorov, 2016). The Kubo-Greenwood formula used to find electronic

conductivity in materials is utilized to calculate the susceptibility tensor $\chi(\omega)$ of the MXene monolayer system (Harrison, 1980). The electric susceptibility of the material system gives the frequency-dependent complex dielectric properties as $1 + \chi(\omega) = \varepsilon(\omega) = Re\ \varepsilon + Im\ \varepsilon$.

2.3 Nonlinear Optical Properties in MXenes

2.3.1 Fundamentals of Nonlinear Optics

In an isotropic material, a generated polarization, $P(t)$ during an instantaneous dielectric response can be associated with electric field, $E(t)$ by

$$P(t) = \varepsilon_0\left(\chi^{(1)}E(t) + \chi^{(2)}E^2(t) + \chi^{(3)}E^3(t) + \cdots\right) \tag{2.7}$$

where ε_0 is the absolute dielectric permittivity of vacuum, $\chi^{(1)}$ is the linear susceptibility, and $\chi^{(2)}$ and $\chi^{(3)}$are the second- and third-order nonlinear susceptibilities, respectively (Boyd, 2020; Leuthold et al., 2010).

Second harmonic generation (SHG), and sum- and difference-frequency generations (SFG and DFG) are attributed to the second-order nonlinearity, $\chi^{(2)}$, where the term can be discarded in material that has inversion symmetry at the molecular level (Boyd, 2020). Therefore, both CNT and graphene do not have the second-order nonlinearity, since the honeycomb carbon structure fulfill the inversion symmetry, except when the symmetry is distributed. Oppositely, large $\chi^{(2)}$ can be found in some 2D semiconductors (Autere et al., 2018). Besides, the electro-optic effect, like the Pockels effect are also associated to $\chi^{(2)}$ (Boyd, 2020).

Third harmonic generation (THG), nonlinear refractive index change (nonlinear Kerr effect), and nonlinear absorption change (multi-photon absorption and saturable

absorption) are attributed to the third-order nonlinearity, $\chi^{(3)}$. Many 2D materials, including CNT, and graphene have shown large $\chi^{(3)}$ (Autere et al., 2018; Yamashita, 2011a). The incident optical intensity influences the changes of refractive index, and optical absorption, where the complex refractive index, *n* can be expressed as (Boyd, 2020; Leuthold et al., 2010)

$$n = n_0 + n_2 I - i\frac{\lambda}{4\pi}(\alpha_0 + \alpha_2 I) \tag{2.8}$$

where *I* corresponds to the optical intensity, n_0 and n_2 are the linear and nonlinear refractive index (Kerr coefficient), respectively, and α_0 and α_2 are the linear and nonlinear absorption coefficient, respectively. The real and complex part of $\chi^{(3)}$ are interconnected to both n_2 and $\alpha_2$as

$$n_2 = \frac{1}{cn_0^2\varepsilon_0}\frac{3}{4}Re\left(\chi^{(3)}\right), \qquad \alpha_2 = \frac{-\omega}{c^2 n_0^2\varepsilon_0}\frac{3}{4}Im\left(\chi^{(3)}\right) \tag{2.9}$$

where *c* is the speed of light in vacuum. The refractive index for wavelengths near the absorption edge is significantly affected by the changes in the optical absorption because of the Kramers-Kronig relation (Boyd, 2020).

2.3.2 Saturable Absorption

One of the associative imaginary part of $\chi^{(3)}$ phenomenon is saturable absorption, where the material appears translucent to high intensity light and decreases the optical absorption, which can be conveyed as

$$\alpha(I) = \frac{\alpha_0}{1 + I/I_s} \tag{2.10}$$

where α_0 is the linear absorption coefficient, I is the intensity of light and I_s is the saturation intensity. The relatively weak incident optical intensity during linear regime will be attenuated by the material due to the absorption. However, during high incident optical intensity, the electrons in the lower energy states are diminished, filling the upper energy states. Hence, the light attenuation starts to decrease due to the occurrence of saturation of absorption. If the I value becomes insignificantly small, the Eq. 2.10 can be approximated to $\alpha \sim \alpha_0 - \alpha_0 I/I_s$. The saturable absorption property can be simulated as shown in Figure 2.7 in black curve, where the intensity and absorption are normalized as I/I_s and $(1 - e^{-\alpha l})/(1 - e^{-\alpha_0 l})$, respectively, since the attenuation of non-absorbed light transmission across a sample of thickness l is $e^{-\alpha l} I$ and $\alpha_0 l = 0.1$. The absorption cross section, σ, and the recovery time, τ influence the saturation intensity, I_s as

$$I_s = \frac{\hbar\omega}{\sigma\tau} = \frac{E_s}{\tau} \tag{2.11}$$

where ω corresponds to the optical angular frequency and E_s represents the saturation fluence (Ursula Keller et al., 1996).

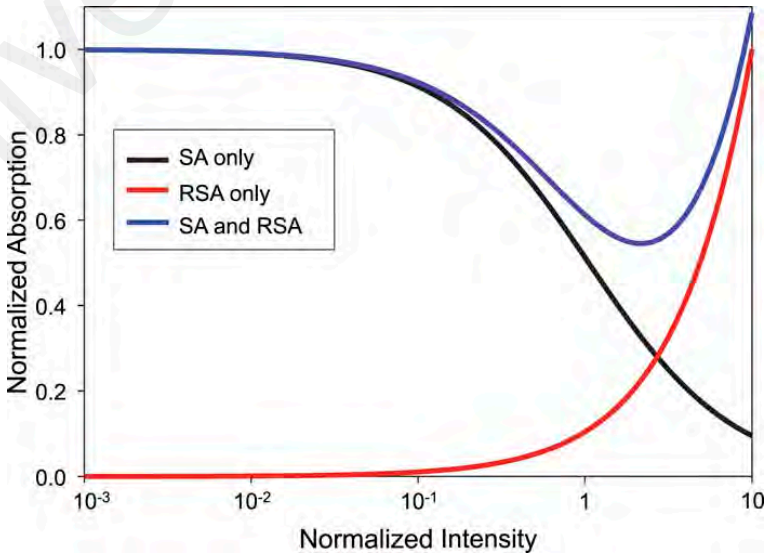

Figure 2.7: Computed SA and RSA properties (Copyright permission from Yamashita, 2019).

Saturable absorption is a common phenomenon in any material that manifests optical absorption owing to the electronic transition between two energy states. Nevertheless, a fast recovery time that is suitable for creating ultrashort pulses at time frames of a few picoseconds to a few hundred femtoseconds is rare to be observed in saturable absorber, except for both CNT and graphene (Martinez et al., 2014; Martinez & Sun, 2013; Yamashita, 2011a, 2011b; Yamashita et al., 2014). Figure 2.8(a) and (c) shows the optical absorption of CNT and graphene, respectively. Saturation occurs when the valence band are cleared at intense optical power and all the allowed states in the conduction band are entirely populated as in Figure 2.8(b) and (d).

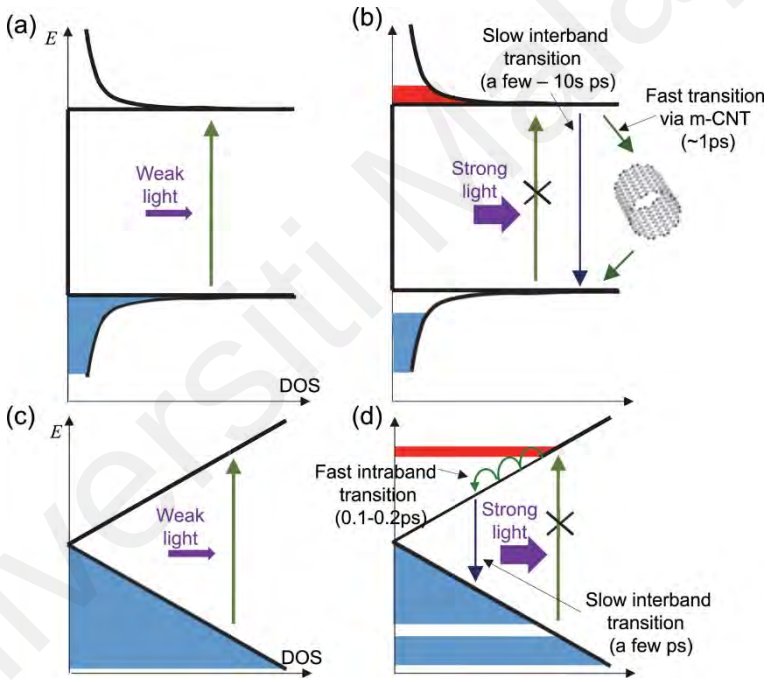

Figure 2.8: Optical absorption and saturation of [(a) and (b)] CNT and [(c) and (d)] graphene (Copyright permission from Yamashita, 2019).

Reverse saturable absorption (RSA) or optical limiting is the opposite effect of saturable absorption that may exist in some materials. Multiphoton absorption such as two-photon absorption (TPA) is the primary cause of RSA (Tutt & Boggess, 1993). SA and RSA can occur at the same time, altering the Eq. 2.10 into

$$\alpha = \frac{\alpha_0}{1 + I/I_s} + \beta I \tag{2.12}$$

where β represents the TPA coefficient. Figure 2.7 shows the absorption characteristic with only RSA in the red curve, while the blue curve corresponds to the absorption characteristic during the coexistent of SA and RSA, assuming $\beta_0 I I_s = 10^{-2}$. The RSA dominates in GO as it has been reported, whereas SA is dominant in reduced GO (rGO) (X.-F. Jiang et al., 2012).

Commonly in precursor MXene $Ti_3C_2T_x$, the structure and electronic properties could be greatly affected by the surface termination group T_x, hence playing significant part in the optical properties. In particular, the imaginary part of dielectric constant could be affected by the interband and intraband electronic transitions, whereby the total contribution of material interband transition is proportional to the calculated absorption spectrum (Chaudhuri et al., 2019). In term of structural differences, since only one electron can be accepted in hydroxylated and fluorinated terminations, hence, they have similar performance in visible range. On the contrary, two electrons are needed to stabilize oxygen termination (X. Jiang et al., 2020). Based on the study of functionalization dependence optical properties through utilizing computational methods by Berdiyorov, the static dielectric function was reduced by functionalization at the capacity of more than two times (Berdiyorov, 2016). In Figure 2.9(a), the surface fluorination results in weaker absorption in the visible spectrum range as compared to oxidized sample which portray a larger absorption relative to the pristine Ti_3C_2. The remarkable contribution of oxygen atoms to the total density of states of MXenes near the Fermi level develop the optical performance differences between oxygen and hydroxylated or fluorinated terminations.

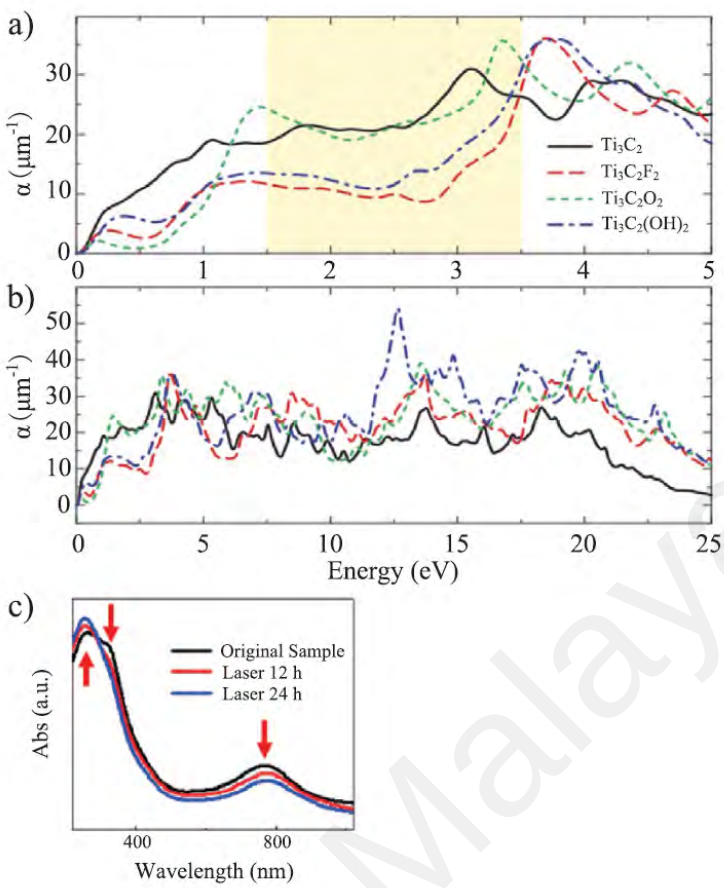

Figure 2.9: Absorption spectrum of Ti_3C_2 and absorption spectrum calculation of $Ti_3C_2T_x$ in (a) visible range, and (b) UV range. (c) Experimental absorption spectrum of $Ti_3C_2T_x$ and partially oxidized $Ti_3C_2T_x$ in water solution (Copyright permission from Bo Fu et al., 2021)

Surface terminations cause higher absorption and reflectivity relative to the pristine Ti_3C_2 in the ultraviolet (UV) range as depicted in Figure 2.9(b). On the other hand, only oxygen termination increases both absorption and reflectivity in the visible range, while the hydroxylated and fluorinated terminations are more transparent than pristine Ti_3C_2, indicating lower both absorption and reflectivity. In wet surrounding, $Ti_3C_2T_x$ surface could be partially oxidized in many long-run applications (C. J. Zhang et al., 2017). In the optical absorption perspective, the $Ti_3C_2T_x$ absorption peak in the UV range at 260 nm was increased, while in the visible range at 780 and 325 nm were decreased as presented in Figure 2.9(c) (J. Li et al., 2019). Hence, this shows the possibility to modify the optical properties of MXenes in various applications. The optical absorption of MXenes in this

work, particularly saturable absorption will be used in pulse generation and optical modulation.

2.3.3 Kerr Effects

The nonlinear refractive index change, or the nonlinear Kerr effect corresponds to the real part of $\chi^{(3)}$ in Eq. 2.9 which cause by the electric fields and proportional to the square of the electric field strength. It can take place when light propagates in crystal, glass as well as gases. Generally, it can be described in two different operations, those are Kerr electro-optic effect and optical Kerr effect. Kerr electro-optic effect uses external electric field to modify the refractive index while the optical Kerr effect uses the electric field from the high intensity light beam itself to modify the refractive index. The refractive index can be modified according to

$$\Delta n = n_2 I \tag{2.13}$$

and Eq. 2.9 can give the n_2. I is the optical intensity and n_2 is the nonlinear refractive index. The change in n_2 can be measured with several methods including Z-scan.

The theoretical prediction of n_2 value in graphene (Semnani et al., 2016) is aligned with the reported figures of $10^{-11}\, m^2/W$ (Hendry et al., 2010; Saynatjoki et al., 2013; H. Zhang et al., 2012). Similar figures of $n_2 = 10^{-13}\, m^2/W$ in GO and rGO has also been reported (J. Ren et al., 2016; X. Zheng et al., 2014). Besides graphene, the measurement of n_2 in other 2D materials have also been reported, such as TMDs (N. Dong et al., 2016; G. Wang et al., 2015), BP (Youngblood et al., 2017; J. Zhang et al., 2016), and TIs (Miao et al., 2016; Shi et al., 2015). TMDs, and BP have small n_2 value of approximately $< 10^{-13}\, m^2/W$, whereas TIs has a higher n_2 value of $\sim 10^{-12}\, m^2/W$. The primordial MXene $Ti_3C_2T_x$ has n_2 value of $\sim 10^{-4}\, m^2/W$ when calculated with spatial self-phase modulation (SSPM) technique (L. Wu et al., 2018) but has a lower value

of $\sim 10^{-16}\, m^2/W$ when calculated with Z-scan technique as obtained by Jiang et al. (X. Jiang et al., 2018). The difference in characterization techniques result in the existence of significant discrepancy. Nonetheless, the Kerr effect of MXenes in this work will be used to produce all-optical modulator.

2.4 First Principles of Fiber Lasers

2.4.1 Fundamental Concept of Fiber Lasers

A light bulb does not release a 'white-coloured'-light as human eyes perceive, instead, it is created of many different colour or wavelength of the electromagnetic spectrum (EMS) that is visible to human eyes. Some parts of the EMS are not visible to human, such as ultraviolet (UV) and infrared (IR) light. However, the combination of all these visible wavelengths or frequencies of light makes what we recognize as white light, ranging from about 400 nm to 700 nm.

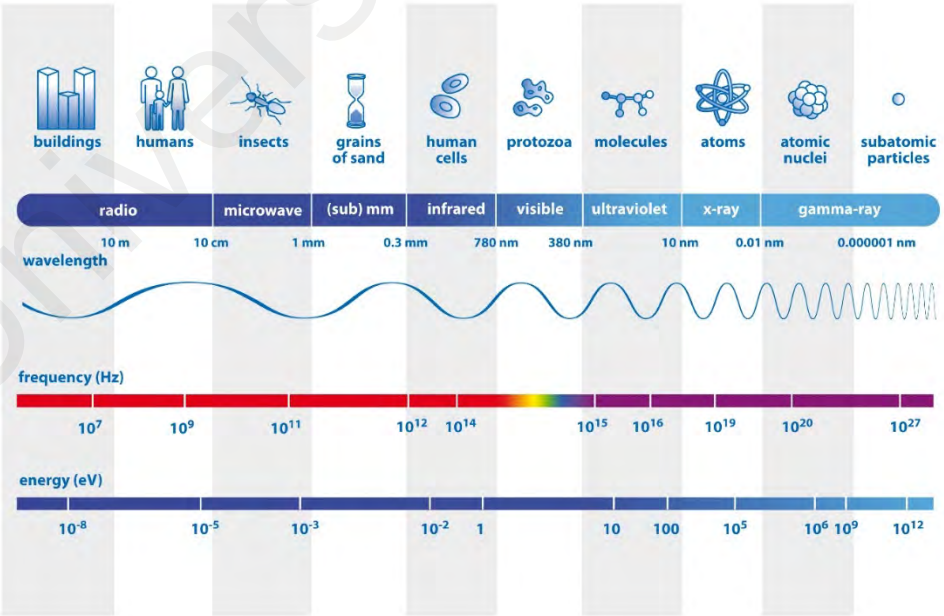

Figure 2.10: Full spectrum of electromagnetic wave with relative comparison (Copyright permission from sci.esa.int).

Unlike ordinary light that we see, laser differs in a few ways. Laser is monochromatic, which contain only one colour due to the emission of an exceptionally narrow range of light wavelengths. Laser travels in the same direction or collimated with insignificant divergence, whereby conventional light sources spread in all directions. This attribute is necessary to reduce loss of power through the beam travelling systems such as articulated arm or fiber optics. Above all, coherent source is the most important attribute of laser, where the waves are very spatially ordered, and time correlated. This will exponentially multiply the amplitude or power of the laser. Besides, a coherent source also allows the ability to focus to a far smaller spot size compared to an incoherent source, which can produce exceedingly high-power density in a small area.

The formation of laser occurs when electrons of an active medium change energy levels by an excitation source such as flashlight, electric current, or another laser. The electrons will absorb the input energy if the energy satisfy the appropriate level, then move freely to a higher, yet less stable energy level. Consequently, the electrons will return to a lower energy level due to the unstable state of the atom. A photon is spontaneously emitted in this process. If the emitted photon or photon of the same energy is passed through the excited atom, it will trigger atoms with electrons in their excited state to release photon of identical energy and frequency by forcing them to the lower energy level or also known as stimulated emission. These identical photons are travelling in the same phase and called coherent light. The energy of photon is meticulously explained in the novel work of Albert Einstein regarding the effect of photoelectric as below

$$\Delta E = \hbar v = E_2 - E_1 \tag{2.14}$$

where E_2 is an upper energy level and E_1 is a lower energy level. Figure 2.11 illustrates the light-matter interactions.

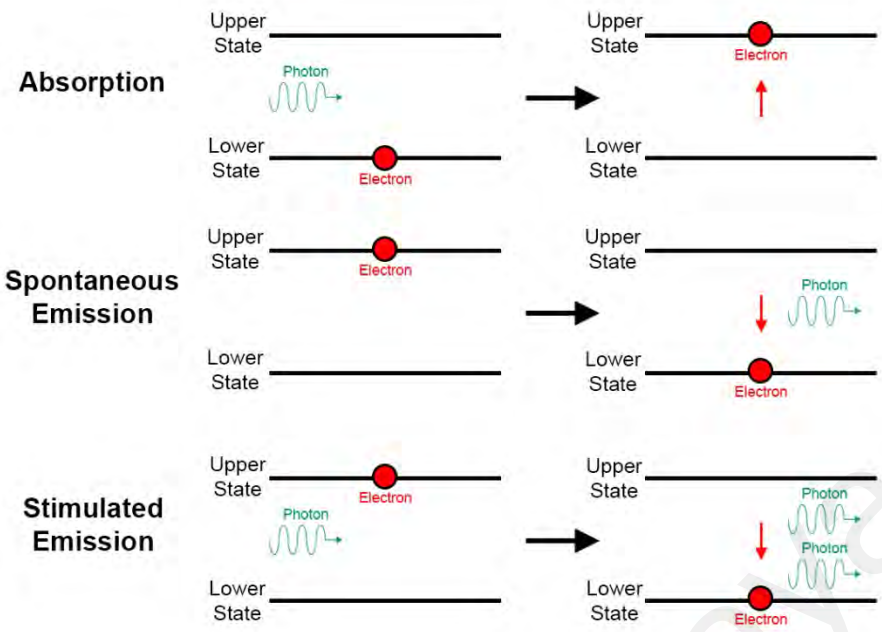

Figure 2.11: All types of light matter interaction (absorption, spontaneous emission, and stimulated emission).

The amplification take place when photons scattering with other excited atoms to release more photons simultaneously. This process will only survive if the population of electrons in the higher energy level, N_1 are higher than the electrons in the lower energy level, N_2, where this situation is usually referred to population inversion. To create this condition, the active medium containing the atoms must be kept excited by the energy source. A pair of mirrors is placed in the laser system to reflect light back and forth as illustrated in Figure 2.12 in free space laser. One of the mirrors must be partially transmitted to release the light in the form of laser, which are monochromatic, coherent, and very low divergence. However, population inversion cannot be achieved with two-level system as the highest number of population in the upper energy level can only be half of the lower energy level, $E_2 = ½ E_1$, such condition is called saturation. In practical application, three-level or four-level energy system is often used to induce laser as shown in Figure 2.13.

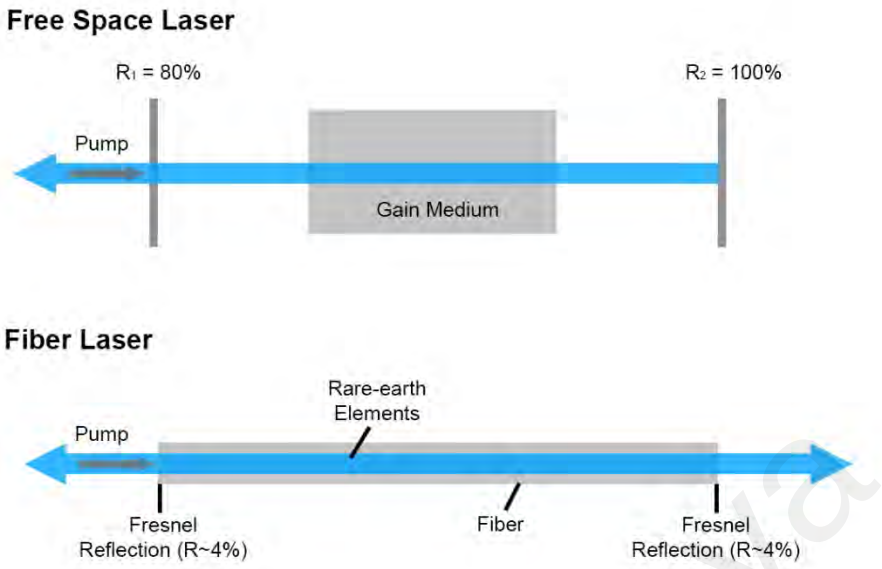

Figure 2.12: Elemental components of laser (top) and fiber laser (bottom).

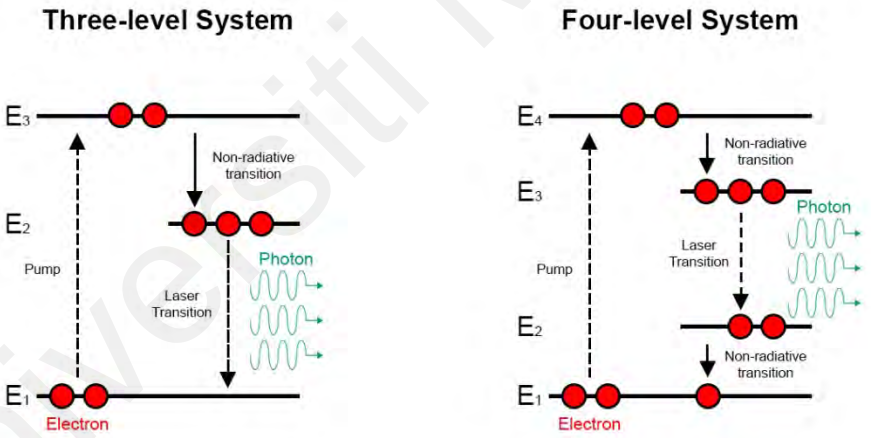

Figure 2.13: (a) Three-level and (b) four-level laser systems.

In a three-level system, the electrons in the ground state or lowest energy level, E_1 absorb the incoming photons from pump and jump to the upper energy level, E_3. Electrons in the upper energy level other than the ground state are not stable and need to release energy to return to their stable state. The excited electrons in E_3 will decay to the lower

energy level, E_2 through non-radiative transition. The electrons will accumulate in the energy level E_2, forming a population inversion due to the metastable state of E_2. The population will maintain until a spontaneous emission of electron occurs. The spontaneous emission will trigger the other electrons in that state to release energy to return to the ground state, resulting in stimulated emission that form an intense identical photon number simultaneously and empty the energy level E_2. Unfortunately, this system needs high power to pump all the electrons all over again from the ground state to the energy level E_3 and need time to form the population inversion again in the energy level E_2. On the contrary, only small power is ample to pump the electrons in the ground state of four-level system to the upper energy level, E_4. The electrons in the E_4 will immediately decay to lower energy level, E_3 through non-radiative transition and form a population inversion in that state. After an electron in the E_3 has finished its lifetime, the electron will drop to the lower energy level, E_2 through spontaneous emission and trigger the other electrons in the same state to release their energy through stimulated emission. The electrons will accumulate in the E_2 before immediately drop to the ground state, E_1 through non-radiative transition. If the rate of relaxation of atoms from E_2 to E_1 is faster than the rate of arrival of electrons into E_2, the population inversion on E_3 can be obtained with small power. This result in the continuous wave lasing to the output, unlike three-level system.

Other than a solid-state laser, laser can also be made from optical fiber as light can travel in different medium. Most of fiber laser components are using fiber as the medium. Rare-earth doped fiber are usually used as active medium or gain medium in fiber lasers, where the fiber core is doped with rare-earth elements as in Figure 2.12. The rare-earth elements are frequently used due to its electronically stable atomic structure. The host materials that hold the doped elements do not affect the electronic transition occurred in the f-orbital of the rare-earth elements which permit it to preserve its atomic-like

structure. Silica glass (SiO_2) is a common host material in optical fiber for telecommunication purposes due to the fine performance in near-infrared wavelengths, enabling it to secure a long-haul telecommunication as transmission loss is low. Other than silica glass, fluoride glass (ZBLAN) is also a common host material in optical fiber, but instead of telecommunication purposes, it is frequently used in research activities. In a basic linear fiber laser system, the fiber ends are transformed into 'mirrors' by cleaving them perpendicularly to replace the physical mirror in free space laser system. The Fresnel reflection at the fiber ends provide enough feedback for stimulated emission because of the difference in refractive index between glass and air. The lasing will arise once the gain has exceeded the total loss of the system. Nevertheless, the characteristic of the fiber laser output depends on the laser parameters.

2.4.2 Laser Modes and Quality Factor (Q-factor)

Standing waves or stationary waves are commonly known as longitudinal modes in lasers which are usually defined between two fixed reflectors or mirrors. It is created when the incident waves interfere with the reflected waves to form a standing still waves as in Figure 2.14. However, such patterns only exist at specific frequencies called harmonics, whereby the other frequencies other than harmonics will collapse and form irregular and non-repeating waves. The longitudinal modes are definite and separated by the spacing of harmonic frequencies which expressed as

$$\Delta v = \frac{c}{2L} \tag{2.15}$$

where L is the length of the cavity and c is the speed of light. In the case of a loop cavity fiber laser, the whole length of one complete loop is considered as 2L.

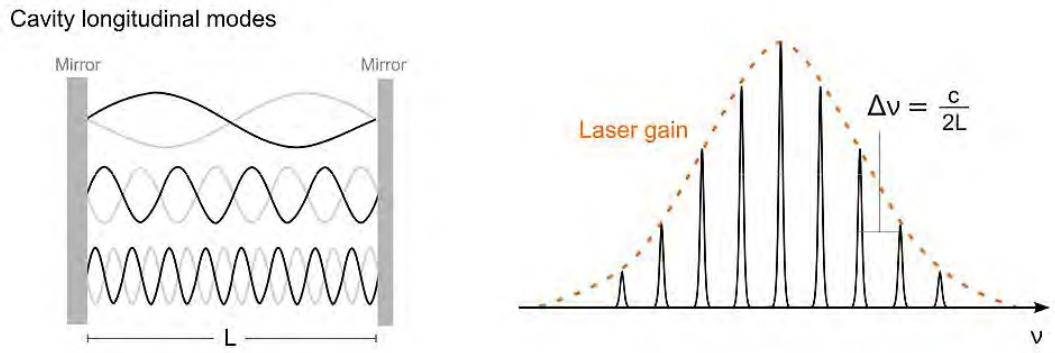

Figure 2.14: Longitudinal modes (harmonic frequency) in laser cavity (left) and allowed multi-mode lasing in laser gain bandwidth (Copyright permission from Hu et al., 2015).

The number of longitudinal modes, N_{LM} is given by

$$N_{LM} = \frac{\Delta V}{\Delta v} \tag{2.16}$$

where ΔV is the measured laser linewidth. Besides that, the harmonic frequencies spacing can be inversed to estimate the repetition rate of mode-locked pulses as follow

$$\tau_{rp} = \frac{1}{\Delta v} \tag{2.17}$$

where τ_{rp} is the time needed for the signal light to fulfil one complete cycle of the cavity.

The quality factor (Q-factor) of a resonator is a measure of the strength of the damping of its oscillations. The idea was originally appeared in electronic circuits but later became customary in the context of optical resonators or lasers. The Q-factor as defined via energy storage is 2π multiplies the ratio of the stored energy to the energy dissipated per oscillation cycle as follow.

$$Q = 2\pi \frac{stored\ energy}{energy\ dissipated\ per\ oscillation\ cycle} \tag{2.18}$$

However, the Q-factor of a laser in specific manner is given as

$$Q = \frac{2\pi v_0 \tau_{rt}}{l} \tag{2.19}$$

where v_0 is the optical frequency, l is the fractional power loss per round trip, and τ_{rt} is the round-trip time. The Q-factor values of a cavity can be managed by introducing additional losses, modify the pumping power, or the other cavity parameters.

2.4.3 Rare-earth Doped Fiber and Fiber Hosts

The idea of fiber lasers and amplifiers was originally revealed by Koester and Snitzer as early as 1964, three years after the first laser operation of neodymium (Nd^{3+}) doped crystalline materials and glasses. Laser work in a core or cladding waveguide with end pumping procedure by Stone and Burrus was then achieved about six years later, utilizing the technological breakthrough trump card in the quality of fiber, particularly its transparency. However, the first reveal of a single mode rare-earth doped fiber lasers by D.N. Payne et al. was in 1985, who addressed the very low laser threshold. The evolution of chemical vapour deposition techniques in the manufacture of fabricating low-loss single mode fiber for long haul optical transmission systems has made it possible. The existence of such low-loss single mode fibers can be regarded as the opening technical revolution in optical telecommunications, accompanied by the demonstration of Erbium-Doped Fiber Amplifier (EDFA) in 1987 by several groups around the same time. This amplifier has exceptional gains with a low pump power, a low noise feature, and a high saturation power, which operates in the third telecommunication window at 1.55 μm.

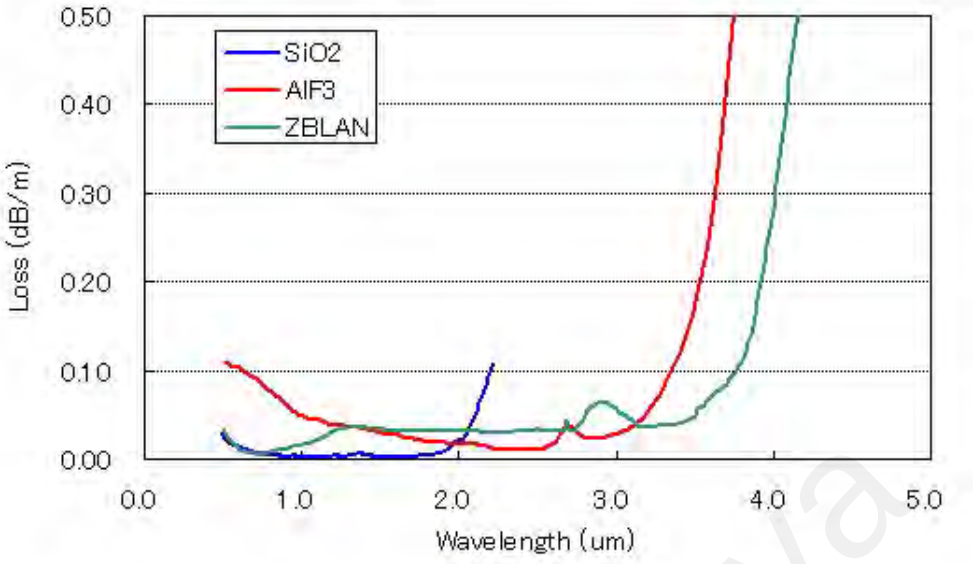

Figure 2.15: Attenuation spectrum of Silica (SiO_2) and Fluoride (ZBLAN and AlF3) fibers (Copyright permission from www.fiberlabs.com).

To date, rare-earth elements such as ytterbium, holmium, praseodymium, and thulium are also commonly used as dopant in fiber due to their interesting property of stable triplet ionized form ($^{3+}$). During the last decades, much attempt has been concentrated on other types of glasses as the host fiber, such as fluoride, tellurite, chalcogenide, and others. Fluoride fiber exhibits losses lower than silica in the near infrared region (NIR) as in Figure 2.15 and the main fluoride fiber composition (ZBLAN-based) was especially suitable for doping high concentration or rare-earth ions. Furthermore, the number of metastable states in fluoride is higher than silica due to its low phonon energy quality, making it possible to radiate in the whole infrared or visible or UV range. Hence, various wavelengths of laser in fluoride fiber have been reported than in silica fiber. AlF_3 is another material base in fluoride fiber, but exhibits narrower IR transmission range than ZBLAN, and its emission characteristic is not as exotic as ZBLAN fibers. On the contrary, as compared to ZBLAN-based, AlF_3-based has higher laser damage threshold, better mechanical property, better durability against moisture, and lower optical loss at 2.94 µm. Unfortunately, fluoride fiber is difficult to fabricate, thus expensive, delicate to handle

due to their fragility and contain hygroscopic nature, resulting to a short lifetime. Silica fiber on the other hand is relatively easy to handle, the fiber is not sensitive to air and can be stored without demanding conditions.

Single rare-earth ions are usually doped into the fiber core, although in some occurrence, they can be doped together to manipulate the output of the laser. The frequently used single rare-earth doped silica fibers with their usual pump and emission wavelengths in the near-IR range are recorded in Table 2.1.

Table 2.1: Rare-earth doped fiber with their typical pump and emission wavelength in near-IR.

Rare-earth	λ_{pump} (μm)	$\lambda_{emission}$ (μm)	Gain bandwidth (nm)	Reference
Ytterbium	0.98	1.06	~30	(Sousa et al., 1999)
Erbium	0.98, 1.48	1.55	~40	(Tachibana et al., 1991)
Thulium	0.79, 1.55	1.93	~200	(Z. Li et al., 2013)
Neodymium	0.59, 0.79	1.06	~20	(Zawischa et al., 1999)
Praseodymium	1.02	1.3	~20	(Whitley, 1995)

2.4.3.1 Spectroscopic Properties of Thulium

Rare-earth element or lanthanides are a set of seventeen chemical elements in the periodic table as established by the International Union of Pure and Applied Chemist (IUPAC). The idea of rare-earth element is addressed to an insignificant quantity of elements at the mining site to support economical mineral development. They are in fact present relatively abundant in the crust of the earth, where it starts from the atomic

number 57 (lanthanum, La^{3+}) to 71 (lutetium, Lu^{3+}), including 21 (scandium, Sc^{3+}) and 39 (yttrium, Y^{3+}). Scandium and yttrium are considered rare-earth elements since their emergence favour in the same ore deposits as the lanthanides and display similar chemical properties. Figure 2.16 shows the position of lanthanides in the periodic table.

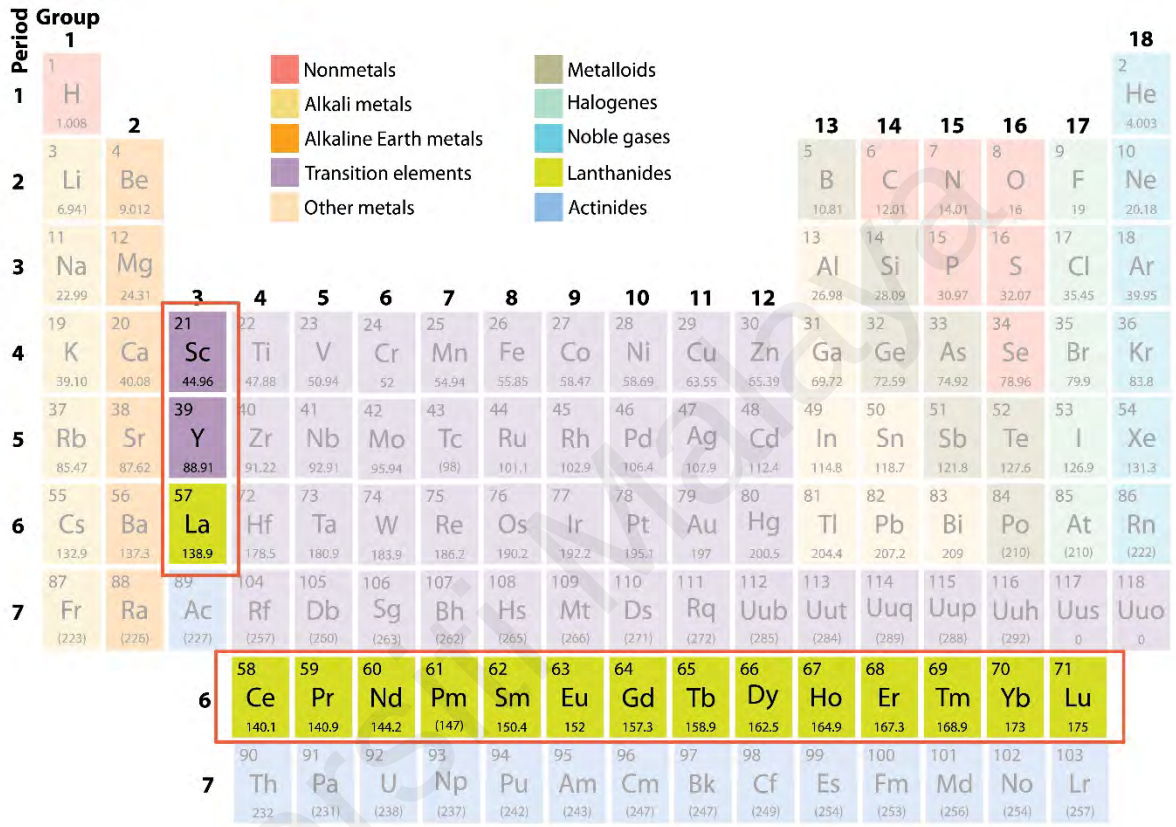

Figure 2.16: Periodic table of rare-earth elements or lanthanides.

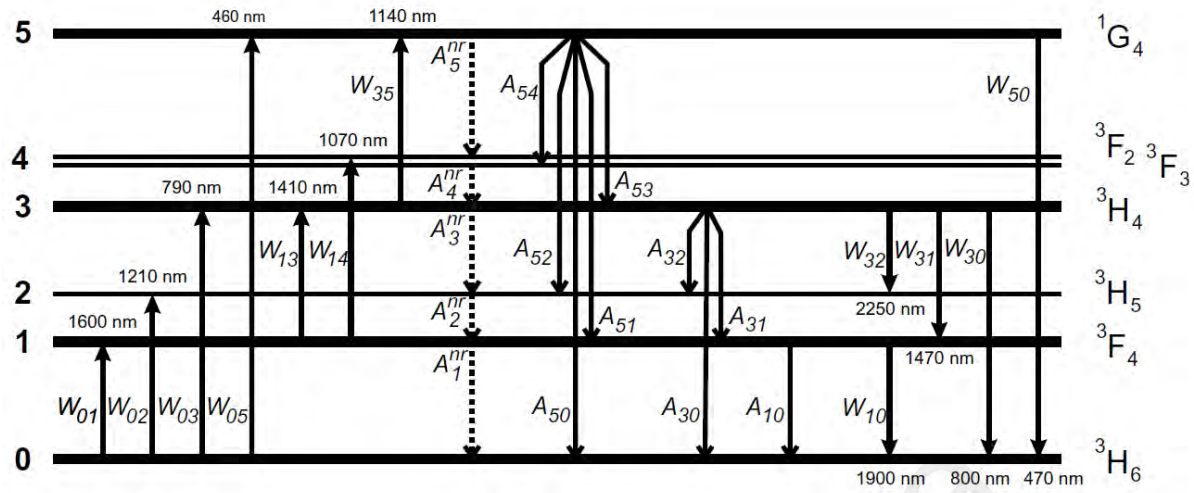

Figure 2.17: Thulium ions (Tm^{3+}) energy level diagram with all transitions involved (Copyright permission from Peterka et al., 2004).

Thulium has an atomic number of 69 and 12 electrons in its 4*f* shell. Lasers generated from thulium ions (Tm^{3+}) has a wide range wavelength flexibility due to its broad optical bandwidth. Tm^{3+} is influenced by the Stark effect because of the interaction with the local crystal field that causes its energy level to break into broad energy bands, hence exhibits wide operating wavelength (Monerie et al., 1990). This process is commonly known as inhomogeneous broadening effect. The rise of phonon energy due to a change in temperature can also contribute to the broadening effect. One of its emission spectra from energy level $^3F_4 \rightarrow {}^3H_6$ transition covers the wavelength range of 400 nm from 1700 nm to 2100 nm. Figure 2.17 shows the main energy levels of thulium with all the possible transitions involved, excluding the sub-energy levels. Nevertheless, these sub-energy levels have influence on the main energy levels output emission, particularly, $^3F_4 \rightarrow {}^3H_6$ transition. The electrons drop from $^3F_4$ to a different sub-energy level of $^3H_6$ causing a broader emission spectrum. The stimulated absorption and emission rates, W_{ij} responsible for amplified spontaneous emission (ASE), whereby A_{ij} and $A^{nr}{}_i$ represent spontaneous decay processes, those are the radiative and nonradiative decay rates, respectively.

There are two types of absorption involved during the transition, ground state absorption (GSA) and excited state absorption (ESA). GSA is the absorption that occurs in the energy level $^3H_6$ to a higher energy level, such as $^3F_4$ or $^3H_4$, depends on the photon energy absorbed. While ESA is the absorption that occurs in an excited state to a higher energy excited state, which can take place when there are a single or multiple higher energy levels than the populated excited states, and there is a population in the starting excited state, which can easily be fulfilled if the excited state is a metastable state.

2.4.3.2 S-band Emissions of Thulium-doped Fluoride Fiber Lasers

The absorption spectrum of Tm^{3+} ions in fluoride host (ZBLAN) for S-band emission takes place at energy levels $^3F_4 \rightarrow {}^3H_4$ with a lasing wavelength around 1470 nm. Both dual-wavelength and single up-conversion pumping schemes can be used to achieve S-band emission as reported by Florida et al. (Floridia et al., 2004) and Aozasa et al. (Aozasa et al., 2006). Two-energy level hoping is accomplished by using two pump lasers of different wavelengths in the dual-pumping scheme, such as utilizing 800 nm and 1050 nm wavelength lasers in a co-pumping mechanism (Gomes et al., 2003). In the process, the electrons in $^3H_6$ absorb the 800 nm pump and jump to $^3H_4$, while the 1050 nm pump excites the population in the lower energy level $^3F_4$ using a strong ESA to energy level $^3F_2$, which the electrons simultaneously populates the energy level $^3H_4$ to create population inversion. The emission in S-band is thus attained through the radiative transition of $^3F_4 \rightarrow {}^3H_4$.

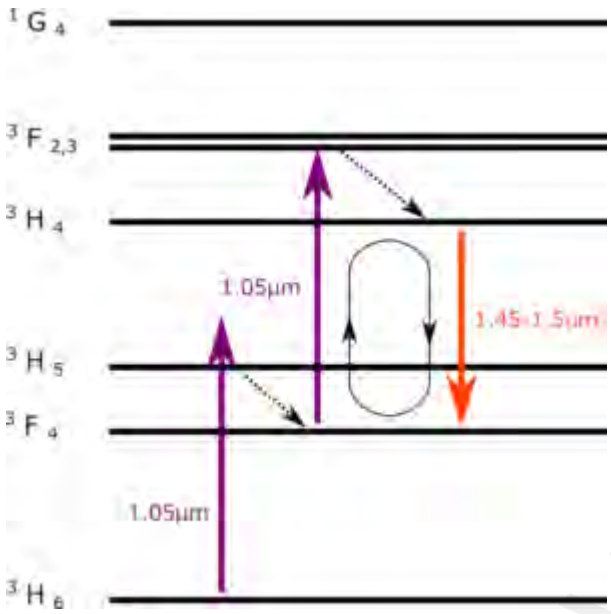

Figure 2.18: Energy level diagram of Tm^{3+} in fluoride fiber with 1050 nm pumping scheme (Copyright permission from www.fiberlabs.com).

The single-up conversion pumping scheme is simpler to execute as it needs only a single pump. There are two common wavelengths that are used in this scheme, those are 1050 nm and 1400 nm (Floridia et al., 2004; S. Aozasa, T. Sakamoto, T. Kanamori, K. Hoshino, K. Kobayashi, 2000). Both wavelength pumps have GSA from $^3H_6 \rightarrow {}^3F_4$ and ESA from $^3F_4 \rightarrow {}^3H_4$ generally, but in details, 1050 nm needs two depopulation processes from $^3H_5 \rightarrow {}^3F_4$ and $^3F_2 \rightarrow {}^3H_4$ and the efficiency is fundamentally lower because of the larger energy difference between the pump and signal that can lead to excess heat as depicted in Figure 2.18. Hence, the 1400 nm pumping scheme has the advantage of uninterrupted GSA and ESA as compared to the 1050 nm pumping scheme. Previous work by Aozasa et al. proves that 1400 nm is an efficient pumping source to produce laser in the S-band since its gain covers a wavelength range of 1480 nm to 1510 nm. Figure 2.19 shows a weak Tm^{3+} ions GSA from $^3H_6 \rightarrow {}^3F_4$ and a strong ESA from $^3F_4 \rightarrow {}^3H_4$ at 1400 nm. A small quantity of electrons are excited to the $^3F_4$ and most of the electrons at $^3F_4$ are excited to the $^3H_4$. The electrons at the $^3H_4$ emit photons and drop to the $^3F_4$, then repeat the cycle without returning to the ground state. Fluoride glass

is preferred for S-band amplification because of the poor emission efficiency of silica glass due to its large phonon energy. In silica glass, the excited electrons at the $^3H_4$ quickly relax to the $^3H_5$ by multiphonon relaxation, hence, does not emit photons.

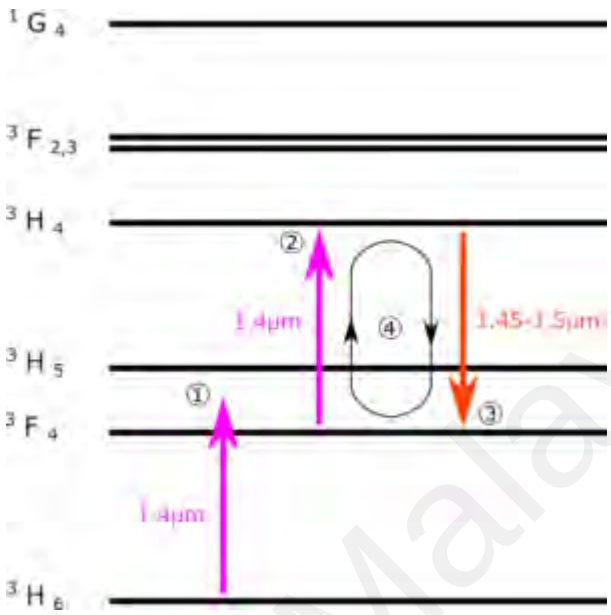

Figure 2.19: Energy level diagram of Tm^{3+} in fluoride fiber with 1400 nm pumping scheme (Copyright permission from www.fiberlabs.com).

The rate equation of 1400 nm pumping scheme only concerns a four-level system (Kozak et al., 2004) that contains the rate equations for the population of electrons at the ground state, first, and third excited states, N_0, N_1, and N_3 as follows

$$\frac{dN_0}{dt} = -N_0(w_{01} + w_{03}) + N_1(A_{10} + A_1^{nr}) + N_3A_{30} \tag{2.32}$$

$$\frac{dN_1}{dt} = N_0w_{01} - N_1(w_{13} + A_1^{nr} + A_{10}) + N_3(w_{31} + A_3^{nr} + A_{32} + A_{31}) \tag{2.33}$$

$$\frac{dN_3}{dt} = N_1w_{13} + N_3(w_{31} + A_3^{nr} + A_{31} + A_{30}) \tag{2.34}$$

$$N_t = N_0 + N_1 + N_3 \tag{2.35}$$

where w_{ij} is the stimulated absorption and emission rates responsible for the ASE, whereby A_{ij} and A_i^{nr} are the spontaneous decay rate for the radiative and non-radiative decay rates from level *i* to *j*, respectively. The total thulium dopant concentration is N_t. The rate equation presented in this section is only describing the continuous-wave (CW) operation in thulium-doped fluoride fiber host.

2.4.3.3 2.0 µm Emissions of Thulium-doped Silica Fiber Lasers

The absorption spectrum of Tm^{3+} ions in silica host for 2.0 µm emission is shown in Figure 2.20(a). There are four possible options as seen in the spectrum, those are 660 – 685 nm, 780 – 800 nm, ~1200 nm, and 1550 – 1750 nm. However, the pump schemes of 660 – 685 nm, and ~1200 nm are not appropriate due to the ESA that degrade the laser efficiency. ESA in the $^3F_4 \rightarrow {}^1G_4$ transition can occur with the 660 – 685 nm pumping scheme, while ESA in the $^3F_4 \rightarrow {}^3F_{2,3}$ happens when the $^3F_4$ is pumped with 1050 – 1120 nm pumping scheme (Miniscalco, 2001) near 1200 nm as seen in Figure 2.20(b). Thus, 780 – 800 nm, and 1550 – 1750 nm are superior candidates to pump the Tm^{3+} for the generation of laser near 2.0 µm (Khamis & Ennser, 2016; Richardson et al., 2010). The ~790 nm pumping scheme possesses the potential to produce cross-relaxation process which can give rise to high conversion efficiency (Moulton et al., 2009). Whereas in Figure 2.20(a), the 1550 – 1750 nm pumping scheme (Yamamoto et al., 1994) also shows strong absorption and possible to generate a higher power level than the 780 – 800 nm (Shen et al., 2006). This wavelength pumping scheme is known as in-band pumping and can excite the electrons in the ground state to the $^3F_4$ excited state. The emission of signal photon will be produced through the radiative transition of $^3F_4 \rightarrow {}^3H_6$. Fortunately, this pumping wavelength can be realized with 1550 nm EDFA technology.

Since this technology is well-developed and matured, the technology has become a low-cost option due to the commercially accessible fiber parts in the market.

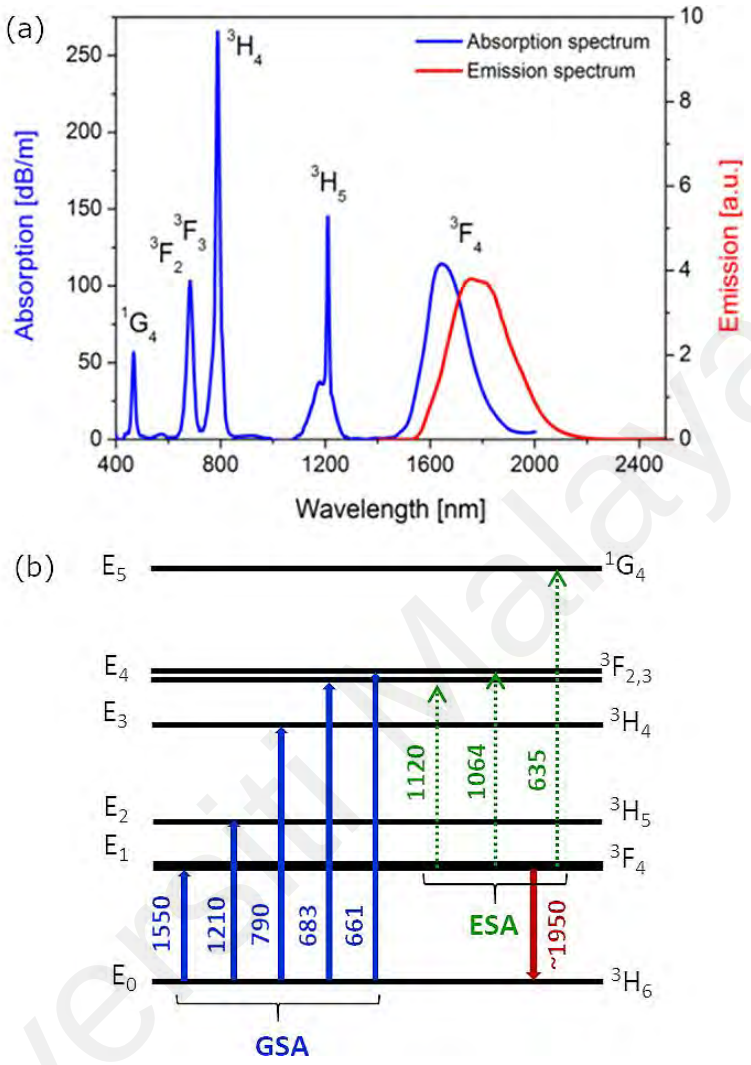

Figure 2.20: (a) Tm-doped silica fiber absorption spectra and (b) energy level diagram of Tm^{3+} in silica fiber with ground state absorption (GSA) and excited state absorption (ESA).

The rate equation of Thulium-Doped Fiber Amplifier can be described by using Jackson's model (Jackson & King, 1999) at any position of the thulium-doped fiber length by including the cross-relaxation process (Evans et al., 2009). When the 1550 nm pump scheme directly excite electrons to the energy level $^3F_4$ as depicted in Figure 2.21, the rate equations can be expressed as follows

$$\frac{dN_3(z,t)}{dt} = -\frac{N_3(z,t)}{\tau_3} - C \tag{2.20}$$

$$\frac{dN_1(z,t)}{dt} = w_{p01} - w_{p10} - \frac{N_1(z,t)}{\tau_1} - \frac{\beta_{31}N_3(z,t)}{\tau_3} - w_{s10} + w_{s01} + 2C \tag{2.21}$$

$$N_0(z,t) = N_T - N_1(z,t) - N_3(z,t) \tag{2.22}$$

where C is the cross-relaxation process and is given by

$$C = K_{3101}N_0(z,t)N_3(z,t) - K_{1310}N_1^2(z,t) \tag{2.23}$$

the expression of w_{p01}, w_{p10}, w_{s10}, and w_{s01} are describe as follows

$$w_{p01} = \frac{\lambda_p \Gamma_p}{hcA_{core}}\sigma_a(\lambda_p)N_0(z,t)\left[p_p^-(z) + p_p^+(z)\right] \tag{2.24}$$

$$w_{p10} = \frac{\lambda_p \Gamma_p}{hcA_{core}}\sigma_e(\lambda_p)N_1(z,t)\left[p_p^-(z) + p_p^+(z)\right] \tag{2.25}$$

$$w_{s01} = \frac{\lambda_s \Gamma_s}{hcA_{core}}\sigma_a(\lambda_s)N_0(z,t) \times \left[p_s(z) + ASE_f(z) + ASE_b(z)\right] \tag{2.26}$$

$$w_{s10} = \frac{\lambda_s \Gamma_s}{hcA_{core}}\sigma_e(\lambda_s)N_1(z,t) \times \left[p_s(z) + ASE_f(z) + ASE_b(z)\right] \tag{2.27}$$

The lifetime of population density N_2 in its energy level can be neglected since it is too short relative to the other energy levels, which is typically 0.007 μs. The expression of the power distribution of the pump light and the signal light in the fiber are given as

$$\frac{dp_p^{\pm}}{dz} = \pm p_p^{\pm}(z)\left[\Gamma_p\left(\sigma_e(\lambda_p)N_1(z) - \sigma_a(\lambda_p)N_0(z)\right) - a_p\right] \tag{2.28}$$

$$\frac{dp_s}{dz} = p_s(z)\left[\Gamma_s\left(\sigma_e(\lambda_s)N_1(z) - \sigma_a(\lambda_s)N_0(z)\right) - a_s\right] \tag{2.29}$$

The positive sign in Eq. 2.28 suggests a forward direction, while the negative sign suggest the opposite direction. The distribution of the ASE power in the fiber can be described as

$$\frac{dASE_f}{dz} = ASE_f(z)\left[\Gamma_s\left(\sigma_e(\lambda_s)N_1(z) - \sigma_a(\lambda_s)N_0(z)\right) - a_s\right] + 2\sigma_e(\lambda_s)N_1(z)\frac{hc^2}{\lambda_s^3}\Delta\lambda \tag{2.30}$$

$$\frac{dASE_b}{dz} = ASE_b(z)\left[\Gamma_s\left(\sigma_e(\lambda_s)N_1(z) - \sigma_a(\lambda_s)N_0(z)\right) - a_s\right] + 2\sigma_e(\lambda_s)N_1(z)\frac{hc^2}{\lambda_s^3}\Delta\lambda \tag{2.31}$$

the variables used in Eq. 2.20 – Eq. 2.31 are described in Table 2.2. The rate equation presented in this section is only describing the CW operation in thulium-doped silica fiber host.

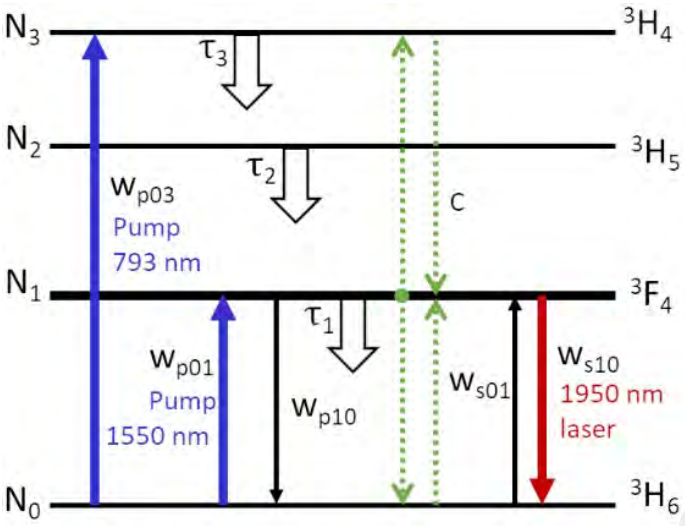

Figure 2.21: Energy level diagram of Tm^{3+} in silica fiber with 1550 nm and 793 nm pumping schemes.

Table 2.2: Variable definitions of thulium-doped silica fiber rate reaction.

Variable	Definition
$\boldsymbol{\tau_i}$	Spontaneous lifetime of *i* th energy level
$\boldsymbol{N_i(z,t)}$	Population density of *i* th energy level
$\boldsymbol{N_T}$	Density of Tm^{3+}
$\boldsymbol{\beta_{ij}}$	Branching ratio of the spontaneous transition
$\boldsymbol{K_{ij}}$	Cross relaxation rates
$\boldsymbol{w_{pij}}$	Pumping and de-excitation rates
$\boldsymbol{w_{sij}}$	Stimulated emission and absorption rates
$\boldsymbol{h}$	Planck constant
$\boldsymbol{c}$	Speed of light in vacuum
$\boldsymbol{\lambda_{p/s}}$	Wavelength of the pump/signal light
$\boldsymbol{\Gamma_{p/s}}$	Confinement factor for pump/signal light
$\boldsymbol{A_{core}}$	Cross-section area of the fiber core

Table 2.2, continued.

Variable	Definition
$\boldsymbol{\sigma_a(\lambda_{p/s})}$	Absorption cross-sections of pump/signal light
$\boldsymbol{\sigma_e(\lambda_{p/s})}$	Emission cross-sections of pump/signal light
$\boldsymbol{P^{\pm}_{p/s}(z)}$	Pump (corresponding to forward and backward)/signal power at position z
$\boldsymbol{ASE_{f/b}(z)}$	Forward and backward amplified spontaneous emission power at position z
$\boldsymbol{\alpha_{p/s}}$	Intrinsic absorption at pump/signal wavelength
$\boldsymbol{\Delta\lambda}$	Bandwidth of the amplified spontaneous emission
$\boldsymbol{C}$	Cross relaxation

2.5 Q-switching and Mode-locking

2.5.1 Q-switching Fundamentals

Q-switching is a technique for acquiring energetic short pulse from lasers by modulating the intracavity losses and hence, the Q-factor of the laser cavity. The intracavity losses can be exploited to manipulate the Q-factor as discussed previously, to generate nanosecond pulses or giant pulses of high energy and peak power. At first, the cavity is highly attenuated to prevent lasing, while the pumping mechanism accumulates the energy into the gain medium. The total stored energy is usually restricted only by spontaneous emission, that is continuous pumping, or in strong enough gain cases, by the emergence of parasitic lasing or strong ASE, if not directly by the onset pump energy.

However, the stored energy can be a manifold of the saturation energy. After that, the power of the laser radiation intensify rapidly in the cavity when the cavity losses are brought down to a small value in a sudden. Hundreds or thousands of resonator round trips will amplify the spontaneous emission noise to macroscopic power levels. The gain starts to be saturated once the intracavity power has attained the order of the saturation energy of the gain medium. When the gain matches the low cavity losses, the pulse is at the highest peak. The enormous intracavity power available at that instant promote further depletion of the existing stored energy where the power decays. Typically, the emerging pulse shape is approximately symmetric due to the energy withdrawn after the pulse peak is similar to that before the pulse peak. As shown in Figure 2.22, the loss modulator is allocated in the laser cavity to switch the intra-cavity losses effectively.

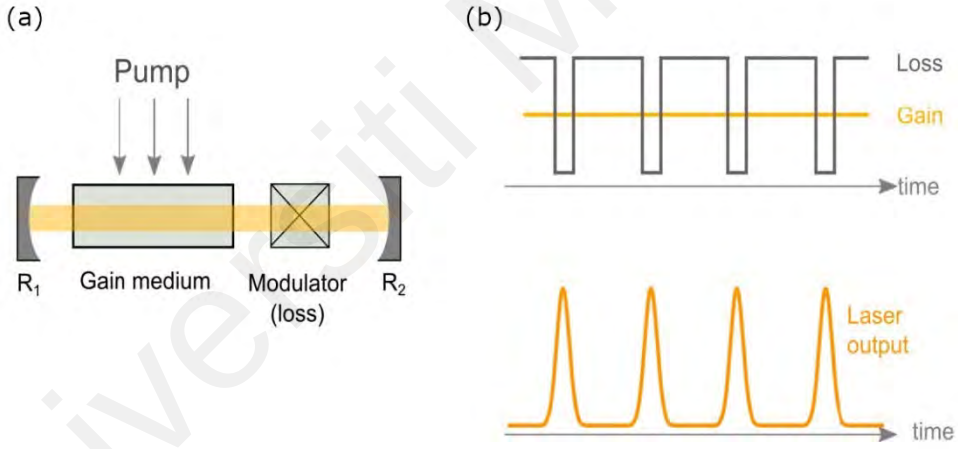

Figure 2.22 a) A basic elements in laser cavity comprising of a pump source, a gain medium, and two mirrors R1 and R2. A modulator is put to introduce intra-cavity loss. b) The gain and modulated loss profile of the cavity give rise to 'burst' of energy for every decreased loss below the available gain (Copyright permission from Hu et al., 2015).

The cavity losses can basically be switched in different ways through active and passive methods. The utilization of the Kerr-call loss modulator is among the first verifications that manipulates the polarization of the light in the cavity to influence the gain efficiency of the crystal, creating a polarization-dependent losses (Kozak et al.,

2004). In general, commonly classified active methods require an electrical input to manipulate the loss modulator, like electro-optic modulators (EOMs) and acousto-optic modulators (AOMs) (Karlsson et al., 2003; Mao et al., 2018; Schnell et al., 1990; Zhao et al., 2006). On the contrary, passive methods usually incorporate the use of a nonlinear material known as saturable absorber that negate the use of electrical input to operate.

2.5.1.1 Active Q-switching

Modulation of losses with an active control unit in the laser cavity, normally either EOMs or AOMs is called active Q-switching. In this method, the light pulse is released as soon as an electrical trigger signal arrives and drives the intracavity losses quickly to a low level. Besides electrical, there are also mechanical Q-switches, for instance spinning mirrors, used as output mirrors of laser resonators. Either case, the generated pulse energy and pulse duration revolve around the energy stored in the gain medium, that is on the pump power and the pulse repetition rate. The progression of gain and total losses in an actively Q-switched laser is shown in Figure 2.23.

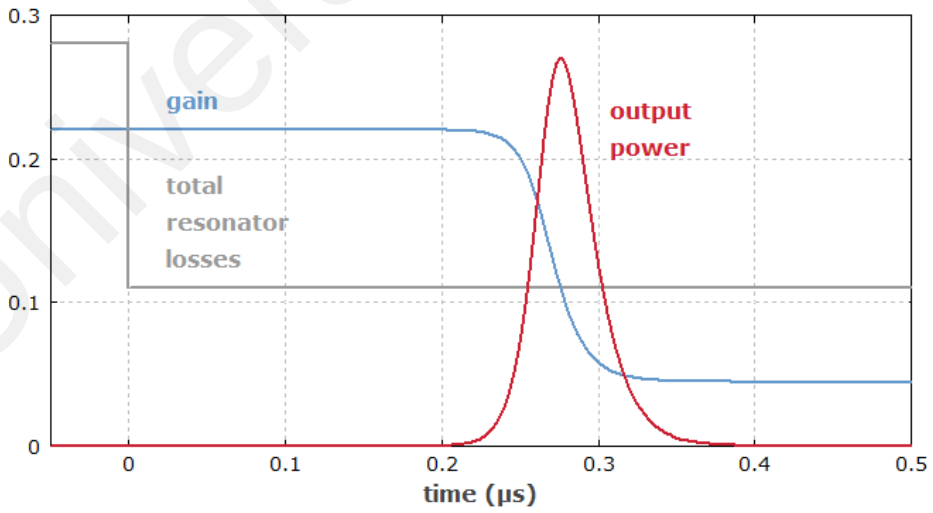

Figure 2.23: Temporal development of losses and gain in an actively Q-switched laser. The Q-switch power starts to escalate exponentially at $t = 0$, however becomes high only after $\approx 0.2\mu s$. The delay time is commonly far longer than the pulse duration in real practical situation (Copyright permission from www.rp-photonics.com).

Intriguingly, equivalency is not necessary between the switching time of the modulator and the pulse duration. In reality, the switching time can be much longer than the pulse duration because an intense pulse is formed from many cavity round trips. However, an over dragged switching time may result to double pulses or to certain instabilities. One of the active Q-switching advantages is it grant more control on the pulse repetition rate since the pulses are generated in a periodic manner. Even so, external power is a requirement in typical active Q-switches to modulate the laser resonator signal, hence, turning the setup into a bulky and costly system.

2.5.1.2 Passive Q-switching

Passive Q-switching requires a saturable absorber (SA) to self-modulate the loss in the cavity. SA is an intensity-dependent nonlinear material which its absorption coefficient changes with the intensity of light. The absorption of the SA significantly reduced when the illuminating light becomes more intensified. Under such circumstances, the states in the conduction band of the SA will be completely occupied which stop further absorption based on the Pauli exclusion principle (N. Dong et al., 2017; H. Lin et al., 2017). This phenomena is called Pauli blocking effect, where the SA becomes saturated at the end point. The progression of gain and total losses in a passively Q-switched laser is shown in Figure 2.24.

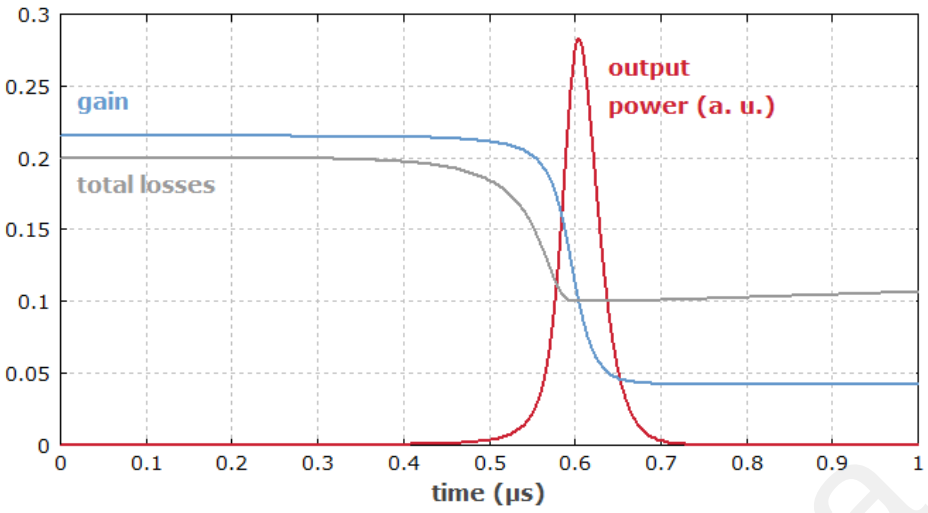

Figure 2.24: Temporal development of losses and gain in a passively Q switched laser. A short pulse is emitted soon after the gain surpasses the cavity losses. The power escalates quickly once the absorber starts to be saturated, till the gain is saturated to the level of the losses (Copyright permission from www.rp-photonics.com).

The SA prohibits lasing in its opaque state due to the high absorption of low intensity signal light in the beginning. Through times, the cavity starts to lase at a negligible power when the gain raises slightly above the total loss of the cavity and continue grow at a slow rate. As the power is accumulating in the cavity, it will fill the available upper states in the conduction band. Thus, the conduction band starts to develop population as the pumping power gradually increased until it reaches population inversion and make the SA to be saturated. At the saturation point, the SA rapidly becomes transparent to the signal light until the gain drops below the total losses of the cavity as it rapidly becomes opaque to the signal light again. The peak of the pulse occurs when the gain is equal to the total losses. This massive energy release will give rise to the gain saturation, hence end the lasing action. If the SA has a fast recovery time returning to its initial state completely, a train of pulse can be generated (Paschotta, 2008).

The interaction in passively Q-switched laser involves three dynamic variables, light field, laser gain and saturable absorption. Approximation of three coupled differential equations can be used to describe these dynamics as follows (Paschotta, 2008)

$$\frac{\delta P}{\delta t} = \frac{g - \alpha_{ns} - \alpha}{T_{rt}} P + \frac{P_{fl}(g)}{T_{rt}} \tag{2.36}$$

$$\frac{\delta g}{\delta t} = \frac{g - g_{ss}}{\tau_g} + \frac{gP}{E_{sat,g}} \tag{2.37}$$

$$\frac{\delta \alpha}{\delta t} = \frac{\alpha - q_0}{\tau_a} - \frac{\alpha P}{E_{sat,a}} \tag{2.38}$$

where P corresponds to the optical power in the laser resonator, g represents the laser gain, α is the saturable absorber loss, and α_{ns} is the non-saturable loss. T_{rt} is the round-trip time of the laser resonator, the small amount of fluorescence light enter the laser mode(s) is represented by P_{fl}, g_{ss} corresponds to the small-signal gain. τ_g and $E_{sat,g}$ refer to the relaxation time and the saturation energy of the gain medium, whereas τ_a and $E_{sat,a}$ refer to the relaxation time and the saturation energy of the SA, respectively.

2.5.1.3 Recent Progress on Q-switched Thulium-doped ZBLAN Fiber Laser

Various configurations of Q-switched thulium-doped ZBLAN lasers have been published till now, utilizing diverse SAs and active modulators. For instance, M. Eichhorn has demonstrated a Q-switched thulium-doped double clad ZBLAN by using AOM that can provide up to 90 µJ pulse energy with maximum repetition rates of 100kHz and minimum pulse width of 160 ns, that is 9 W average output power (Eichhorn, 2007). Graphene-based Q-switched lasers have also been realized by J.H. Lee et al. and C. Jia et al. at different wavelengths of 1.9 µm and 1.48 µm, respectively. J.H. Lee et al. has

managed to get 6 mW average output power with maximum repetition rates of ~25 kHz and minimum pulse width of ~1.4 μs, by using 790 nm wavelength to pump the gain medium (J. H. Lee et al., 2014). While C. Jia et al. has displayed a higher average output power of 13.37 mW with maximum repetition rates of 29.9 kHz and minimum pulse width of ~9 μs, by using 1064 nm pumping wavelength (Jia et al., 2015). Later on, they also has succeeded to produce Q-switching at 1.9 μm and 2.3 μm with bidirectional pumping at 795 nm (Jia et al., 2017). To date, H. Ahmad et al. has published quite amount of reports on passive Q-switched thulium-doped ZBLAN laser by using various SAs, including rGO-Ag (H Ahmad, Azmy, Reduan, et al., 2020), Cu_2Te (H Ahmad, Azmy, Yusoff, et al., 2020) and GaSe (Harith Ahmad et al., 2018). In spite of these reports, passive Q-switched pulse in thulium-doped ZBLAN fiber is still in its early stage.

2.5.2 Mode-locking Fundamentals

Mode-locking is a technique to acquire ultrashort pulses from lasers by inducing phase locking at different frequency modes, which are then called mode-locked lasers. The laser resonator or cavity contains a mode-locking device, either an active element called optical modulator, or a nonlinear passive element called saturable absorber that responsible for the formation of ultrashort pulse circulating in the cavity. The gain bandwidth of rare-earth-doped glasses medium able to underpin the overlapping multiple cavity modes due to inhomogeneous broadening. Interaction of individual absorbing or radiating atoms with different wavelength component cause the linewidth of an atomic transition to expand in inhomogeneous broadening.

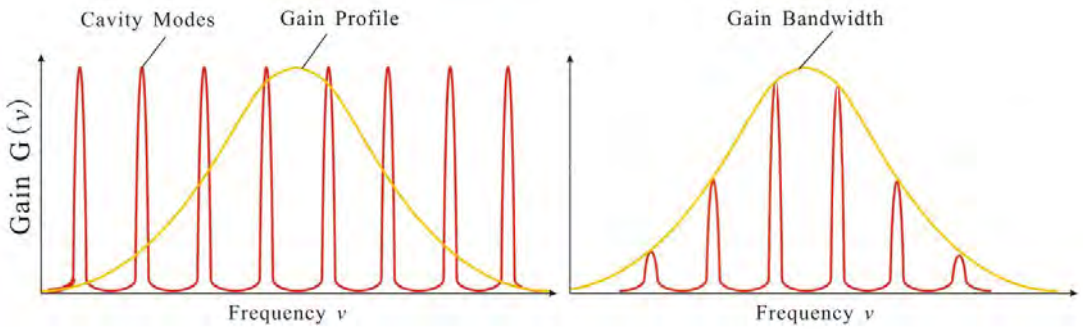

Figure 2.25: The gain profile and modes of a laser. The overlapping of allowed cavity modes with gain profile results in multi-mode lasing.

The intersection of the gain bandwidth with the cavity modes is depicted in Figure 2.25. The total lasing cavity modes as a function of time is expressed in the following

$$E(t) = \sum_{n}^{N} E_n e^{i(\omega_n t + \phi_n)} \tag{2.39}$$

where E_n referes to the amplitude at the n^{th} mode, ω_n is the angular frequency of the oscillation of the n^{th} mode, and ϕ_n is the phase of the n^{th} mode. If cavity modes are randomly distributed and out-of-phase, a CW laser will be generated as shown in Figure 2.26. On the contrary, by 'locking' the in-phase modes together through active or passive methods, a constructive interference between the modes will occur at the frequency corresponding to the laser cavity round trip time, generating mode-locked pulses with intense burst. The significant features of mode-locking including repetition rate, pulse duration, and group velocity dispersion are explained in the following subsections.

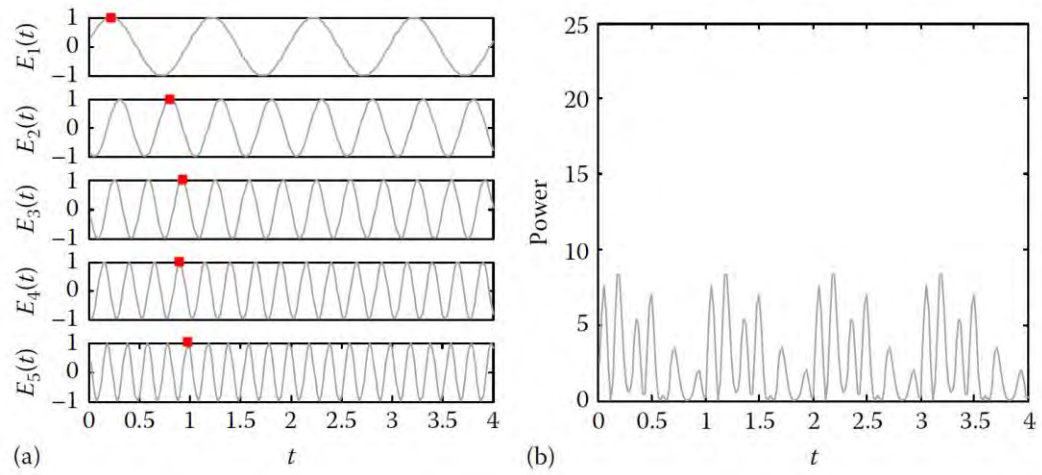

Figure 2.26: The absence of coherent phase in (a) the electric field amplitude of five distinct modes and (b) net amplitude of the multi-mode laser. The units of power and time, *t* are arbitrary (Copyright permission from Ngo & others, 2011).

2.5.2.1 Active Mode-locking

A group of researchers led by Hargrove in 1964 has demonstrated the first active mode-locking (Hargrove et al., 1964). The active mode-locking was theoretically explored by Kuizenga et al. a few years later through Gaussian pulse analysis (D Kuizenga & Siegman, 1970; Dl Kuizenga & Siegman, 1970). External modulators such as Amplitude Modulator (AM) and Phase Modulator (PM) are common modulators utilized to produce mode-locking typically in the range of picoseconds pulse. It can be accomplished by synchronize the periodically pumping modulated laser gain frequency and the round-trip frequency. Gain medium with nanosecond relaxation time can attain shorter pulse through this synchronous pumping method. Figure 2.27 shows the basic concept of an active of active mode-locking.

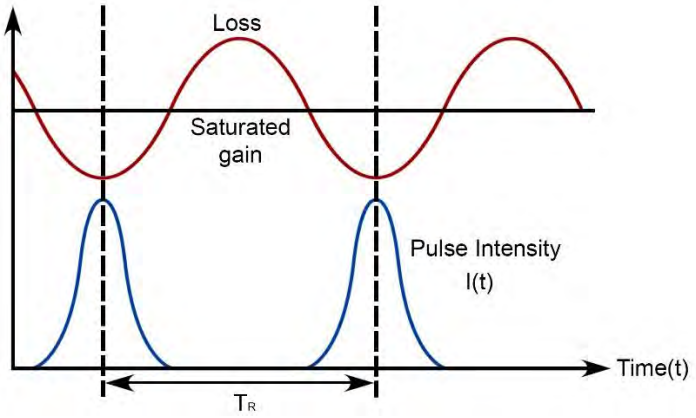

Figure 2.27: Saturated gain and modulated loss of cavity in active mode-locking process with repetition rate, T_R.

The pulse output that emerges from the minimum loss is determined by the process of modulating the loss, thus, the intra-cavity field demands to match the repetition rate of the modulator. The pulse is compressed at every round-trip as the wings accumulate the attenuation. However, the gain narrowing effect counteracts the compression as the pulse tends to spread out.

Figure 2.28 depicts the schematic diagram of active mode-locking laser. The typical active mode-locking cavity comprises similar components as active Q-switching, those are gain medium, modulator loss, and a pair of mirrors to resonate the light. The installed modulator is externally driven at the precise frequency separation of the axial modes, $\omega_m = c/2L$, where L is the cavity length and c is the speed of light in the medium. The periodical external electric trigger assign the modulator to exhibit periodical transmission rate. The periodical frequency of the modulator behaves like a door that only authorize the pulse transmission during minimum loss.

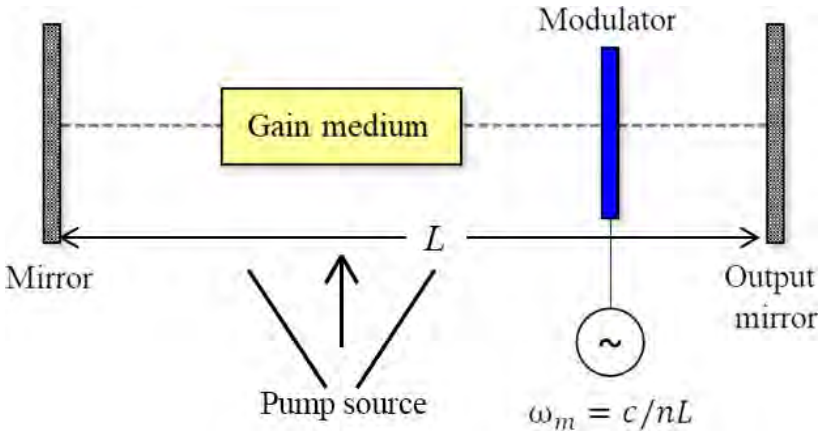

Figure 2.28: A basic elements in actively mode-locked laser comprising of a pump source, a gain medium, and two mirrors. A modulator is introduced and driven at precise frequency separation of the axial modes.

2.5.2.2 Passive Mode-locking

A method that uses internal loss modulation as opposed to active mode-locking to produce pulse can be simply called passive mode-locking. In passive mode-locking, a passive optical "modulator" is integrated in the cavity without external trigger which permits lower losses and higher gain (Ippen, 1994). A common example that has been extensively utilized as passive modulator is saturable absorption of material; a nonlinear effect that has optical intensity dependent on nonlinear absorption coefficient. Similar to the saturable absorber used in passive Q-switching, the absorption rapidly declines and saturates when the optical intensity increases, therefore, allowing the optical signal to transmit. Figure 2.29 shows the schematic diagram of passive mode-locking laser.

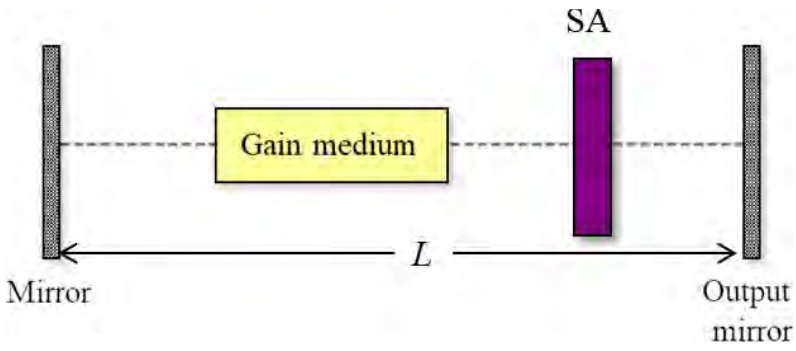

Figure 2.29: The incorporation of a saturable absorber (SA) into the cavity to induce passive mode-locking laser.

Although the setup is akin to the passive Q-switching, but passive mode-locking generates pulse in the range of femtosecond, which usually referred to ultrafast pulse. So far, ultrafast pulse of 5 fs is the shortest that has been demonstrated in communication band (Morgner et al., 1999; Mücke et al., 2001). Besides ultrafast pulse, the other benefit of passive mode-locking is it does not need external components to trigger the modulation loss. However, it comes with a likelihood of not equally spaced pulses in which precise timing mechanism is crucial for high-speed optical transmission systems.

2.5.2.3 Group Velocity Dispersion (GVD)

In optical transmission system, a signal distortion is unavoidable as it travels over a significant distance regardless of its travelling medium (Kuriakose & Porsezian, 2010). The distortion or often known as dispersion is investigated to a great extent in optical waveguide research. It is described as an optical phenomenon that involves the dispersion of optical signal as it passes through a travelling medium. Intramodal dispersion and intramodal delay effects are the two governing factors in dispersion.

Material dispersion and waveguide dispersion are the two components of intramodal dispersion or chromatic dispersion. The dispersion that is originated from the change in refractive index of fiber core with respect to the wavelength change is referred to material dispersion, whilst the dispersion that is originated from waveguide with relatively small effective mode area is referred to waveguide dispersion. For instance, the waveguide dispersion in small effective mode area of a single mode fiber (SMF) core cause a part of the optical power to escape into the cladding. As the pulse propagates at different velocities due to the non-identical refractive index between the core and the cladding, the pulse will spread out along the fiber. The group velocity, v_g of the guided modes or velocity of the wave envelope is used to quantify the chromatic dispersion effect. It can

be represented as the derivative of angular frequency ω with respect to the frequency-dependent wavenumber, k as follows (Kuriakose & Porsezian, 2010)

$$v_g = \frac{d\omega}{dk} \tag{2.40}$$

The waves and their envelopes move at the same velocity in a non-dispersive medium, thus, the pulse preserves itself during the propagation. Nevertheless, such phenomenon is quite uncommon in normal situation.

The refractive index of optical medium and the wavelength of optical signal can influence the velocity of an optical signal, given by (Kuriakose & Porsezian, 2010)

$$v = \frac{\omega}{k} = \frac{c}{n} \tag{2.41}$$

where n is the refractive index of the medium and c is the velocity of the wave in vacuum. Each spectral component possesses individual phase velocity or time delay per unit wavelength, hence, broadening the pulse as it travels along the fiber. This phenomenon is called group velocity dispersion (GVD) and can be determined through the following equation

$$\beta_2 = -\frac{\lambda^2 D_\lambda}{2\pi c} \tag{2.42}$$

The dispersion parameter, D depends on the signal wavelength, λ, where it evolves proportionally. The signal wavelength at 1310 nm is identified as zero-dispersion wavelength, λ_0 because of the zero value of D.

2.5.2.4 Mode-locking operation regime

There are a few optical pulse dispersion regime in mode-locked pulse, specifically soliton laser, stretched-pulse laser and net-normal dispersion laser as portrayed in Figure 2.30. An optical pulse that propagates in a fiber with a group velocity dispersion (GVD) coefficient, $\beta_2 < 0$ is referred to anomalous dispersion regime. The arrangement of frequency position caused by self-phase modulation (SPM) locates the high frequency components at the trailing edge, while the low frequency components at the leading edge. Pulse compression will occur as the high frequency components move faster than the low frequency components. However, the SPM-induced frequency chirping will be restrained by the anomalous dispersion, causing the pulse to preserve its width along the entire length of the fiber during propagation. This category of pulse envelope is named soliton.

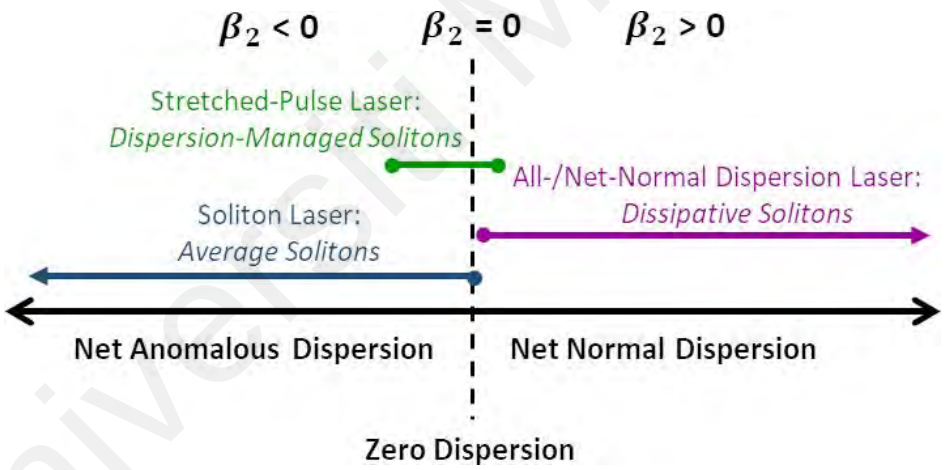

Figure 2.30: The operating regimes of mode-locked fiber laser.

The behaviour of soliton pulse is described in the nonlinear Schrödinger equation (NLSE) with a sech profile shape solution is defined as follows (C. Guo, 2010)

$$U(t) = P_0 sech\left(\frac{T}{T_0}\right) \tag{2.43}$$

where P_0 and T_0 are the peak power and pulse width, respectively. The quality of T_0 is predetermined by the FWHM, T_{FWHM} as follows

$$T_0 = \frac{T_{FWHM}}{1.665} \tag{2.44}$$

The initial peak power P_0 that is needed to form the first-order soliton is described as

$$P_0 = \frac{|\beta_2|}{1.665} \tag{2.45}$$

Kelly's sideband is a distinguished characteristic of soliton in fiber laser that can be observed in optical spectrum (Kelly, 1992). A quasi-soliton pulse in the laser cavity encounters the effects of nonlinearities and chromatic dispersion when propagating. If the resultant effect per round trip is weak, the pulse approximately undergoes their average values and an amount of periodic disturbance due to the distinct nature of dispersion and nonlinearity, leading to periodically occurring amplification and losses in the laser cavity.

The periodical disturbances couple the soliton to a perturbed soliton or dispersive wave. Since the relative phase of dispersive wave and soliton is always changing because of only the soliton experiences the nonlinearity solitarily, usually the coupling does not have strong effects. Nevertheless, a type of resonant coupling can take place particularly in fiber laser, where the relative phase of soliton and dispersive wave for some optical frequencies change by an integer multiple of 2π per round trip. This arises the formation of narrow peaks in optical spectrum due to the constructive interference between soliton and dispersive wave.

2.5.2.5 Recent Progress on Mode-locked Thulium-doped Silica Fiber Laser

The progression of mode-locked thulium-doped silica fiber laser has grown steadily over the years, comprising countless techniques and structures. SA such as CNT has been

reported to successfully generate passive mode-locked pulse as demonstrated by M.A. Solodyankin et al. and Y. Meng et al., where both have fundamental repetition rate of 37 MHz and 18.4 MHz, respectively. The pulse width and maximum average output power given in both of the reports are 1.32 ps and 3.4 mW (Solodyankin et al., 2008), and 2.38 ps and ~1 mW (Y. Meng et al., 2017), accordingly. Although Y. Meng et al. displayed lower average output power, but the laser produced has a tuning range of 200 nm wide. Besides CNT, graphene has also been utilized by Y. Wang by laying a single-layer graphene onto a tapered fiber as SA. It has a fundamental repetition rate of 19.3 MHz, a pulse width of 0.98 ps, and a maximum average output power of ~10 mW. Other than carbon-based SA, SA from TMD family also shows promising results as demonstrated by Z. Tian et al. by using MoS_2 (Z. Tian et al., 2015). Multilayer of MoS_2 was extracted through liquid-phase exfoliation and transferred onto a gold mirror to be SA. The SA was integrated into a linear cavity and produced mode-locked pulse with a fundamental repetition rate of 9.67 MHz and maximum average output power of 150 mW. A 1550 nm pumping wavelength with maximum pump power of 730 mW was operated during the experiment. Although various SAs such as gold nanorods (Kang et al., 2015), WSe_2 (J. Wang et al., 2017), and MoS_2 (Z. Tian et al., 2015) have shown progress to generate better quality mode-locked pulse, yet MXenes is still in its beginning point.

2.5.3 Pulse Width of Q-switched and Mode-locked Lasers

The measurement of full width at half maximum (FWHM) of the optical power as a function of time refers to pulse duration or pulse width of pulse. In Q-switched laser, the pulse width is power dependent, where the pulse width become shorter when the input power of the laser increases. The highest pulse energy and shortest pulse width can be achieved at the lowest pulse repetition rate, however, at the expense of reduced average

output power. In addition, in mode-locked laser, the pulse width is fixed although the input power of the laser increases. The pulse width is usually measured at the fundamental pulse repetition rate of the laser.

The fascinating fact in mode-locked lasers is it has exceptionally ultrashort pulse duration in the order of a few tens of picosecond that is usually possible through passive method. Ultrashort pulse duration is sought in some application because of its requirement in fast time resolving process and high-rate optical data transmission. On the other side, nanoseconds pulse duration can preserve its shape during propagation which makes it practical in the use of long-haul communications.

The high tendency of ultrashort pulse laser to grow distortion because of the nonlinearity of the silica fiber makes it hard to utilize. Besides, the application of ultrashort pulse laser can also be restrained by the built-in optical filter with typical narrow bandwidth in a mode-locking system. This could efficiently create temporal broadening in the optical spectrum, thus, widen the pulse duration of the laser as suggested by the Fourier transform. Hence, in ideal case, a soliton pulse is preferred in mode-locking regime as the obtained pulse can preserve its shape over long distances

2.5.4 Repetition Rate of Q-switched and Mode-locked Lasers

Repetition rate of pulse is characterized by the number of pulse generated in a second or commonly refers to the frequency of the pulses. A series of optical pulses with a fixed spacing between them is called as pulse train and it can be estimated by evaluating the cavity round-trip time, ΔT that is defined as

$$\Delta T = \frac{nL}{c} \tag{2.46}$$

where n represents the refractive index of the medium, c is the speed of light in vacuum, and L is the cavity total length. The repetition rate, f can then be determined by taking the reciprocal value of ΔT as follows

$$f = \frac{1}{\Delta T} \tag{2.47}$$

The repetition rate of pulse can be modified accordingly due to its dependent nature on the cavity length.

In Q-switched laser, the pulse repetition rate is also power dependent, where the pulse repetition rate increases as the input power increases. The peak power of the pulse is highest at the highest pulse repetition rate, nonetheless, the average output power will be reduced. On the other hand, in mode-locked laser, the pulse repetition rate is harmonic, where the fundamental repetition rate will develop to a higher harmonic after a certain power level is fulfilled. Normally, at the higher harmonic, the pulse will be unstable, hence results usually taken at the fundamental harmonic.

2.6 Four Wave Mixing (FWM)

A nonlinear effect that is originated from a third-order optical nonlinearity is four wave mixing as expressed with a $\chi^{(3)}$ coefficient. At the minimum of two distinct optical frequency components are required to propagate at the same time in a nonlinear medium such as an optical fiber to generate this effect.

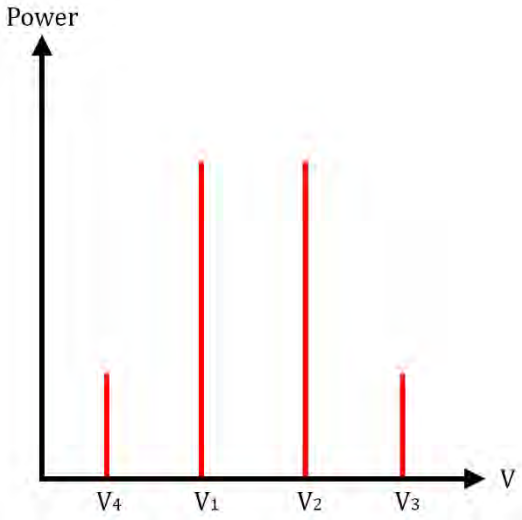

Figure 2.31: Generation of new frequency components through FWM.

In the case of two copropagating optical frequency components v_1 and v_2, two extra frequency components are produced because of the refractive index modulation at the difference frequency. Both of the new frequency components can be determined by the following

$$v_3 = v_1 - (v_2 - v_1) = 2v_1 - v_2 \tag{2.48}$$

$$v_4 = v_2 + (v_2 - v_1) = 2v_2 - v_1 \tag{2.49}$$

The additional frequency components are illustrated in Figure 2.31. The amplification of a pre-existing wave at the frequency v_3 or v_4 is allowed through parametric amplification, where it involves a parametric nonlinearity and a pump wave to boost the signal. It is also possible to get the frequencies $v_5 = 2v_1 + v_2$ and $v_6 = v_1 + 2v_2$, but highly unlikely due to the difficult phase-matched condition.

2.6.1 Non-degenerate and Degenerate FWM

The four different frequency components from the above model supposed to couple via four wave mixing; this is called non-degenerate FWM. Nonetheless, it possesses the

possibility of degenerate FWM, where two of the four frequencies coexist. For instance, a neighboured frequency component (signal) can gain amplification from a single pump wave. Two photons are removed from the pump wave for every photon included to the signal wave, where the other one is added into an idler wave with a frequency at a distance from the pump.

Self-phase modulation and cross-phase modulation are associated to FWM in fiber; all these effects derive from the same Kerr nonlinearity and vary only in the degeneration of the waves involved.

2.6.2 Phase Matching

Four wave mixing revolve around on the relative phases of all beams, as such, it is a phase-sensitive process. As a consequence, its effect can effectively stockpile over long haul, such as in a fiber with a phase matching condition, which is regulated by the chromatic dispersion and nonlinear phase shifts.

In a state where the frequencies involved are in close proximity or the chromatic dispersion profile has an appropriate shape, phase matching is roughly given. It can also be realized using a suitable angles between the beams in bulk media. On the contrary, four wave mixing is efficiently subdued in a significant phase mismatch.

2.6.3 Recent Progress on FWM

The effect of four wave mixing (FWM) has been used in many areas in photonics field by using many nonlinear material to induce or aid the performance of it. W. Mathlouthi et al. and Y. Ding et al. have used silicon planar waveguide to produce the FWM in wavelength conversion application (Ding et al., 2014; Mathlouthi et al., 2008). However, semiconductor optical amplifier (SOA) is commercially used instead for wavelength conversion due to its practicality (D'ottavi et al., 1997). The development of SOA is still continued until today as being displayed by S.L. Lee et al. (S.-L. Lee et al., 2002), N.A.

Awang et al. (Awang et al., 2011), A. Fardi (Fardi et al., 2021), and P. Hejib (Hejib & Sharma, 2021). The dominant of SOA in industry does not halt the progression of other FWM-induced options. W. Mathlouthi et al. managed to unveil the competency of silicon planar waveguide in comparison to SOA by offering broader conversion bandwidth, higher optical signal-to-noise ratio (SNR), and negligible channel crosstalk (Mathlouthi et al., 2008). Other than planar waveguide, fiber also has been used to create the FWM effect such as photonic crystal fiber (PCF) (Chow et al., 2007; T. Yang et al., 2005), holey fiber (J. H. Lee et al., 2003), and As_2S_3 doped fiber (Szpulak & Février, 2009). Research groups such as K.K. Chow et al. and B. Xu et al. have found a way to reduce the length size of the used fiber by depositing SAs onto a modified fiber to initiate FWM effect (Chow et al., 2010; Chow & Yamashita, 2009; Xu et al., 2012, 2013). As such, X. Jin et al. has used graphdiyne-microfiber based to demonstrate FWM with a maximum conversion efficiency of -39 dB (X. Jin et al., 2022), whereby M.Li et al. has demonstrated a higher maximum conversion efficiency of -19.1 dB with borophene-microfiber based (M. Li et al., 2022). This method has pique interest in FWM-induced fiber's research groups due to its practical length size.

2.7 All-Optical Modulation

In principle, the optical response of materials can be represented by the complex refractive index or dielectric constant as in Eq. 2.8

$$n = n_0 + n_2 I - i\frac{\lambda}{4\pi}(\alpha_0 + \alpha_2 I) \tag{2.8}$$

which the real part, $n_0 + n_2 I$ describes the refractive index and the imaginary part, $\frac{\lambda}{4\pi}(\alpha_0 + \alpha_2 I)$ describes the absorption property. External stimulus such as optical fields,

electric fields, magnetic fields, pressure, and temperature, can be used to alter the refractive index, which impose the basis for optical modulation. The operation of optical modulation can be anticipated based on passive and active modulation (signal light is modulated by itself or another light beam). It can be group as phase modulation, amplitude modulation, polarization modulation, and so forth in accordance with attribute of light. Also, the principles of operation further classify into electro-optic, thermo-optic, magneto-optic, all-optic and so forth. The change in property of materials through light modulation determine either refractive modulation or absorptive modulation, according to essentially the change in the real and imaginary part of the refractive index, sequentially.

All-optical modulation is a light-control-light regime, where a switching light beam such as ultrafast laser pulse is utilized to control the propagation of signal light beam. Figure 2.32 illustrates the optical nonlinear effects of nonlinear media used to achieve the light-to-light interaction.

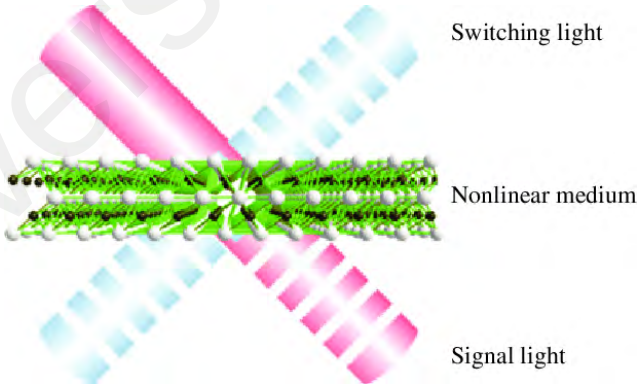

Figure 2.32: Basic of all-optical modulation. Switching light beam is used to control and modulate signal light (Copyright permission from H. Chen et al., 2020).

The carrier densities and distribution in 2D materials might change significantly when trigger by laser pulse, consequently initiate the change in both the real and imaginary parts of their complex refractive index; hence, both phase modulation and amplitude modulation can be used by 2D materials. To date, majority of all-optical modulation with

2D materials are established on third-order nonlinear response of a material (saturable absorption and Kerr effect), and thermo-optic effect (temperature-dependent refractive index change of a material). However, in this work, absorptive modulation utilizing saturable absorption is being demonstrated.

2.7.1 Absorptive Modulation

Credit to the ultrafast optical response and practicalities to integrate onto functional photonic structures, a graphene-clad microfiber all-optical modulator has been reported by Li et al. in 2014 (Wei Li et al., 2014). Figure 2.33(a) shows the elemental structure of the modulator; a mechanically exfoliated double-layer graphene film was wrapped onto a single-mode tapered fiber with a waist diameter of approximately 1 μm. A signal light of 1500 nm wavelength was coupled into the fiber, where it encountered considerable loss by graphene as it travel along. The absorption loss reduced when a 1064 nm pulse laser was instigated because of the saturable absorption effects, hence authorizing effective modulation of the signal light.

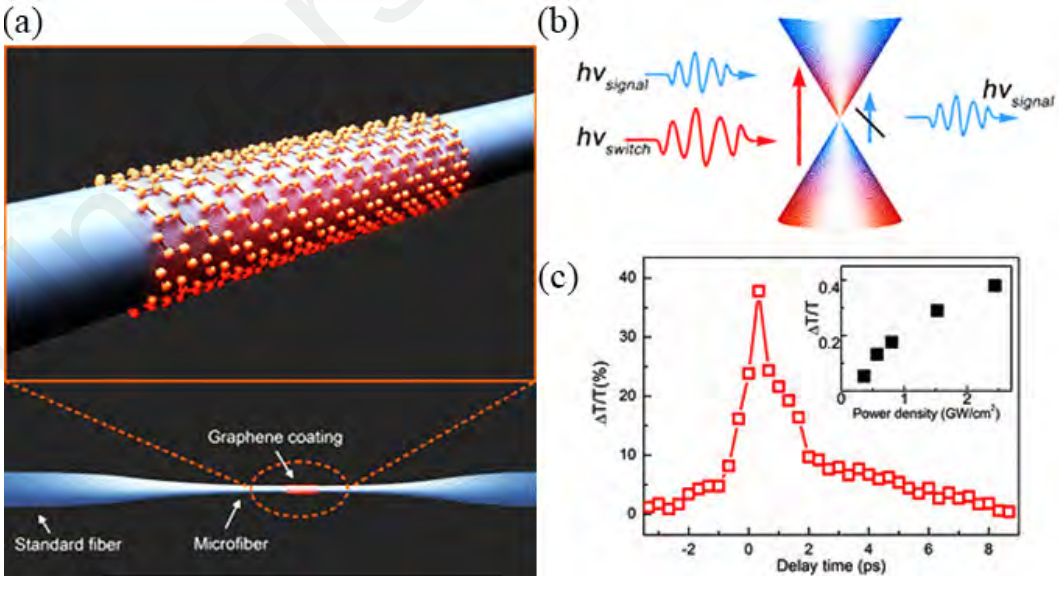

Figure 2.33: 2D material-based absorptive modulator. (a) Graphene-clad microfiber, (b) mechanism of all-optical modulation by using saturable absorption, and (c) the modulator response time measured by using pump-probe technique (Copyright permission from Wei Li et al., 2014).

The working mechanism is illustrated in Figure 2.33(b). The modulator has a calculated response time of ~2 ps, manifesting the potential of several hundred GHz bandwidth for optical signal processing. The modulator possess modulation depth and switching laser peak power of 38% and about 40 W, where it can be improved by optimizing the graphene coating and the geometries of fiber (P. Wang et al., 2013). The pulse peak power can be trimmed down to ~3 W by applying a graphene-coated polymer nanofiber as displayed by Meng et al., to minimize the threshold of the saturable absorption (C. Meng et al., 2015).

The same absorptive modulation light-control-light system has been applied to $Ti_3C_2T_x$ MXene by Wu et al. through spatial cross-phase modulation (SXPM) effect (L. Wu et al., 2018). Instead of usual modulated CW operation, their group employed the modulation study based on SXPM effect, where the phase of a light field is changed by the other co-propagating light field, that showed both ring numbers and diameters of the probe light on a flat surface (Agrawal, 1987; Y.-F. Chen et al., 2006; Lu et al., 2017). In general, two main properties of having a narrow bandgap to attain a broadband of nonlinear optical response and a large nonlinear refractive index to induce a strong nonlinear optical response are favourable in light-control-light system.

2.7.2 Recent Progress on All-Optical Modulator

Optical modulators are designated by several interplayed variables, involving modulation depth, insertion loss, modulation speed, and energy consumption. The operation mechanism and structures determine the pros and cons of 2D material-based all-optical modulators. For instance, because of the slow thermal diffusion of thermo-optic all-optical modulation, the speed is often under 1 MHz. The modulation speed is however can be tweaked by optimizing the dimension and structure of the components. In particular, when narrowing the fiber diameter from 10 μm (Gan et al., 2015) to 1 μm (Yu et al., 2016), the modulation speed of a graphene-coated microfiber can be escalated

dramatically to the order of two. On the contrary, the intrinsic response of the materials plays significant role on the modulation speed of all-optical modulators based on nonlinear effects, working at the capacity up to hundreds of GHz (Wei Li et al., 2014) or even higher (Dawlaty et al., 2008; D. Sun et al., 2008). Gan et al. and Y. Wang et al. have displayed light-to-light modulation by using graphene and BP with modulation efficiency of 0.018 and 0.36 (Gan et al., 2015; Y. Wang et al., 2018). The materials also possess rise/fall time constant of 4/1.4 ms and 2.5/2.1 ms for graphene and BP, respectively. WS_s also possesses modulation efficiency of 0.035, that is almost twice higher of the mentioned graphene, however, has a slower rise/fall time constant of 7.3/3.5 ms as displayed by Wu et al (K. Wu et al., 2017). Although Q. Guo et al. has demonstrated a modulation efficiency of Boron nanosheet almost half of the BP, but it has a faster rise/fall time constant of 0.48/0.69 ms (Q. Guo et al., 2019). Among the latest work on optical modulation has been displayed by L. Wu et al. on a high-performance all-optical modulation by using graphdiyne oxide (GDYO) nanosheets with a saturable absorption of more than 98%. Other than that, H. Wang et al. has also displayed a terahertz wave all-optical modulator by using a quartz-based methylammonium lead iodide ($MAPbI_3$) thin film with a saturable absorption of 66.24%. The difference of modulation efficiency and rise/fall time constant are influenced by the interaction length and saturable absorption of the 2D materials.

CHAPTER 3: FABRICATION AND CHARACTERIZATION OF MOLTEN FLUORIDE SALT-ASSISTED SYNTHESIS OF MXENES

3.1 Introduction to Molten Salt Etchants

The etching process of nitride-based MAX phases by using aqueous acidic solution have proven failed. The hypothesis underlying this failure was due to the lower cohesion energies of nitride MXenes than carbides and the formation of nitride MXenes from nitride-based MAX phase consume higher energies than that of carbide MXenes from carbide-based MAX phase (Urbankowski et al., 2016). However, as opposed to the method above, nitride MXenes, particularly Ti_4N_3, have been fabricated through selective etching of Al from Ti_4AlN_3 by using molten salts, such as sodium fluoride (NaF), potassium fluoride (KF), and lithium fluoride (LiF). Molten salts with fluoride-based are known as molten fluoride salt. During the etching process, the molten salt and Ti_4AlC_3 was heated in Argon for 30 minutes at 550 °C to overcome the energy gaps in bonding between metals in a nitride-based MAX phase by potentially providing the reaction with more energy. Afterwards, sulfuric acid (H_2SO_4) solutions were mixed with the powders and repeatedly washed to bring out residues and excess fluorides after etching. The molten salt etchants have demonstrated several advantages over aqueous acidic solution, hence have been adapted in this work.

The synthesis method and a series of characterization of MXenes are presented in this chapter. MXenes with chemical composition of M_2X, specifically titanium carbide (Ti_2C), niobium carbide (Nb_2C), and vanadium carbide (V_2C), are fabricated by using molten fluoride salt synthesis which is categorized in solution-based chemical synthesis. The details of physical characterization including field emission scanning electron (FESEM), high-resolution transmission electron microscopy (HRTEM), X-ray diffraction (XRD) and Raman spectroscopy, and optical response description including

linear absorption and nonlinear absorption (saturable absorption and Z-scan) are discussed in separate sections. The experimental configuration for each optical response measurement are also reported in this chapter.

3.2 Fabrication of Molten Fluoride Salt-Assisted MXenes

3.2.1 Molten Fluoride Salt Synthesis of MXenes (M_2X)

The MXenes were synthesized by removing the aluminium (Al) layers from MAX phases through etching process. Hydrofluoric acid (HF) was used predominantly in the beginning to etch away the A group layers from MAX phase although it is considered harmful due to its corrosive property. Subsequently, researchers have found an alternative solution to replace the HF with a mixture containing fluoride salt (lithium fluoride (LiF), sodium fluoride (NaF), potassium fluoride (KF)) and hydrochloric acid (HCl) to act as etching agent (Das et al., 2020; M. Wu et al., 2018). Nonetheless, in this work, only a mixture of LiF and HCl was utilized as etching agent to remove the A group layers from MAX phases, specifically, titanium aluminium carbide (Ti_2AlC), niobium aluminium carbide (Nb_2AlC), and vanadium aluminium carbide (V_2AlC) following the works that have been done by Guan et al. and Li et al. (Guan et al., 2020; L. Li et al., 2017). The MAX phases were ready made material purchased from 2D Semiconductors corporation.

The first step in this fabrication was preparing the etching solution by adding LiF powder in a container filled with HCl solution and heated for some time with teflon magnetic stir bar to completely dissolve the LiF. There were two types of heating process used to mix MAX phases with LiF + HCl solution, those are normal heating process and hydrothermal heating process; whereby, both were done at specific temperatures according to the individual MAX phase. In normal heating process, the container was rested on a hot plate with thermometer dipped in the solution to observe the temperature,

while the solution was stirred continuously by using Teflon magnetic stir bar. On the other hand, in hydrothermal heating process, the solution was transferred in a Teflon chamber and tightly sealed in autoclave reactor before heated in autoclave machine with a set temperature. After the etching process, the resultant solution contained acidic pH value that come from the etching agent. Since only MXene was required as final product, the solution was centrifuged at 6000 rpm for 10 minutes to separate the supernatant and MXene. The supernatant was removed, leaving a thin layer of solution above the solid MXene, then rinsed the solution with deionized water before centrifuged again. The decantation was repeated several times until the pH value reached neutral line, which suggested the elimination of unwanted products. The rotational speed and centrifuge time were increased up to 7000 rpm and 15 minutes gradually as the pH value approaching 7 due to the hydrophilic nature of MXene in neutral pH value. After the decanting process, the MXene was left to dry for 4 hours at 60 °C in a drying oven to obtain the MXene powder. Table 3.1 shows the parameters used during the whole fabrication process for each MXene.

Table 3.1: MXenes fabrication process parameters.

MXenes / **Variable**	**Ti_2C**	**Nb_2C**	**V_2C**
Type of MAX phase	Ti_2AlC	Nb_2AlC	V_2AlC
HCl volume	20 ml	20 ml	2 ml
HCl concentration	37%	38%	38%
LiF weight	2.07 g	2.07 g	0.2 g

Table 3.1, continued.

MXenes / Variable	Ti_2C	Nb_2C	V_2C
HCl + LiF temperature and time	Room temperature, 15 minutes	Room temperature, 15 minutes	Room temperature, 30 minutes
MAX phase weight	0.5 g	0.5 g	0.1 g
Heating type	Normal	Normal	Hydrothermal
HCl + LiF + M_2AlX temperature and time	50 °C, 48 hours	50 °C, 48 hours	90 °C, 120 hours

3.2.2 Experimental Procedures for Molten Fluoride Salt-Assisted MXenes

This molten fluoride salt synthesis is the common method to fabricate MXenes which involves several processes. Those processes are (i) the making of in-situ HF (molten fluoride salt) that act as etching agent, (ii) the elimination of Al layer from MAX phase, and (iii) the drying process of MXene. Figure 3.1 shows the step-by-step of MXene's physical and chemical processes.

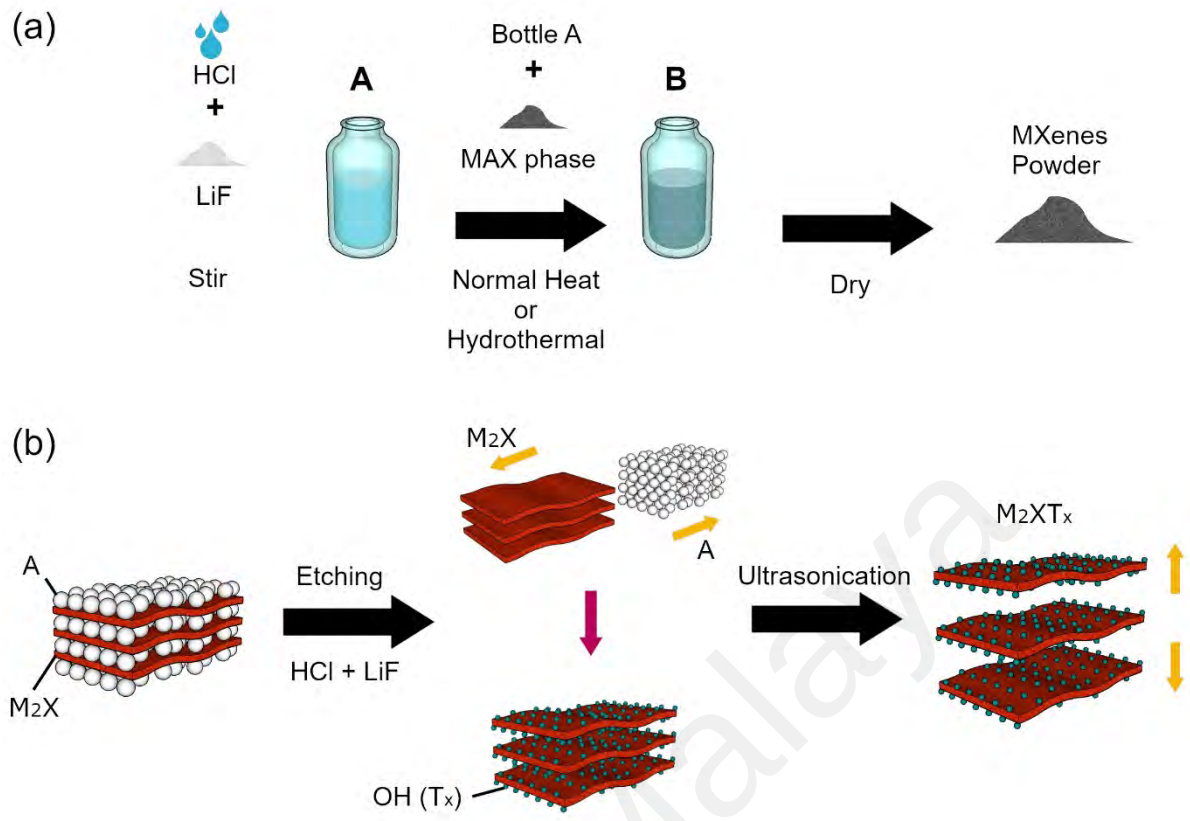

Figure 3.1: The schematic diagram of molten fluoride salt synthesis of MXenes in (a) physical, and (b) chemical processes.

In the first step, LiF powder was taken out from the bottle by using spatula and carefully measured by using analytical balance. Then, HCl solution was poured into a beaker from the bottle and measured by using a measuring cylinder by using pipette until the required volume; the excess HCl solution must be correctly disposed. The HCl was transferred in an appropriate size beaker, then gradually added the LiF powder while heating and stirring by using hot plate magnetic stirrer. The temperature of the chemical reaction was observed by using thermometer clamped onto a retort stand as shown in Figure 3.2.

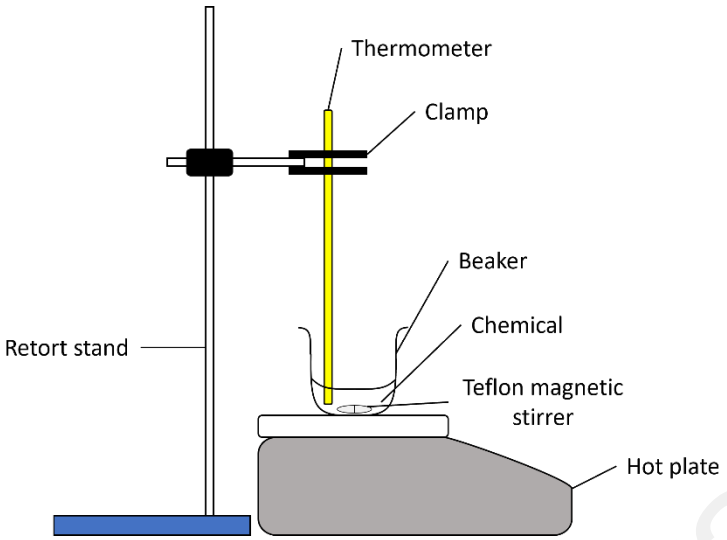

Figure 3.2: Standard heating configuration.

In the second step, MAX phase (Ti_2AlC, Nb_2AlC, or V_2AlC) powder was measured by using analytical balance and rest aside. In standard heating process, the MAX phase powder was gradually added into the LiF + HCl solution while heating and stirring by using hot plate magnetic stirrer at a set temperature until a required time. On the other hand, in hydrothermal heating process, the MAX phase powder and LiF + HCl solution were premixed before added into a Teflon chamber. The chamber was tightly sealed in autoclave reactor and then heated in autoclave machine at a set temperature until a required time.

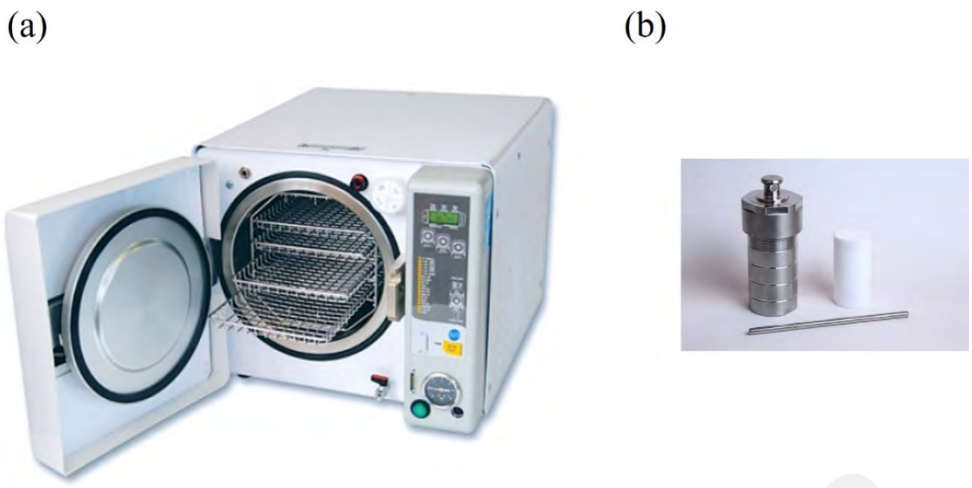

Figure 3.3: (a) Autoclave machine, and (b) autoclave reactor for hydrothermal heating process (Copyright permission from www.keydiagnostics.com.au).

In the last step, a MXene-containing solution was obtained after the etching process. The solution was transferred into a conical tube to be centrifuged. Before began the process, another conical tube filled with water about the same volume as the conical tube containing solution was prepared to place on the opposite side to maintain balance rotation. Both of the conical tubes were placed in the rotor of centrifuge machine. The first centrifugation began at 6000 rpm for 10 minutes, then increased the rotation to 7000 rpm for 15 minutes after the MXene started to become hydrophilic in neutral pH value. After each centrifugation, the supernatant was carefully removed from the tube into a beaker and the remaining solution inside the conical tube was rinsed with deionized water. The pH value of the supernatant was observed by using pH meter until the pH value reached neutral. The pH electrode was washed with deionized water after every measurement to clean the residue of the supernatant and kept in buffer solution. After a neutral pH value was obtained, the solution was transferred into a petri dish and left to dry at 60 °C for 4 hours in drying oven.

(a) (b)

Figure 3.4: (a) Centrifuge machine to separate the supernatant from MXenes, and (b) pH meter to verify the pH value of MXenes (Copyright permission from hk.techcomp.com.hk).

3.3 Characterization of Molten Fluoride Salt-Assisted MXenes

In this topic, the characterization of the fabricated MXenes are explained in detail including the physical and optical properties of the material. Both properties are characterized to validate the accomplishment of fabrication as well as to investigate the important parameters in optical interaction.

3.3.1 Material Characterization of Molten Fluoride Salt-Assisted MXenes

In this section, the morphological characterization such as the lateral size, elemental composition, and crystal structure are disclosed. Hence, among the analysis that have been conducted are FESEM, HRTEM, XRD and Raman spectroscopy. The outcome of this section will give insight into the effects of various physical properties on the performance of the MXenes as nonlinear material.

3.3.1.1 Field Emission Scanning Electron Microscopy (FESEM) and High-Resolution Transmission Electron Microscopy (HRTEM) of Molten Fluoride Salt-Assisted MXenes

FESEM is an advanced technology employed to capture the microstructure image of the materials, which typically executed in a high vacuum due to the disturbance of gas molecules towards the electron beam and the emitted secondary and backscattered electrons used for imaging. HRTEM is an imagining mode of the transmission electron microscopy (TEM) that permits the imagining of the crystallographic structure of a sample at an atomic scale. As such, nanoscale properties of crystalline material can be investigated due to its high resolution. At high resolution, the interactions between the electron beam and the atomic columns of a crystalline specimen develop different contrast mechanism known as phase contrast. This effect can be utilized for visualizing the atomic distances in appropriately oriented crystals. Both FESEM and HRTEM imaging were performed on Ti_2C, Nb_2C, and V_2C, which Hitachi SU8220 was used for FESEM.

From Figure 3.5(a), it can be seen that the Ti_2C grain compose of multiple Ti_2C sheets with thickness centred around 0.08 µm per sheet. The existence of gaps between the layers can be observed as anticipated after the etching process of Ti_2AlC MAX phase as presented in Figure 3.5(b). The gaps were assigned to the elimination of the aluminium (Al) layers, hence demonstrating the success of the etching process to obtain Ti_2C. However, there were other unwanted substances remained around the layers coming from the excess of Al layers and titanium dioxide (TiO_2) formed from the exothermic reaction indicating the low purity of Ti_2C MXene. The structure of Ti_2C was further investigated by HRTEM and the results are displayed in Figure 3.5(c) and (d). The crystalline lattice of Ti_2C is distinguishable at higher magnification, which upholds the crystallinity of the material. It has an interlayer spacing of about 1.2 nm.

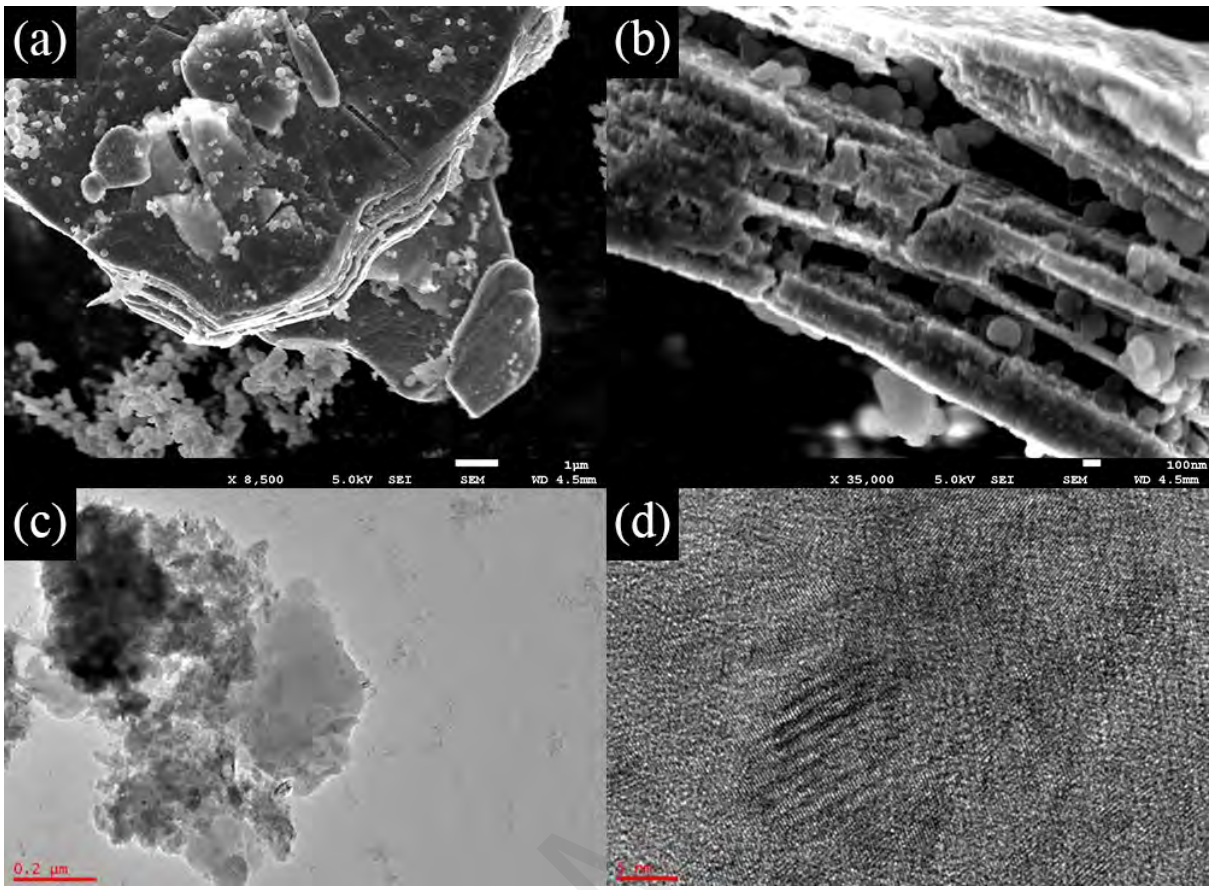

Figure 3.5: FESEM and HRTEM images of Ti_2C MXene.

Figure 3.6(a) and (b) show the FESEM images of multiple Nb_2C grains. The grain is made of multiple sheets stacked together with an estimated thickness around 1 µm per sheet. It consists of spaces between each layer, showing the successful of Al layers removal from Nb_2AlC MAX phase. The Nb_2C is cleared from any residue of Al layers or waste products. The HRTEM images of Nb_2C is shown in Figure 3.6(c) and (d). The crystallinity of Nb_2C structure is demonstrated by the crystalline lattice pattern with an approximate spacing of 1.8 nm.

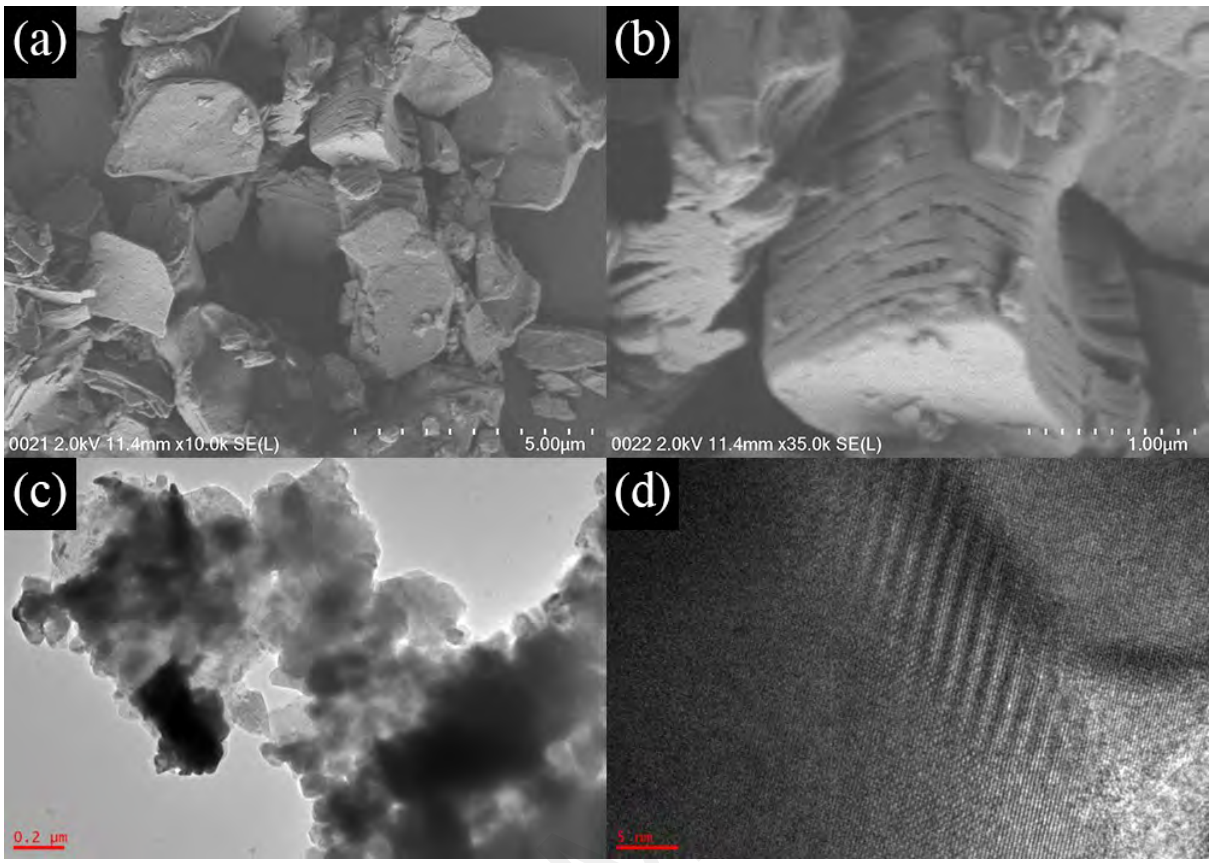

Figure 3.6: FESEM and HRTEM images of Nb_2C MXene.

The FESEM images of V_2C are shown in Figure 3.7(a) and (b), where it displays the V_2C grain composing multiple V_2C sheets. These constituent sheets are stacked one upon another with an approximate thickness of 5 μm per sheet. Because of the successful etching process of V_2AlC MAX phase to V_2C MXene, the elimination of Al layers leave gaps within each layer. Unlike Ti_2C, the waste or unwanted products are unspotted in the V_2C image. In addition, the HRTEM of V_2C is presented in Figure 3.7(c) and (d). The images display the crystalline lattice of V_2C that prove crystallinity of its structure with an approximate interlayer spacing of 1.8 nm.

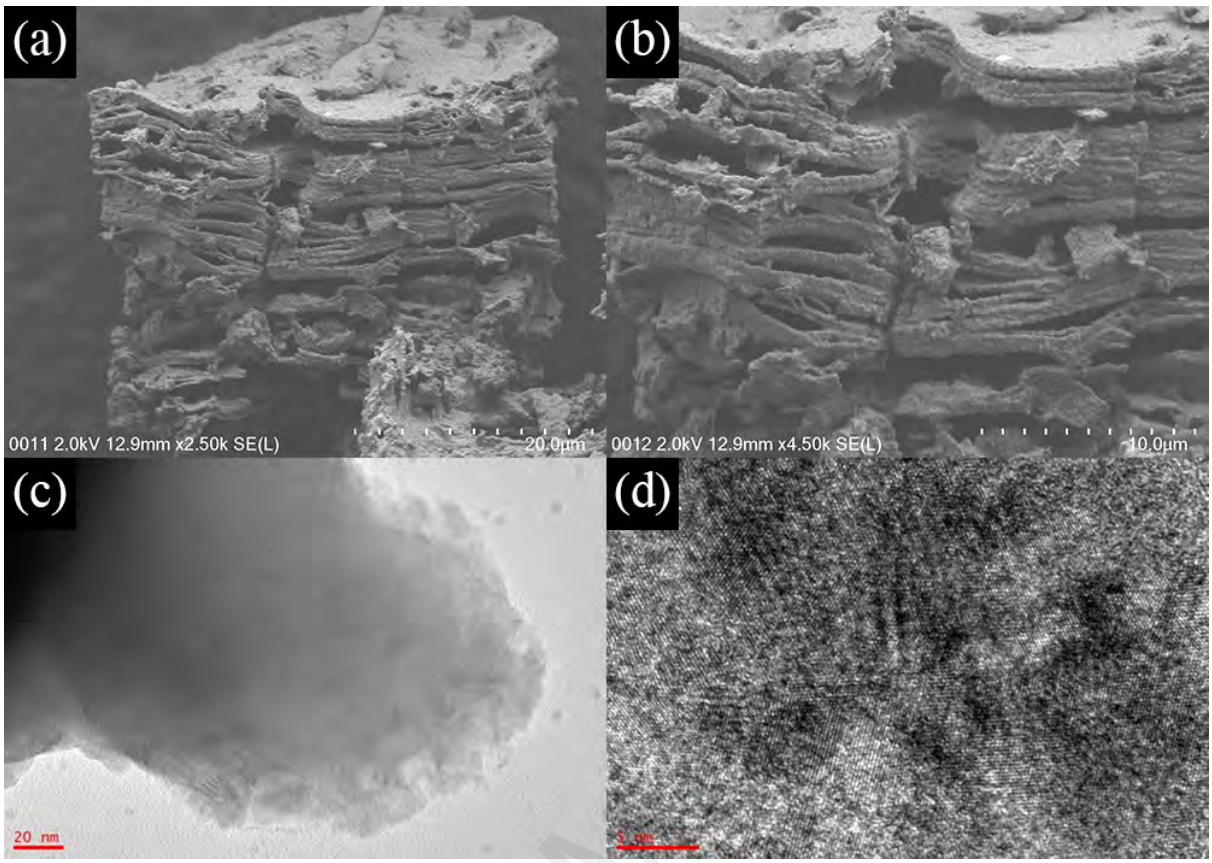

Figure 3.7: FESEM and HRTEM images of V_2C MXene.

3.3.1.2 X-ray Diffraction (XRD) Analysis of Molten Fluoride Salt-Assisted MXenes

In this section, XRD analyses were performed on Ti_2C, Nb_2C, and V_2C by using Malvern Panalytical Empyrean. In this analysis, X-rays beam is shot towards the material, where the crystal atoms will scatter the incident X-rays through elastic scattering, where the interactions are mainly with the atom's electrons or also known as scatterer. A regular array of scatterer create a regular array of spherical waves. These waves nullify each other in the majority of directions by destructive interference, but merge constructively in a particular directions as regulated by Bragg's law

$$2d \sin\theta = n\lambda \tag{3.1}$$

where d represents the spacing between diffracting planes, θ is the incident angle, n represents an integer, and λ is the beam wavelength. The particular directions emerge as spots on the diffraction pattern called reflections. Therefore, the pattern is a consequent from electromagnetic waves impinging on a regular array of scatterers. The wavelength of X-rays are used because they are often of the same order of magnitude as the spacing, d between the crystal planes (1-100 angstroms).

The crystallographic structure of Ti_2C is determined by the XRD pattern Figure 3.8. The X-ray scattering angles, 2θ was examined from 5° to 80°. As foresee in the FESEM images, the peaks of Ti_2C and Ti_2AlC are intermingling across the pattern. The diffraction peaks at 34.61°, 36.24°, 41.99°, 60.61°, 65.13°, and 71.76° are assigned to the (1 1 3), (2 2 2), (0 0 4), (0 4 4), (2 4 4), and (3 3 5) crystal plane of Ti_2C MXene as described in JCPDS file 98-007-7473, respectively. A few other peaks at 13.62°, 33.92°, 39.58°, and 53.26° are attributed to Ti_2AlC MAX phase, however, the intensity of the peaks are less significant as compared to the peaks of Ti_2C.

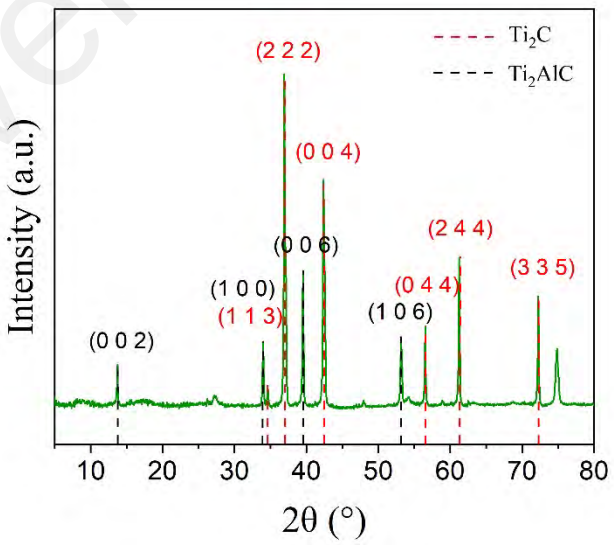

Figure 3.8: XRD pattern of Ti_2C MXene.

In Figure 3.9, the XRD pattern of Nb_2C was investigated in the 2θ range of 5° to 70°. A peak at 9.02° is spotted in the XRD spectrum remarks the (0 0 2) plane of the Nb_2C. The peak is caused by the widening of the interlayer spacing that arise from the interruption on the Nb-Al bonds. The other diffraction peaks emerge at 33.66°, 38.01°, and 59.98° are given to the (1 0 0), (1 0 1), and (1 1 0) planes of the hexagonal Nb_2C MXene as specified in the JCPDS file 00-015-0127. The traces of Nb_2AlC MAX phase are also spotted at 25.08° and 45.62° of the (0 0 4) and (1 0 4) planes as stated in JCPDS file 00-030-0033. Nonetheless, the MAX phase's signals are not significant as compared to the MXene's signals, indicating the dominant of Nb_2C.

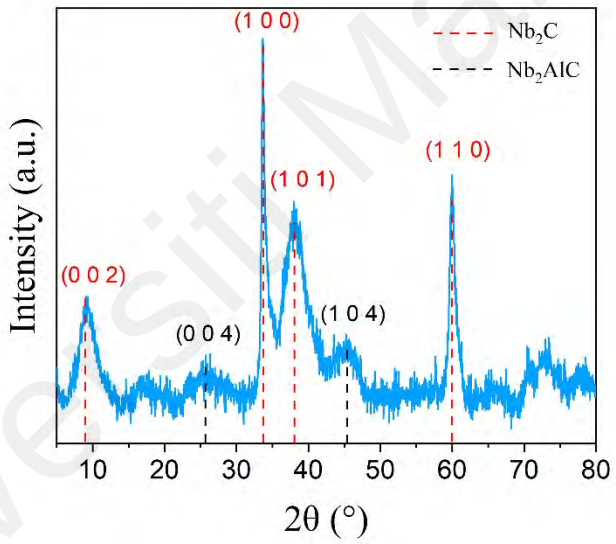

Figure 3.9: XRD pattern of Nb_2C MXene.

The XRD pattern of V_2C was analysed in Figure 3.10 in the 2θ range of 5° to 70°. The diffraction peak at 7.48° is significantly high, which is assigned to the (0 0 2) plane of V_2C. This value is on par with the high purity V_2C reported by M. Wu et al. (M. Wu et al., 2018), whereby the fabrication method is referred to in this work. The other diffraction peaks at 14.79°, 25.73°, 35.41°, 42.06°, and 63.36° are assigned to the (0 0 4), (0 0 6), (1 0 0), (1 0 3), and (1 1 0) crystal planes of V_2C MXene as specified in JCPDS file

01-073-1320, respectively. However, although the remains of V_2AlC MAX phase are revealed by the trivial peaks at 29.96°, 38.45°, and 46.25° as stated in JCPDS file 00-029-0101, the final product of V_2C is still dominant.

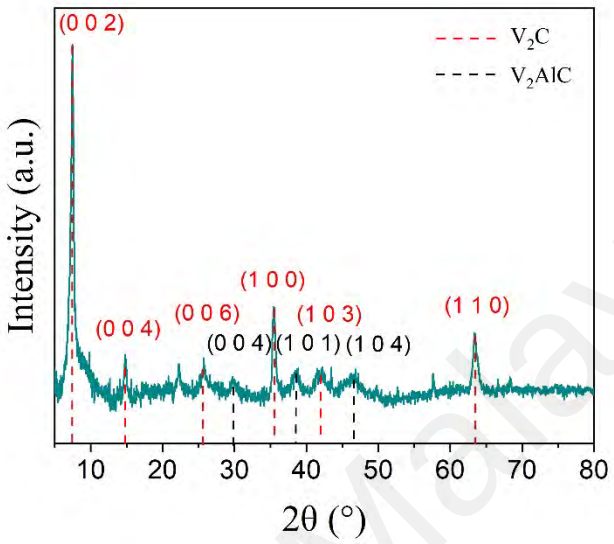

Figure 3.10: XRD pattern of V_2C MXene.

3.3.1.3 Raman Spectroscopy of Molten Fluoride Salt-Assisted MXenes

Raman spectroscopy is a non-destructive chemical analysis approach that brings forth particular information about chemical structure, crystallinity, phase and polymorphy, and molecular interactions. The basis of this analysis is on the interaction of light with the chemical bonds within a material, where an incident light from a high intensity laser light source is scattered by a molecule. Most of the incident light undergone Rayleigh scattering, which gives the same wavelength as the laser source, hence, does not give useful information. Nonetheless, a small-scale amount of light approximately in the order of 10^{-7} percent is scattered at different wavelengths through Raman scattering. The scattered wavelength depends on the chemical structure of the analyte.

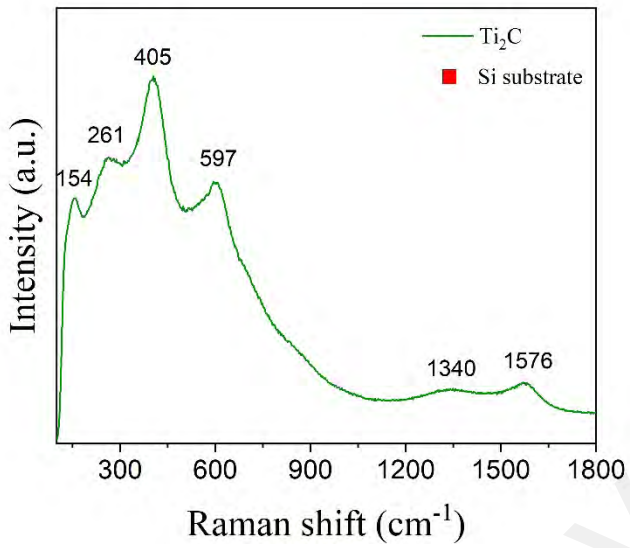

Figure 3.11: Raman spectroscopy of Ti_2C MXene.

Figure 3.11 displays the Raman spectrum of Ti_2C MXene after the etching process from Ti_2AlC MAX phase. The Raman spectrum of Ti_2C demonstrates spectral shifting and peak broadening from the original precursor's peaks. This should indicate the elimination of Al layers as the spectral shifting is because of the intercalation of surface groups and the peaks broadening is because of decrease in order as is expected of the etching process (Lai et al., 2015; F. Liu et al., 2016). In addition, the D and G bands of amorphous carbon peaks are also observed at 1340 cm^{-1} and 1576 cm^{-1}. In general, disordered graphite owing to the defects in carbon-based materials corresponds to the D band, whilst the vibration of sp^2 hybridized carbon atoms in a 2D hexagonal lattice corresponds to the G band (Wen et al., 2019). Hence, the appearance of free carbon and the disorders that has taken place in Ti_2C are implied by both of the peaks.

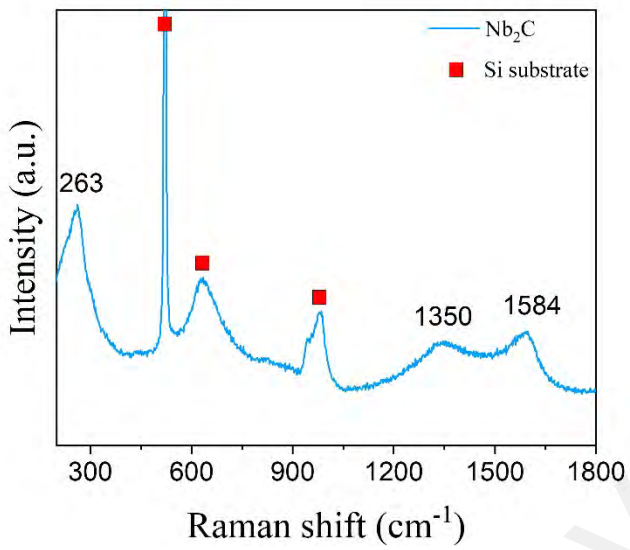

Figure 3.12: Raman spectroscopy of Nb_2C MXene.

The Raman spectrum of Nb_2C is displayed in Figure 3.12 A peak can be observed at 263 cm^{-1} which represents the A_{1g} mode that appears due to the symmetry out-of-plane vibrations of Nb and C atoms and the closed layer spacing, however, it is expected to be downshifted if the layer spacing is increased. Besides, D and G bands of carbon species are present in the spectrum by confirming the two peaks located at 1350 cm^{-1} and 1584 cm^{-1}. The degree of sp^2 carbon atom is associated with the G band, whilst the carbon disordered structure is associated with the D band, which the presence of both bands are the outcome of the carbon atom from Nb_2C.

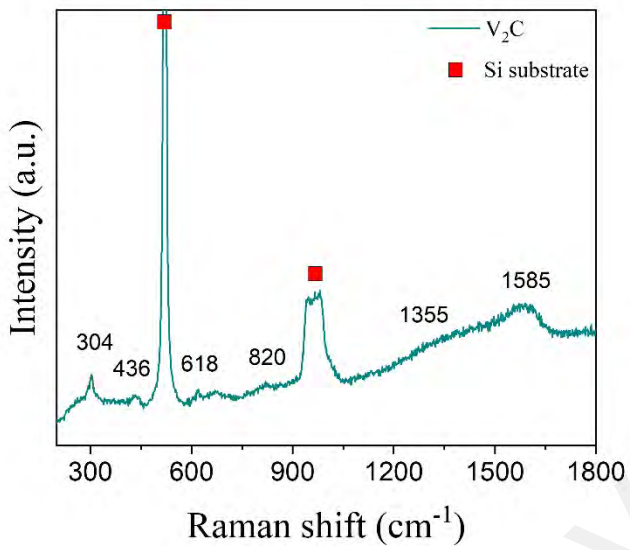

Figure 3.13: Raman spectroscopy of V_2C MXene.

The Raman spectrum of V_2C MXene in Figure 3.13 transforms into broader peaks as compared to the precursor V_2AlC MAX phase peaks due to the wide interlayer spacing as suggested by Champagne and others (Champagne et al., 2018). The E_{2g} mode at 158 cm^{-1} and 239 cm^{-1} that describes the in-plane vibration of V and Al atoms are absence from the spectrum. On the contrary, the V_2C indicates Raman peaks at 304 cm^{-1}, 436 cm^{-1}, and 618 cm^{-1} which are adjacent to those vibrations calculated elsewhere. The Raman peak at 304 cm^{-1} is assigned to A_{1g} mode that represents the out-of-plane vibrations of V atoms in V_2C system, whilst the Raman peak at 436 cm^{-1} is assigned to E_g mode that represents the in-plane vibrations of V atoms in $V_2C(OH)_2$ species (Champagne et al., 2018; M. Wu et al., 2018). The occupancy of mixed heterogenous terminal functionalities (O, F, OH) are attributed to the 618 cm^{-1} peak. In addition, a trivial peak can be observed at 820 cm^{-1} due to the terminal functionalities (F, OH) that usually emerge below 750 cm^{-1} for V_2C without F or OH terminations (Champagne et al., 2018). The other reports have also showed the same shift (Yorulmaz et al., 2016).

3.3.2 Optical Properties of Molten Fluoride Salt-Assisted MXenes

The optical properties characterization in this sub-topic comprise of linear and nonlinear optical absorption, where the nonlinear optical absorption covers both saturable absorption and Z-scan analysis.

3.3.2.1 Experimental Configuration of Linear Optical Absorption

The 2 µm ASE source was used to measure the linear absorption, α_0 of MXenes. Laser diode (LD) at 1556 nm was used to pump thulium-doped fiber to get the ASE at 2 µm region through 1550/2000 nm wavelength division multiplexer (WDM). An isolator was placed after the LD to protect the LD from any backscattered signal light. The ASE were introduced directly to the MXenes and monitored the optical spectrum from the opposite side as displayed in Figure 3.14. The low power of ASE sources enabled the linear absorption measurement to be taken before the beginning of nonlinear absorption in MXenes samples. Both measurement on thin film and tapered fiber-based MXenes were measured. The same procedures were applied to measure the linear absorption at S-band region, where a 1400 nm LD and 1400/1480 nm WDM were used to pump thulium-doped fluoride fiber.

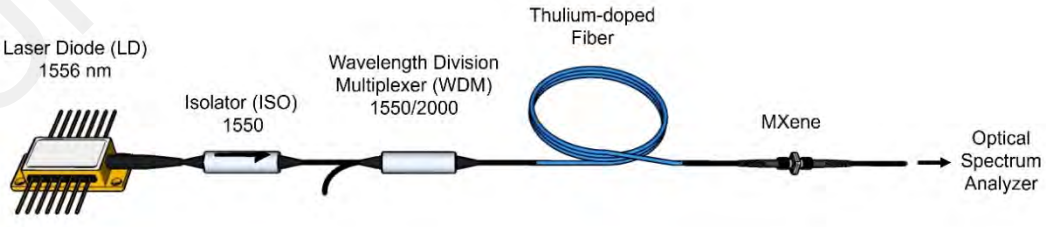

Figure 3.14: Amplified spontaneous emission (ASE) configuration for linear absorption measurement.

3.3.2.2 Linear Absorption of Molten Fluoride Salt-Assisted MXenes

Linear absorption is usually defined in low power, which the absorption coefficient is independent of the optical intensity. It can be calculated by the following equation

$$a_0 = P_{ASE} - P_{material} \tag{3.2}$$

where P_{ASE} is the output power of ASE and $P_{material}$ is the output power of the ASE injected through material.

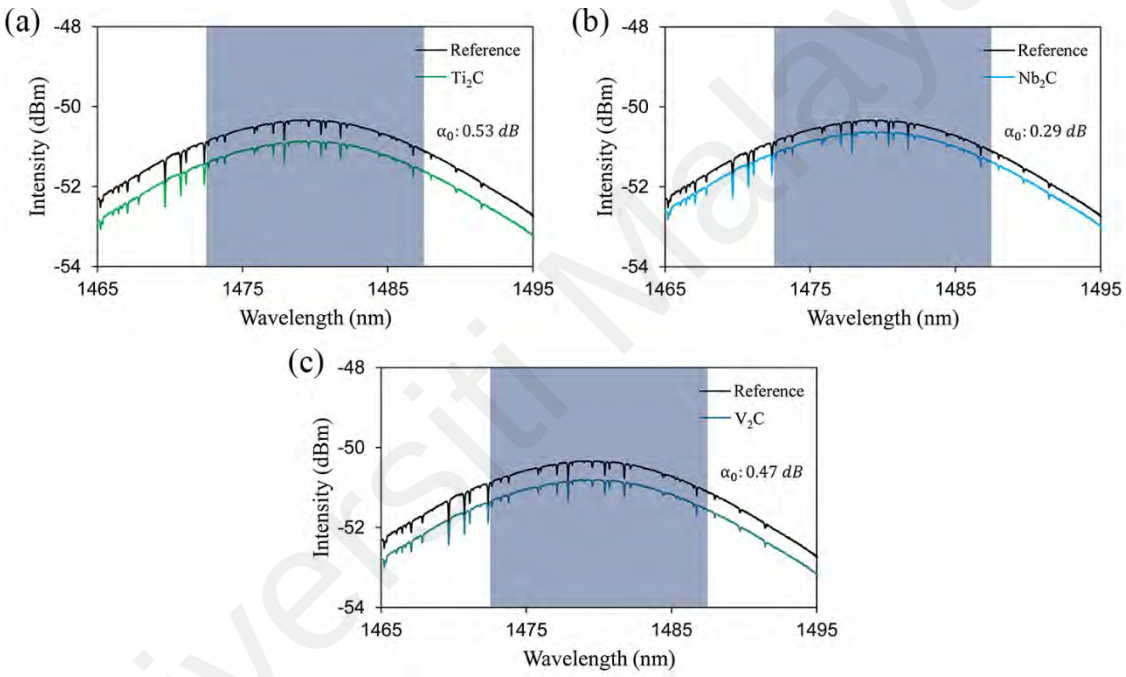

Figure 3.15: Optical linear absorption of (a) Ti_2C, (b) Nb_2C, and (c) V_2C molten fluoride salt-assisted MXenes at S-band region.

The linear absorption of all the fabricated MXenes in the wavelength range of 1470 nm to 1490 nm can be observed in Figure 3.15. From the figure, Nb_2C and V_2C exhibit linear absorption of 0.29 dB and 0.47 dB, respectively. On the other hand, Ti_2C demonstrates a linear absorption of 0.53 dB, which has absorption relatively higher than the other two MXenes. This may be due to the impure fabricated Ti_2C as can be noticed in the physical qualities.

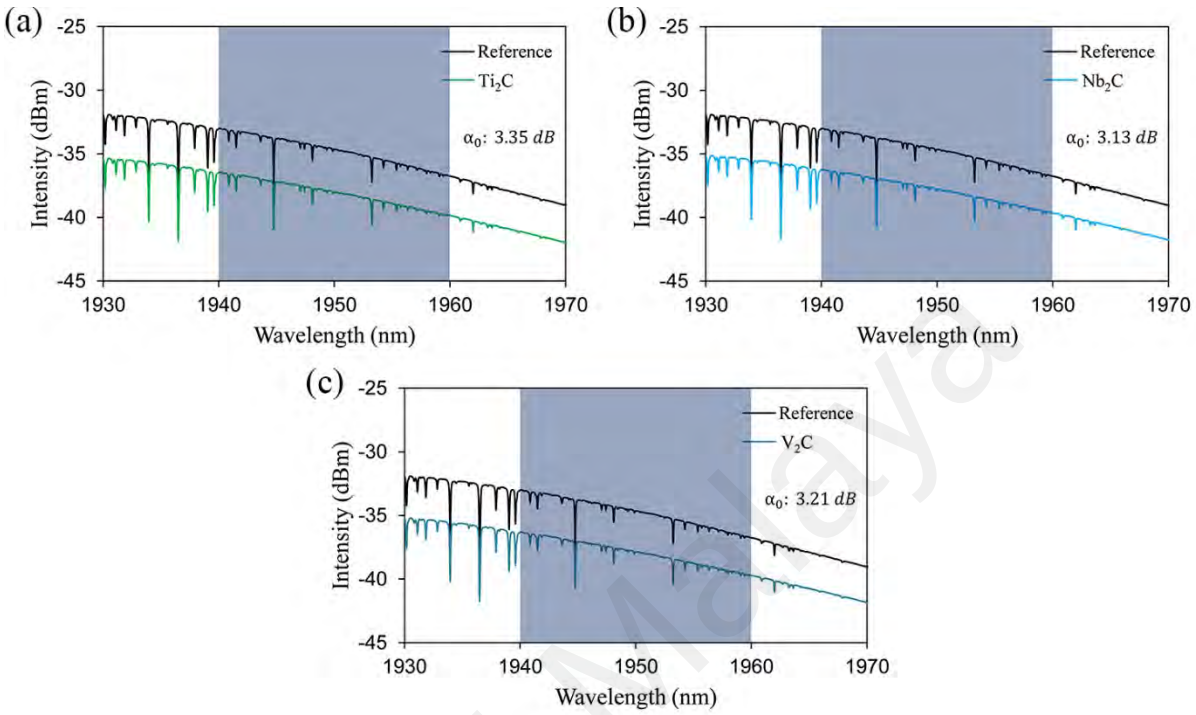

Figure 3.16: Optical linear absorption of (a) Ti_2C, (b) Nb_2C, and (c) V_2C molten fluoride salt-assisted MXenes at 2 µm region.

The linear absorption of all the fabricated MXenes in the wavelength range of 1940 nm to 1960 nm can be observed in Figure 3.16. From the figure, Nb_2C and V_2C exhibit linear absorption of 3.13 dB and 3.21 dB, respectively. On the other hand, Ti_2C demonstrates a linear absorption of 3.35 dB, which has absorption relatively higher than the other two MXenes. This may be due to the impure fabricated Ti_2C as can be noticed in the physical qualities. Figure 3.16 represents both of the thin film and tapered fiber hosts of MXenes since both exhibit approximately the same loss.

3.3.2.3 Experimental Configuration of Saturable Absorption

To evaluate the saturable absorption of MXenes, balanced twin-detector configuration was setup by using a pulse source as in Figure 3.17. A femtosecond laser from Toptica

(FemtoFErb 1950) with a repetition rate of 30 MHz and a pulse width of 100 fs at 1950 nm was used. The high output power due to the high peak power of the pulse initiated the nonlinear properties in the MXenes. Variable attenuator was used to modify the output power injected into the MXenes thin film through one arm of 1x2 50:50 optical coupler, while another arm was used as reference power. Both arms were coupled to power meter to measure the output power. To measure the saturable absorption of the MXenes at S-band region, a commercial mode-locked laser from Menlo Systems with a repetition rate of 100 MHz and a pulse width of 2.88 ps at 1564 nm was used as it is the closest commercialized laser available to the S-band region.

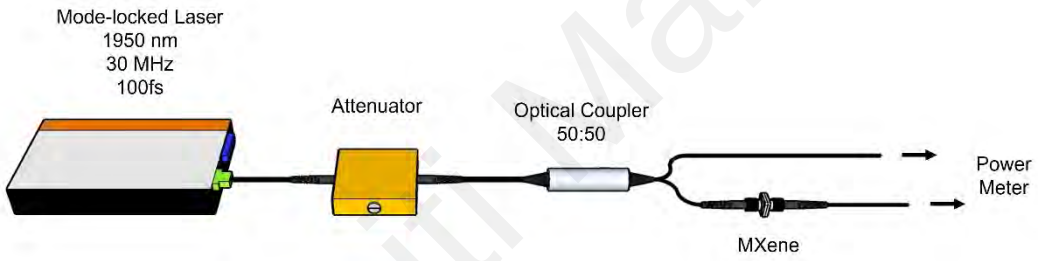

Figure 3.17: Balanced twin-detector configuration with mode-locked laser source for saturable absorption measurement.

3.3.2.4 Saturable Absorption of Molten Fluoride Salt-Assisted MXenes

Saturable absorption is a type of nonlinear absorption, which can be discovered at high optical intensities. The saturable absorption of the material can be fitted based on the expression in chapter 2

$$\alpha = \frac{\alpha_0}{1 + I/I_s} \tag{2.10}$$

where α_0 is linear absorption that can be taken from previous calculation, I is the intensity of light beam, and I_s is the saturation intensity.

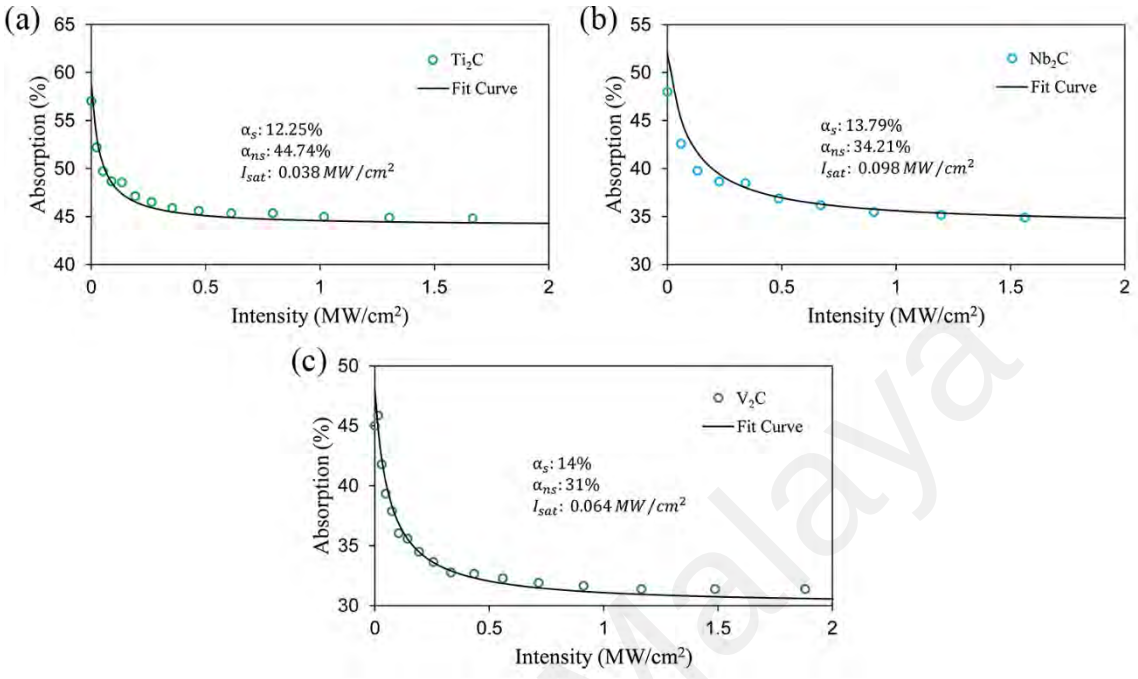

Figure 3.18: Optical saturable absorption of (a) Ti_2C, (b) Nb_2C, and (c) V_2C MXenes thin film at S-band.

The saturable absorption of MXenes at S-band is presented in Figure 3.18. Ti_2C has saturable and non-saturable absorption of 12.25 % and 44.74 %, with I_s of 0.038 MW/cm^2. Whereas, Nb_2C has saturable and non-saturable absorption of 13.79 % and 34.21 %, with I_s of 0.098 MW/cm^2 and V_2C has saturable and non-saturable absorption of 14 % and 31 %, with I_s of 0.064 MW/cm^2.

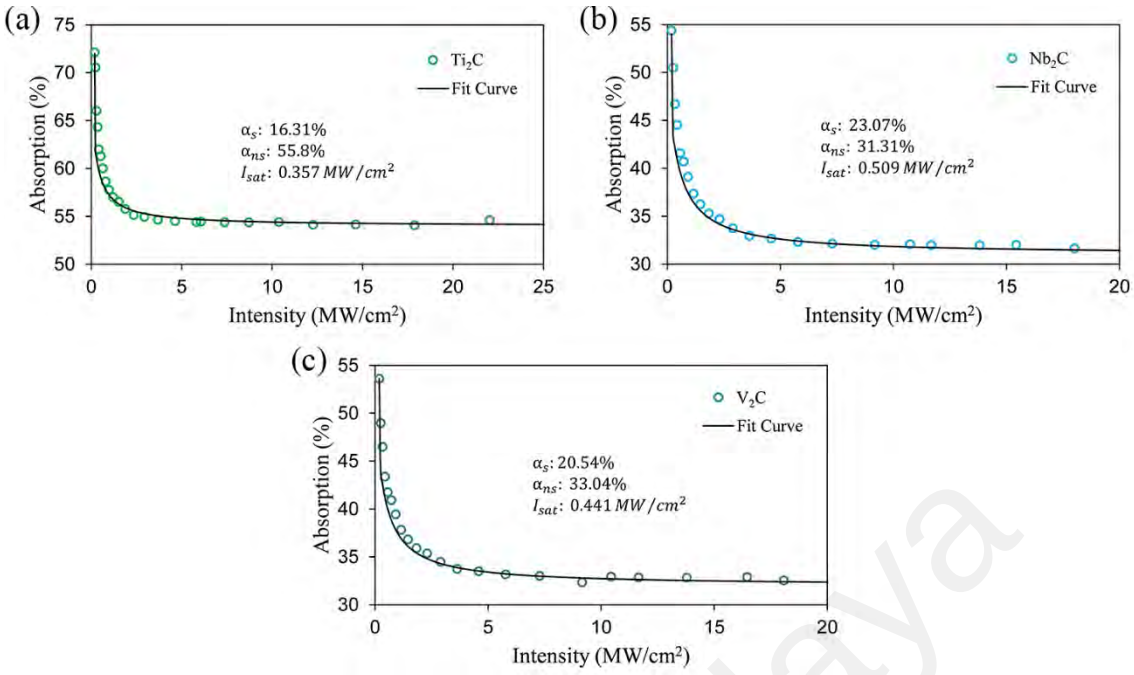

Figure 3.19: Optical saturable absorption of (a) Ti_2C, (b) Nb_2C, and (c) V_2C MXenes thin film at 2 µm.

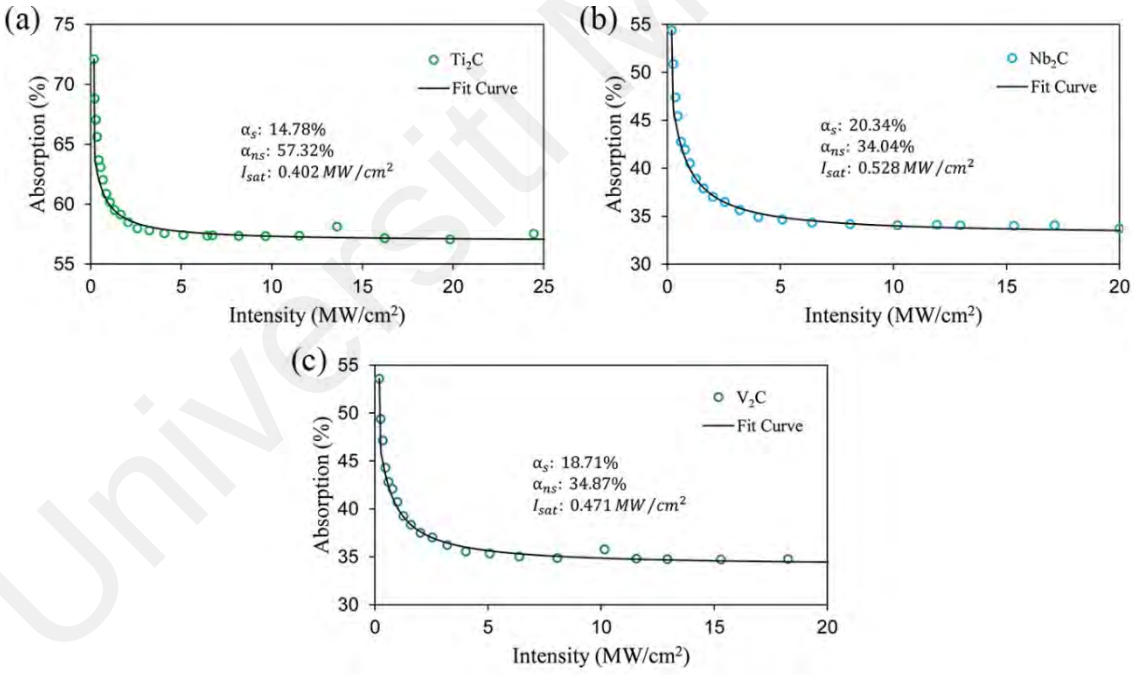

Figure 3.20: Optical saturable absorption of (a) Ti_2C, (b) Nb_2C, and (c) V_2C MXenes tapered fiber at 2 µm.

Additionally, the saturable absorption of MXenes at 2 µm are also presented in Figure 3.19 and Figure 3.20. In thin film host, Ti_2C has saturable and non-saturable absorption of 16.31 % and 55.8 %, with I_s of 0.357 MW/cm^2. Whereas, Nb_2C has

saturable and non-saturable absorption of 23.07 % and 31.31 %, with I_s of 0.509 MW/cm^2 and V_2C has saturable and non-saturable absorption of 20.54 % and 33.04 %, with I_s of 0.441 MW/cm^2. Whereby in tapered fiber host, generally the saturable absorption are reduced, while the non-saturable absorption and saturation intensity are increased slightly. Ti_2C has saturable and non-saturable absorption of 14.78 % and 57.32 %, with I_s of 0.402 MW/cm^2. Whereas, Nb_2C has saturable and non-saturable absorption of 20.34 % and 34.04 %, with I_s of 0.528 MW/cm^2 and V_2C has saturable and non-saturable absorption of 18.71 % and 34.87 %, with I_s of 0.471 MW/cm^2

3.3.2.5 Experimental Configuration of Z-scan

A 1557 nm femtosecond laser with a repetition rate of 953 kHz and average power of 29.7 mW was used in Z-scan analysis as shown in Figure 3.21. A 1x2 99:1 optical coupler was used in the setup, where 99% port was directed into air through GRIN lens, while the other 1% was observed in oscilloscope. The MXene samples were mounted on a translation stage (linear stage) to change the position during the measurement. There were two operational modes conducted during the analysis, those are open-aperture (OA) and close-aperture (CA). In OA Z-scan analysis, power meter 1 was used to measure the total transmitted power. Along the Z direction, the light converged and diverged, placing the focal point within the path. The MXenes experienced different light intensities since it was translated along the Z direction, where any changes in the total transmitted power is associated with multi-photon absorption.

In CA Z-scan analysis, power meter 2 was used to measure the fraction of transmitted power. The sample experienced nonlinear phase shift since it was translated along the Z direction, where the Kerr lens produced in the material will change light detected by the power meter (photodiode). A peak-valley trend was portrayed in the measurement, and the normalized transmittance between peak and valley is associated with the nonlinear

phase shift, Δϕ_0. The illustration of the experimental setup for Z-scan analysis is depicted in Figure 3.21.

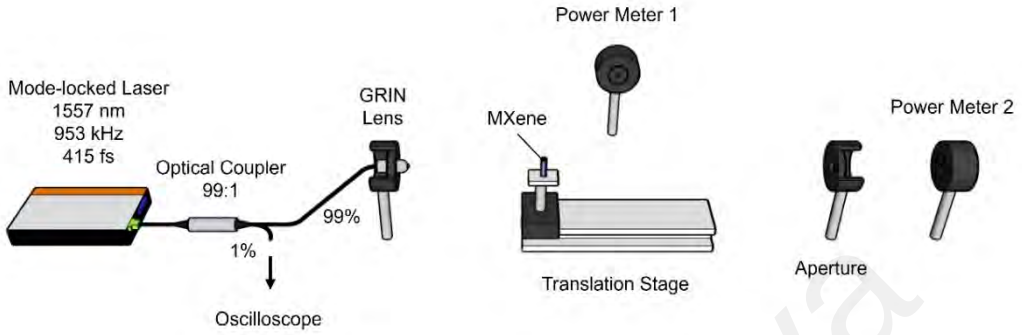

Figure 3.21: Z-scan configuration to measure the nonlinear absorption coefficient, β and nonlinear refractive index, n_2 of MXene.

3.3.2.6 Z-scan Analysis of Molten Fluoride Salt-Assisted MXenes

In OA, the normalized change in transmitted power can be estimated as the following if the effect was restricted to two-photon absorption (TPA)

$$\Delta T(Z) \approx \frac{q_0}{2\sqrt{2}} \frac{1}{\left[1 + \frac{Z^2}{{Z_0}^2}\right]} \tag{3.3}$$

where $q_0 = \beta I_0 L_{eff}$, β is the TPA coefficient or nonlinear absorption coefficient, I_0 is the peak intensity at the focus, and $L_{eff} = (1 - e^{-\alpha L})$, with L and α are the sample length and linear absorption coefficient, respectively. The position of the sample relative to the focal point is represented by Z, and Z_0 is the Rayleigh range which is expressed by $Z_0 = \pi\omega_0/\lambda$ with ω_0 represents the beam waist radius and λ represents the wavelength of the laser.

In CA, the normalized transmittance between peak and valley ΔT_{pv} is associated by the following expression

$$|\Delta\phi_0| = \frac{\Delta T_{pv}}{0.406(1-S)^{0.27}} \tag{3.4}$$

where $\Delta\phi_0 = \left(\frac{2\pi}{\lambda}\right)\left(n_2 I_0(t)\right)\left(L_{eff}\right)$, I_0 represents the peak intensity at focus, S represents the transmittance at aperture, and n_2 is the nonlinear refractive index of the sample. The normalized transmittance of the CA Z-scan measurement can be fitted by using the following expression

$$T(z, \Delta\phi_0) \cong 1 - \frac{4\Delta\phi_0 z}{(z^2+9)(z^2+1)} \tag{3.5}$$

From Figure 3.22, the nonlinear absorption coefficient, β for Ti_2C. Nb_2C, and V_2C are $3.48 \times 10^{-10}\, m/W$, $4.82 \times 10^{-10}\, m/W$, and $5.11 \times 10^{-10}\, m/W$, respectively, where V_2C has the highest β as portrayed by the highest normalized transmittance peak in the figure compared to the other MXenes.

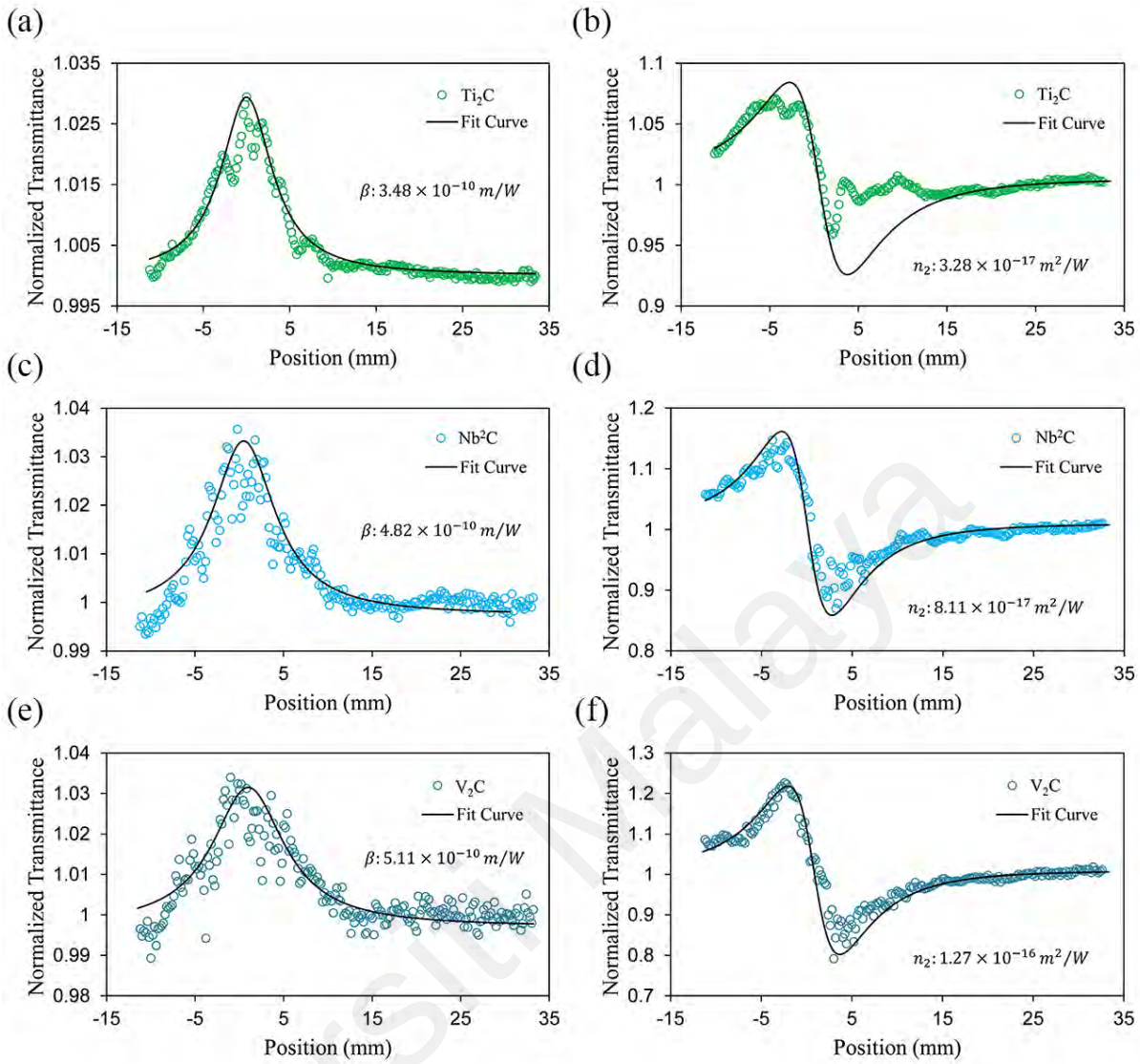

Figure 3.22: Normalized transmittance spectrum by (a) open-aperture (OA), and (b) closed-aperture (CA) of Ti_2C, (c) OA, and (d) CA of Nb_2C, and (e) OA, and (f) CA of V_2C MXenes Z-scan measurement at 11 mW ($I_0 = 0.9\ GW/cm^2$).

Additionally, V_2C also possesses the highest nonlinear refractive index, n_2 of $1.27 \times 10^{-16}\ m^2/W$, which propose has relatively largest nonlinear phase shift $\Delta\phi_0$. Ti_2C and Nb_2C have n_2 of $3.28 \times 10^{-17}\ m^2/W$, and $8.11 \times 10^{-17}\ m^2/W$.

3.4 Summary and Discussion of Fabrication and Characterization of Molten Fluoride Salt-Assisted MXenes

On the whole, fabrication method by using lithium fluoride (LiF) and hydrochloric acid (HCl) to replace hydrofluoric acid (HF) was used to etch MAX phases into MXenes. The parameters of the processes followed the previous works that have been done by Guan et al. and Li et al. with the same chemical ratio (Guan et al., 2020; L. Li et al., 2017). Since the parameters of the fabrication is controlled and have supporting data from the previous works, the MXenes in this work is highly reproducible. On that note, the MXenes used in this work is not a first time-fabricated material. The synthesized samples were characterized mainly in two parts, physical structure, and optical response of the materials. Among the scientific tools used for physical characterization are FESEM, and HRTEM, while for optical response are Raman spectroscopy, linear absorption, saturable absorption, and Z-scan analysis.

Table 3.2: Overall physical and optical characterization of molten fluoride salt-assisted MXenes.

Properties \ **MXenes**		**Ti_2C**	**Nb_2C**	**V_2C**
Physical				
FESEM	**Sheet size (μm)**	0.08	1	5
HRTEM	**Crystalline lattice size (nm)**	1.2	1.8	1.8
Optical				
Linear Absorption	**S-band linear absorption coefficient, α_0 (dB)**	0.53	0.29	0.47

Table 3.2, continued.

Properties \ MXenes		Ti_2C	Nb_2C	V_2C
Linear Absorption	**2 µm linear absorption coefficient, α_0 (dB)**	3.35	3.13	3.21
Saturable Absorption	**S-band Thin Film**			
	Saturable absorption, α_s (%)	12.25	13.79	14
	Non-saturable absorption, α_{ns} (%)	44.74	34.21	31
	Saturation intensity, I_{sat} (MW/cm^2)	0.038	0.098	0.064
	2 µm Thin film			
	Saturable absorption, α_s (%)	16.31	23.07	20.54
	Non-saturable absorption, α_{ns} (%)	55.8	31.31	33.04
	Saturation intensity, I_{sat} (MW/cm^2)	0.357	0.509	0.441
	2 µm Tapered fiber			
	Saturable absorption, α_s (%)	14.78	20.34	18.71
	Non-saturable absorption, α_{ns} (%)	57.32	34.04	34.87

Table 3.2, continued.

Properties \ MXenes		Ti_2C	Nb_2C	V_2C
Saturable Absorption	**Saturation intensity, I_{sat} (MW/cm^2)**	0.402	0.528	0.471
Z-Scan	**Nonlinear absorption coefficient, β (m/W)**	3.48×10^{-10}	4.82×10^{-10}	5.11×10^{-10}
	Nonlinear refractive index, n_2 (m^2/W)	3.28×10^{-17}	8.11×10^{-17}	1.27×10^{-16}

From the findings summarized in Table 3.2, the MXenes generally have crystalline lattice spacing of about 1.2 nm to 1.8 nm, with lateral sheet size of about 0.08 µm for Ti_2C, 1 µm for Nb_2C, and 5 µm for V_2C. The XRD pattern and Raman spectroscopy showed partial existence of MAX phase precursors in all of the samples but didn't dominate the MXene. Among the three samples, Ti_2C showed the most impure MXene that was surrounded by TiO_2 and excess Al layers probably due to exothermic reaction and ineffective etching agent. The linear absorption of the three MXenes showed around 3 dB and at the same time, the saturable absorption of the three MXenes also displayed performance of around 14 % to 23 % at 2 µm, whereby between 12 % to 14 % at S-band. Besides, all three of them have nonlinear absorption coefficients, and nonlinear refractive index on the order of 10 magnitude, and 16 to 17 magnitude, respectively. The linear and saturable absorption of the MXenes showed a favourable merit for pulsed laser and optical modulator, while the Z-scan analysis revealed good β and n_2 values for four-wave mixing effect.

CHAPTER 4: PASSIVE Q-SWITCHED AND MODE-LOCKED MOLTEN FLUORIDE SALT-ASSISTED MXENES FIBER LASER

4.1 Introduction

Pulsed fiber lasers have grabbed considerable interest because of their functionality to fit into extensive range of scientific and industrial applications. Active pulsed fiber laser provides controllable laser performance involving repetition rate and pulse duration. However, the usage of external modulator in the system can be a significant limitation towards the development of robust and portable fiber laser system. In contrast, passive pulsed fiber laser possesses the benefits of compact size, flexible, and economical by utilizing nonlinear effect such as saturable absorption which commonly recognized in 2D materials. Such advantages in laser source are desired for many applications including biomedical research and spectroscopy.

All of the underlining theoretical details were discussed in depth previously in chapter 2. This chapter sets forth content related to Q-switched and mode-locked pulses by using the fabricated MXenes. Two different wavelength regions were occupied from two different host fibers of silica and fluoride (ZBLAN) with the same thulium dopant to generate Q-switched and mode-locked pulses. Q-switched pulse was operated in lower region S-band, while mode-locked pulse was operated in 2 μm region. These two wavelength regions were deliberately chosen to show the potential of MXenes in different wavelengths. Two incorporating methods of MXenes as saturable absorber (SA) into the fiber laser system were also employed tailored to each setup, comprising of thin film sandwiching between fiber ferrules and material depositing onto tapered fiber. Low loss MXenes thin film is suitable for Q-switched fiber laser since thulium-doped fluoride fiber damage threshold is low. On the other hand, tapered fiber is suitable for mode-locked fiber laser because the configuration was pumped at relatively high power, in which the

tapered fiber contains the ability to restrain the power without being damaged. The performance of MXenes SA in all setups were investigated by using an optical spectrum analyzer (OSA) AQ6375 (Yokogawa), oscilloscope (OSC) DSOX 3102T (Keysight), optical power meter (OPM) S148C (Thorlabs), autocorrelator PulseCheck (APE), and radio frequency spectrum analyzer (RFSA) FPC1000 (Rohde & Schwarz). Plus, an additional 10 GHz photodetector 818-BB-51F (Newport) was used as an optical to electrical signal converter. The finding of the experiments are addressed in separate sections according to the MXenes type.

4.2 Molten Fluoride Salt-Assisted MXenes as Saturable Absorber (SA)

4.2.1 Molten Fluoride Salt-Assisted MXenes Thin Film

A thin film is a layer of material, particularly polyvinyl alcohol (PVA) in this work, that has thickness in the range of micrometres and use to host 2D materials. The controlled synthesis of PVA thin film exhibits an essential step in various different applications subjected to the thickness, structure, and geometry of the produced film. It is commonly created by deposition, either physically or chemically, that produce both amorphous and crystalline materials. 2D materials that has been deposited into the thin film possess different electrical and mechanical properties from those of the bulk materials, which ascribed to the nanostructure of the materials.

To integrate the MXenes into the optical fiber laser system, a 10 mg/ml concentration of MXenes were developed into thin film. To produce a thin film, 50 mg of MXene was added into 5 ml of deionized water, then sonicated for 1 hour. In the meantime, 10 mg/ml of PVA was prepared by dissolving 100 mg of PVA powder into 10 ml of deionized water through heating and stirring for 30 minutes at 80 °C. After that, 3 ml of MXene was gently poured into 5 ml of the PVA solution while keep stirring at 80 °C for 30 minutes

to secure a homogeneous solution. Finally, the mixed solution was left to dry at 60 °C for 4 hours on a petri dish to form a thin film. Figure 4.1 shows one of the fabricated thin film MXene.

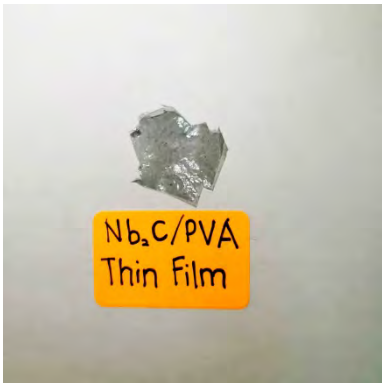

Figure 4.1: Molten fluoride salt-assisted MXene Nb_2C thin film.

4.2.2 Molten Fluoride Salt-Assisted MXenes Tapered Fiber

The flaming brush method was employed to fabricate tapered fiber as shown in Figure 4.2(a). A bare fiber of 15 cm was taken from the spool and the fiber was stripped in the middle about 4 cm before fixed onto a translational stage from Newport (FCL 100) by using fiber holders. After that, the exposed part of the fiber was softened by using oxy-LPG flames for 3 seconds statically and stretched by moving the stages outward in opposite direction while the flame still softening the fiber for 5 seconds. The waist of the fiber was reduced to about 6 µm and the tapered length was about 2.5 cm. The insertion loss of the tapered fiber was evaluated by using 2 µm light source and an optical power meter (OPM) upon completion, which usually has a value of approximately 2.5 dB.

The MXenes in isopropyl alcohol (IPA) solution was then deposited onto the tapered fiber and left to dry at room temperature. To prepare the solution, 20 mg of MXene powder was added into 2 ml of IPA, then sonicated for 1 hour to obtain a homogeneous solution. The typical microscopic image of the fabricated tapered fiber and 2D material

coated tapered fiber can be seen in Figure 4.2(b) and (c) as demonstrated by H. Ahmad et al. by using Ti_2AlC (H Ahmad, Azri, et al., 2021). Whereas in Figure 4.2(d), the graphical illustration of the coated tapered fiber is represented.

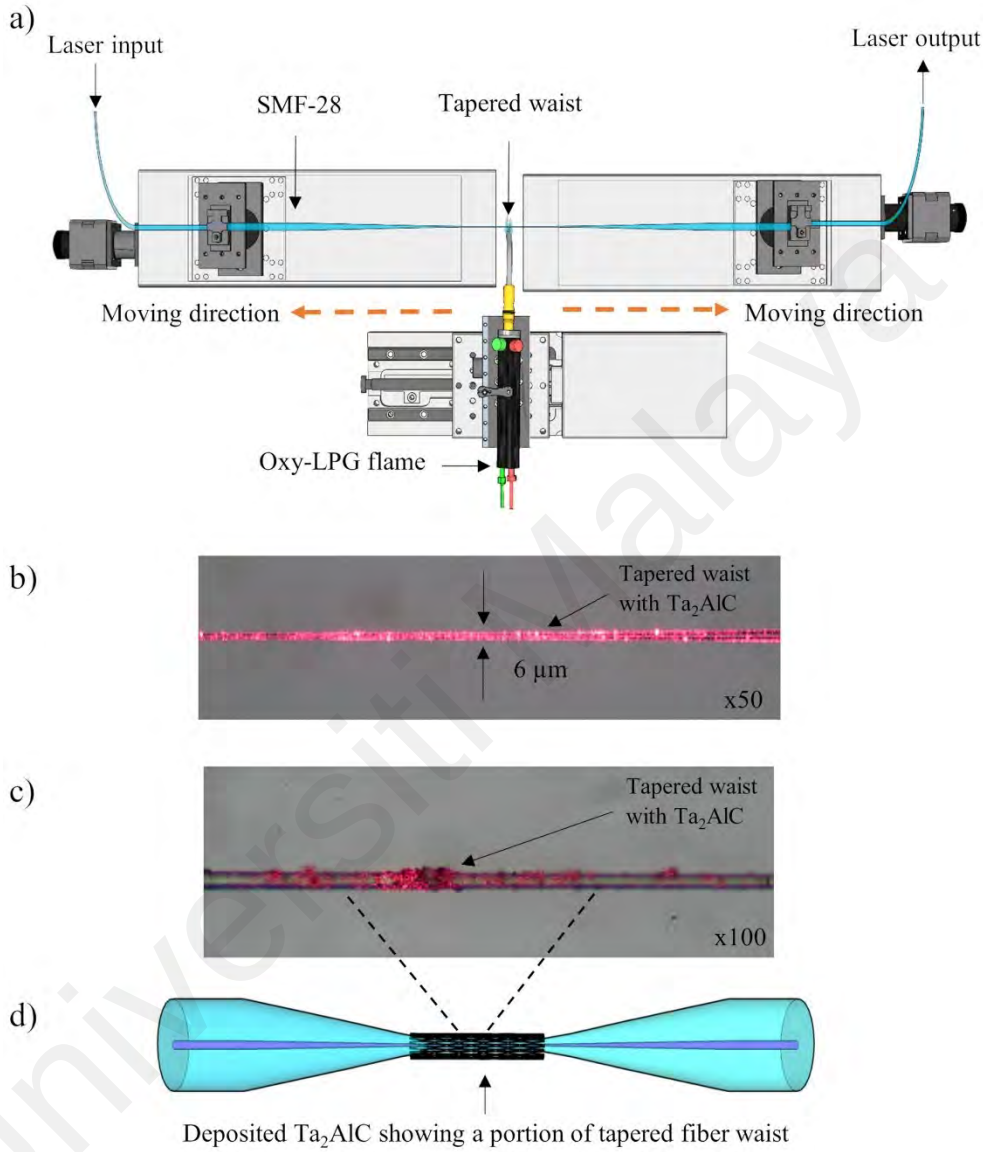

Figure 4.2: The configuration of flame brushing method to make tapered fber, (b) microscopic image of the tapered fiber at ×50 magnification, (c) microscopic image of the tapered fiber with 2D materials at ×100 magnification, and (d) schematic diagram of the coated tapered fiber with 2D material (Copyright permission from H. Ahmad et al., 2021).

4.2.3 Optical Characterization of Molten Fluoride Salt-Assisted MXenes

The optical characterization of MXenes after integrated into the host are presented in the table below, as taken from Table 3.2 in Chapter 3.

Table 3.2: Optical characterization of Molten Fluoride Salt-Assisted MXenes.

Properties \ MXenes		Ti_2C	Nb_2C	V_2C
Linear Absorption	S-band linear absorption coefficient, α_0 (dB)	0.53	0.29	0.47
	2 µm linear absorption coefficient, α_0 (dB)	3.35	3.13	3.21
Saturable Absorption	S-band Thin Film			
	Saturable absorption, α_s (%)	12.25	13.79	14
	Non-saturable absorption, α_{ns} (%)	44.74	34.21	31
	Saturation intensity, I_{sat} (MW/cm^2)	0.038	0.098	0.064
	2 µm Thin film			
	Saturable absorption, α_s (%)	16.31	23.07	20.54
	Non-saturable absorption, α_{ns} (%)	55.8	31.31	33.04
	Saturation intensity, I_{sat} (MW/cm^2)	0.357	0.509	0.441

Table 3.2, continued.

Properties \ MXenes		Ti_2C	Nb_2C	V_2C
Saturable Absorption	**2 µm Tapered fiber**			
	Saturable absorption, α_s (%)	14.78	20.34	18.71
	Non-saturable absorption, α_{ns} (%)	57.32	34.04	34.87
	Saturation intensity, I_{sat} (MW/cm^2)	0.402	0.528	0.471
Z-Scan	**Nonlinear absorption coefficient, β (m/W)**	3.48×10^{-10}	4.82×10^{-10}	5.11×10^{-10}
	Nonlinear refractive index, n_2 (m^2/W)	3.28×10^{-17}	8.11×10^{-17}	1.27×10^{-16}

4.3 Passive Q-switched Thulium-doped Fluoride Fiber Laser (TDFFL) by using Molten Fluoride Salt-Assisted MXenes

4.3.1 Experimental Configuration of Passive Q-switched TDFFL

The experimental configuration of passive Q-switched TDFFL integrating MXene film as SA is shown in Figure 4.3.

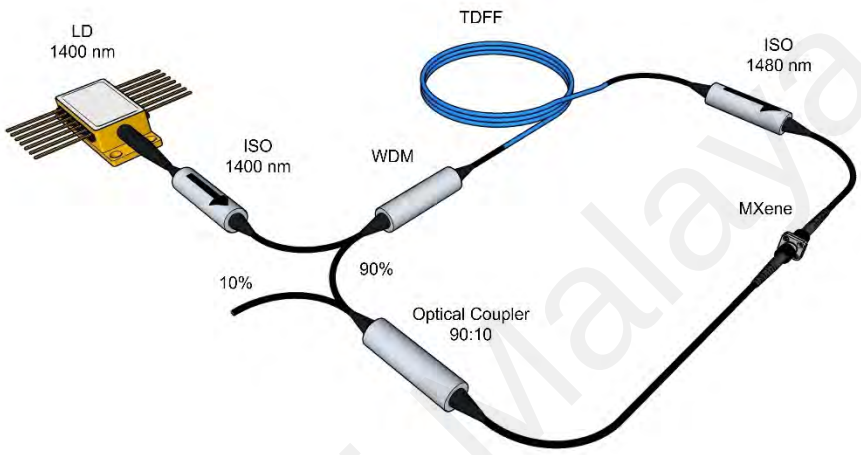

Figure 4.3: Schematic diagram of Q-switched MXene TDFFL.

The cavity also employed a ring configuration with an 11.6-meter-long thulium-doped fluoride fiber (TDFF) from Fiberlabs Inc. as the gain medium. The gain medium was pumped by using a 1400 nm laser diode (LD) that has a maximum power of 250 mW. The LD was fixed to the 1400 nm port of 1400/1480 nm WDM with a 500 mW threshold rating. Then, the common port of the WDM was connected to the TDFF that has a peak absorption of 15 dB/m at 1400 nm, a core diameter of 3.3 µm, and a numerical aperture of 0.28. The opposite side of the TDF was attached to a 1480 nm ISO to constrain the signal propagation in one direction that help to optimize the cavity output power. The MXene film of approximately 1 mm × 1 mm was placed between two fiber ferrules before incorporated into the system after the ISO and then connected to a 90:10 OC. To reduce the reflection between the surfaces of fiber ferrules and film as well as to fix the position

of the film, an index matching gel (FIS F10001V) was applied to the fiber ferrules. The 90% port was looped back into the cavity by connecting to the 1480 nm port of the WDM, while the 10% port was extracted to analyze the Q-switched pulses. To validate the effect of saturable absorption, the cavity was run initially with the absence of SA. The continuous wave (CW) of the TDFFL is displayed in Figure 4.4 that operated at 250 mW with a center wavelength of 1493.40 nm.

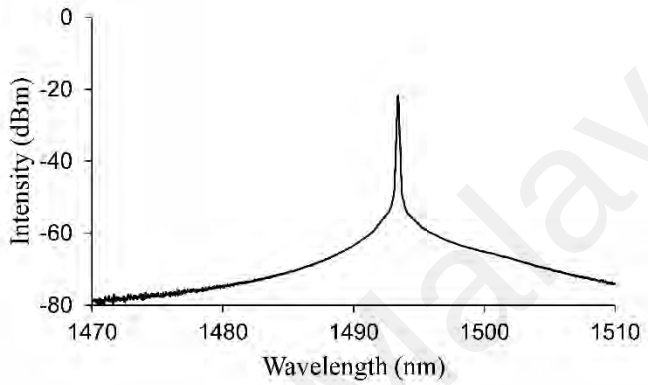

Figure 4.4: CW operation of TDFFL at 250 mW without MXenes.

4.3.2 Passive Q-switched Thulium-doped Fluoride Fiber Laser by using Ti_2C Thin Film

The TDFFL was first operated by gradually increasing the pump power until CW laser output was established at a pump power of 110 mW. The CW operation was then changed to a Q-switching operation when the pump power reached 151.10 mW. The cavity maintained in Q-switching operation until a maximum power of 237.90 mW. The Q-switched pulses degraded and the center wavelength in optical spectrum shifted towards lower wavelength when the pump power went beyond 237.90 mW. This state was due to the additional loss incurred by the damaged thin film and this condition was irreversible. The optical spectrum of the passive Q-switched TDFFL at the maximum pump power is displayed in Figure 4.5(a). The Q-switched had a center wavelength, λ_c of 1488.19 nm and a bandwidth or full-width at half maximum (FWHM), $\Delta\lambda$ of 2.88 nm.

Self-phase modulation (SPM) effect arose when a high-intensity signal light propagated in the fiber core, thus broadening the optical spectrum of the TDFFL.

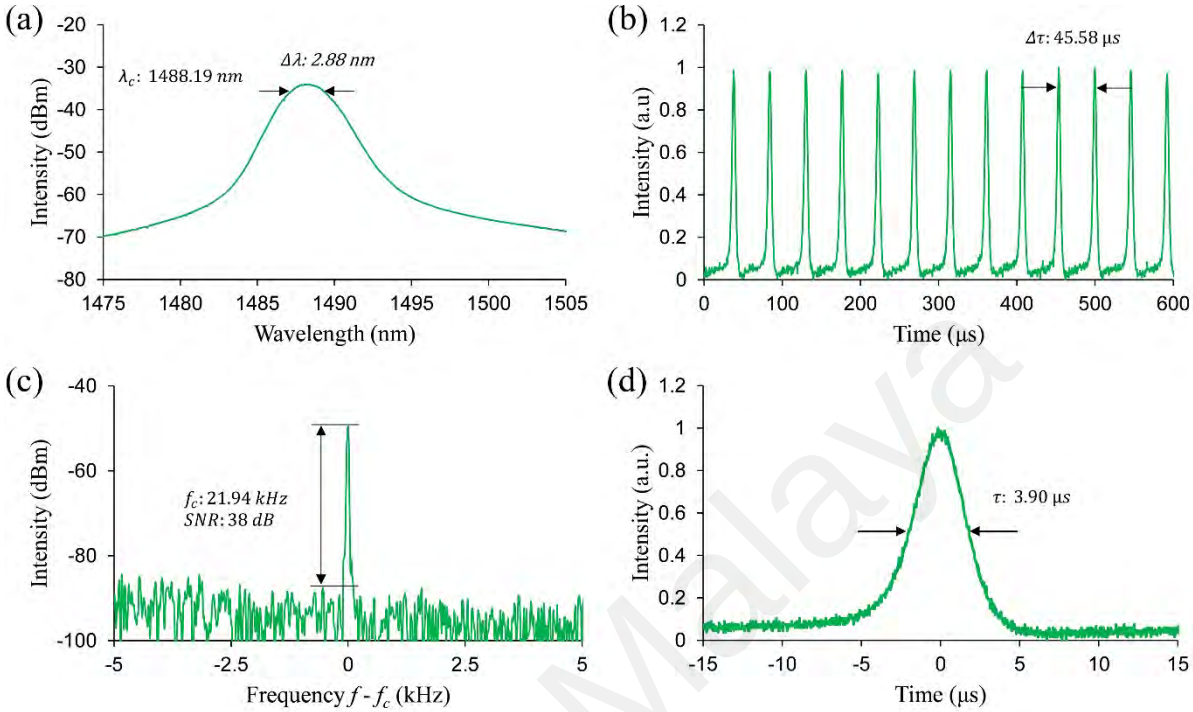

Figure 4.5: (a) Optical spectrum, (b) pulse train, (c) pulse repetition rate, and (d) Q switched single pulse of Ti_2C MXene at 237.90 mW.

Characteristics of the Q-switched pulse at maximum pump power are presented in Figure 4.5(b), (c), and (d). The Q-switched pulse train had a maximum pulse repetition rate, f_c of 21.94 kHz with unremarked intensity fluctuation in the pulse train in Figure 4.5(b). The stability can be clarified further in the frequency domain, where it had a signal-to-noise ratio (SNR) of 38 dB at pulse repetition rate of 21.94 kHz as in Figure 4.5(c). Additionally, single pulse profile of the Q-switched pulse was taken and is presented in Figure 4.5(d), where it had a pulse width, τ of 3.90 µs.

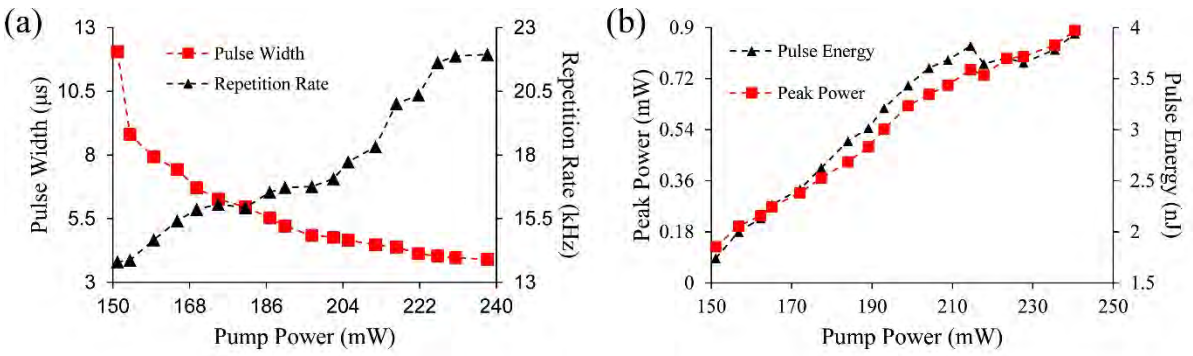

Figure 4.6: Evolution of (a) pulse width and pulse repetition rate, and (b) pulse energy and peak power during Ti_2C MXene Q-switched operation.

The pulse width was recorded to be 12.05 μs at a pump power of 151.10 mW, then narrowed to 3.90 μs at the pump power of 237.90 mW as shown in Figure 4.6(a). Pulse energy and peak power of the Q-switched pulses can be evaluated with the given pulse repetition rate with its corresponding average output power, and pulse width by considering the pulse shape. The maximum pulse energy and peak power of 3.78 nJ and 0.84 mW were recorded at the maximum pump power of 237.90 mW as shown in Figure 4.6(b).

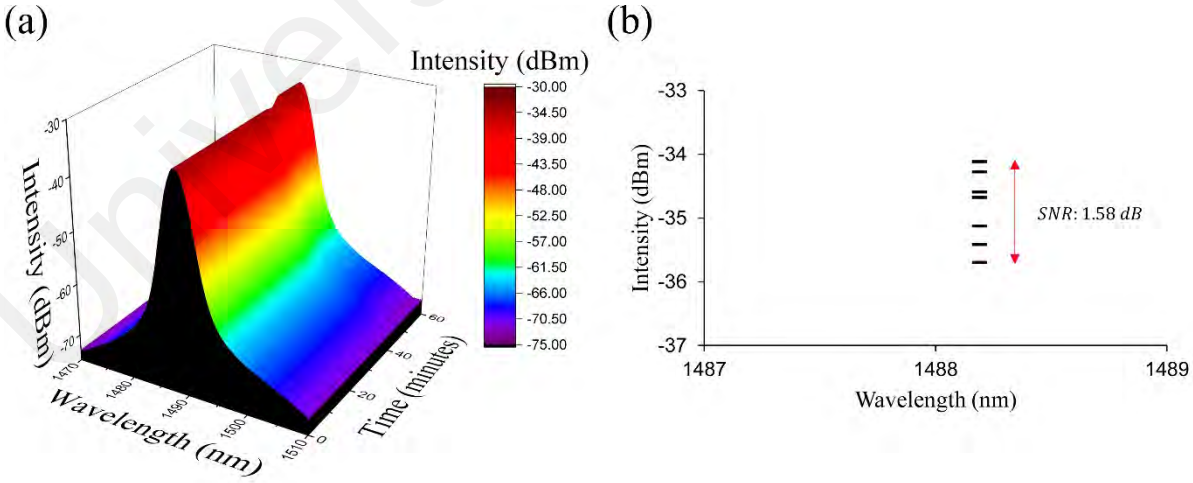

Figure 4.7: Ti_2C Mxene (a) Q-switched optical spectrum, and (b) SNR of center wavelength over 1 hour period.

The stability of Ti_2C SA Q-switched operation was further evaluated by monitoring the optical spectrum and SNR of center wavelength over 1 hour period at 237.90 mW as displayed in Figure 4.7. The Q-switched optical spectrum slightly shifted to the lower wavelength at minute 40 in Figure 4.7(a), which could be due to the Ti_2C SA experiencing damage. However, Figure 4.7(b) shows the center wavelength only fluctuated at a negligible range of 1.58 dB along the period.

4.3.3 Passive Q-switched Thulium-doped Fluoride Fiber Laser by using Nb_2C Thin Film

In the beginning, the TDFFL was first operated by slowly increasing the pump power until CW laser output was established at a pump power of 105 mW. The CW operation was then changed to a Q-switching operation when the pump power reached 151.10 mW. The cavity maintained in Q-switching operation until a maximum power of 249.70 mW. The operation was constrained by the LD maximum output limit, although the Nb_2C SA could endure a higher pump power. The optical spectrum of the passive Q-switched TDFFL at the maximum pump power is displayed in Figure 4.8(a). The Q-switched had a center wavelength of 1489.63 nm and a FWHM of 3.08 nm. SPM effect took place in the medium when a high-intensity signal light propagated in cavity, hence widening the optical spectrum of the TDFFL.

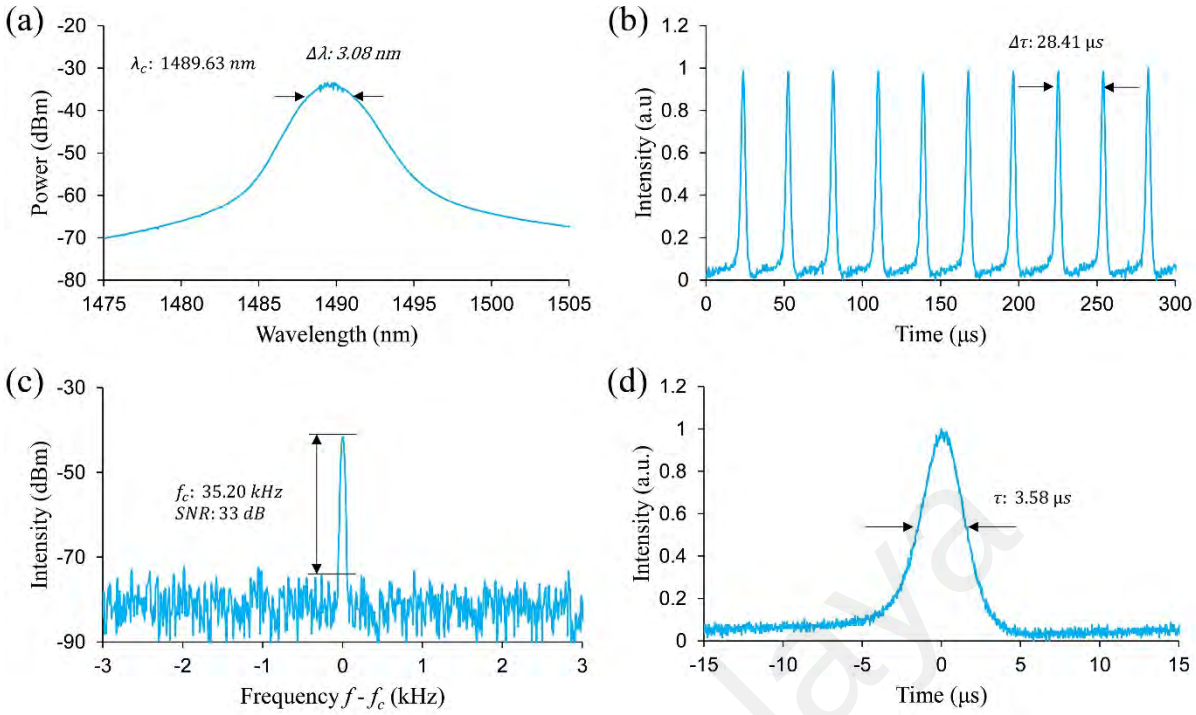

Figure 4.8: (a) Optical spectrum, (b) pulse train, (c) pulse repetition rate, and (d) Q-switched single pulse of Nb_2C MXene at 249.70 mW.

Characteristics of the Q-switched pulse at maximum pump power are presented in Figure 4.8(b), (c), and (d). The Q-switched pulse train had a maximum pulse repetition rate of 35.20 kHz with minor intensity fluctuation in the pulse train in Figure 4.8(b). The fundamental peak in the frequency domain was measured to further define the stability, where it had a SNR of 33 dB at pulse repetition rate of 35.20 kHz as in Figure 4.8(c). Additionally, single pulse profile of the Q-switched pulse was taken and is presented in Figure 4.8(d), where it had a pulse width of 3.58 µs.

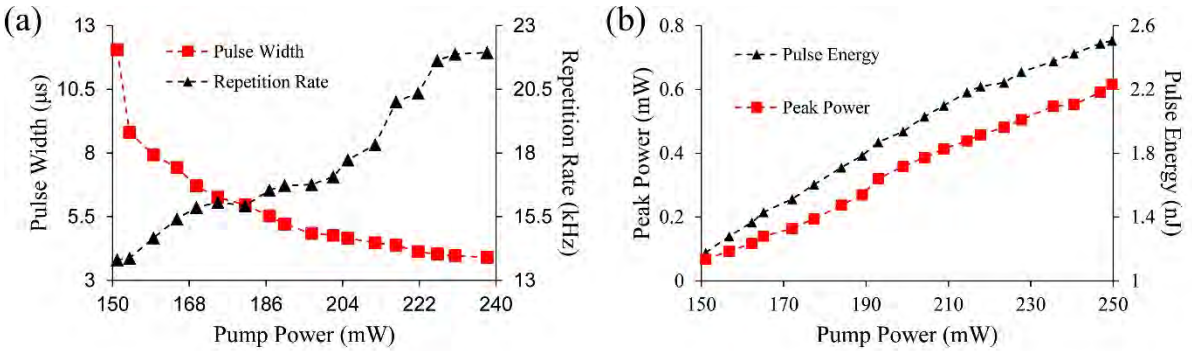

Figure 4.9: Evolution of (a) pulse width and pulse repetition rate, and (b) pulse energy and peak power during Nb_2C MXene Q-switched operation.

The pulse width was recorded to be 15.37 μs at a pump power of 151.10 mW, then compressed down to 3.58 μs at the pump power of 249.70 mW as shown in Figure 4.9(a). Pulse energy and peak power of the Q-switched pulses can be evaluated with the given pulse repetition rate with its respective average output power, and pulse width. The maximum pulse energy and peak power of 2.51 nJ and 0.62 mW were recorded at the maximum pump power of 249.70 mW as shown in Figure 4.9(b).

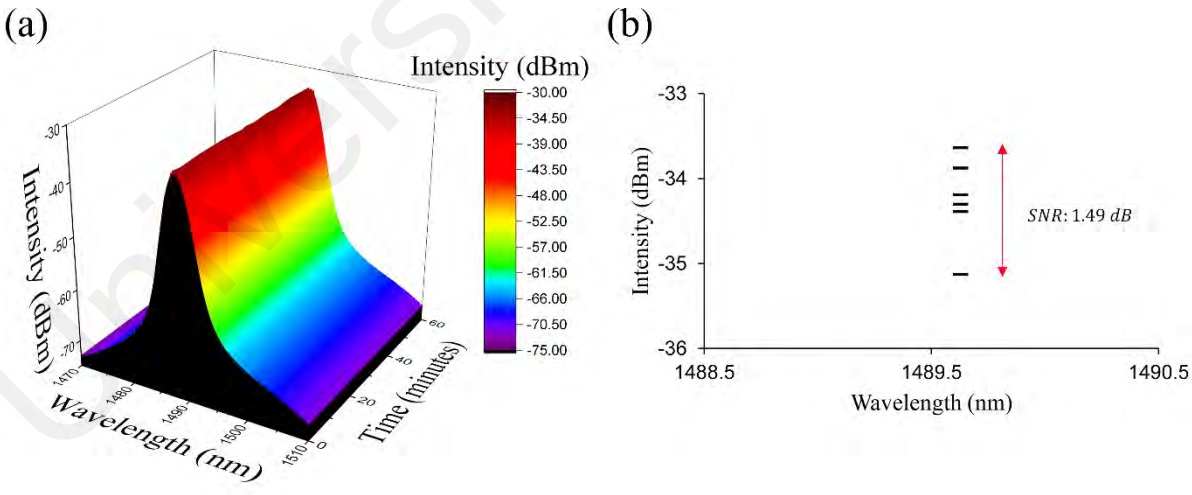

Figure 4.10: Nb_2C MXene (a) Q-switched optical spectrum, and (b) SNR of center wavelength over 1 hour period.

The stability of Nb_2C MXene Q-switched operation was further assessed by tracking the optical spectrum and SNR of center wavelength over 1 hour period at 249.70 mW as

displayed in Figure 4.10. The Q-switched optical spectrum preserved its position without any shifting during the measurement in Figure 4.10(a), whilst Figure 4.10(b) shows the center wavelength only fluctuated at a negligible range of 1.49 dB along the period.

4.3.4 Passive Q-switched Thulium-doped Fluoride Fiber Laser by using V_2C Thin Film

The TDFFL was initially engaged by steadily increasing the pump power until CW laser output was established at a pump power of 125 mW. The CW operation was then changed to a Q-switching operation when the pump power reached 159.60 mW. The cavity maintained in Q-switching operation until a maximum power of 249.70 mW. The operation was also constrained by the LD maximum output limit, where the V_2C SA can endure higher pump power such as Nb_2C SA. The optical spectrum of the passive Q-switched TDFFL at the maximum pump power is displayed in Figure 4.11(a). The Q-switched had a center wavelength of 1492.52 nm and a FWHM of 3.37 nm. SPM effect took place in the medium when a high-intensity signal light propagated in cavity, hence broadening the optical spectrum of the TDFFL.

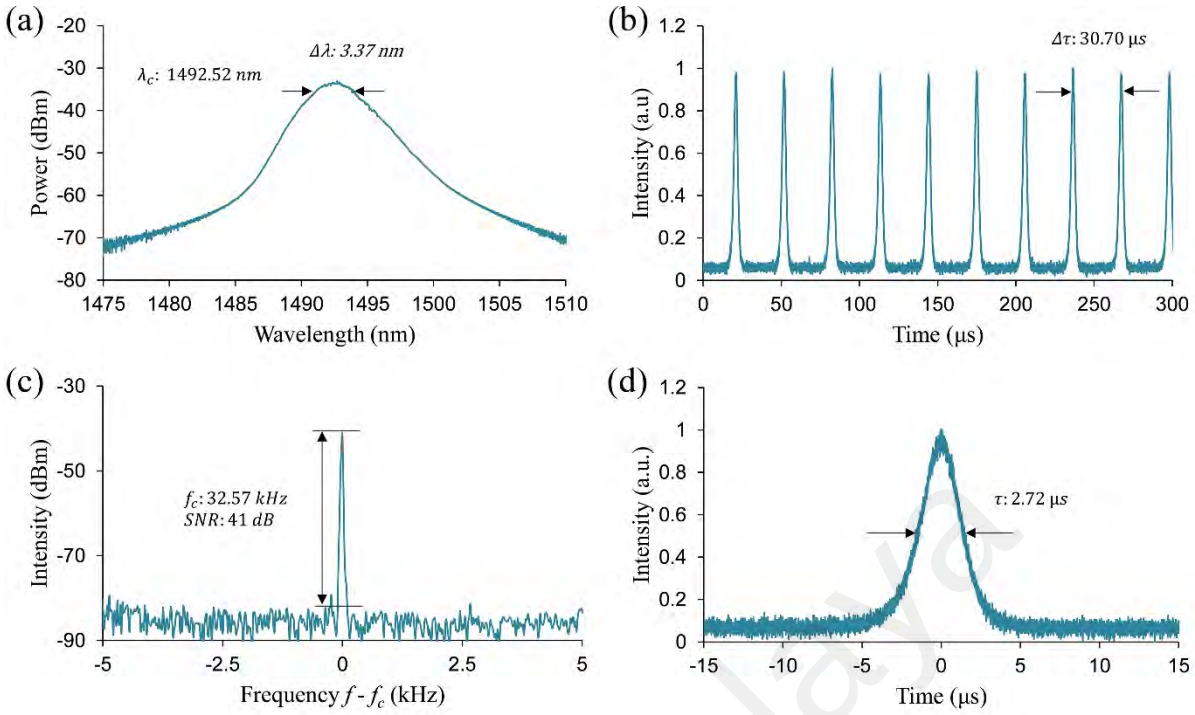

Figure 4.11: (a) Optical spectrum, (b) pulse train, (c) pulse repetition rate, and (d) Q-switched single pulse of V_2C MXene at 249.70 mW.

Characteristics of the Q-switched pulse at maximum pump power are presented in Figure 4.11(b), (c), and (d). The Q-switched pulse train had a maximum pulse repetition rate of 32.57 kHz with trivial intensity fluctuation in the pulse train in Figure 4.11(b). The fundamental peak in the frequency domain was measured to further define the stability, where it had a SNR of 41 dB at pulse repetition rate of 32.57 kHz as in Figure 4.11(c). Furthermore, single pulse profile of the Q-switched pulse was recorded and is displayed in Figure 4.11(d), where it had a pulse width of 2.72 μs.

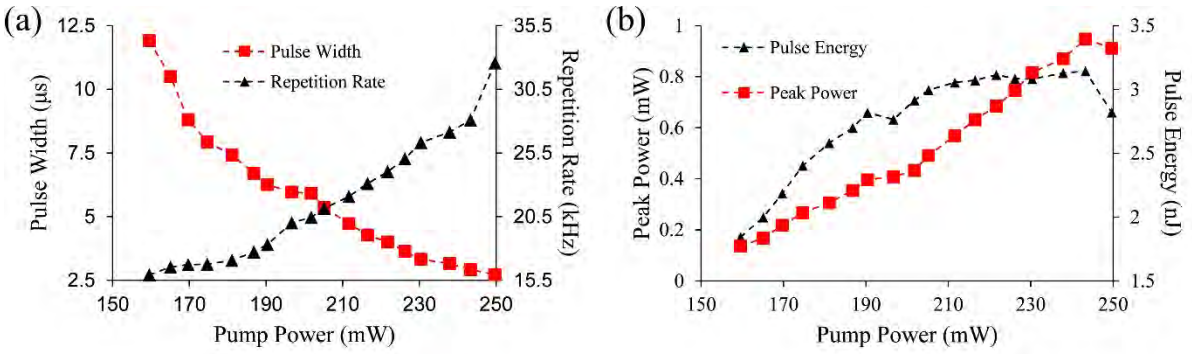

Figure 4.12: Evolution of (a) pulse width and pulse repetition rate, and (b) pulse energy and peak power during V_2C MXene Q-switched operation.

The pulse width was recorded to be 11.90 μs at a pump power of 159.60 mW, then reduced to 2.72 μs at the pump power of 249.70 mW as shown in Figure 4.12(a). The peak power and pulse energy of the Q-switched were slightly decreasing beyond 230 mW due to the saturated energy in the gain medium compensating for the higher pulse repetition rate and shorter pulse width. Pulse energy and peak power of the Q-switched pulses can then be calculated with the given pulse repetition rate with its respective average output power, and pulse width. The maximum pulse energy and peak power of 2.82 nJ and 0.91 mW were recorded at the maximum pump power of 249.70 mW as shown in Figure 4.12(b).

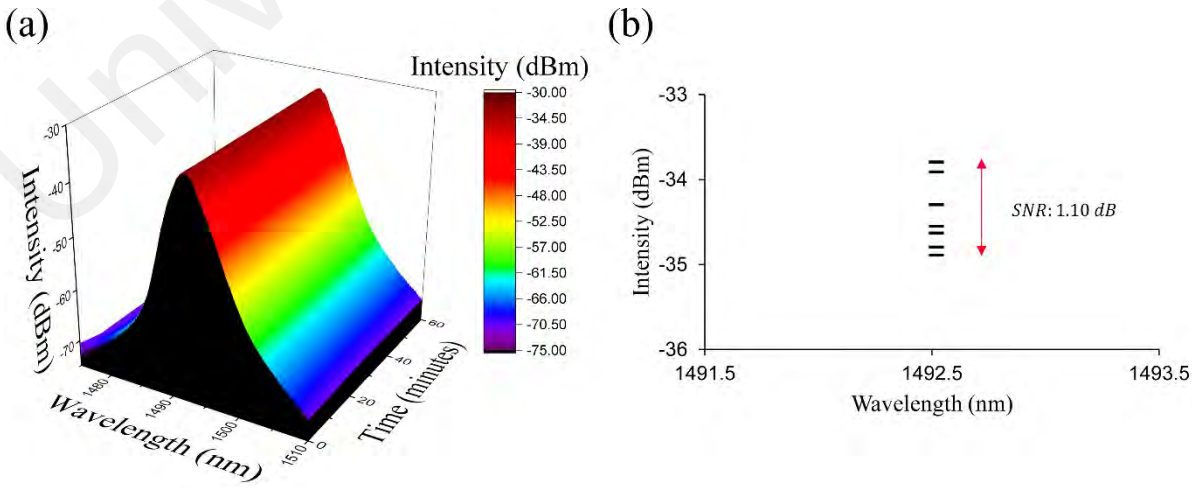

Figure 4.13: V_2C MXene (a) Q-switched optical spectrum, and (b) SNR of center wavelength over 1 hour period.

The stability of V_2C MXene Q-switched operation was further assessed by observing the optical spectrum and SNR of center wavelength over 1 hour period at 249.70 mW as displayed in Figure 4.13. The Q-switched optical spectrum maintained its position without any shifting during the measurement in Figure 4.13(a), whereby in Figure 4.13(b), the center wavelength only fluctuated at a negligible range of 1.10 dB along the period.

4.3.5 Performance Comparison of Molten Fluoride Salt-Assisted MXenes Q-Switched Fiber Laser

In this section, the generation of Q-switched pulsed fiber laser has been successfully demonstrated by using all of the MXene SAs, those are Ti_2C, Nb_2C, and V_2C. The MXenes were incorporated into the systems by using polyvinyl alcohol (PVA) thin film as the host. All of the Q-switched fiber lasers generated at about 1490 nm center wavelength, which Ti_2C hold the shortest wavelength at 1488.19 nm as shown in Table 4.1. As a pulse is always triggered when the laser gain falls across the total loss of the cavity, hence, low saturation intensity and low non-saturable absorption can contribute to the high repetition rate of the pulsed laser. Ti_2C nonetheless has the lowest pulse repetition rate, while Nb_2C has the highest pulse repetition rate as compared to the others. Although Ti_2C has a lower saturation intensity than Nb_2C, but the non-saturable loss of the Ti_2C SA is significantly higher than Nb_2C. Hence, the repetition rate of Ti_2C only manage to achieve 21.94 kHz at maximum.

The pulse width on the other hand is dependent on the exponential growth of the power before reaching gain saturation and the fall of power before the recovery of the SA. Thus, high saturable absorption and short recovery time of the SA can lead to a short pulse width. Concurrently, higher repetition rate of the pulsed laser tends to cause a shorter pulse duration. This is due to the distribution of the energy that cause the pulse to be

relatively thinner and higher peak. Among the MXenes SAs, V_2C has the shortest pulse width although it has lower saturable absorption as opposed to Nb_2C, possibly due to a faster recovery time. On the contrary, Ti_2C has the longest pulse width among the others as it has the lowest saturable absorption. To date, there is no literature on the recovery time of the MXenes included in this study. Despite the high repetition rate and saturable absorption of Nb_2C, the pulse width is still longer than V_2C, showing the dominance of its slower recovery time.

Table 4.1: Q-switched TDFFL characteristics of all molten fluoride salt-assisted MXenes SAs.

Properties \ MXenes		Ti_2C	Nb_2C	V_2C
Linear Absorption, α_0 (%)		11	7	10
Nonlinear Absorption	**Saturable absorption, α_s (%)**	16.31	23.07	20.54
	Non-saturable absorption, α_{ns} (%)	55.8	31.31	33.04
	Saturation intensity, I_{sat} (MW/cm^2)	0.357	0.509	0.441
Center Wavelength, λ_c (nm)		1488.19	1489.63	1492.52
Repetition Rate, f_c (kHz)		21.94	35.20	32.57
Pulse Width, τ (µs)		3.90	3.58	2.72
Pulse Energy, E_p (nJ)		3.78	2.51	2.82

Furthermore, the amount of energy accumulated in the gain medium affects the energy of the generated pulse laser. A high repetition rate pulses can have a lower pulse energy

average because of the stored energy is being distributed to the pulses as the laser system maintains its stored energy. Among the MXenes, Ti_2C has the highest pulse energy due to the lowest pulse repetition rate on top of supposedly longer recovery time which authorize high storage of energy in the gain medium and possesses the lowest saturation intensity. Nb_2C has a higher saturable absorption and slightly lower non-saturable absorption compared to V_2C, hence V_2C has a lower pulse energy than Nb_2C as it holds the second highest saturation intensity and second highest pulse repetition rate. The peak power and pulse energy of all of the MXenes were expected to be decreasing after pumped beyond certain power, however, the values were just increasing towards the maximum pump power of 250 mW. This shows that the pump power can be increased further to fully explored the damage threshold of the MXenes in S-band region.

The performance of the different MXenes SA as passive Q-switcher are strongly associated to their absorption properties and recovery time. In term of pulse energy, Ti_2C performs the best as passive Q-switcher with the highest pulse energy in the controlled system with a few drawbacks of largest pulse width and lowest pulse repetition rate. However, in the perspective of pulse repetition rate, Nb_2C works the best as passive Q-switcher with the highest pulse repetition rate in the controlled system with a few limitations of intermediate pulse width and lowest pulse energy.

Furthermore, a comparison with the other experimental results of SA at about the same operating region in literature is given in Table 4.2. From the table, WS_2 has the highest maximum repetition rate of 120 kHz, while Bi_2Te_3 has the lowest maximum repetition rate of 12.8 kHz. The maximum repetition rate of MXene SAs stay at average values relative to the other SAs. However, the output power of MXene SAs are significantly lower than the other SAs, this could be contributed by the slightly optically damaged gain medium of TDFFL. On the opposite note, GO records the highest output power of 9.3 mW along with the highest pulse energy of 63.9 nJ relative to the other SAs. Whereby,

WS_2 has the lowest pulse energy of 0.05 nJ recorded as compared to the others. Lastly, V_2C has the shortest pulse width of 2.72 ps at the maximum repetition rate, while Bi_2Te_3 has the longest pulse width of 49 ps at the maximum repetition rate. From this comparison, it is shown that the fabricated MXene SAs of this work are comparable to the other SAs with more room for development.

Table 4.2: Performance summary of near S-band Q-switched of other SAs with molten fluoride salt-assisted MXenes.

SA	Repetition Rate (kHz)	Output Power (mW)	Pulse Energy (nJ)	Pulse Width (μs)	Center Wavelength (nm)	Reference
Graphene	3.3 – 65.9	1.1	16.7	3.7	1566.17	(Luo et al., 2010)
GO	22 – 61	9.3	63.9	6.6 – 13.7	1550	(H Ahmad et al., 2012)
Bi_2Se_3	4.5 – 12.88	-	13.3	13.4 – 36	1545 - 1565	(Yu Chen et al., 2013)
Bi_2Te_3	2.15 – 12.8	-	15.25	13 – 49	1510 - 1589	(Yu Chen et al., 2013)
MoS_2	26.6 – 40.9	3.5	-	3.9 – 5.4	1552	(Khazaeinezhad et al., 2015)

Table 4.2, continued.

SA	Repetition Rate (kHz)	Output Power (mW)	Pulse Energy (nJ)	Pulse Width (μs)	Center Wavelength (nm)	Reference
WS_2	80 – 120	-	0.05	1 – 3.1	1547.5	(J. Lin et al., 2015)
Ti_2C	13.1 – 21.94	0.09	3.78	3.90	1488.19	This work
Nb_2C	20 – 35.2	0.092	2.51	3.58	1489.63	
V_2C	15.5 – 32.57	0.092	2.82	2.72	1492.52	

4.4 Passive Q-switched Thulium-doped Fiber Laser (TDFL) by using Molten Fluoride Salt-Assisted MXenes

4.4.1 Experimental Configuration of Passive Q-switched TDFL

The experimental setup schematic diagram is shown in Figure 4.14. The cavity employed ring configuration with a 4-meter-long thulium-doped silica fiber (TDF) TmDF200 (OFS Inc.) as the gain medium. The gain medium was pumped by using a 1565 nm optical source (Naku Technology) that has a maximum power of 1 W.

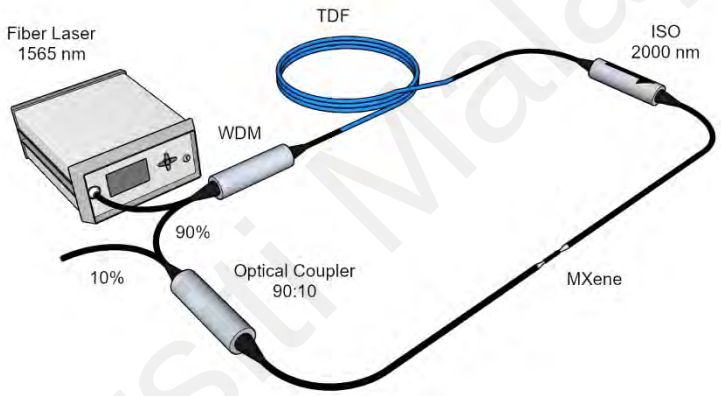

Figure 4.14: Schematic diagram of Q-switched MXene TDFL.

The optical source output was fixed to the 1550 nm port of 1550/2000 nm wavelength division multiplexer (WDM) with a 1 W threshold rating. Then, the common port of the WDM was connected to the TDF that has a peak absorption of 22 dB/m at 1550 nm, a core diameter of 4.5 µm, and a numerical aperture of 0.26. The opposite side of the TDF was attached to a 2000 nm isolator (ISO) to constrain the signal propagation in one direction that help to optimize the cavity output power. The MXene-based tapered fiber SA was connected after the ISO and then to a 90:10 optical coupler (OC). The 90% port was used as feedback into the cavity by connecting to the 2000 nm port of the WDM,

while the 10% port was extracted to analyze the mode-locked pulses. The continuous wave (CW) of the TDFL is displayed in Figure 4.15 that operated at 200 mW with a center wavelength of 1973.54 nm.

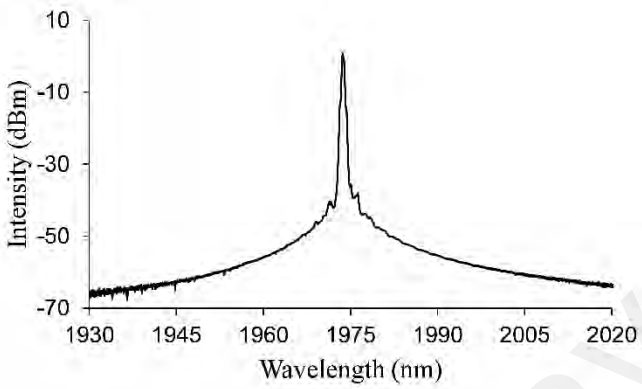

Figure 4.15: CW operation of TDFL at 200 mW without MXenes.

4.4.2 Passive Q-swtiched Thulium-doped Silica Fiber Laser by using Ti_2C Tapered Fiber

The TDFFL was first operated by gradually increasing the pump power until CW laser output was established at a pump power of 120 mW. The CW operation changed to a Q-switching operation when the pump power reached 150 mW. The cavity maintained in same operation until a maximum power of 260 mW. The center wavelength of the Q-switched in optical spectrum gradually shifted towards lower wavelength when the pump power went to 260 mW. The optical spectrum of the passive Q-switched TDFL at the maximum pump power is displayed in Figure 4.16(a). The Q-switched had a center wavelength, λ_c of 1953 nm and a bandwidth or full-width at half maximum (FWHM), $\Delta\lambda$ of 5.25 nm. Self-phase modulation (SPM) effect arose when a high intensity signal light propagated in the fiber core, thus broadening the optical spectrum of the TDFL.

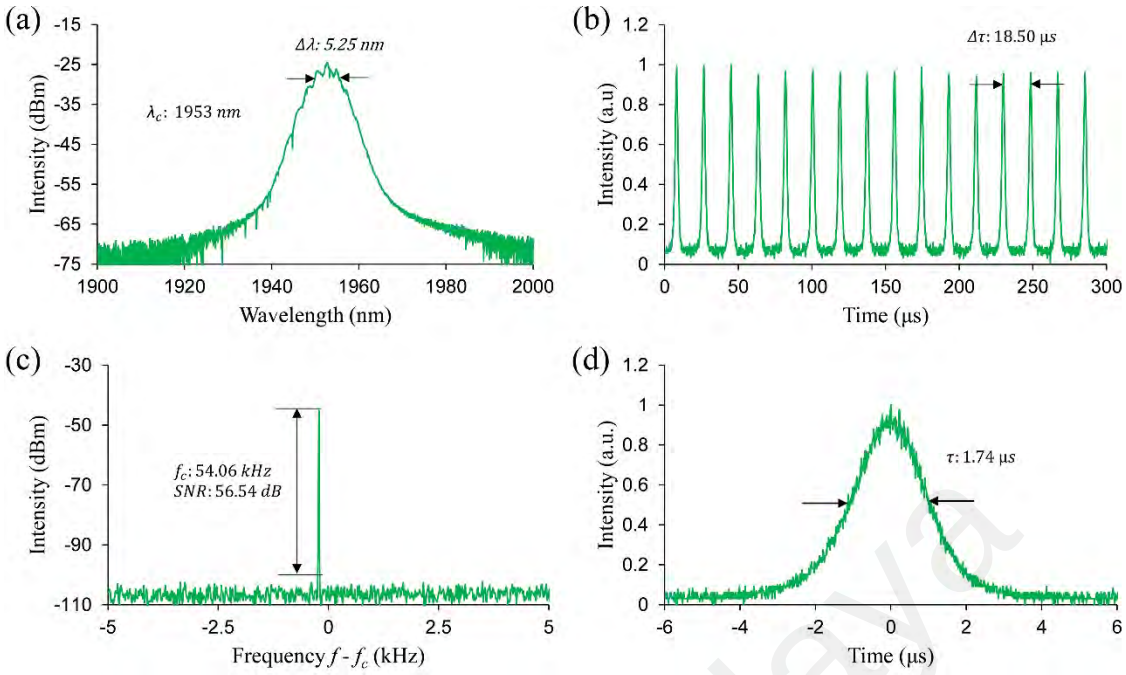

Figure 4.16: (a) Optical spectrum, (b) pulse train, (c) pulse repetition rate, and (d) Q-switched single pulse of Ti_2C MXene at 260 mW.

Characteristics of the Q-switched pulse at maximum pump power are presented in Figure 4.16(b), (c), and (d). The Q-switched pulse train had a maximum pulse repetition rate, f_c of 54.06 kHz with insignificant intensity fluctuation in the pulse train in Figure 4.16(b). The stability can be clarified further in the frequency domain, where it had a signal-to-noise ratio (SNR) of 56.54 dB at pulse repetition rate of 54.06 kHz as in Figure 4.16(c). Additionally, single pulse profile of the Q-switched pulse was taken and is presented in Figure 4.16(d), where it had a pulse width, τ of 1.74 μs.

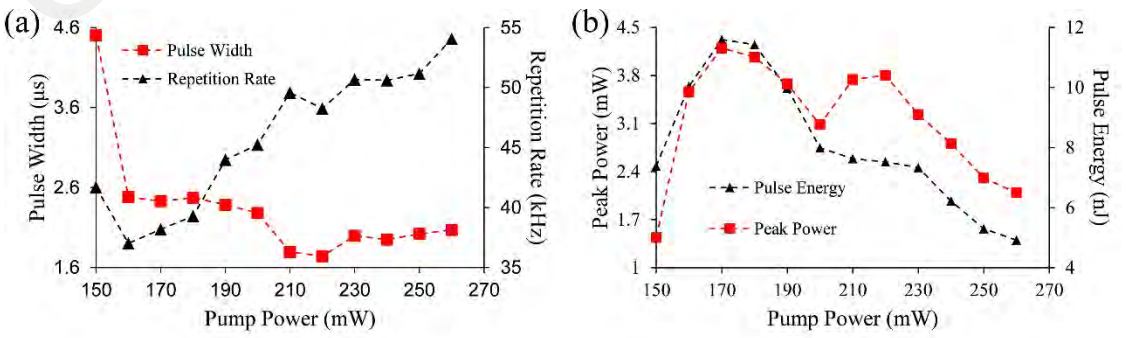

Figure 4.17: Evolution of (a) pulse width and pulse repetition rate, and (b) pulse energy and peak power during Ti_2C MXene Q-switched operation.

The minimum pulse width was recorded to be 1.74 µs at 220 mW pump power, whereby the maximum pulse repetition rate was recorded to be 54.06 kHz at 260 mW pump power as shown in Figure 4.17(a). The peak power and pulse energy of the Q-switched were decreasing beyond 180 mW due to the saturated energy in the gain medium compensating for the higher pulse repetition rate and shorter pulse width. Pulse energy and peak power of the Q-switched pulses can be evaluated with the given pulse repetition rate with its corresponding average output power, and pulse width by considering the pulse shape. The maximum pulse energy and peak power of 11.6 nJ and 4.2 mW were recorded at the maximum pump power of 170 mW as shown in Figure 4.17(b).

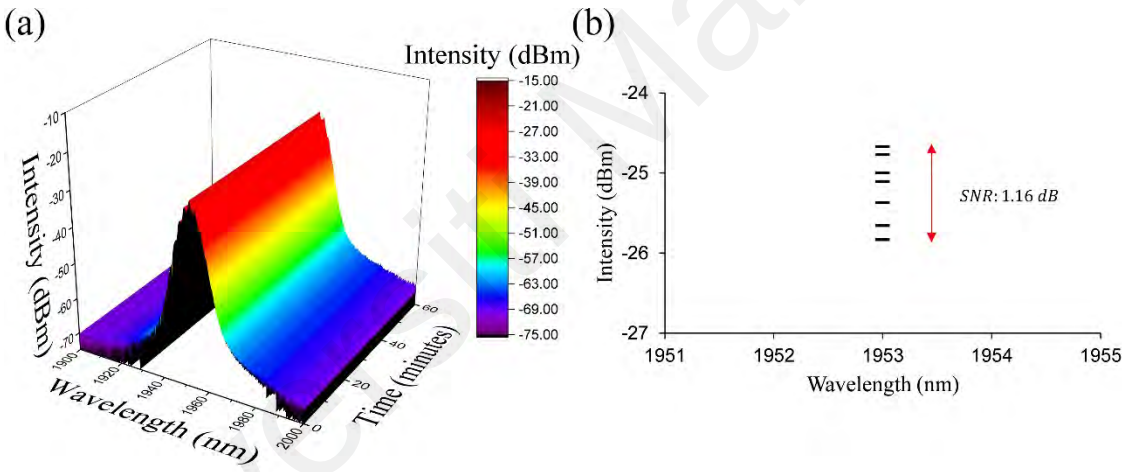

Figure 4.18: Ti_2C Mxene (a) Q-switched optical spectrum, and (b) SNR of center wavelength over 1 hour period.

The stability of Ti_2C SA Q-switched operation was further evaluated by monitoring the optical spectrum and SNR of center wavelength over 1 hour period at 260 mW as displayed in Figure 4.18. The Q-switched optical spectrum maintains its center wavelength during the whole period in Figure 4.18(a), whereby the center wavelength only fluctuated at a negligible range of 1.16 dB along the test as in Figure 4.18(b).

4.4.3 Passive Q-switched Thulium-doped Fluoride Fiber Laser by using Nb_2C Tapered Fiber

In the beginning, the TDFFL was first operated by slowly increasing the pump power until CW laser output was established at a pump power of 130 mW. The CW operation was then changed to a Q-switching operation when the pump power reached 170 mW. The cavity maintained in Q-switching operation until a maximum pump power of 300 mW. The optical spectrum of the passive Q-switched TDFL at the maximum pump power is displayed in Figure 4.19(a). The Q-switched had a center wavelength of 1948 nm and a FWHM of 6.31 nm. SPM effect took place in the medium when a high-intensity signal light propagated in cavity, hence widening the optical spectrum of the TDFL.

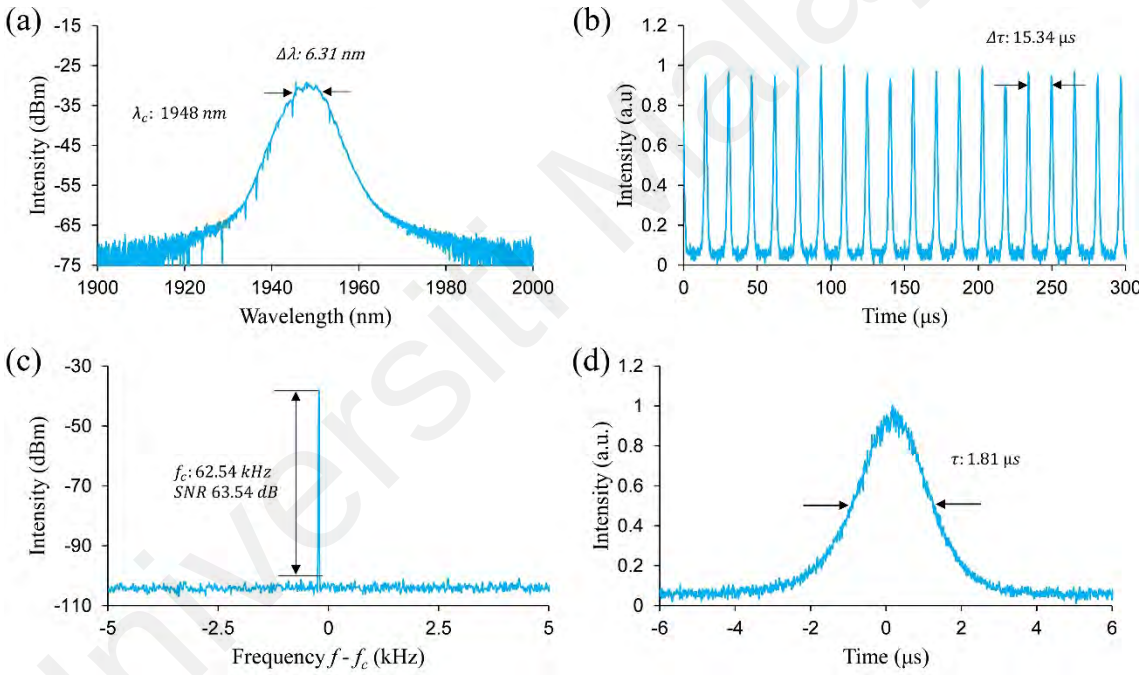

Figure 4.19: (a) Optical spectrum, (b) pulse train, (c) pulse repetition rate, and (d) Q-switched single pulse of Nb_2C MXene at 300 mW.

Characteristics of the Q-switched pulse at maximum pump power are presented in Figure 4.19(b), (c), and (d). The Q-switched pulse train had a maximum pulse repetition rate of 62.54 kHz with minor intensity fluctuation in the pulse train in Figure 4.19(b). The fundamental peak in the frequency domain was measured to further analyze the stability, where it had a SNR of 63.54 dB at pulse repetition rate of 62.54 kHz as in Figure 4.19(c).

Additionally, single pulse profile of the Q-switched pulse was taken and is presented in Figure 4.19(d), where it had a pulse width of 1.81 µs.

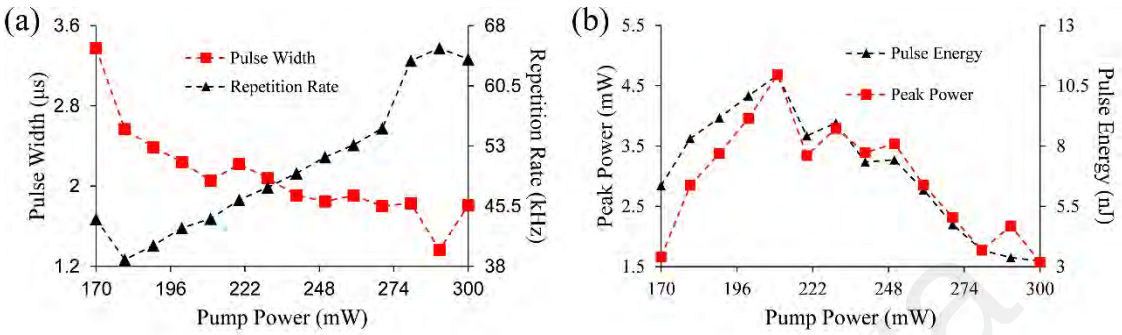

Figure 4.20: Evolution of (a) pulse width and pulse repetition rate, and (b) pulse energy and peak power during Nb_2C MXene Q-switched operation.

The minimum pulse width was recorded to be 1.36 µs at a pump power of 290 mW, whereby the maximum pulse repetition rate was recorded to be 65.17 kHz at 290 mW pump power as shown in Figure 4.20(a). The peak power and pulse energy of the Q-switched were decreasing beyond 200 mW due to the saturated energy in the gain medium compensating for the higher pulse repetition rate and shorter pulse width. Pulse energy and peak power of the Q-switched pulses can be evaluated with the given pulse repetition rate with its respective average output power, and pulse width. The maximum pulse energy and peak power of 10.90 nJ and 4.68 mW were recorded at the maximum pump power of 210 mW as shown in Figure 4.20(b).

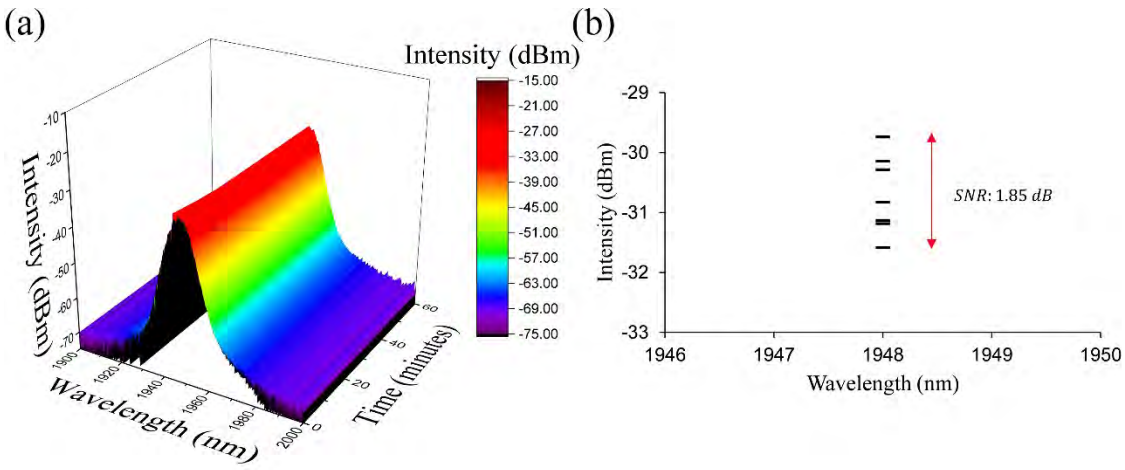

Figure 4.21: Nb_2C MXene (a) Q-switched optical spectrum, and (b) SNR of center wavelength over 1 hour period.

The stability of Nb_2C MXene Q-switched operation was further assessed by tracking the optical spectrum and SNR of center wavelength over 1 hour period at 300 mW as displayed in Figure 4.21. The Q-switched optical spectrum preserved its position without any shifting during the measurement as can be seen in Figure 4.21(a), while Figure 4.21(b) shows the center wavelength only fluctuated at a negligible range of 1.85 dB along the period.

4.4.4 Passive Q-switched Thulium-doped Fluoride Fiber Laser by using V_2C Tapered Fiber

The TDFFL was initially engaged by steadily increasing the pump power until CW laser output was established at a pump power of 110 mW. The CW operation was then switched to a Q-switching operation when the pump power reached 130 mW. The cavity maintained in Q-switching operation until a maximum power of 250 mW. The optical spectrum of the passive Q-switched TDFL at the maximum pump power is displayed in Figure 4.22(a). The Q-switched had a center wavelength of 1941 nm and a FWHM of 6.53 nm. SPM effect took place in the medium when a high-intensity signal light propagated in cavity, hence broadening the optical spectrum of the TDFL.

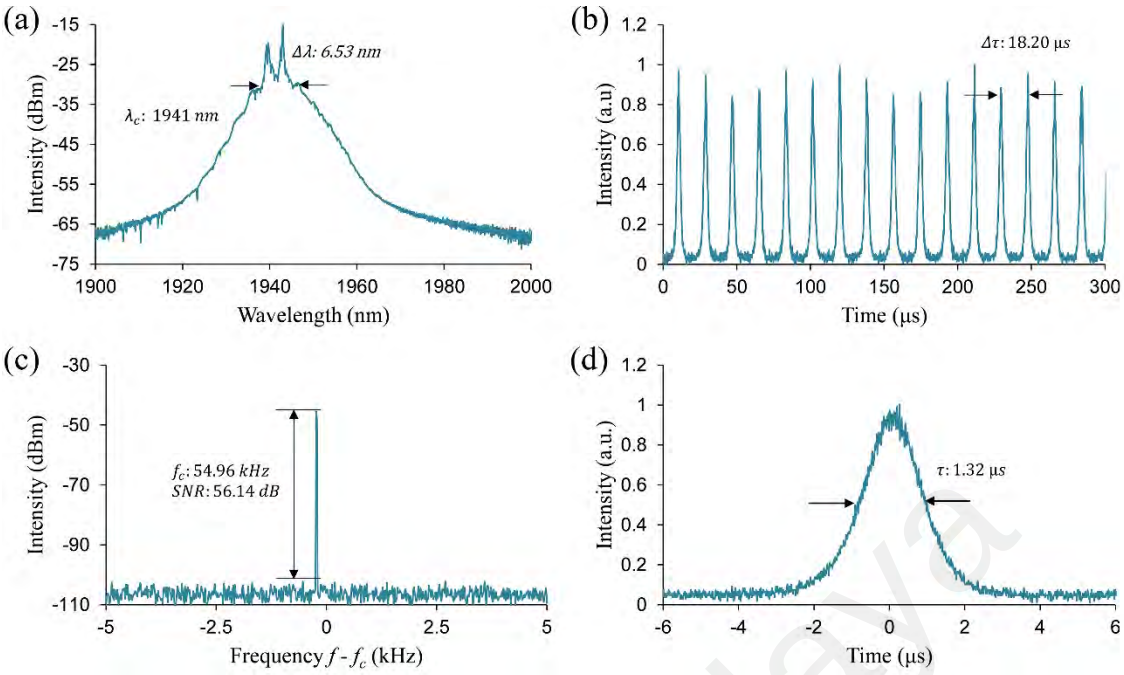

Figure 4.22: (a) Optical spectrum, (b) pulse train, (c) pulse repetition rate, and (d) Q switched single pulse of V_2C MXene at 250 mW.

Characteristics of the Q-switched pulse at maximum pump power are presented in Figure 4.22(b), (c), and (d). The Q-switched pulse train had a maximum pulse repetition rate of 54.96 kHz with trivial intensity fluctuation in the pulse train in Figure 4.22(b). The fundamental peak in the frequency domain was measured to further analyze the stability of the laser, where it had a SNR of 56.14 dB at pulse repetition rate of 54.96 kHz as in Figure 4.22(c). Furthermore, single pulse profile of the Q-switched pulse was recorded and is displayed in Figure 4.22(d), where it had a pulse width of 1.32 µs.

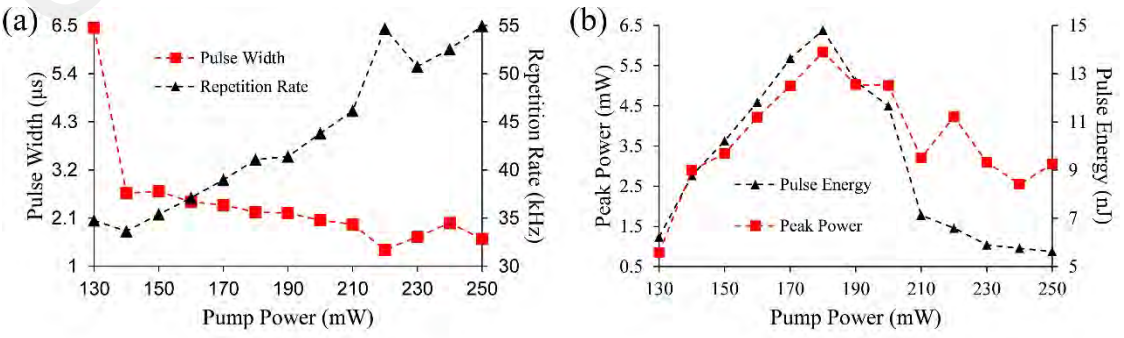

Figure 4.23: Evolution of (a) pulse width and pulse repetition rate, and (b) pulse energy and peak power during V_2C MXene Q-switched operation.

The minimum pulse width was recorded to be 1.37 μs at a pump power of 220 mW, whereby the maximum pulse repetition rate was recorded to be 54.96 kHz at a pump power of 250 mW as displayed in Figure 4.23(a). The peak power and pulse energy of the Q-switched were decreasing beyond 180 mW due to the saturated energy in the gain medium compensating for the higher pulse repetition rate and shorter pulse width. Pulse energy and peak power of the Q-switched pulses can then be calculated with the given pulse repetition rate with its respective average output power, and pulse width. The maximum pulse energy and peak power of 14.80 nJ and 5.84 mW were recorded at the pump power of 180 mW as shown in Figure 4.23(b).

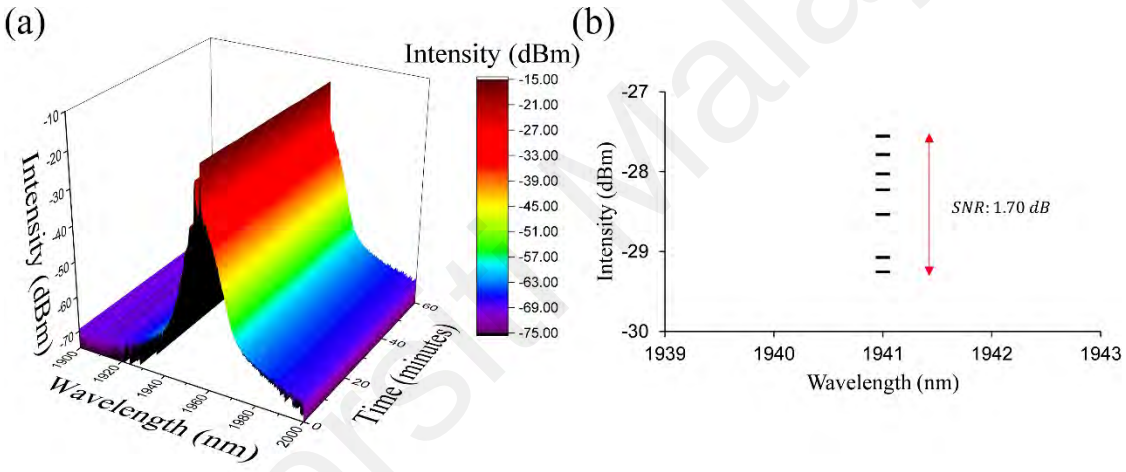

Figure 4.24: V_2C MXene (a) Q-switched optical spectrum, and (b) SNR of center wavelength over 1 hour period.

The stability of V_2C MXene Q-switched operation was further assessed by observing the optical spectrum and SNR of center wavelength over 1 hour period at 250 mW as displayed in Figure 4.24. The Q-switched optical spectrum maintained its position without any shifting during the measurement as displayed in Figure 4.24(a), while Figure 4.24(b) shows the center wavelength fluctuated at only a negligible range of 1.70 dB along the period.

4.4.5 Performance Comparison of Molten Fluoride Salt-Assisted MXenes Q-Switched Fiber Laser

In this section, the generation of Q-switched pulsed fiber laser has been successfully demonstrated by using all of the MXene SAs, those are Ti_2C, Nb_2C, and V_2C. The MXenes were incorporated into the systems by using tapered fiber as the host. All of the Q-switched fiber lasers generated at about 1950 nm center wavelength, which V_2C hold the shortest wavelength at 1941 nm as shown in Table 4.3. As a pulse is always triggered when the laser gain falls across the total loss of the cavity, hence, low saturation intensity and low non-saturable absorption can contribute to the high repetition rate of the pulsed laser. Ti_2C nonetheless has the lowest pulse repetition rate, while Nb_2C has the highest pulse repetition rate as compared to the others. Although Ti_2C has a lower saturation intensity than Nb_2C, but the non-saturable loss of the Ti_2C SA is significantly higher than Nb_2C. Hence, the repetition rate of Ti_2C only manage to achieve 54.06 kHz at maximum.

The pulse width on the other hand is dependent on the exponential growth of the power before reaching gain saturation and the fall of power before the recovery of the SA. Thus, high saturable absorption and short recovery time of the SA can lead to a short pulse width. Concurrently, higher repetition rate of the pulsed laser can cause a shorter pulse duration. This is due to the distribution of the energy that cause the pulse to be relatively thinner and higher peak. Among the MXenes SAs, V_2C has the shortest pulse width although it has lower saturable absorption as opposed to Nb_2C, possibly due to a faster recovery time of the SA. On the contrary, Nb_2C has the longest pulse width among the others although it has the highest saturable absorption. Despite the high repetition rate and high saturable absorption of Nb_2C, the pulse width is still longer than V_2C and Ti_2C, showing the dominance of its slow recovery time.

Table 4.3: Q-switched TDFL characteristics of all molten fluoride salt-assisted MXenes SAs.

Properties \ MXenes		Ti_2C	Nb_2C	V_2C
Linear Absorption, α_0 (%)		54.06	51.39	52.35
Nonlinear Absorption	**Saturable absorption, α_s (%)**	14.78	20.34	18.71
	Non-saturable absorption, α_{ns} (%)	57.32	34.04	34.87
	Saturation intensity, I_{sat} (MW/cm^2)	0.402	0.528	0.471
Center Wavelength, λ_c (nm)		1953	1948	1941
Repetition Rate, f_c (kHz)		54.06	62.54	54.96
Pulse Width, τ (µs)		1.74	1.81	1.32
Pulse Energy, E_p (nJ)		11.6	10.90	14.80

Furthermore, the amount of energy accumulated in the gain medium affects the energy of the generated pulse laser. A high repetition rate pulses can have a lower pulse energy average because of the stored energy is being distributed to the pulses as the laser system maintains its stored energy. Among the MXenes, V_2C has the highest pulse energy due to the low pulse repetition rate on top of low saturation intensity. Nb_2C has a highest pulse repetition rate as compared to Ti_2C and V_2C, hence Nb_2C holds the lowest pulse energy below Ti_2C. The peak power and pulse energy of all of the MXenes were decreasing after went beyond certain pump power due to the accumulated energy in the gain medium compensating for the higher pulse repetition rate and shorter pulse width.

Overall, the performance of the different MXenes SA as passive Q-switcher are strongly associated to their absorption properties and recovery time. In terms of pulse energy, V_2C performs the best as passive Q-switcher with the highest pulse energy in the controlled system with an advantage of shortest pulse. However, in the perspective of pulse repetition rate, Nb_2C works the best as passive Q-switcher with the highest pulse repetition rate in the controlled system with a few limitations of longest pulse width and lowest pulse energy.

Furthermore, a comparison with the other experimental results of SA at about the same operating region in literature is given in Table 4.4. From the table, GO has the highest maximum repetition rate of 83.2 kHz, while $MoSe_2$ has the lowest maximum repetition rate of 21.8 kHz. The maximum repetition rate of MXene SAs stay at average values relative to the other SAs. However, the output power of MXene SAs are noticeably lower than the other SAs. On the opposite note, MoS_2 records the highest output power of 47.3 mW along with the highest pulse energy of 63.9 nJ relative to the other SAs. Whereby, WS_2 has the lowest pulse energy of 1 μJ recorded as compared to the others. Lastly, GO has the shortest pulse width of 1.1 ps at the maximum repetition rate, while CNT has the longest pulse width of 21.6 ps at the maximum repetition rate. From this comparison, it is shown that the fabricated MXene SAs of this work are comparable to the other SAs with more room for development.

Table 4.4: Performance summary of near 2 μm Q-switched of other SAs with molten fluoride salt-assisted MXenes.

SA	Repetition Rate (kHz)	Output Power (mW)	Pulse Energy (nJ)	Pulse Width (μs)	Center Wavelength (nm)	Reference
CNT	~46.1	2.2	21.6	21.6	1892.4	(Saidin et al., 2016)
Graphene	12 – 26	1.8	70	2.3	1884	(F. Wang et al., 2012)
GO	33.5 – 83.2	61	730	1.1	1950.27	(F. Wang et al., 2012)
MoS_2	33.6 – 48.1	47.3	1000	1.76	2032	(Luo et al., 2014)
$MoSe_2$	14 – 21.8	0.91	42	5.5	1924	(Woodward et al., 2015)

Table 4.4, continued.

SA	Repetition Rate (kHz)	Output Power (mW)	Pulse Energy (nJ)	Pulse Width (μs)	Center Wavelength (nm)	Reference
TiO_2	30.12 – 36.96	11	300	1.91	1935	(Woodward et al., 2015)
Ti_2C	41.68 – 54.06	0.44	11.6	2.07	1953	This work
Nb_2C	43.9 – 63.83	0.48	10.94	1.81	1948	
V_2C	33.63 – 54.96	0.61	14.8	1.37	1941	

4.5 Passive Mode-locked Thulium-doped Silica Fiber Laser by using Molten Fluoride Salt-Assisted MXenes

4.5.1 Experimental Configuration of Passive Mode-locked Thulium-doped Silica Fiber Laser (TDFL)

The experimental setup schematic diagram is shown in Figure 4.25. The cavity employed ring configuration with a 4-meter-long thulium-doped silica fiber (TDF) TmDF200 (OFS Inc.) as the gain medium. The gain medium was pumped by using a 1565 nm optical source (Naku Technology) that has a maximum power of 1 W.

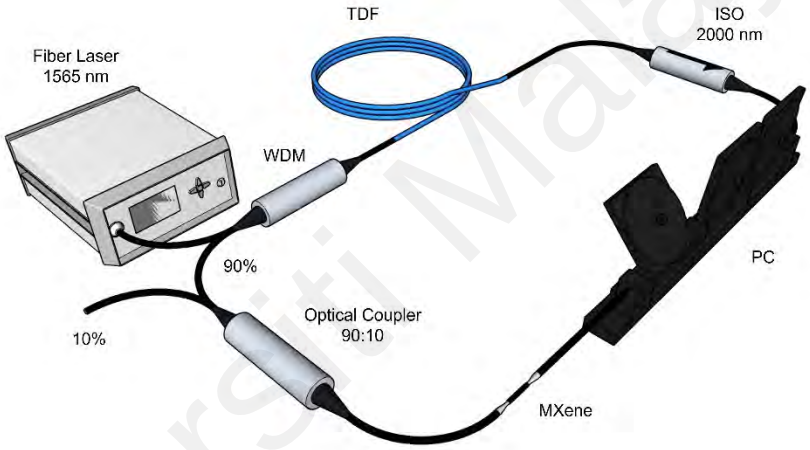

Figure 4.25: Schematic diagram of mode-locked MXenes TDFL.

The optical source output was fixed to the 1550 nm port of 1550/2000 nm wavelength division multiplexer (WDM) with a 1 W threshold rating. Then, the common port of the WDM was connected to the TDF that has a peak absorption of 22 dB/m at 1550 nm, a core diameter of 4.5 µm, and a numerical aperture of 0.26. The opposite side of the TDF was attached to a 2000 nm isolator (ISO) to constrain the signal propagation in one direction that help to optimize the cavity output power. A polarization controller (PC) was also integrated into the cavity to manipulate the signal polarization state. The MXene-based tapered fiber SA was connected after the PC and then to a 90:10 optical coupler

(OC). The 90% port was used as feedback into the cavity by connecting to the 2000 nm port of the WDM, while the 10% port was extracted to analyze the mode-locked pulses.

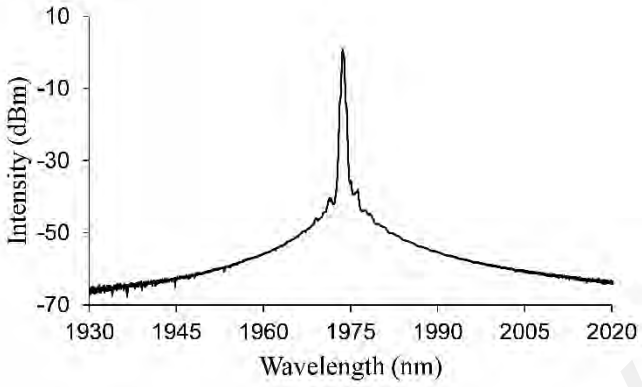

Figure 4.26: CW operation of TDFL at 200 mW without MXenes.

The continuous wave (CW) of the TDFL is displayed in Figure 4.26 that operated at 200 mW with a center wavelength of 1973.54 nm. The cavity was operating in anomalous dispersion regime which can be determined by using the following expression

$$Dispersion_{net} = Length_{SMF} GVD_{SMF} + Length_{TDF} GVD_{TDF} \quad (4.1)$$

where the length, and group velocity dispersion (GVD) of the single-mode fiber (SMF) is 14.5 meter, and -0.0674 ps^2/m, while the length, and GVD of the TDF is 4 meter and -0.0222 ps^2/m, respectively. With these figures, the net cavity dispersion was calculated to be -1.066 ps^2. Hence, a typical characteristic of soliton-like mode-locking with Kelly sidebands was expected in the optical spectrum since it ran in anomalous dispersion.

4.5.2 Passive Mode-locked Thulium-doped Silica Fiber Laser by using Ti_2C Tapered Fiber

The laser cavity with the Ti_2C tapered fiber was first characterized by gradually increasing the pump power, whereby a continuous wave (CW) laser output was observed

at a pump power of 90 mW. The CW operation then shifted to a mode-locking process when the pump power increased to 120 mW. To initiate the mode-locking operation, the PC was adjusted to modify the modes in the cavity by altering the polarization states in the laser cavity. The mode-locking process was well sustained until a pump power of 350 mW. Figure 4.3 shows the measured output laser performance at the threshold pump power of 120 mW, in which the mode-locked TDFL was operating in the fundamental harmonic mode-locking. The mode-locked laser optical spectrum had a center wavelength of 1951.13 nm with a FWHM of 2.88 nm, as shown in Figure 4.27(a). Figure 4.27(b) shows the mode-locked pulse train had a pulse interval of 88.47 ns, which corresponds to a repetition rate of 11.30 MHz. Figure 4.27(c) shows the pulse duration of the mode-locked pulse obtained during the autocorrelation measurement, which was fitted with the sech^2 profile. The pulse duration, τ_{AC}, was measured to be 1.72 ps, corresponding to a time-bandwidth product (TBP) of 0.412. It was slightly larger than the sech^2 transform-limited TBP value of 0.315, suggesting the output pulse was chirped

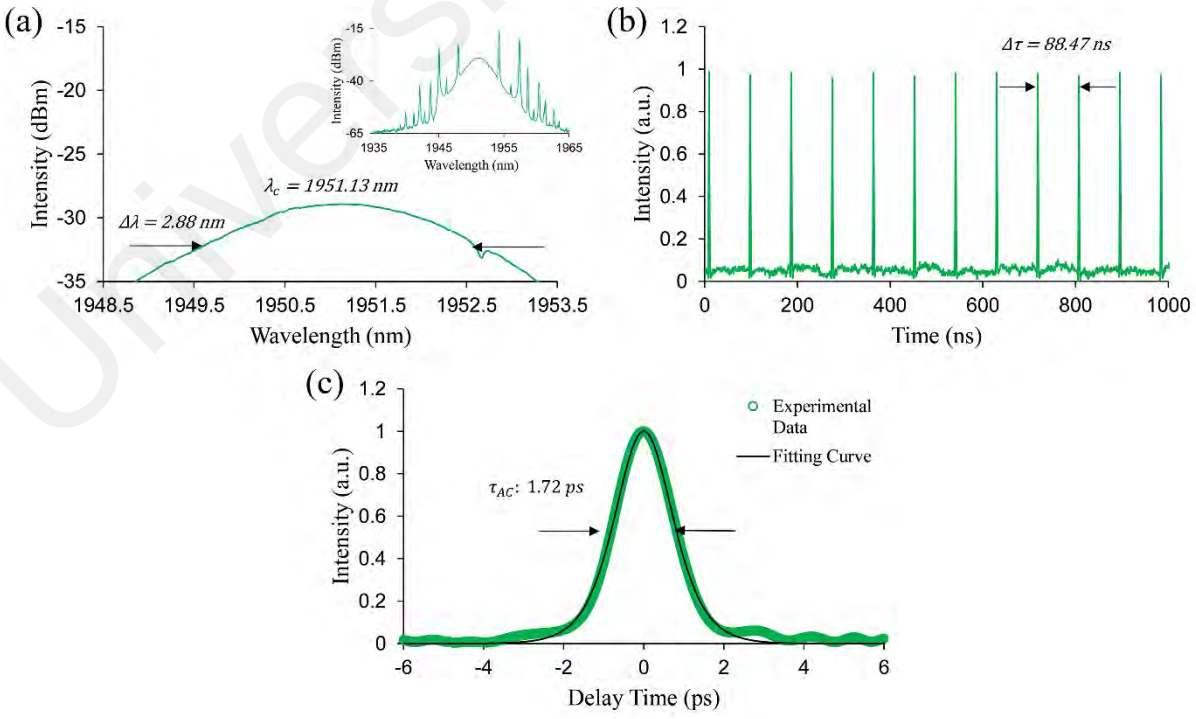

Figure 4.27: (a) Optical spectrum, (b) pulse train, and (c) autocorrelator trace of Ti_2C MXene at 120 mW.

Furthermore, the mode-locking stability was determined by recording the radio frequency spectrum with a bandwidth resolution of 300 Hz at a pump power of 120 mW. The obtained spectrum in Figure 4.28(a) had a clear peak with a fundamental frequency, at 11.30 MHz. The output pulses had a SNR of 45.46 dB, signifying a stable mode-locking pulse. The span of the spectrum was then increased to 500 MHz at 10 kHz bandwidth resolution in Figure 4.28(b) to observe the harmonic frequencies without any significant modulation instability, which further denotes the mode-locking stability.

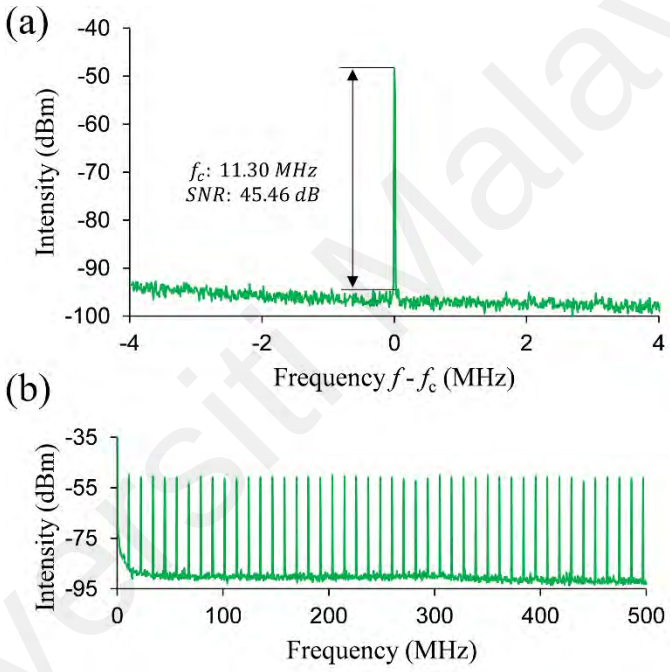

Figure 4.28: RFSA spectrum (a) fundamental frequency, and (b) harmonic frequencies of Ti_2C MXene at 100 mW.

Figure 4.29 shows the plot of the average output power of the mode-locked laser against an increasing pump power from 120 mW to 350 mW. The average output power of the mode-locked laser at the threshold pump power of 120 mW was measured to be 0.44 mW. At the maximum pump power of 350 mW, the average output power increased to 2.54 mW. When the pump power was further increased above 350 mW, the mode-locked pulses disappeared, however, appeared back when the pump power was turned

down within its operating range. The average output power was directly proportional to the pump power but started to decline when nearing the maximum pump power denoting the material was approaching its saturation point. The disappearance of the mode-locked pulses above 350 mW indicated the saturation of Ti_2C MXene. The maximum pulse energy, E_{max} of 0.112 nJ was calculated by dividing the recorded output power by its corresponding repetition rate. The corresponding maximum peak power, P_{max} of 0.060 kW can then be obtained from the maximum pulse energy considering $sech^2$ temporal pulse shape (constant factor of 0.88) as shown in Figure 4.27(c) through the following equation.

$$P_{max} \approx 0.88 \frac{E_{max}}{\tau_{AC}} \tag{4.2}$$

where P_{max}, E_{max}, and τ_{AC} are peak power, pulse energy, and pulse duration, respectively.

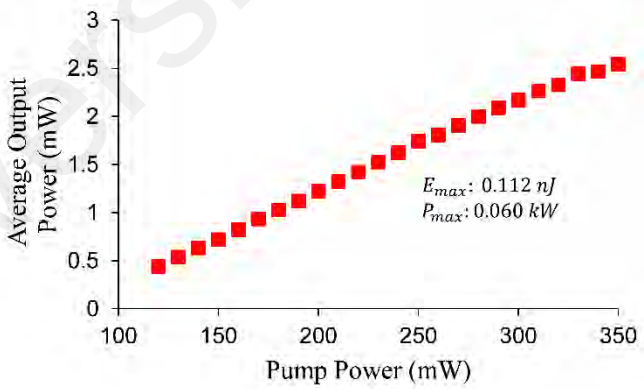

Figure 4.29: The average output power against pump power of the mode-locked TDFL Ti_2C MXene.

To further evaluate the stability of the laser, the mode-locked pulse was monitored in the wavelength and frequency domain over 2 hours at an interval of 10 minutes, as illustrated in Figure 4.30.

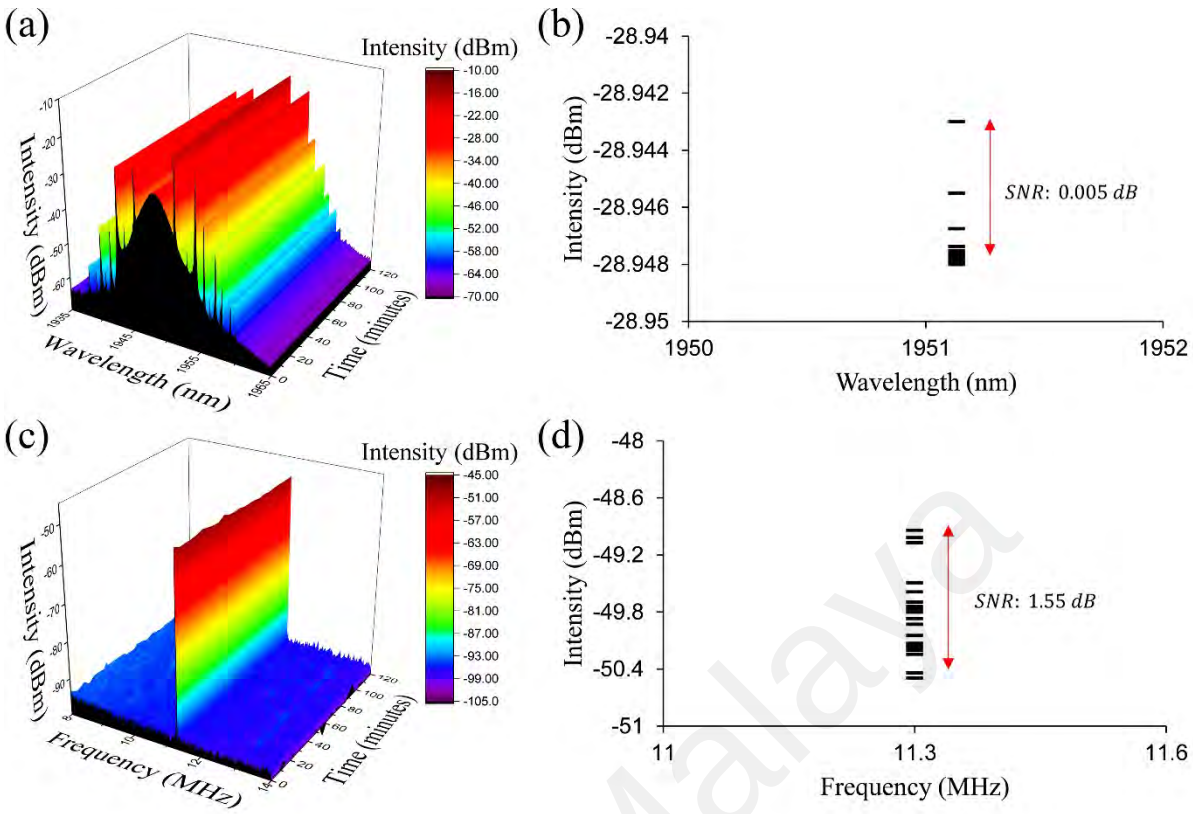

Figure 4.30: Stability of Ti_2C MXene (a) optical spectrum, (b) center wavelength, (c) radio frequency spectrum, and (d) fundamental frequency for 2 hours.

The pump power was kept at 120 mW during the measurement. No sign of significant wavelength and frequency drifting was notified over the whole period, as appeared in the intensity color variation of Figure 4.30(a) and (c). A single point was selected from each wavelength and radio frequency spectrum data, specifically at the center wavelength and the fundamental frequency. Figures 4.30(b) and (d) show the fluctuation of the single points during the 2 hours. The output power indicates no notable changes as the variation was as little as 0.005 dB and 1.55 dB for the center wavelength and fundamental frequency, respectively.

4.5.3 Passive Mode-locked Thulium-doped Silica Fiber Laser by using Nb_2C Tapered Fiber

The laser cavity with the Nb_2C-based tapered fiber was first identified by slowly increasing the pump power, whereby a continuous wave (CW) laser output was observed

at a pump power of 70 mW. The CW operation then shifted to a mode-locking process when the pump power increased to 100 mW. To introduce the mode-locking operation, the PC was adjusted to modify the modes in the cavity by altering the polarization states in the laser cavity. The mode-locking process was well sustained until a pump power of 370 mW. Figure 4.31 shows the measured output laser performance at the threshold pump power of 100 mW, in which the mode-locked TDFL was operating in the fundamental harmonic mode-locking. The mode-locked laser optical spectrum had a center wavelength of 1956.43 nm with a FWHM of 3.54 nm, as shown in Figure 4.31(a). Figure 4.31(b) shows the mode-locked pulse train had a pulse interval of 82.28 ns, which corresponds to a repetition rate of 12.15 MHz. Figure 4.31(c) shows the pulse duration of the mode-locked pulse obtained during the autocorrelation measurement, which was fitted with the sech^2 profile. The pulse duration, τ_{AC}, was measured to be 1.67 ps, corresponding to a TBP of 0.38. It was slightly wider than the sech^2 transform-limited TBP value of 0.315, proposing the output pulse was chirped

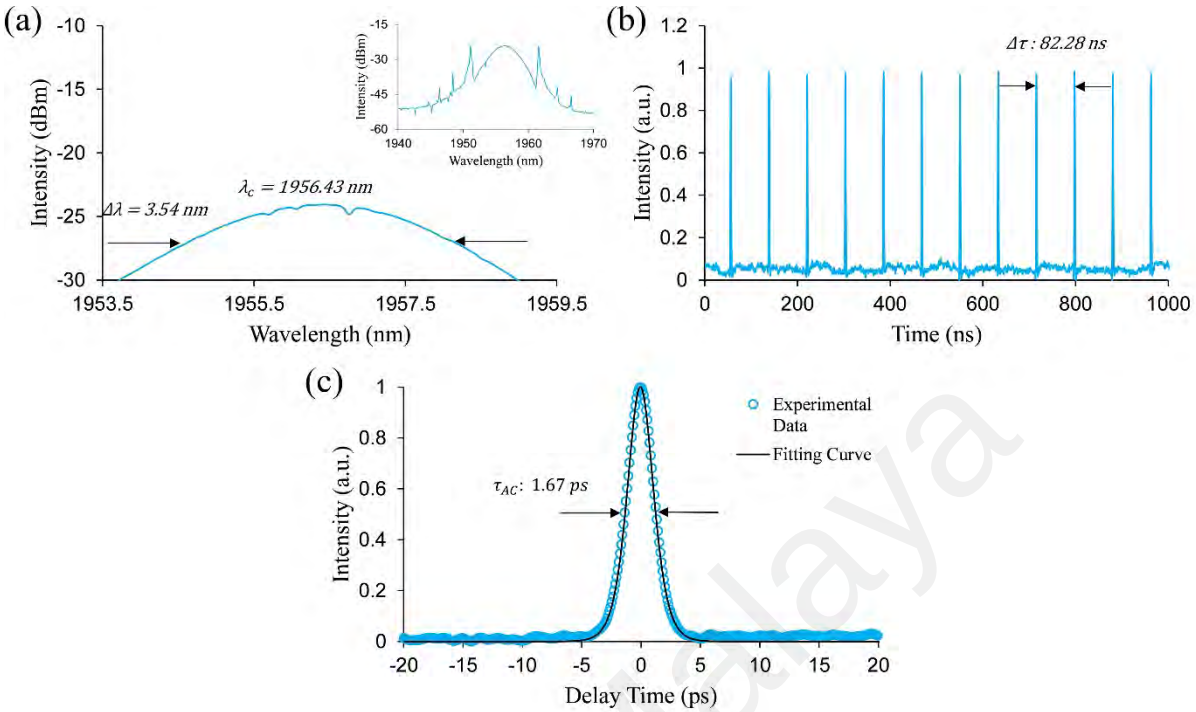

Figure 4.31: (a) Optical spectrum, (b) pulse train, and (c) autocorrelator trace of Nb_2C MXene at 100 mW.

Additionaly, the mode-locking stability was analyzed by recording the radio frequency spectrum with a bandwidth resolution of 300 Hz at a pump power of 100 mW. The obtained spectrum in Figure 4.32(a) had a clear peak with a fundamental frequency at 12.15 MHz. The output pulses had a SNR of 55.30 dB, manifesting a stable mode-locking pulse. The span of the spectrum was then increased to 500 MHz at 10 kHz bandwidth resolution in Figure 4.32(b) to observe the harmonic frequencies. There was no significant instability observed along the span but negligible fluctuation in the initial harmonic frequencies, which represents the mode-locking stability.

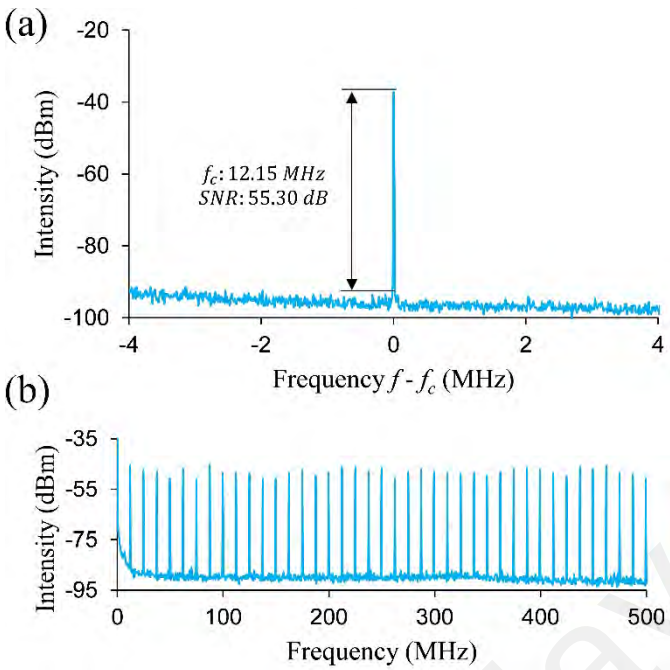

Figure 4.32: RFSA spectrum (a) fundamental frequency, and (b) harmonic frequencies of Nb_2C MXene at 100 mW.

Figure 4.33 shows the plot of the average output power of the mode-locked laser against an increasing pump power from 100 mW to 370 mW. The average output power of the mode-locked laser at the threshold pump power of 100 mW was measured to be 0.29 mW. At the maximum pump power of 370 mW, the average output power increased to 3.07 mW. When the pump power was further increased above 370 mW, the mode-locked pulses disappeared, but appeared back when the pump power was reduced within its operating range. The average output power was directly proportional to the pump power. The disappearance of the mode-locked pulses above 370 mW implied the saturation of Nb_2C MXene. The maximum pulse energy of 0.136 nJ was calculated by dividing the recorded output power by its corresponding repetition rate. The corresponding maximum peak power, P_{max} of 0.073 kW can then be obtained from the maximum pulse energy as described previously.

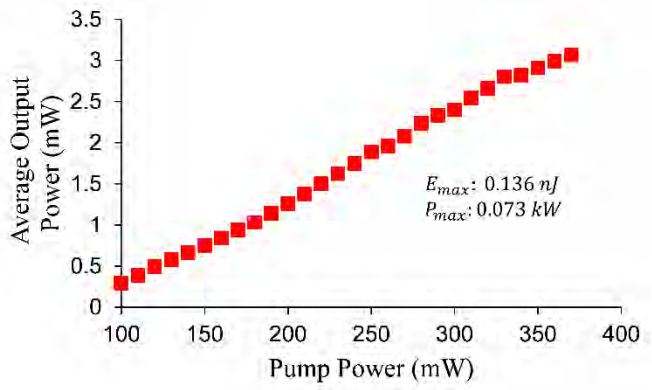

Figure 4.33: The average output power against pump power of the mode-locked TDFL Nb_2C MXene.

To further evaluate the stability of the laser, the mode-locked pulse was monitored in the wavelength and frequency domain over 2 hours at an interval of 10 minutes, as illustrated in Figure 4.34.

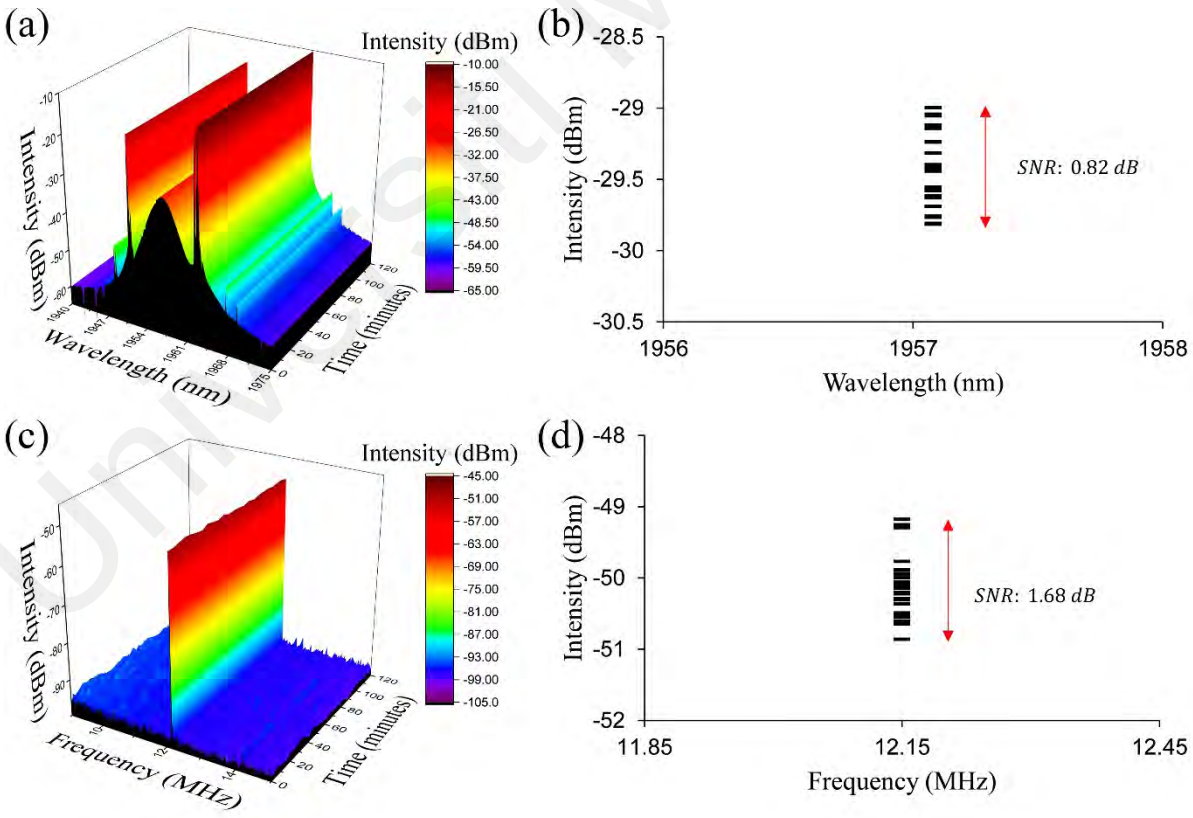

Figure 4.34: Stability of Nb_2C MXene (a) optical spectrum, (b) center wavelength, (c) radio frequency spectrum, and (d) fundamental frequency for 2 hours.

The pump power was maintained at 100 mW during the measurement. No sign of significant wavelength and frequency drifting was detected over the whole period, as appeared in the intensity color variation of Figure 4.34(a) and (c). A single point was selected from each wavelength and radio frequency spectrum data, specifically at the center wavelength and the fundamental frequency. Figures 4.34(b) and (d) show the fluctuation of the single points during the 2 hours. The output power indicates no particular changes as the variation was as little as 0.82 dB and 1.68 dB for the center wavelength and fundamental frequency respectively.

4.5.4 Passive Mode-locked Thulium-doped Silica Fiber Laser by using V_2C Tapered Fiber

The laser cavity with the V_2C-based tapered fiber was first characterized by gradually increasing the pump power, whereby a continuous wave (CW) laser output was observed at a pump power of 80 mW. The CW operation then shifted to a mode-locking process when the pump power increased to 110 mW. To initiate the mode-locking operation, the PC was adjusted to modify the modes in the cavity by altering the polarization states in the laser cavity. The mode-locking process was well sustained until a pump power of 390 mW. Figure 4.35 shows the measured output laser performance at the threshold pump power of 110 mW, in which the mode-locked TDFL was operating in the fundamental harmonic mode-locking. The mode-locked laser optical spectrum had a center wavelength of 1957.08 nm with a FWHM of 3.06 nm, as shown in Figure 4.35(a). Figure 4.35(b) shows the mode-locked pulse train had a pulse interval of 83.89 ns, which corresponds to a repetition rate of 11.92 MHz. Figure 4.35(c) shows the pulse duration of the mode-locked pulse obtained during the autocorrelation measurement, which was fitted with the sech^2 profile. The pulse duration, τ_{AC}, was measured to be 1.70 ps, corresponding to a TBP of 0.407. It was slightly larger than the sech^2 transform-limited TBP value of 0.315, suggesting the output pulse was chirped

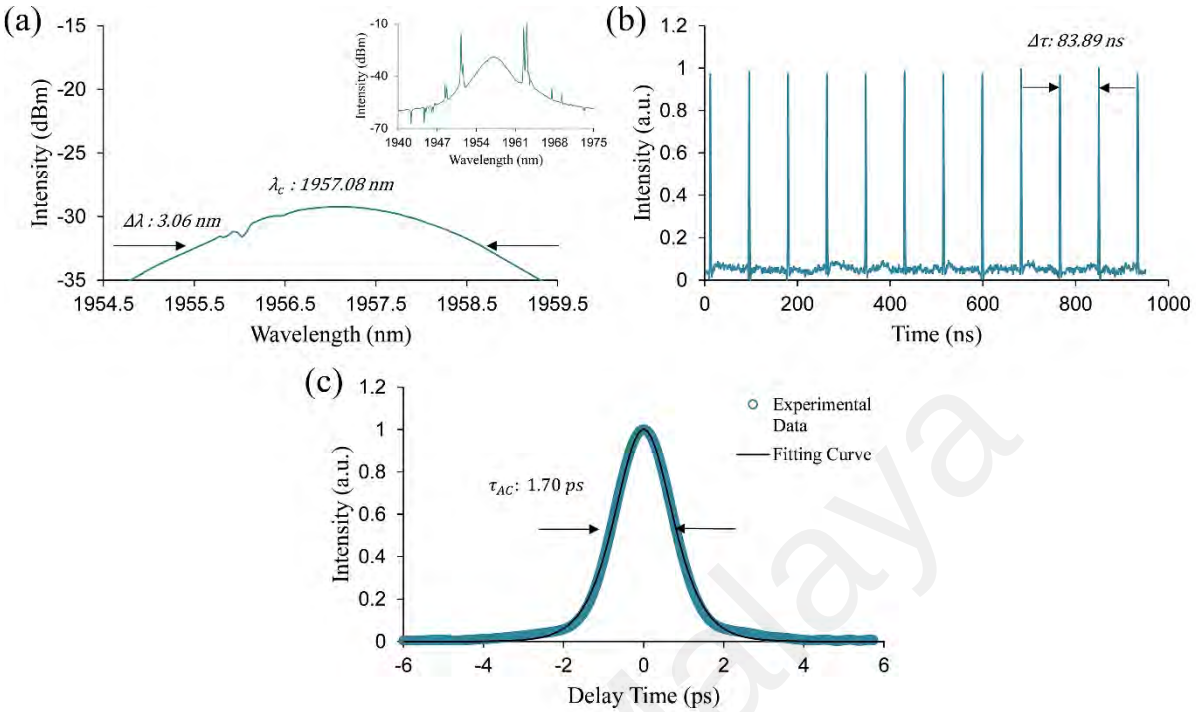

Figure 4.35: (a) Optical spectrum, (b) pulse train, and (c) autocorrelator trace of V_2C MXene at 110 mW.

Furthermore, the mode-locking stability was determined by recording the radio frequency spectrum with a bandwidth resolution of 300 Hz at a pump power of 110 mW. The obtained spectrum in Figure 4.36(a) had a clear peak with a fundamental frequency at 11.92 MHz. The output pulses have a SNR of 45.46 dB, signifying a stable mode-locking pulse. The span of the spectrum was then increased to 500 MHz at 10 kHz bandwidth resolution in Figure 4.36(b) to observe the harmonic frequencies without any significant modulation instability, which further indicates the mode-locking stability.

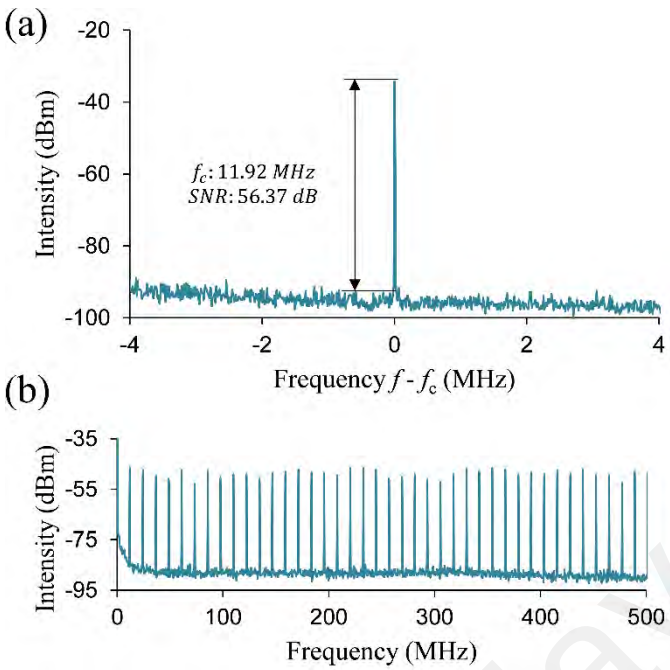

Figure 4.36: RFSA spectrum (a) fundamental frequency, and (b) harmonic frequencies of V_2C MXene at 110 mW.

Figure 4.37 shows the plot of the average output power of the mode-locked laser against an increasing pump power from 110 mW to 390 mW. The average output power of the mode-locked laser at the threshold pump power of 110 mW was measured to be 0.30 mW. At the maximum pump power of 390 mW, the average output power increased to 3.14 mW. When the pump power was further increased above 390 mW, the mode-locked pulses disappeared, but emerged back when the pump power was decreased within its operating range. The average output power was directly proportional to the pump power but barely declined when nearing the maximum pump power denoting the material was approaching its saturation point. The disappearance of the mode-locked pulses above 390 mW indicated the saturation of V_2C MXene. The maximum pulse energy, E_{max} of 0.139 nJ was calculated by dividing the recorded output power by its corresponding pulse repetition rate. The corresponding maximum peak power, P_{max} of 0.074 kW can then be obtained from the maximum pulse energy.

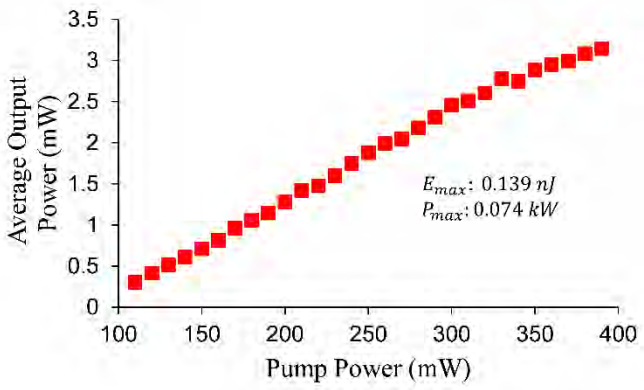

Figure 4.37: The average output power against pump power of the mode-locked TDFL V_2C MXene.

To further evaluate the stability of the laser, the mode-locked pulse was monitored in the wavelength and frequency domain over 2 hours at an interval of 10 minutes, as illustrated in Figure 4.38.

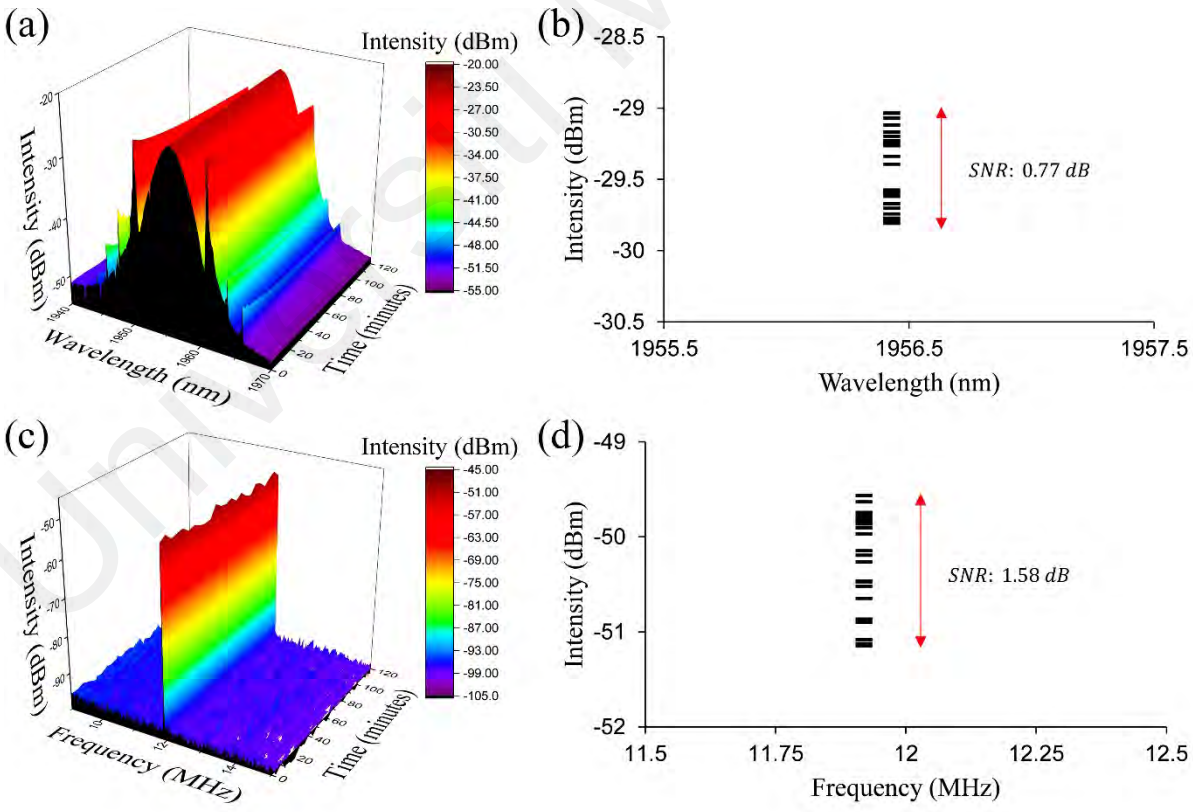

Figure 4.38: Stability of V_2C MXene (a) optical spectrum, (b) λ_c, (c) radio frequency spectrum, and (d) f_c for 2 hours.

The pump power was kept at 110 mW during the measurement. No sign of significant wavelength and frequency shifting was observed during the whole period, as appeared in the intensity color variation of Figure 4.38(a) and (c). A single point was selected from each wavelength and radio frequency spectrum data, particularly at the center wavelength and the fundamental frequency. Figures 4.38(b) and (d) show the fluctuation of the single points during the 2 hours. The output power indicates no pronounced changes as the fluctuation was as small as 0.77 dB and 1.58 dB for the center wavelength and fundamental frequency, respectively.

4.5.5 Performance Comparison of Molten Fluoride Salt-Assisted MXenes Mode-locked Fiber Laser

In this section, the generation of mode-locked pulsed fiber laser has been successfully demonstrated by using all of the MXene SAs, those are Ti_2C, Nb_2C, and V_2C. Unlike Q-switched laser, the formation of mode-locked laser not only occurs due to the absorption properties of the SAs, but also occurs due to the in-phase modes constructive interference in which frequency corresponds to the laser cavity round trip time. The MXenes SAs were incorporated into the systems by using tapered fiber as the host. All of the mode-locked fiber lasers generated at about 1950 nm center wavelength, which V_2C hold the longest wavelength at 1956.43 nm as shown in Table 4.6. As the absorption of SAs quickly decline and saturates when the optical intensity increase, optical signal is then allowed to transmit. Low non-saturable loss of the SA and low total loss of the cavity can contribute to the high pulse repetition rate; however, it is limited by the length of the cavity. Among the MXenes, Ti_2C has the lowest pulse repetition rate, while Nb_2C has the highest pulse repetition rate. This is due to the Ti_2C has a remarkably higher non-saturable loss than Nb_2C. Nevertheless, the pulse repetition rate of all of the MXenes are approximately the same because they were taken at the fundamental harmonic frequency.

Table 4.5: Mode-locked characteristics of all molten fluoride salt-assisted MXenes.

Properties \ MXenes		Ti_2C	Nb_2C	V_2C
Linear Absorption, α_0 (%)		54.06	51.39	52.35
Nonlinear Absorption	**Saturable absorption, α_s (%)**	14.78	20.34	18.71
	Non-saturable absorption, α_{ns} (%)	57.32	34.04	34.87
	Saturation intensity, I_{sat} (MW/cm^2)	0.402	0.528	0.471
Center Wavelength, λ_c (nm)		1951.13	1957.08	1956.43
Bandwidth, $\Delta\lambda$ (nm)		2.88	3.54	3.06
Repetition Rate, f_c (MHz)		11.30	12.15	11.92
Pulse Width, τ_{AC} (ps)		1.72	1.67	1.70
Pulse Energy, E_{max} (nJ)		0.112	0.136	0.139
Peak Power, P_{max} (kW)		0.060	0.073	0.074

Conversely, high saturable absorption can lead to a short pulse width and wider bandwidth as mentioned by Churin et al. in their investigation on the effect of SAs in mode-locked fiber laser (Churin et al., 2012). Nb_2C has the shortest pulse width which agree with its highest saturable absorption as compared to the others. On the contrary, Ti_2C has the longest pulse width among the others as it has the lowest saturable absorption. In addition, the FWHM (bandwidth) of the mode-locked laser spectrum is the widest from Nb_2C, while the shortest is from Ti_2C as anticipated by Churin et al. Lastly, V_2C has the highest pulse energy and approximately the same as Nb_2C, whereby Ti_2C has the lowest pulse energy. V_2C also hold the highest in term of peak power as compared to

the other two per anticipated from the given pulse energy, with Ti_2C hold the lowest peak power.

Additionally, a comparison with the other experimental results of SA at the same operating region in literature is given in Table 4.6. In the table, all of the other SAs have higher repetition rate as compared to the MXene SAs presented in this works. However, there are possibilities of higher harmonic repetition rate being reported as the literatures don't specifically mention the harmonic. Oppositely, the MXene SAs in this work show higher output power than the other SAs with V_2C records the highest of 3.14 mW as compared to graphene, which records the lowest of 1.41 mW. Naturally, with lower repetition rate and higher output power, MXene SAs of this work have higher pulse energy. Therefore, V_2C has a pulse energy of 0.139 nJ, which records the highest pulse energy as compared to the others. Whereby, WS_2 has a pulse energy of 0.0172 nJ, which records the lowest relative to the others. Nevertheless, GO displays the shortest pulse width of 0.59 ps, while graphene displays the longest pulse width of 2.1 ps. Nonetheless, MXene SAs of this work manifest average pulse width as compared to the others, thus, this comparison shows the MXene SAs fabricated in this work are on par with the other SAs with more capacity to be developed.

Table 4.6: Performance summary of 2 μm mode-locked of other SAs with molten fluoride salt-assisted MXenes.

SA	Repetition Rate (MHz)	Output Power (mW)	Pulse Energy (nJ)	Pulse Width (ps)	FWHM Bandwidth (nm)	Center Wavelength (nm)	Reference
Graphene	16.93	1.41	0.081	2.1	2.2	1953.3	(Q. Wang et al., 2013)
BP	36.8	1.5	0.0407	0.739	5.8	1910	(Q. Wang et al., 2013)
CNT	21.05	2.3	0.109	0.9730	4.2	1950	(Yanping Chen et al., 2017)
GO	33.6	-	4.3	0.59	6.9	1950	(Jung et al., 2013)
WS_2	34.8	0.6	0.0172	1.3	5.6	1941	(Jung et al., 2015)

Table 4.6, continued.

SA	Repetition Rate (MHz)	Output Power (mW)	Pulse Energy (nJ)	Pulse Width (ps)	FWHM Bandwidth (nm)	Center Wavelength (nm)	Reference
Ti_2C	11.3	2.54	0.112	1.67	2.88	1951.13	This work
Nb_2C	12.15	3.07	0.136	1.72	3.54	1957.08	
V_2C	11.92	3.14	0.139	1.7	3.06	1956.43	

CHAPTER 5: FOUR WAVE MIXING AND ALL-OPTICAL MODULATOR OF MOLTEN FLUORIDE SALT-ASSISTED MXENES.

5.1 Generation of FWM by using Molten Fluoride Salt-Assisted MXenes

5.1.1 Experimental Configuration of FWM Generation

The experimental configuration of FWM generation incorporating MXene-based tapered fiber as saturable absorber is shown in Figure 5.1.

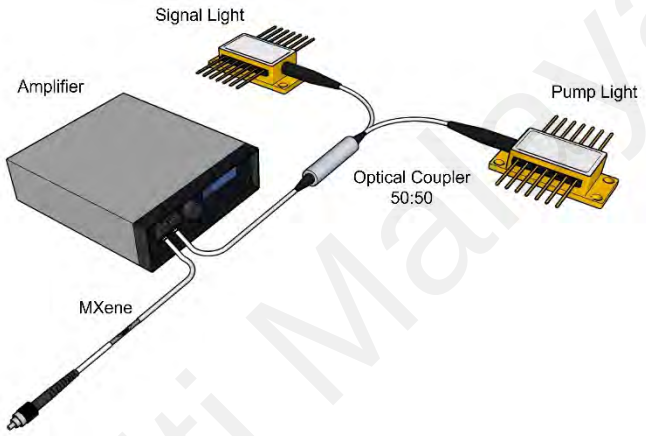

Figure 5.1: Schematic diagram of FWM generation by using MXene-based tapered fiber.

Two external cavity lasers were used to pump the MXene that acted as pump light and signal light at wavelength of 1999.5 nm and 2000.1 nm, respectively. Both of the light beams were kept at equivalent power and combined by using a 1×2 50:50 OC. The output from the OC was amplified by using 2 μm amplifier to a maximum power of 34 dBm. The amplified light was injected into the MXene-based tapered fiber with measured length of about 2.5 cm that acted as a nonlinear medium to give rise to the FWM effect. The opposite end of the tapered fiber was attenuated to be less than 10 dBm by using a fixed attenuator as a safety measure for the OSA that was used to analyze the optical spectrum. The MXene underwent interaction with the evanescent field of the light at the

tapered area, which this mechanism is favourable to exploit the interaction length with the nonlinear material. The FWM conversion efficiency, η can be defined by the following expression (Agrawal, 2000) with short interaction length and short pump/signal wavelength interval are considered

$$\eta(L) = \eta_2 \times P_{pump}^2 \times L \tag{5.1}$$

where L is the interaction length, η_2 represents the nonlinear refractive index, and P_{pump} is the pump power.

5.1.2 Generation of Four-Wave Mixing by using Ti_2C

The amplified light beams from both signal and pump light at 34 dBm input power with about 0.5 nm wavelength spacing generating FWM is presented in Figure 5.2. The tapered fiber was initially injected with the light beams at the same power to observe any response. Two new apparent wavelengths known as idlers, λ_3 and λ_4 were produced from the bare tapered fiber at 1999 nm and 2000.7 nm. This was due to the increase in fiber nonlinearity after the tapering process that reduced the fiber core diameter. The generated idlers fulfilled the FWM interaction of $1/\lambda_1 + 1/\lambda_2 = 1/\lambda_3 + 1/\lambda_4$, thus confirmed their existence by the FWM effect.

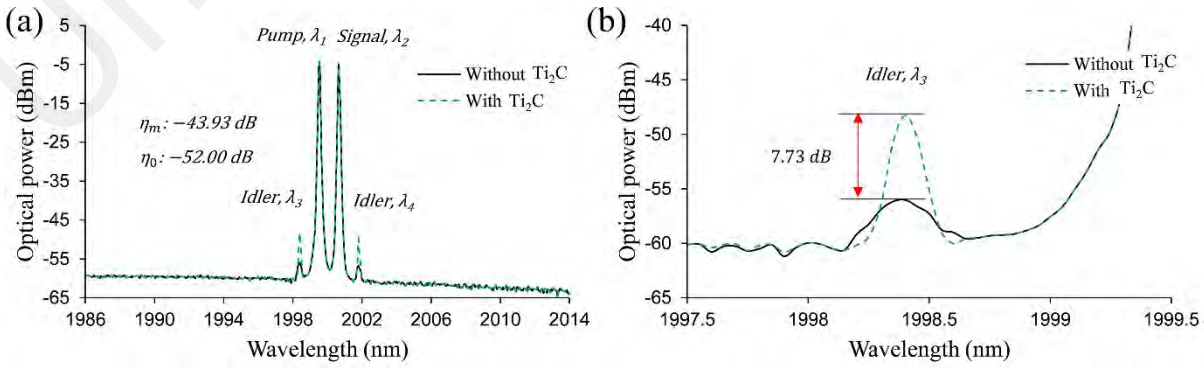

Figure 5.2: Optical spectrum of the (a) generated idlers, and (b) SNR of λ_3 based on the FWM effect by the Ti_2C-based tapered fiber.

However, after the deposition of Ti_2C MXene onto the tapered fiber, the idlers were increased by 7.73 dB as shown in Figure 5.2(b). The ratio of light power of the newly generated wavelength to the input signal power is described as the FWM conversion efficiency (Agrawal, 2000). The FWM conversion efficiency, η_m was significantly enhanced by 8.07 dB at -43.93 dB as compared to the original FWM conversion efficiency, η_0 of -52 dB in the bare tapered fiber as presented in Figure 5.2(a).

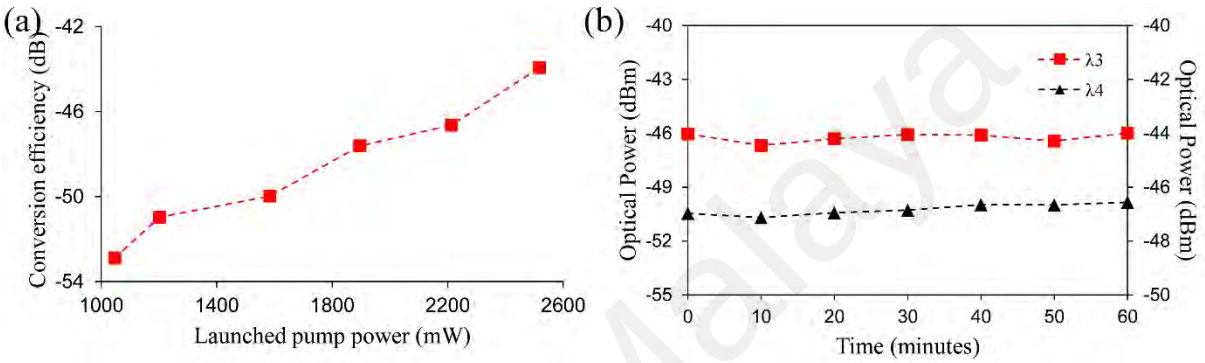

Figure 5.3: Ti_2C-based tapered fiber (a) FWM conversion efficiency against launched input power, and (b) stability of λ_3 and λ_4 over 1 hour.

In addition, the relationship of input power with FWM conversion efficiency, and the stability of generated idlers were explored as shown in Figure 5.3. It can be seen in Figure 5.3(a) that the conversion efficiency was proportional with the square of the pump power. When the pump power was approximately 1 W, the conversion efficiency was about -52.90 dB. Whilst at the maximum pump power of about 2.6 W, the conversion efficiency was -43.93 dB. Furthermore, the peak power of both λ_3 and λ_4 fluctuated not more than 0.68 dB and 0.57 dB during the whole period as in Figure 5.3(b), suggesting stable generated idlers.

5.1.3 Generation of Four-Wave Mixing by using Nb_2C

The amplified light beams from both signal and pump light at 34 dBm input power with about 0.5 nm wavelength spacing generating FWM is presented in Figure 5.4. In the

beginning, the tapered fiber was injected with the light beams at the same power to observe any response. Two new apparent wavelengths known as idlers, λ_3 and λ_4 were produced from the bare tapered fiber at 1999 nm and 2000.7 nm. This was due to the increase in fiber nonlinearity after the tapering process that reduced the fiber core diameter. The generated idlers fulfilled the FWM interaction of $1/\lambda_1 + 1/\lambda_2 = 1/\lambda_3 + 1/\lambda_4$, thus confirmed their existence by the FWM effect.

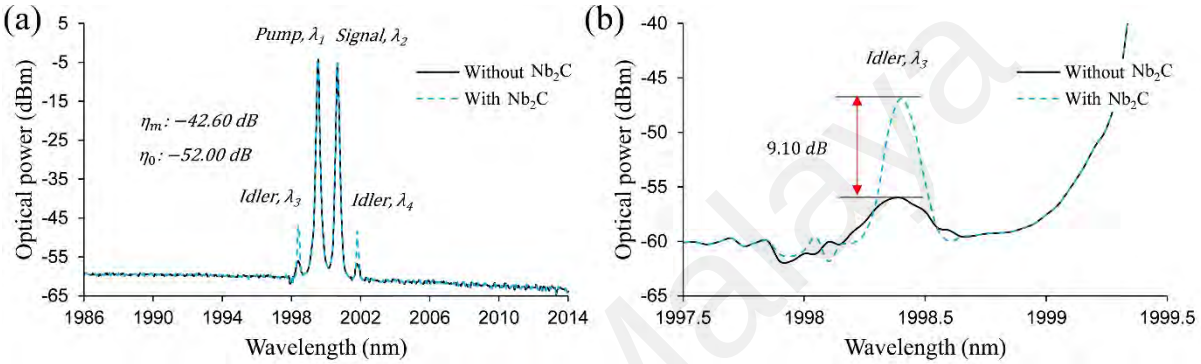

Figure 5.4: Optical spectrum of (a) generated idlers, and (b) SNR of λ_3 based on the FWM effect by the Nb_2C-based tapered fiber.

Nonetheless, after the deposition of Nb_2C MXene onto the tapered fiber, the idlers were increased by 9.10 dB as shown in Figure 5.4(b). The FWM conversion efficiency, η_m was significantly enhanced by 9.40 dB at -42.60 dB as compared to the original FWM conversion efficiency, η_0 of -52 dB in the bare tapered fiber as presented in Figure 5.4(a).

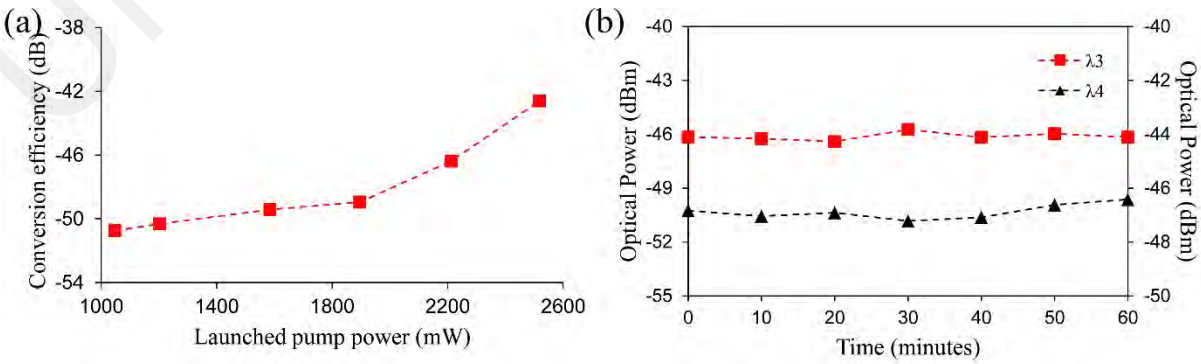

Figure 5.5: Nb_2C-based tapered fiber (a) FWM conversion efficiency against launched input power, and (b) stability of λ_3 and λ_4 over 1 hour.

Moreover, the relationship of input power with FWM conversion efficiency, and the stability of generated idlers were explored as shown in Figure 5.5. It can be seen in Figure 5.5(a) that the conversion efficiency was proportional with the square of the pump power. When the pump power was approximately 1 W, the conversion efficiency was about -50.75 dB. Whilst at the maximum pump power of about 2.6 W, the conversion efficiency was -42.61 dB. Furthermore, the peak power of both λ_3 and λ_4 fluctuated not more than 0.68 dB and 0.80 dB during the whole period as can be seen in Figure 5.5(b), suggesting stable generated idlers.

5.1.4 Generation of Four-Wave Mixing by using V_2C

The amplified light beams from both signal and pump light at 34 dBm input power with about 0.5 nm wavelength spacing generating FWM is presented in Figure 5.6. In the beginning, the tapered fiber was injected with the light beams at the same power to observe any response. Two new apparent wavelengths known as idlers, λ_3 and λ_4 were produced from the bare tapered fiber at 1999 nm and 2000.7 nm. The reduction of the fiber core diameter during tapering process resulted in increasing in the fiber nonlinearity, particularly third-order nonlinearity that associates with FWM. The generated idlers realized the FWM interaction of $1/\lambda_1 + 1/\lambda_2 = 1/\lambda_3 + 1/\lambda_4$, thus validated their existence by the FWM effect.

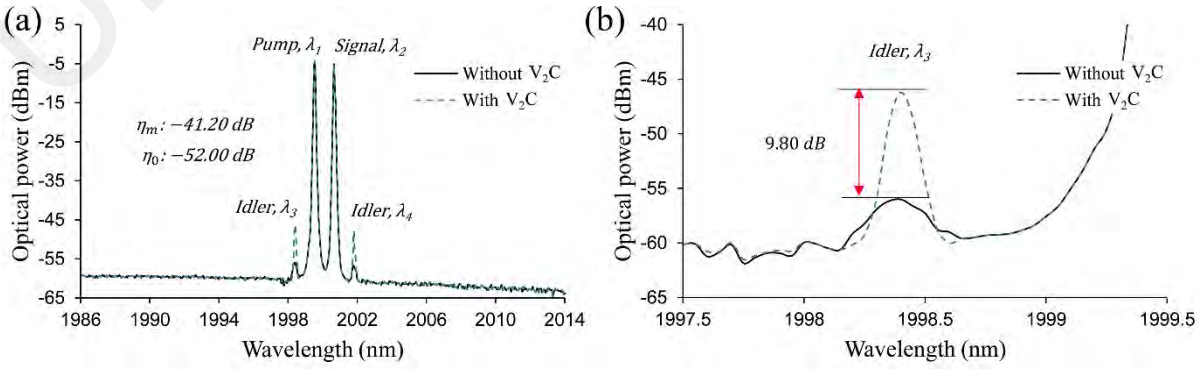

Figure 5.6: Optical spectrum of (a) generated idlers, and (b) SNR of λ_3 based on the FWM effect by the V_2C-based tapered fiber.

However, after the deposition of V_2C MXene onto the tapered fiber, the idlers were risen by 9.80 dB as shown in Figure 5.6(b). The FWM conversion efficiency, η_m was significantly enhanced by 10.80 dB at -41.20 dB as compared to the original FWM conversion efficiency, η_0 of -52 dB in the bare tapered fiber as presented in Figure 5.6(a).

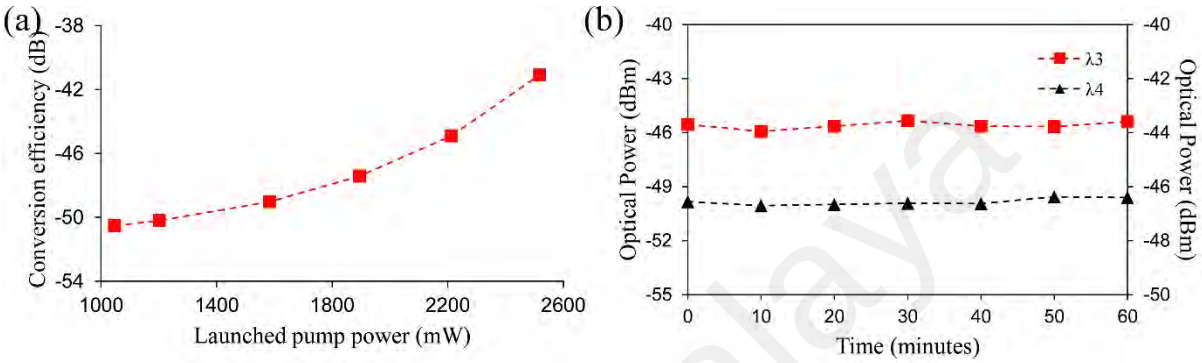

Figure 5.7: V_2C-based tapered fiber (a) FWM conversion efficiency against launched input power, and (b) stability of λ_3 and λ_4 over 1 hour.

The relationship of input power with FWM conversion efficiency, and the stability of generated idlers were analyzed as shown in Figure 5.7. It can be seen in Figure 5.7(a) that the conversion efficiency was proportional with the square of the pump power. When the pump power was approximately 1 W, the conversion efficiency was about -50.52 dB. Whilst at the maximum pump power of about 2.6 W, the conversion efficiency was -41.08 dB. Furthermore, the peak power of both λ_3 and λ_4 fluctuated not more than 0.60 dB and 0.32 dB during the whole period as presented in Figure 5.7(b), suggesting stable generated idlers.

5.1.5 Performance Comparison of Molten Fluoride Salt-Assisted MXenes FWM

In this section, the generation of FWM has been successfully demonstrated by using all of the MXene SAs, those are Ti_2C, Nb_2C, and V_2C. The nonlinear refractive index of MXene plays important role in the generation of FWM. In Table 5.1, V_2C possesses the highest nonlinear refractive index as compared to the others, while Nb_2C comes in second.

The nonlinear refractive index of all of the MXenes are at the magnitudes of around -17 to -16. As should be anticipated by the values, V_2C has the highest conversion efficiency of FWM, where the idler was increased by 9.80 dB. Ti_2C has the lowest conversion efficiency with idler increment of 7.73 dB, while Nb_2C has the second highest conversion efficiency with idler increment of 9.10 dB. The value of the nonlinear refractive index of these MXenes are comparable to the work that has been done by Jiang et al. (X. Jiang et al., 2018) but significantly different from the work of Wu et al. (L. Wu et al., 2018) due to the different techniques in characterizing the materials, whereby, Jiang et al. employed Z-scan technique, while Wu et al. employed spatial self-phase modulation (SSPM).

Table 5.1: FWM characteristics of all molten fluoride salt-assisted MXenes.

MXenes / **Properties**	**Ti_2C**	**Nb_2C**	**V_2C**
Nonlinear Absorption Coefficient, β (m/W)	3.48×10^{-10}	4.82×10^{-10}	5.11×10^{-10}
Nonlinear Refractive Index, n_2 (m^2/W)	3.28×10^{-17}	8.11×10^{-17}	1.27×10^{-16}
Idler SNR, $\Delta\lambda$ (dB)	7.73	9.10	9.80
Conversion Efficiency, η_m (dB)	-43.93	-42.60	-41.20
Conversion Efficiency Difference, $\Delta\eta$ (dB)	8.07	9.40	10.80

Additionally, the performance of the molten fluoride salt-assisted MXenes in the generation of FWM effect are compared with the other nonlinear materials in Table 5.2. From the previous works, CNT, graphene, and $MoTe_2$ have higher conversion efficiency than this work, which are -31 dB, -30 dB, and -38 dB, respectively. Nevertheless, BP, antimone, and Ti_3C_2 recorded lower conversion efficiency than this work, which

are -60 dB, -65 dB, and -59 dB. The fabricated MXenes in this work report higher conversion efficiency than the Ti_3C_2 MXene from the previous report to about 10 dB difference. This suggest the advantages to produce high nonlinear material MXene with low chemical ratio formula and in-situ HF fabrication.

Table 5.2: Performance comparison of nonlinear material-based FWM system.

Nonlinear Material	Wavelength (μm)	Conversion Efficiency (dB)	Reference
CNT	1.5	-31	(Chow & Yamashita, 2009)
Graphene	1.5	-30	(Y. Wu et al., 2013)
BP	1.5	-60	(J. Zheng et al., 2017)
Antimonene	1.5	-65	(Y. Song et al., 2018)
$MoTe_2$	1.5	-38	(H Ahmad, Zaini, et al., 2021)
Ti_3C_2	1.5	-59	(Y. Song et al., 2019)
Ti_2C	2.0	-43.93	This work
Nb_2C	2.0	-42.60	
V_2C	2.0	-41.20	

5.2 Optical Modulation by using Molten Fluoride Salt-Assisted MXenes

5.2.1 Experimental Configuration of All-Optical Modulator

The experimental configuration of all-optical modulator incorporating MXene thin film is portrayed in Figure 5.8.

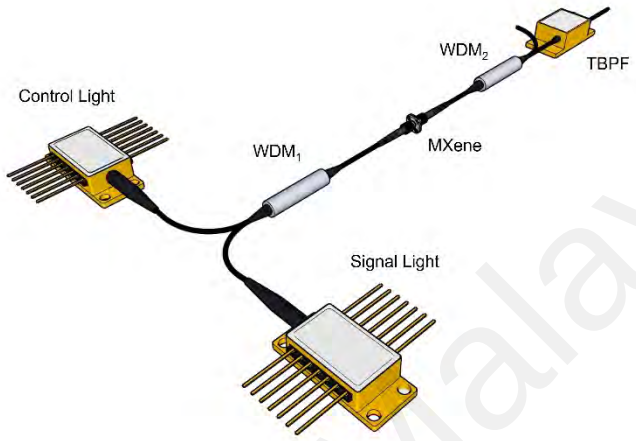

Figure 5.8: Schematic diagram of all-optical modulator by using MXene thin film.

A 793 nm LD and a 2000 nm CW laser source with fixed center wavelength were used as control and signal light. Both of the light sources were coupled by using 793/2000 nm WDM, where the control light was chosen based on the availability of component. Two WDM labelled WDM_1 and WDM_2 were utilized in the configuration, which WDM_1 combined the control and signal light, whilst WDM_2 filtered out the control light from the output. Hence, leaving only the modulated signal light to be analyzed. Additionally, a tunable bandpass filter (TBPF) was attached at the 2000 nm port of WDM_2 to remove entirely any control light leakage. The TBPF has a 1 nm bandwidth and insertion loss of 2.80 dB. Lastly, the MXene thin film was incorporated at the common port of the WDMs to act as optical modulator.

5.2.2 Optical Modulation by using Ti_2C

The modulation characteristic of Ti_2C all-optical modulator was initially identified by introducing CW signal light at 2000 nm with modulated control light at 793 nm into the Ti_2C thin film, while maintaining the optical power of the control and signal light at 8 mW and 5 mW, respectively. The frequency of control light was adjusted at 1 kHz with a duty cycle of 50% as portrayed in Figure 5.9(a). The oscilloscope trace of both of the input control light and the output modulated signal light were also shown in the figure. A successful modulation was verified when the modulated signal light possessed similar duty cycle and frequency as the control light. Furthermore, the modulated signal light dropped to baseline noise when the CW signal light was turned off. However, the leading and trailing edges of the modulated signal light appeared smoother as compared to the control light, showing a time delay between the lower and upper amplitudes interchange as shown in Figure 5.9(b).

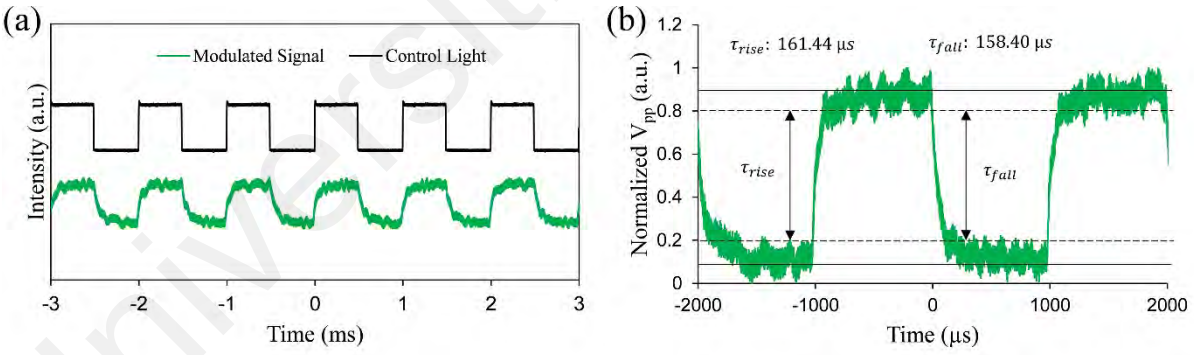

Figure 5.9: (a) Modulated control light and signal light, and (b) rising time, τ_{rise} and falling time, τ_{fall} of Ti_2C thin film modulated signal light.

When the control light reached Ti_2C thin film, the light was absorbed by the Ti_2C atoms. The atoms occupied the excited state of Ti_2C until a saturation point with time τ_{rise}. At this point, the Ti_2C became translucent to the signal light, thus allowing the signal light to pass through the thin film. When the control light was turned off, which is described by the lower amplitude in Figure 5.9, the atoms at the excited state returned to

the ground state with time τ_{fall}. During this point, the Ti_2C became opaque to the signal light, hence blocking the signal light from passing through. Therefore, the rise time, τ_{rise} and fall time, τ_{fall} are in fact describing the time it takes for the atoms to fully occupy the excited state until become translucent to the signal light and the excited atoms to fully return to the ground state to become opaque again to the signal light. The τ_{rise} and τ_{fall} of the modulated signal light were measured to be 161.44 µs and 158.40 µs, respectively.

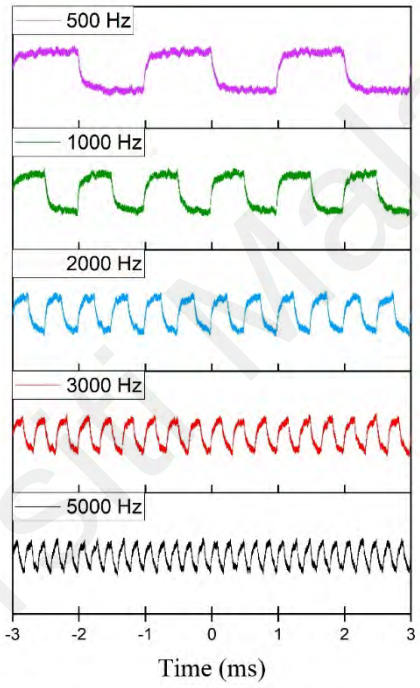

Figure 5.10: Modulated signal light of Ti_2C thin film at various frequencies.

The frequency of the control light was varied to observe the frequency response dependence. The emerging output waveform of the modulated signal light was successfully modified up to a frequency of 5 kHz as displayed in Figure 5.10. At a higher frequency, the modulated signal degraded by diminishing its amplitude and distorting its shape into sharp edges, thus providing difficulties to detect its frequency. This is due to the modulating frequency dominates the rising and falling time of the material.

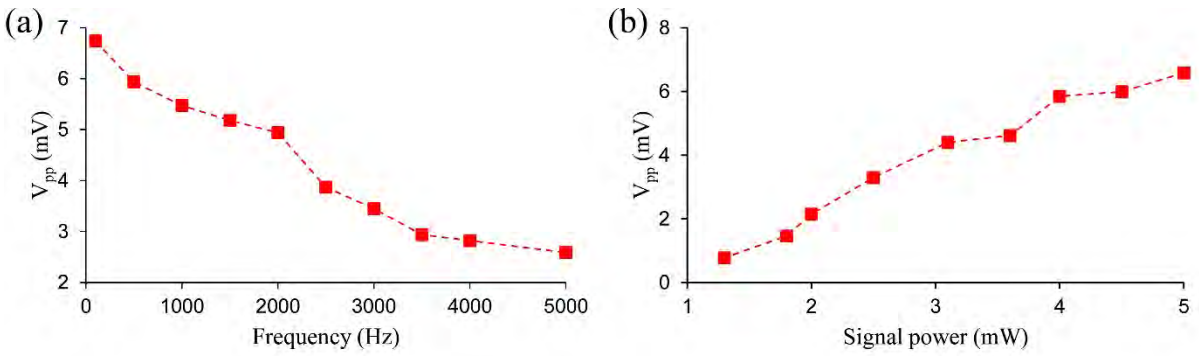

Figure 5.11: V_{pp} Ti_2C thin film against (a) frequency, and (b) signal power.

Figure 5.11(a) displays the relationship of peak-to-peak voltage, V_{pp} and modulation frequency. The V_{pp} is inversely proportional to the modulation frequency, where the V_{pp} was 6.74 mV at the lowest frequency of 100 Hz, while the V_{pp} value dropped to 2.59 mV at the frequency of 5 kHz. Lastly, the reading of V_{pp} was also recorded by increasing the signal power as shown in Figure 5.11(b). At the minimum signal power of 1.3 mV, the V_{pp} of the modulated signal was 0.77 mV, while when the signal power was increased to 5 mV, the V_{pp} was 6.59 mV. Thus, the V_{pp} of the modulated signal depended on both of the signal power and modulation frequency.

5.2.3 Optical Modulation by using Nb_2C

The modulation characteristic of Nb_2C all-optical modulator was initially identified by introducing CW signal light at 2000 nm with modulated control light at 793 nm into the Nb_2C thin film, while maintaining the optical power of the control and signal light at 8 mW and 5 mW, respectively. The frequency of control light was adjusted at 1 kHz with a duty cycle of 50% as portrayed in Figure 5.12(a). The oscilloscope trace of both of the input control light and the output modulated signal light were shown in the figure. A successful modulation was verified when the modulated signal light possessed similar duty cycle and frequency as the control light. Furthermore, the modulated signal light dropped to baseline noise when the CW signal light was turned off. However, the leading

and trailing edges of the modulated signal light appeared smoother as compared to the control light, showing a time delay between the lower and upper amplitudes interchange as shown in Figure 5.12(b).

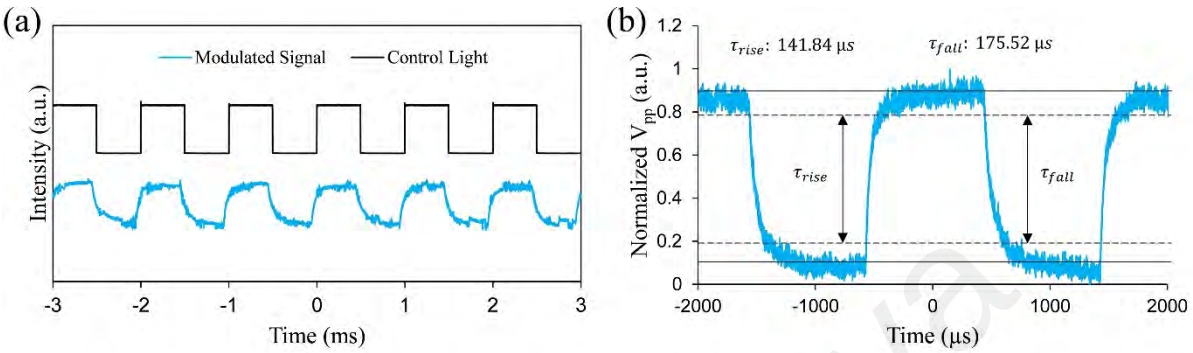

Figure 5.12: (a) Modulated control light and signal light, and (b) rising time, τ_{rise} and falling time, τ_{fall} of Nb_2C thin film modulated signal light.

When the control light reached Nb_2C thin film, the light was absorbed by the Nb_2C atoms. The atoms occupied the excited state of Nb_2C until a saturation point with time τ_{rise}. At this point, the Nb_2C became transparent to the signal light, thus allowing the signal light to pass through the thin film. When the control light was turned off, which is described by the lower amplitude in Figure 5.12, the atoms at the excited state returned to the ground state with time τ_{fall}. Right at this time, the Nb_2C became opaque to the signal light, hence blocking the signal light from passing through. The rising time, τ_{rise} and falling time, τ_{fall} outline the time taken for the atoms to fully occupy the excited state until saturation point to become translucent to the signal light and the excited atoms to fully return to the ground state to become opaque to the signal light. The τ_{rise} and τ_{fall} of the modulated signal light were measured to be 141.84 µs and 175.52 µs, respectively.

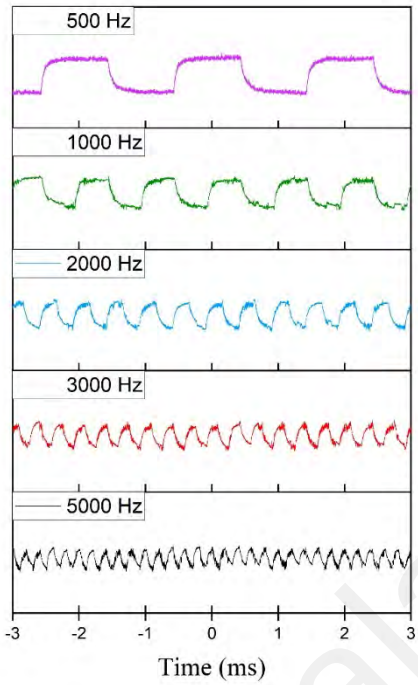

Figure 5.13: Modulated signal light of Nb_2C thin film at various frequencies.

The frequency of the control light was varied to observe the frequency response dependence. The emerging output waveform of the modulated signal light was successfully modified up to a frequency of 5 kHz as displayed in Figure 5.13. At a higher frequency, the modulated signal degraded by diminishing its amplitude and distorting its shape into sharp edges, thus providing difficulties to detect its frequency. This is due to the modulating frequency dominates the rising and falling time of the material.

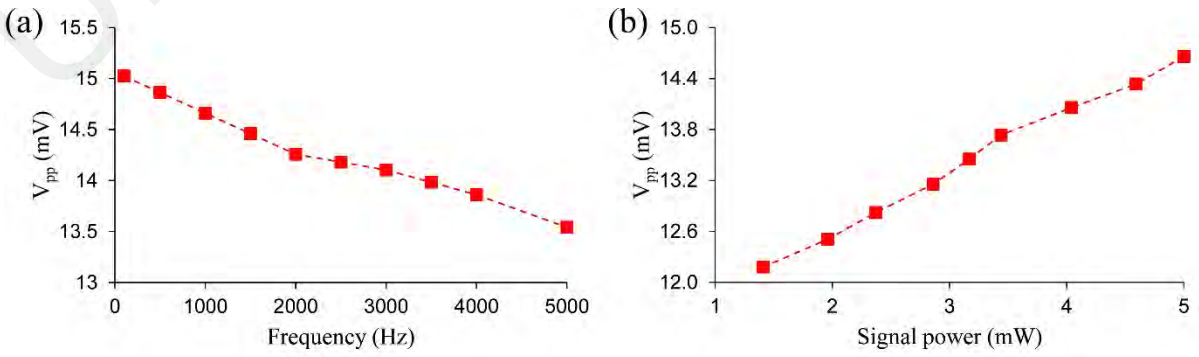

Figure 5.14: V_{pp} Nb_2C thin film against (a) frequency, and (b) signal power.

Figure 5.14(a) displays the relationship of peak-to-peak voltage, V_{pp} and modulation frequency. The V_{pp} is inversely proportional to the modulation frequency, where the V_{pp} was 15.02 mV at the lowest frequency of 100 Hz, while the V_{pp} value dropped to 13.54 mV at the frequency of 5 kHz. Lastly, the reading of V_{pp} was also recorded by increasing the signal power as shown in Figure 5.14(b). At the minimum signal power of 1.41 mV, the V_{pp} of the modulated signal was 12.18 mV, while when the signal power was increased to 5 mV, the V_{pp} was 14.66 mV. Thus, the V_{pp} of the modulated signal depended on both of the signal power and modulation frequency but in inversed relation.

5.2.4 Optical Modulation by using V_2C

The modulation characteristic of V_2C all-optical modulator was initially identified by introducing CW signal light at 2000 nm with modulated control light at 793 nm into the V_2C thin film, while maintaining the optical power of the control and signal light at 8 mW and 5 mW, respectively. The frequency of control light was adjusted at 1 kHz with a duty cycle of 50% as portrayed in Figure 5.15(a). The oscilloscope trace of both of the input control light and the output modulated signal light were shown in the figure. A successful modulation was verified when the modulated signal light possessed similar duty cycle and frequency as the control light. Furthermore, the modulated signal light dropped to baseline noise when the CW signal light was turned off. However, the leading and trailing edges of the modulated signal light appeared smoother as compared to the control light, showing a time delay between the lower and upper amplitudes interchange as shown in Figure 5.15(b).

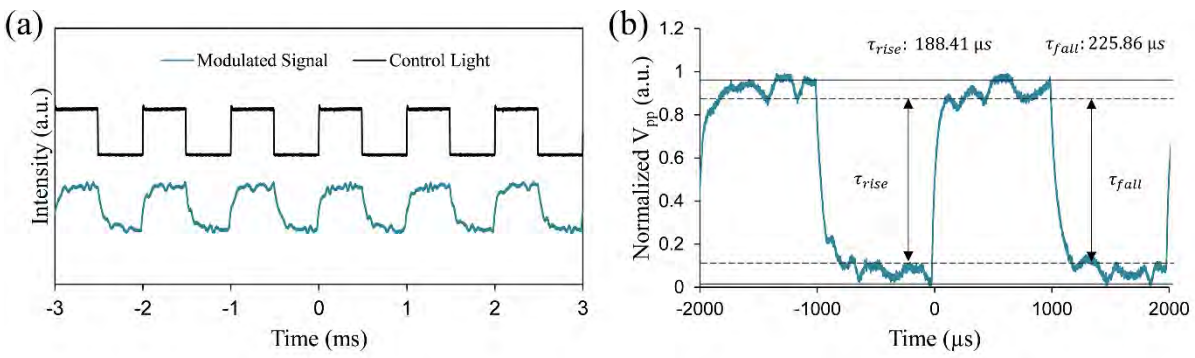

Figure 5.15: (a) Modulated control light and signal light, and (b) rising time, τ_{rise} and falling time, τ_{fall} of V_2C thin film modulated signal light.

When the control light reached V_2C thin film, the light was absorbed by the V_2C atoms. The atoms occupied the excited state of V_2C until a saturation point with time τ_{rise}. At this point, the V_2C became transparent to the signal light, thus allowing the signal light to pass through the thin film. When the control light was turned off, which is described by the lower amplitude in Figure 5.15, the atoms at the excited state returned to the ground state with time τ_{fall}. At this moment, the V_2C became opaque to the signal light, hence blocking the signal light from passing through. Therefore, the occupying time for the atoms to go to the excited state until saturation point to become translucent to the signal light and the returning time for the atoms from the excited state to the ground state to become opaque to the signal light again are described by the rising time, τ_{rise} and falling time, τ_{fall}, respectively. The τ_{rise} and τ_{fall} of the modulated signal light were measured to be 188.41 µs and 225.86 µs, respectively.

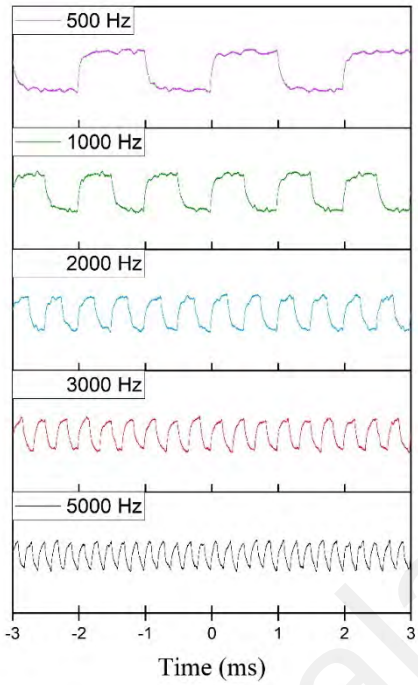

Figure 5.16: Modulated signal light of V_2C thin film at various frequencies.

The frequency of the control light was varied to observe the frequency response dependence. The emerging output waveform of the modulated signal light was successfully modified up to a frequency of 5 kHz as displayed in Figure 5.16. At a higher frequency, the modulated signal degraded by diminishing its amplitude and distorting its shape into sharp edges, thus providing difficulties to detect its frequency.

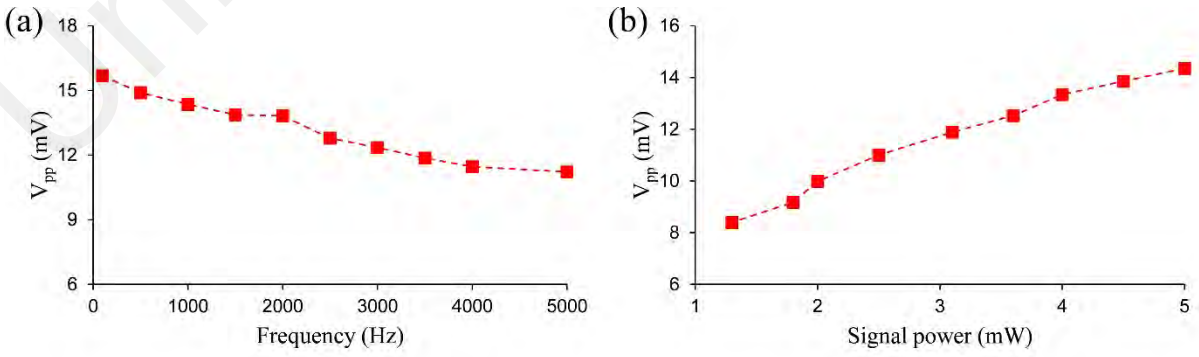

Figure 5.17: V_{pp} V_2C thin film against (a) frequency, and (b) signal power.

Figure 5.17(a) displays the relationship of peak-to-peak voltage, V_{pp} and modulation frequency. The V_{pp} is inversely proportional to the modulation frequency, where the V_{pp} was 15.68 mV at the lowest frequency of 100 Hz, while the V_{pp} value dropped to 11.22 mV at the frequency of 5 kHz. Lastly, the reading of V_{pp} was also recorded by increasing the signal power as shown in Figure 5.17(b). At the minimum signal power of 1.3 mV, the V_{pp} of the modulated signal was 8.4 mV, while when the signal power was increased to 5 mV, the V_{pp} was 14.36 mW. Thus, the V_{pp} of the modulated signal depended on both of the signal power and modulation frequency but in inversed relation.

5.2.5 Performance Comparison of Molten Fluoride Salt-Assisted MXenes Optical Modulation

In this section, the generation of all-optical modulation has been successfully demonstrated by using all of the MXene SAs, those are Ti_2C, Nb_2C, and V_2C. The optical modulation in this work are based on the saturable absorption effect, where the MXenes become translucent to the signal light when the control light pumps the atoms in the ground state to the excited state until saturation point. When the control light is off, the atoms in the excited state return to the ground state and become opaque again to the signal light. As such, high saturable absorption should have the longer rising time and falling time in general.

Nb_2C has the highest saturable absorption, but the rising time is the fastest as compared to the others, this may be due to the lowest non-saturable absorption. Besides, V_2C has the second highest saturable absorption but has longer rising time than Nb_2C, which can be attributed to the slightly higher non-saturable absorption. Lastly, Ti_2C has the second fast rising time, which was anticipated to be the fastest but was hampered by the highest non-saturable absorption. Nonetheless, Ti_2C has the fastest falling time, this could be due

to the fast recovery time of the atoms. On the other hand, V_2C has the slowest falling time suits to the saturable and non-saturable absorption properties, and probably supported by its slow recovery time. Finally, Nb_2C has the second longest falling time next to V_2C due to the slightly lower non-saturable absorption.

Table 5.3: Optical modulation characteristics of molten fluoride salt-assisted MXenes.

MXenes / Properties	Ti_2C	Nb_2C	V_2C
Saturable Absorption, α_s (%)	16.31	23.07	20.54
Non-saturable Absorption, α_{ns} (%)	55.8	31.31	33.04
Rising Time, τ_{rise} (µs)	161.44	141.84	188.41
Falling Time, τ_{fall} (µs)	158.40	175.52	225.86
V_{pp} at Maximum Frequency, V_{pp} f_{max} (mV)	2.59	13.54	11.22
V_{pp} at Maximum Power, V_{pp} P_{max} (mV)	6.59	14.66	14.36

Furthermore, the performance of fabricated MXenes in the all-optical modulation system are compared to that of other SA in Table 5.4. From the table, the previous work of fluorinated phosphorene (FP), graphene, and antimonene were only limited to 1.5 µm and the highest operating frequency is only between 0.4 to 4.0 kHz. While in this work, the fabricated MXenes offer operation at longer wavelength as well as highest operating frequency of 5.0 kHz. This suggest the advantages of operating at eye-safe region and higher optical response as compared to the other SA.

Table 5.4: Performance comparison of all-optical modulation systems using different SAs.

SA	Wavelength (μm)	Highest Modulation Frequency (kHz)	Reference
FP	1.5	0.4	(Y. Wang et al., 2018)
Graphene	1.5	4.0	(Liao et al., 2018)
Antimonene	1.5	2.0	(Y. Wang et al., 2019)
Ti_2C	2.0	5.0	This work
Nb_2C	2.0	5.0	
V_2C	2.0	5.0	

CHAPTER 6: CONCLUSIONS AND FUTURE WORKS

6.1 Conclusions

The development of various configurations in photonics application consisting of Q-switched laser, mode-locked laser, FWM generation, and all-optical modulator by using MXenes are the primary focus in this study. This thesis has completed three main objectives: (i) Three MAX phases (Ti_2AlC, Nb_2AlC, and V_2AlC) are chosen and successfully synthesized as MXenes (Ti_2C, Nb_2C, and V_2C) by using in situ HF as etching agent, particularly a mixture of LiF and HCl. The procedure is selected as an option to avoid the harmful HF, which is a common etching agent used to synthesize MXenes in the early stage. (ii) The morphological structure of the synthesized MXenes are characterized by using FESEM, HRTEM, XRD and Raman spectroscopy, while the optical property of the synthesized MXenes are characterized by using linear absorption, saturable absorption, and Z-scan analysis. Then, (iii) the MXenes are incorporated into four different setups of Q-switched laser, mode-locked laser, FWM, and all-optical modulator to investigate the performance of the MXenes in photonics application. Therefore, all of the objectives of this work have been met and fulfilled. In this chapter, the findings of this study are summarized and drawn conclusions. The continuity of this study can be implemented from the proposed possible future works as put at the end of this chapter.

6.1.1 Fabrication of MXenes by using LiF and HCl

The first attempt to weaken the M-A metallic bonds while preserve the strength of the M-X bonds was by exposing a layered precursor such as Ti_3AlC_2 to concentrated solutions of aqueous HF (50 wt%). This brought about the etching of A layer from several $M_{n+1}AX_n$ systems (Naguib et al., 2011b). According to literatures, the exposure time in

HF and the etching temperature are varied from few hours to days and from room temperature to higher temperatures (Anasori et al., 2017; Mashtalir, Naguib, Dyatkin, et al., 2013). Not only that, but the concentration selection also determine the condition of materials produced, where in particular case, the defect concentration increases as well as increasing in HF content in the etchant solution when the concentration of HF changes from ~3 wt% to 7 wt% (Sang et al., 2016). There exist numerous routes to selectively etch A layer; but generally, the thinner $M_{n+1}AX_n$ lamellas, the less time it needs to expose to HF. Alternatives were discovered in attempt to minimize the quantity of HF and make the reaction safer because of the nature of HF being very dangerous and environmental damaging such as opted in this thesis.

The fabrication of three types of MXenes, Ti_2C, Nb_2C, and V_2C are achieved by using the optional in situ HF or specifically HF-forming etchants (LiF + HCl). A few other MXenes such as Ti_3C_2 and Mo_2C were also synthesized by using the same reacting fluoride salts as shown by the other researchers (Ghidiu et al., 2014; Halim et al., 2016). In this reaction, LiF must act as the limiting reagent (Alhabeb et al., 2017). MXene synthesized with HF-forming etchants usually display larger interlayer spacing due to intercalation of cations of fluoride as opposed to using only HF as the etchant. Nevertheless, although this method is favoured because of shorter delamination time is needed, but it often contains unetched MAX phase as can be seen in some of the FESEM images and XRD pattern of the MXenes. The concentration of the excess HCl remaining and HF and LiCl produced revolves around the molarity of both reactants. For that reason, the remaining portion of unetched MAX phases (Ti_2AlC, Nb_2AlC, and V_2AlC) create an issue when it comes to scalability. In some cases, the facilitated exfoliation of MXenes into single flakes after sonication due to the presence of intercalants (Li^+) turn the lateral dimension of MXenes (single flake) into nanometer-size makes the studying properties of single flake MXene difficult (Ghidiu et al., 2014; Mashtalir, Naguib, Mochalin, et al.,

2013). One of the ways to address this problem is through optimization of the concentration of exchanged cations since the intercalation process is dependent on the concentration of H^+ exchanged with Li^+.

Therefore, the option to replace the HF by using a mixture of LiF and HCl as HF-forming etchants is successful in the matter of avoiding harmful substances. However, in the matter of scalability, both routes are still lacking to produce pure MXenes. Instead of using HF which is also not promising to completely etch MAX phase, different concentration of LiF and HCl can be further studied to produce pure MXene or alternatively, using different combination of HF-forming etchants.

6.1.2 The Optical Performance of Molten Fluoride Salt-Assisted MXenes in Passive Q-switched TDFFL (S-band)

The generation of Q-switched pulses in TDFFLs are designed and demonstrated by using Ti_2C, Nb_2C, and V_2C as SAs. The laser cavity consist of LD with 250 mW output power, a 1400/1480 nm WDM, a 1480 nm ISO, a 90:10 OC, and an 11.6 meter TDFF. The MXenes are integrated into the cavity by using thin film as their host, which has lower loss as compared to tapered fiber which use evanescent field to interact with 2D material. Q-switching outputs are acquired by using the three MXenes, Ti_2C, Nb_2C, and V_2C that have displayed Q-switching optical spectrum at center wavelengths of 1488.19 nm, 1489.63 nm, and 1492.52 nm, respectively. In typical TDFFL, the lasing wavelength is red shifted when the pump power is increasing, and blue shifted when the pump power is decreasing or experiencing loss in the cavity. Plus, it is sensitive to high pump power, thus a 250 mW LD is commonly used to pump the cavity to avoid damaging the gain medium. The pulse width and repetition rate of V_2C are 2.72 µs and 32.57 kHz, while Ti_2C, and Nb_2C are 3.90 µs and 21.94 kHz, and 3.58 µs and 35.20 kHz. Thus, V_2C has the lowest pulse width and Nb_2C has the highest repetition rate. Besides, at maximum pump power of all cavities, Ti_2C has the highest maximum pulse energy of 3.78 nJ and

Nb_2C has the lowest maximum pulse energy of 2.51 nJ. Lastly, Ti_2C, Nb_2C, and V_2C have shown stable pulses with RF spectrum SNR of 38 dB, 33 dB, and 41 dB, respectively. The pulse energy and peak power of Q-switched generally shows an uptrend in the beginning and a downtrend at the end due to the accumulated energy in the cavity compensating the higher repetition rate and shorter pulse width. However, it can be seen from the results of the pulse energy and peak power of the Q-switched of the MXenes which showed an uptrend until the maximum pump power. Hence, this indicates the TDFFL cavity does not fully explored the limitation of the MXenes in S-band region in term of pump power threshold. Nevertheless, this work do highlight the potential of MXenes in other region besides 2 μm region.

6.1.3 The Optical Performance of Molten Fluoride Salt-Assisted MXenes in Passive Q-switched TDFL (2 μm)

The generation of Q-switched pulses in TDFLs are designed and demonstrated by using Ti_2C, Nb_2C, and V_2C as SAs. The laser cavity consist of fiber laser source with 1 W output power, a 1550/2000 nm WDM, a 2000 nm ISO, a 90:10 OC, and a 4 meter TDF. The MXenes are integrated into the cavity by using tapered fiber as their host, which has higher damage threshold compared to thin film to utilize the 1 W pump source. Q-switching outputs are acquired by using the three MXenes, Ti_2C, Nb_2C, and V_2C that have displayed Q-switching optical spectrum at center wavelengths of 1953 nm, 1948 nm, and 1941 nm, respectively. The pulse width and repetition rate of Ti_2C are 1.74 μs and 54.06 kHz, while Nb_2C, and V_2C are 1.81 μs and 62.54 kHz, and 1.32 μs and 54.96 kHz. Thus, V_2C has the lowest pulse width and Nb_2C has the highest repetition rate. Besides, V_2C has the highest pulse energy of 14.80 nJ and Nb_2C has the lowest pulse energy of 10.90 nJ. The decreasing of the peak power and pulse width beyond certain pump power can be seen in all of the MXenes setups, which is due to the total accumulated energy in the gain medium compensating for the higher repetition rate and shorter pulse

width. Unlike in TDFFL, the degeneracy of the peak power and pulse width in TDFL is more obvious as should be anticipated.

6.1.4 The Optical Performance of Molten Fluoride Salt-Assisted MXenes in Passive Mode-locked TDFL

The generation of mode-locked pulses in TDFLs are designed and demonstrated by using Ti_2C, Nb_2C, and V_2C as SAs. The laser cavity consist of fiber laser source with 1 W output power, a 1550/2000 nm WDM, a 2000 nm ISO, a 90:10 OC, a PC, and a 4 meter TDF. The MXenes are integrated into the cavity by using tapered fiber as their host, which has higher damage threshold compared to thin film to utilize the 1 W pump source. Mode-locking outputs are acquired by using the three MXenes, Ti_2C, Nb_2C, and V_2C that have displayed mode-locking optical spectrum with the presence of Kelly sidebands at center wavelengths of 1951.13 nm, 1957.08 nm, and 1956.43 nm, respectively. The lowest repetition rate among them is Ti_2C, that is 11.30 MHz, then followed by V_2C, and Nb_2C, which are 11.92 MHz, and 12.15 MHz, sequentially. This should be anticipated since the non-saturable loss of Ti_2C is 57.32%, which appears to be the highest as opposed to the other two. Hence, it needs more time to build up the consequent pulses. However, although Ti_2C possesses the lowest repetition rate, but it has the lowest pulse width as compared to the others. The saturable absorption of Ti_2C is only 14.78%, where the V_2C, and Nb_2C are 18.71%, and 20.34%, respectively. As the saturable absorption goes higher, the pulse width will be shorter. Since the saturable absorption of Ti_2C is the lowest, it has a pulse width of 1.72 ps, whilst the pulse width of V_2C, and Nb_2C are 1.70 ps, and 1.67 ps accordingly. At the maximum pump power of V_2C at 390 mW, it generates maximum pulse energy and peak power of 0.139 nJ and 0.074 kW. These values suggest the highest between the other two, where the lowest is Ti_2C that generates maximum pulse energy and peak power of 0.112 nJ, and 0.060 kW at maximum pump power of 350 mW. Nb_2C records maximum pulse energy, and peak power of 0.136 nJ, and 0.073 kW at maximum

pump power of 370 mW. Finally, all three of them, Ti_2C, Nb_2C, and V_2C have shown stable pulses with RF spectrum SNR of 45.46 dB, 55.30 dB, and 56.37 dB, respectively.

6.1.5 The Optical Performance of Molten Fluoride Salt-Assisted MXenes in FWM

The generation of FWM in 2 μm are designed and demonstrated by using Ti_2C, Nb_2C, and V_2C as nonlinear materials. The laser cavity consist of a pump light and a signal light from two external cavities, a 50:50 OC, an amplifier, and a fixed attenuator. The MXenes are integrated into the cavity by using tapered fiber as their host, which has high damage threshold that is suitable to receive high amplified power after the amplifier. FWM outputs are acquired by using the three MXenes, Ti_2C, Nb_2C, and V_2C that have displayed FWM optical spectrum with pump light and signal light wavelengths at 1999.5 nm and 2000.1 nm, with two idlers at 1999 nm and 2000.7 nm. The FWM conversion efficiency of V_2C displays the highest between the others, particularly at -41.20 dB, which is proportionate with the β, and n_2 values of 5.11×10^{-10} m/W, and 1.27×10^{-16} m/W. The β, and n_2 values of Ti_2C, and Nb_2C are 3.48×10^{-10} m/W and $3.28.27\times10^{-17}$ m/W, and 4.82×10^{-10} m/W, and 8.11×10^{-17} m/W and their respective FWM conversion efficiency are -43.93 dB, and -42.60 dB, as expected. The idlers of the V_2C are enhanced the highest by 9.80 dB as opposed to the Ti_2C by 7.73 dB, which is the lowest. Whereby, the idlers of Nb_2C are enhanced by 9.10 dB, which sits in between Ti_2C and V_2C. The enhanced idlers can be translated into conversion efficiency difference from the generated FWM with and without MXenes. On that regard, V_2C has the highest conversion efficiency difference of 10.80 as compared to Nb_2C and Ti_2C, which are 9.40 and 8.07, respectively. Lastly, the idlers of FWM generated by Ti_2C, Nb_2C, and V_2C also have shown a stable performance in general, where the highest SNR fluctuation is only 0.80 dB.

6.1.6 The Optical Performance of Molten Fluoride Salt-Assisted MXenes in All-Optical Modulation

The optical modulation configurations are designed and demonstrated by using Ti_2C, Nb_2C, and V_2C as optical modulator. The laser cavity consist of a control light at 793 nm and a signal light at 2000 nm, two 793/2000 nm WDMs and a TBPF. The MXenes are integrated between the common port of the WDMs by using thin film as their host. The control light power is put higher than the signal light at 8 mW and 5 mW, respectively. Nb_2C thin film possesses the fastest rising time of 141.84 µs and Ti_2C thin film possesses the fastest falling time of 158.40 µs. While for V_2C thin film, it records the slowest rising time and falling time of 188.41 µs, and 225.86 µs. During the modulation, both of the control light and signal light are in fact absorbed by the MXenes, but as the amplitude of the control light goes up, more atoms go to the excited state through the control light wavelength, leaving the ground state empty, thus allowing the signal light to pass through the thin film without being absorbed. This is the reason of V_{pp} of modulated signal appear smaller than the modulated control light. At the maximum signal power of 5 mW, Nb_2C has the highest V_{pp} of 14.66 mW, while Ti_2C has the lowest V_{pp} of 6.59 mW. Therefore, in the application of all-optical modulator, Nb_2C performs the best among the other two.

6.2 Future Works

On the whole, the studies have shown that the Ti_2C, Nb_2C, and V_2C MXenes have promising potential in photonics applications. The findings of these experiments perhaps can provide insights on the different fabrication of MXenes and their optical performances as nonlinear material. Nonetheless, there are still many improvements can be made of the existing works in term of fabrication of MXenes and output power of the pulsed laser.

In the fabrication process of MXenes, HF-forming etchants, specifically, LiF and HCl are used. The products of the fabrication are not completely pure with the existence of MAX phase residue after the process. Other concentration of LiF and HCl can be studied to fabricate a pure MXenes, which at the same time will help to improve the scalability of the material in industrial scope. Besides focusing on the removing of the residual MAX phase, there are a few reports on the intercalation of MXenes with other material including graphene (Demiroglu et al., 2019). The intercalation of other material into MXenes have shown improved performance in other field such as batteries and pseudocapacitance (N. Li et al., 2021; Ramachandran et al., 2018; D.-X. Song et al., 2021). On the note, it is unclear what is the effect of different intercalant will be on the optical performance of MXenes. The intercalation of MXenes will change the size of the interlayer spacing depending on the size of the intercalant, thus the interlayer spacing can be controlled by the size of the chosen intercalant. Therefore, there are two studies can be made from MXenes intercalation. Those are the effect of interlayer spacing on the optical performance and the effect of different intercalant type on the optical performance.

Finally, the pulsed fiber laser system in the present research is considered at low power scale. Most of the application in industrial field need high power laser system to be regarded as practical. Among the system that can be utilized to scale the output power on Watt level is by using master oscillator power amplifier (MOPA). However, the optical damage threshold of the MXenes must be thoroughly studied and improved as it is one of the essential criteria for its application in high power laser system. There are not many SAs have been used to create pulsed laser in such system due to low damage threshold capacity. If this limitation can be overcome, this will spark other researchers to explore the other SAs to be utilized in the high power laser system.

REFERENCES

Agrawal, G. P. (1987). Modulation instability induced by cross-phase modulation. *Physical Review Letters*, *59*(8), Article#880.

Agrawal, G. P. (2000). Nonlinear fiber optics. In *Nonlinear Science at the Dawn of the 21st Century* (pp. 195–211). Springer.

Ahmad, H, Azmy, N. F., Reduan, S. A., Yusoff, N., Bayang, L., Zulkifli, M. Z., & Thambiratnam, K. (2020). Tunable passively Q-switched thulium doped fluoride fibre (TDFF) laser using reduced graphene oxide-silver (rGO-Ag) as saturable absorber. *Journal of Modern Optics*, *67*(11), 1022–1030.

Ahmad, H, Azmy, N. F., Yusoff, N., Reduan, S. A., Bayang, L., Ismail, M. F., Zulkifli, M. Z., Thambiratnam, K., & others. (2020). Passively Q-switched S^{+}/S band fiber laser with copper telluride saturable absorber. *Laser Physics Letters*, *17*(9), Article#95102.

Ahmad, H, Azri, M. F. M., Ramli, R., Samion, M. Z., Yusoff, N., & Lim, K. S. (2021). 2 μm passively mode-locked thulium-doped fiber lasers with Ta_2AlC-deposited tapered and side-polished fibers. *Scientific Reports*, *11*(1), 1–17.

Ahmad, H, Muhammad, F. D., Zulkifli, M. Z., & Harun, S. W. (2012). Graphene-oxide-based saturable absorber for all-fiber Q-switching with a simple optical deposition technique. *IEEE Photonics Journal*, *4*(6), 2205–2213.

Ahmad, H, Zaini, M. K. A., Kamely, A. A., Samion, M. Z., Ismail, M. F., Lim, K. S., Zamzuri, A. K., & Thambiratnam, K. (2021). Generation of four-wave mixing in molybdenum ditelluride ($MoTe_2$)-deposited side-polished fibre. *Journal of Modern Optics*, *68*(8), 425–432.

Ahmad, Harith, Ramli, R., Ismail, N. N., Aidit, S. N., Yusoff, N., & Samion, M. Z. (2021). Passively mode locked thulium and thulium/holmium doped fiber lasers using MXene Nb_2C coated microfiber. *Scientific Reports*, *11*(1), 1–12.

Ahmad, Harith, Reduan, S. A., Sharbirin, A. S., Ismail, M. F., & Zulkifli, M. Z. (2018). Q-switched thulium/holmium fiber laser with gallium selenide. *Optik*, *175*, 87–92.

Al-Alimi, A. W., Yaacob, M. H., Abas, A. F., Mahdi, M. A., Mokhtar, M., & Al-Mansoori, M. H. (2013). 150-Channel Four Wave Mixing Based Multiwavelength Brillouin-Erbium Doped Fiber Laser. *IEEE Photonics Journal*, *5*(4), 1501010–1501010.

Al-Mansoori, M. H., Al-Sheriyani, A., Younis, M. A. A., & Mahdi, M. A. (2018). Widely tunable multiwavelength Brillouin-erbium fiber laser with triple Brillouin-shift wavelength spacing. *Optical Fiber Technology*, *41*(December 2017), 21–26.

Alhabeb, M., Maleski, K., Anasori, B., Lelyukh, P., Clark, L., Sin, S., & Gogotsi, Y. (2017). Guidelines for synthesis and processing of two-dimensional titanium carbide ($Ti_3C_2T_x$ MXene). *Chemistry of Materials*, *29*(18), 7633–7644.

Ambrosch-Draxl, C., & Sofo, J. O. (2006). Linear optical properties of solids within the full-potential linearized augmented planewave method. *Computer Physics Communications*, *175*(1), 1–14.

Anasori, B., Lukatskaya, M. R., & Gogotsi, Y. (2017). 2D metal carbides and nitrides (MXenes) for energy storage. *Nature Reviews Materials*, 2(2), 1-17.

Anasori, B., Xie, Y., Beidaghi, M., Lu, J., Hosler, B. C., Hultman, L., ... & Barsoum, M. W. (2015). Two-dimensional, ordered, double transition metals carbides (MXenes). *ACS nano*, 9(10), 9507-9516.

Aozasa, S., Masuda, H., & Shimizu, M. (2006). S-band thulium-doped fiber amplifier employing high thulium concentration doping technique. *Journal of Lightwave Technology*, *24*(10), 3842–3848.

Autere, A., Jussila, H., Dai, Y., Wang, Y., Lipsanen, H., & Sun, Z. (2018). Nonlinear optics with 2D layered materials. *Advanced Materials*, *30*(24), Article#1705963.

Awang, N. A., Ahmad, H., Latif, A. A., Zulkifli, M. Z., & Harun, S. W. (2011). Four-wave mixing in dual wavelength fiber laser utilizing SOA for wavelength conversion. *Optik*, *122*(9), 754–757.

Barsoum, M. W. (2013). *MAX phases: properties of machinable ternary carbides and nitrides*. John Wiley & Sons.

Berdiyorov, G. R. (2016). Optical properties of functionalized $Ti_3C_2T_2$ (T= F, O, OH) MXene: First-principles calculations. *Aip Advances*, *6*(5), Article#55105.

Boyd, R. W. (2008). The nonlinear optical susceptibility. *Nonlinear Optics*, *3*, 1–67.

Boyd, R. W. (2020). *Nonlinear optics*. Academic press.

Boyer, V., Marino, A. M., Pooser, R. C., & Lett, P. D. (2008). Entangled images from four-wave mixing. *Science*, *321*(5888), 544–547.

Champagne, A., Shi, L., Ouisse, T., Hackens, B., & Charlier, J.-C. (2018). Electronic and vibrational properties of V_2C-based MXenes: From experiments to first-principles modeling. *Physical Review B*, *97*(11), Article#115439.

Chaudhuri, K., Wang, Z., Alhabeb, M., Maleski, K., Gogotsi, Y., Shalaev, V., & Boltasseva, A. (2019). Optical properties of MXenes. In *2D Metal Carbides and Nitrides (MXenes)* (pp. 327–346). Springer.

Chen, X., Deng, Z., & Yao, J. (2006). Photonic generation of microwave signal using a dual-wavelength single-longitudinal-mode fiber ring laser. *IEEE Transactions on Microwave Theory and Techniques*, *54*(2), 804–809.

Chen, Y.-F., Wang, C.-Y., Wang, S.-H., & Ite, A. Y. (2006). Low-light-level cross-phase-modulation based on stored light pulses. *Physical Review Letters*, *96*(4), Article#43603.

Chen, Yanping, Zhai, J., Xu, X., Li, L., Wang, J., Zhang, M., Ruan, S., & Tang, Z. (2017). Mode-locked thulium-doped fiber laser based on 0.3 nm diameter single-walled carbon nanotubes at 1.95 μm. *Chinese Optics Letters*, *15*(4), Article#41403.

Chen, Y., Jiang, G., Chen, S., Guo, Z., Yu, X., Zhao, C., ... & Fan, D. (2015). Mechanically exfoliated black phosphorus as a new saturable absorber for both Q-switching and mode-locking laser operation. *Optics express*, 23(10), 12823-12833.

Chen, Yu, Zhao, C., Huang, H., Chen, S., Tang, P., Wang, Z., Lu, S., Zhang, H., Wen, S., & Tang, D. (2013). Self-assembled topological insulator: Bi_2Se_3 membrane as a passive Q-switcher in an Erbium-doped fiber laser. *Journal of Lightwave Technology*, *31*(17), 2857–2863.

Chow, K. K., Kikuchi, K., Nagashima, T., Hasegawa, T., Ohara, S., & Sugimoto, N. (2007). Four-wave mixing based widely tunable wavelength conversion using 1-m dispersion-shifted bismuth-oxide photonic crystal fiber. *Optics Express*, *15*(23), 15418–15423.

Chow, K. K., Tsuji, M., & Yamashita, S. (2010). Single-walled carbon-nanotube-deposited tapered fiber for four-wave mixing based wavelength conversion. *Applied Physics Letters*, *96*(6), Article#61104.

Chow, K. K., & Yamashita, S. (2009). Four-wave mixing in a single-walled carbon-nanotube-deposited D-shaped fiber and its application in tunable wavelength conversion. *Optics Express*, *17*(18), 15608–15613.

Chow, K. K., Yamashita, S., & Song, Y. W. (2009). A widely tunable wavelength converter based on nonlinear polarization rotation in a carbon-nanotube-deposited D-shaped fiber. *Optics Express*, *17*(9), 7664–7669.

Churin, D., Kieu, K., & Peyghambarian, N. (2012, February). The role of the saturable absorber in a mode-locked fiber laser. In *Fiber Laser Applications* (pp. FTh1A-4). Optica Publishing Group.

D'ottavi, A., Girardin, F., Graziani, L., Martelli, F., Spano, P., Mecozzi, A., Scotti, S., Dall'Ara, R., Eckner, J., & Guekos, G. (1997). Four-wave mixing in semiconductor optical amplifiers: A practical tool for wavelength conversion. *IEEE Journal of Selected Topics in Quantum Electronics*, *3*(2), 522–528.

Boota, M., Urbankowski, P., Porzio, W., Barba, L., Osti, N. C., Bleuel, M., ... & Mamontov, E. (2020). Understanding functionalization of titanium carbide (MXene) with quinones and their pseudocapacitance. *ACS Applied Energy Materials*, 3(5), 4127-4133.

Dawlaty, J. M., Shivaraman, S., Chandrashekhar, M., Rana, F., & Spencer, M. G. (2008). Measurement of ultrafast carrier dynamics in epitaxial graphene. *Applied Physics Letters*, *92*(4), Article#42116.

Demiroglu, I., Peeters, F. M., Gulseren, O., Çak\ir, D., & Sevik, C. (2019). Alkali metal intercalation in MXene/graphene heterostructures: a new platform for ion battery applications. *The Journal of Physical Chemistry Letters*, *10*(4), 727–734.

Ding, Y., Xu, J., Ou, H., & Peucheret, C. (2014). Mode-selective wavelength conversion based on four-wave mixing in a multimode silicon waveguide. *Optics Express*, *22*(1), 127–135.

Dong, N., Li, Y., Zhang, S., McEvoy, N., Zhang, X., Cui, Y., Zhang, L., Duesberg, G. S., & Wang, J. (2016). Dispersion of nonlinear refractive index in layered WS 2 and WSe 2 semiconductor films induced by two-photon absorption. *Optics Letters*, *41*(17), 3936–3939.

Dong, N., Li, Y., Zhang, S., Zhang, X., & Wang, J. (2017). Optically induced transparency and extinction in dispersed MoS_2, $MoSe_2$, and graphene nanosheets. *Advanced Optical Materials*, *5*(19), Article#1700543.

Dong, Y., Chen, L., & Bao, X. (2011). Time-division multiplexing-based BOTDA over 100km sensing length. *Optics Letters*, *36*(2), 277–279.

Du, J., Wang, Q., Jiang, G., Xu, C., Zhao, C., Xiang, Y., Chen, Y., Wen, S., & Zhang, H. (2014). Ytterbium-doped fiber laser passively mode locked by few-layer molybdenum disulfide (MoS_2) saturable absorber functioned with evanescent field interaction. *Scientific Reports*, *4*, Article#6346.

Du, Y. T., Kan, X., Yang, F., Gan, L. Y., & Schwingenschlogl, U. (2018). MXene/graphene heterostructures as high-performance electrodes for Li-ion batteries. *ACS applied materials & interfaces*, 10(38), 32867-32873.

Eichhorn, M. (2007). Development of a high-pulse-energy Q-switched Tm-doped double-clad fluoride fiber laser and its application to the pumping of mid-IR lasers. *Optics Letters*, *32*(9), 1056–1058.

Evans, C. A., Ikonic, Z., Richards, B., Harrison, P., & Jha, A. (2009). Theoretical Modeling of a ~2μm Tm^{3+} -Doped Tellurite Fiber Laser: The Influence of Cross Relaxation. *Journal of Lightwave Technology*, *27*(18), 4026–4032.

Fardi, A., Razaghi, M., Das, N. K., & Baghban, H. (2021). Dynamics of four-wave mixing in flared-waveguide semiconductor optical amplifiers. *Optik*, *246*, Article#167805.

Ferrari, A. C. (2007). Raman spectroscopy of graphene and graphite: Disorder, electron--phonon coupling, doping and nonadiabatic effects. *Solid State Communications*, *143*(1–2), 47–57.

Floridia, C., Sundheimer, M. L., Lüthi, S. R., & Gomes, A. S. L. (2004). Simultaneous S+-band amplification and S+--C-band wavelength conversion in CW pumped fibre optic parametric amplifier. *Electronics Letters*, *40*(5), 335–336.

Fox, M. (2002). Optical properties of solids.

Fried, N. M., & Murray, K. E. (2005). High-power thulium fiber laser ablation of urinary tissues at 1.94 μm. *Journal of endourology*, 19(1), 25-31.

Fu, B., Sun, J., Wang, C., Shang, C., Xu, L., Li, J., & Zhang, H. (2021). MXenes: Synthesis, optical properties, and applications in ultrafast photonics. *Small*, *17*(11), Article#2006054.

Gan, X., Zhao, C., Wang, Y., Mao, D., Fang, L., Han, L., & Zhao, J. (2015). Graphene-assisted all-fiber phase shifter and switching. *Optica*, *2*(5), 468–471.

Geim, A. K. (2009). Graphene: status and prospects. *Science*, *324*(5934), 1530–1534.

Ghidiu, M., Lukatskaya, M. R., Zhao, M.-Q., Gogotsi, Y., & Barsoum, M. W. (2014). Conductive two-dimensional titanium carbide 'clay'with high volumetric capacitance. *Nature*, *516*(7529), 78–81.

Gogotsi, Y. G., & Andrievski, R. A. (2012). *Materials science of carbides, nitrides and borides* (Vol. 68). Springer Science & Business Media.

Gomes, A. S. L., Carvalho, M. T., & Sundheimer, M. L. (2003). Comparison of distributed gain in 800 nm+ 1050 nm or 800 nm+ 1410 nm pumping schemes for thulium-doped fiber amplifiers using optical frequency domain reflectometry. *The 16th Annual Meeting of the IEEE Lasers and Electro-Optics Society, 2003. LEOS 2003.*, *2*, 1052–1053.

Guan, Y., Jiang, S., Cong, Y., Wang, J., Dong, Z., Zhang, Q., ... & Li, X. (2020). A hydrofluoric acid-free synthesis of 2D vanadium carbide (V_2C) MXene for supercapacitor electrodes. *2D Materials*, 7(2), Article#025010.

Guo, B., Yao, Y., Xiao, J. J., Wang, R. L., & Zhang, J. Y. (2015). Topological insulator-assisted dual-wavelength fiber laser delivering versatile pulse patterns. *IEEE Journal of Selected Topics in Quantum Electronics*, 22(2), 8-15.

Guo, C. (2010). Global existence of solutions for a fourth-order nonlinear Schrödinger equation in n+ 1 dimensions. *Nonlinear Analysis: Theory, Methods & Applications*, *73*(2), 555–563.

Guo, Q., Wu, K., Shao, Z., Basore, E. T., Jiang, P., & Qiu, J. (2019). Boron nanosheets for efficient all-optical modulation and logic operation. *Advanced Optical Materials*, *7*(13), Article#1900322.

Guo, Z., Zhou, J., Zhu, L., & Sun, Z. (2016). MXene: a promising photocatalyst for water splitting. *Journal of Materials Chemistry A*, 4(29), 11446-11452.

Halim, J., Kota, S., Lukatskaya, M. R., Naguib, M., Zhao, M.-Q., Moon, E. J., Pitock, J., Nanda, J., May, S. J., Gogotsi, Y., & others. (2016). Synthesis and characterization of 2D molybdenum carbide (MXene). *Advanced Functional Materials*, *26*(18), 3118–3127.

Halim, J., Lukatskaya, M. R., Cook, K. M., Lu, J., Smith, C. R., Näslund, L. Å., May, S. J., Hultman, L., Gogotsi, Y., Eklund, P., & Barsoum, M. W. (2014). Transparent conductive two-dimensional titanium carbide epitaxial thin films. *Chemistry of Materials*, 26(7), 2374-2381

Hargrove, L. E., Fork, R. L., & Pollack, M. A. (1964). Locking of He--Ne laser modes induced by synchronous intracavity modulation. *Applied Physics Letters*, *5*(1), 4–5.

Harrison, W. A. (1980). *Solid state theory*. Courier Corporation.

Hejib, P., & Sharma, E. K. (2021). All-Optical AND Gate Using Four Wave Mixing in Wideband Semiconductor Optical Amplifier. In *ICOL-2019* (pp. 775-778). Springer, Singapore.

Hendry, E., Hale, P. J., Moger, J., Savchenko, A. K., & Mikhailov, S. A. (2010). Coherent nonlinear optical response of graphene. *Physical Review Letters*, *105*(9), Article#97401.

Ho, M.-C., & Wong, K. Y. K. (2002). Narrow-linewidth idler generation in fiber four-wave mixing and parametric amplification by dithering two pumps in opposition of phase. *Journal of Lightwave Technology*, *20*(3), Article#469.

Hong, H., Huang, L., Liu, Q., Yan, P., & Gong, M. (2012). Compact high-power, TEM_{00} acousto-optics Q-switched Nd: YVO_4 oscillator pumped at 888 nm. Applied Optics, 51(3), 323-327.

Huang, F., Chen, T., Si, J., Pham, X., & Hou, X. (2019). Fiber laser based on a fiber Bragg grating and its application in high-temperature sensing. *Optics Communications*, *452*, 233–237.

Ingason, A. S., Petruhins, A., Dahlqvist, M., Magnus, F., Mockute, A., Alling, B., Hultman, L., Abrikosov, I. A., & Persson PO Åand Rosen, J. (2014). A nanolaminated magnetic phase: Mn_2GaC. *Materials Research Letters*, *2*(2), 89–93.

Ippen, E. P. (1994). Principles of passive mode locking. *Applied Physics B*, *58*(3), 159–170.

Jackson, S. D., & King, T. A. (1999). Theoretical modeling of Tm-doped silica fiber lasers. *Journal of lightwave technology*, 17(5), Article#948.

Ji, J., Zhu, X., Dai, S., & Wang, C. (2007). Depolarization loss compensated resonator for electro-optic Q-switched solid-state laser. *Optics communications*, 270(2), 301-304.

Jia, C., Shastri, B. J., Prucnal, P. R., Saad, M., & Chen, L. R. (2017). Simultaneous Q - Switching of a Tm^{3+}:ZBLAN Fiber Laser at 1.9~μm and 2.3~μm Using Graphene. *IEEE Photonics Technology Letters*, *29*(4), 405–408.

Jia, C., Shastri, B. J., Rochette, M., Chen, L. R., & Saad, M. (2015). Graphene-based passively Q-switched Tm^{3+}: ZBLAN fiber laser at 1480 nm. *2015 IEEE Photonics Conference (IPC)*, 326–327.

Jiang, X.-F., Polavarapu, L., Neo, S. T., Venkatesan, T., & Xu, Q.-H. (2012). Graphene oxides as tunable broadband nonlinear optical materials for femtosecond laser pulses. *The Journal of Physical Chemistry Letters*, *3*(6), 785–790.

Jiang, X., Kuklin, A. V, Baev, A., Ge, Y., Ågren, H., Zhang, H., & Prasad, P. N. (2020). Two-dimensional MXenes: from morphological to optical, electric, and magnetic properties and applications. *Physics Reports*, *848*, 1–58.

Jiang, X., Liu, S., Liang, W., Luo, S., He, Z., Ge, Y., ... & Zhang, H. (2018). Broadband nonlinear photonics in few-layer MXene $Ti_3C_2T_x$ (T= F, O, or OH). *Laser & Photonics Reviews*, 12(2), Article#1700229.

Jin, B., & Argyropoulos, C. (2016). Enhanced four-wave mixing with nonlinear plasmonic metasurfaces. *Scientific Reports*, *6*(1), 1–9.

Jin, X., Bao, W., Zhang, H., Zheng, Z., & Zhang, M. (2022). Four-wave mixing in graphdiyne-microfiber based on synchronized dual-wavelength pulses. *Photonics Research*, *10*(2), Article#2000503.

Jung, M., Koo, J., Park, J., Song, Y.-W., Jhon, Y. M., Lee, K., Lee, S., & Lee, J. H. (2013). Mode-locked pulse generation from an all-fiberized, Tm-Ho-codoped fiber laser incorporating a graphene oxide-deposited side-polished fiber. *Optics Express*, *21*(17), 20062–20072.

Jung, M., Lee, J., Park, J., Koo, J., Jhon, Y. M., & Lee, J. H. (2015). Mode-locked, 1.94-μm, all-fiberized laser using WS_2-based evanescent field interaction. *Optics Express*, 23(15), 19996-20006.

Kang, Z., Liu, M. Y., Gao, X. J., Li, N., Yin, S. Y., Qin, G. S., & Qin, W. P. (2015). Mode-locked thulium-doped fiber laser at 1982 nm by using a gold nanorods saturable absorber. *Laser Physics Letters*, *12*(4), Article#45105.

Kao, K. C., & Hockham, G. A. (1966). Dielectric-fibre surface waveguides for optical frequencies. *Proceedings of the Institution of Electrical Engineers*, *113*(7), 1151–1158.

Karlsson, G., Pasiskevicius, V., Laurell, F., & Tellefsen, J. A. (2003). Q-switching of an Er--Yb: glass microchip laser using an acousto-optical modulator. *Optics Communications*, *217*(1–6), 317–324.

Kbashi, H. J., Sharma, V., & Sergeyev, S. (2021). Dual-wavelength fiber-laser-based transmission of millimeter waves for 5G-supported Radio-over-Fiber (RoF) links. *Optical Fiber Technology*, *65*, Article#102588.

Keller, U. (2010). Ultrafast solid-state laser oscillators: a success story for the last 20 years with no end in sight. *Applied Physics B*, *100*(1), 15–28.

Keller, Ursula, Weingarten, K. J., Kartner, F. X., Kopf, D., Braun, B., Jung, I. D., Fluck, R., Honninger, C., Matuschek, N., & Der Au, J. A. (1996). Semiconductor saturable absorber mirrors (SESAM's) for femtosecond to nanosecond pulse generation in solid-state lasers. *IEEE Journal of Selected Topics in QUANTUM ELECTRONICS*, *2*(3), 435–453.

Kelly, S. M. J. (1992). Characteristic sideband instability of periodically amplified average soliton. *Electronics Letters*, *28*(8), 806–807.

Khamis, M. A., & Ennser, K. (2016). Theoretical model of a thulium-doped fiber amplifier pumped at 1570 nm and 793 nm in the presence of cross relaxation. *Journal of Lightwave Technology*, *34*(24), 5675–5681.

Khazaei, M., Ranjbar, A., Arai, M., Sasaki, T., & Yunoki, S. (2017). Electronic properties and applications of MXenes: a theoretical review. *Journal of Materials Chemistry C*, *5*(10), 2488–2503.

Khazaeinezhad, R., Kassani, S. H., Nazari, T., Jeong, H., Kim, J., Choi, K., Lee, J.-U., Kim, J. H., Cheong, H., Yeom, D.-I., & others. (2015). Saturable optical absorption in MoS2 nano-sheet optically deposited on the optical fiber facet. *Optics Communications*, *335*, 224–230.

Kim, H., Sheps, T., Collins, P. G., & Potma, E. O. (2009). Nonlinear optical imaging of individual carbon nanotubes with four-wave-mixing microscopy. *Nano Letters*, *9*(8), 2991–2995.

Kim, K. S., Zhao, Y., Jang, H., Lee, S. Y., Kim, J. M., Kim, K. S., Ahn, J.-H., Kim, P., Choi, J.-Y., & Hong, B. H. (2009). Large-scale pattern growth of graphene films for stretchable transparent electrodes. *Nature*, *457*(7230), 706–710.

Klonidis, D., Politi, C., O'Mahony, M., & Simeonidou, D. (2004). Fast and widely tunable optical packet switching scheme based on tunable laser and dual-pump four-wave mixing. *IEEE Photonics Technology Letters*, *16*(5), 1412–1414.

Kozak, M. M., Caspary, R., & Kowalsky, W. (2004). Thulium-doped fiber amplifier for the S-band. *Proceedings of 2004 6th International Conference on Transparent Optical Networks (IEEE Cat. No. 04EX804)*, *2*, 51–54.

Kuchida, S., Muranaka, T., Kawashima, K., Inoue, K., Yoshikawa, M., & Akimitsu, J. (2013). Superconductivity in Lu2SnC. *Physica C: Superconductivity*, *494*, 77–79.

Kuizenga, D, & Siegman, A. (1970). FM and AM mode locking of the homogeneous laser-Part I: Theory. *IEEE Journal of Quantum Electronics*, *6*(11), 694–708.

Kuizenga, Dl, & Siegman, A. (1970). FM and AM mode locking of the homogeneous laser-Part II: Experimental results in a Nd: YAG laser with internal FM modulation. *IEEE Journal of Quantum Electronics*, *6*(11), 709–715.

Kuriakose, V. C., & Porsezian, K. (2010). Elements of optical solitons: An overview. *Resonance*, *15*(7), 643–666.

Lai, S., Jeon, J., Jang, S. K., Xu, J., Choi, Y. J., Park, J.-H., Hwang, E., & Lee, S. (2015). Surface group modification and carrier transport properties of layered transition metal carbides (Ti_2CT_x, T:--OH,--F and--O). *Nanoscale*, *7*(46), 19390–19396.

Land, T. A., Michely, T., Behm, R. J., Hemminger, J. C., & Comsa, G. (1992). STM investigation of single layer graphite structures produced on Pt (111) by hydrocarbon decomposition. *Surface Science*, *264*(3), 261–270.

Lashgari, H., Abolhassani, M. R., Boochani, A., Elahi, S. M., & Khodadadi, J. (2014). Electronic and optical properties of 2D graphene-like compounds titanium carbides and nitrides: DFT calculations. *Solid State Communications*, *195*, 61–69.

Lee, J. H., Belardi, W., Furusawa, K., Petropoulos, P., Yusoff, Z., Monro, T. M., & Richardson, D. J. (2003). Four-wave mixing based 10-Gb/s tunable wavelength conversion using a holey fiber with a high SBS threshold. *IEEE Photonics Technology Letters*, *15*(3), 440–442.

Lee, J. H., Gross, S., Cunning, B. V, Brown, C. L., Kielpinski, D., Monro, T. M., & Lancaster, D. G. (2014). Graphene-based passive Q-switching of a Tm^{3+}: ZBLAN short-infrared waveguide laser. *2014 Conference on Lasers and Electro-Optics (CLEO)-Laser Science to Photonic Applications*, 1–2.

Lee, J., Jung, M., Koo, J., Chi, C., & Lee, J. H. (2014). Passively Q-Switched 1.89-μm fiber laser using a bulk-structured Bi_2Te_3 topological insulator. *IEEE Journal of Selected Topics in Quantum Electronics*, *21*(1), 31–36.

Lee, J., Jung, M., Koo, J., Chi, C., & Lee, J. H. (2014). Passively Q-switched 1.89-μm fiber laser using a bulk-structured Bi_2Te_3 topological insulator. *IEEE Journal of Selected Topics in Quantum Electronics*, 21(1), 31-36.

Lee, J., Koo, J., Chi, C., & Lee, J. H. (2014a). All-fiberized, passively Q-switched 1.06 μm laser using a bulk-structured Bi_2Te_3 topological insulator. *Journal of Optics*, *16*(8), Article#85203.

Lee, J., Koo, J., Chi, C., & Lee, J. H. (2014). All-fiberized, passively Q-switched 1.06 μm laser using a bulk-structured Bi_2Te_3 topological insulator. Journal of Optics, 16(8), Article#085203.

Lee, S.-L., Gong, P.-M., & Yang, C.-T. (2002). Performance enhancement on SOA-based four-wave-mixing wavelength conversion using an assisted beam. *IEEE Photonics Technology Letters*, *14*(12), 1713–1715.

Leuthold, J., Koos, C., & Freude, W. (2010). Nonlinear silicon photonics. *Nature Photonics*, *4*(8), 535–544.

Levy, R. B., & Boudart, M. (1973). Platinum-like behavior of tungsten carbide in surface catalysis. *Science*, *181*(4099), 547–549.

Li, J., Qin, R., Yan, L., Chi, Z., Yu, Z., Li, N., Hu, M., Chen, H., & Shan, G. (2019). Plasmonic Light Illumination Creates a Channel To Achieve Fast Degradation of $Ti_3C_2T_x$ Nanosheets. *Inorganic Chemistry*, *58*(11), 7285–7294.

Li, L., Wang, F., Zhu, J., & Wu, W. (2017). The facile synthesis of layered Ti_2C MXene/carbon nanotube composite paper with enhanced electrochemical properties. *Dalton Transactions*, *46*(43), 14880–14887.

Li, M., Yin, P., Liu, Z., Dong, F., Sui, L., Ma, W., & Wang, T. (2022). Enhanced four-wave mixing in borophene-microfiber waveguides at telecom C-band. *Applied Optics*, *61*(5), 1261–1267.

Li, N., Li, Y., Zhu, X., Huang, C., & Fan, J. (2021). Theoretical investigation of the intercalation mechanism of VS2/MXene heterostructures as anode materials for metal-ion batteries. *Applied Surface Science*, *543*, Article#148772.

Li, Wei, Chen, B., Meng, C., Fang, W., Xiao, Y., Li, X., Hu, Z., Xu, Y., Tong, L., Wang, H., & others. (2014). Ultrafast all-optical graphene modulator. *Nano Letters*, *14*(2), 955–959.

Li, Wensong, Peng, J., Zhong, Y., Wu, D., Lin, H., Cheng, Y., Luo, Z., Weng, J., Xu, H., & Cai, Z. (2016). Orange-light passively Q-switched Pr^{3+}-doped all-fiber lasers with transition-metal dichalcogenide saturable absorbers. *Optical Materials Express*, *6*(6), 2031–2039.

Li, Z., Heidt, A. M., Daniel, J. M. O., Jung, Y., Alam, S. U., & Richardson, D. J. (2013). Thulium-doped fiber amplifier for optical communications at 2 μm. *Optics Express*, *21*(8), 9289–9297.

Liao, Y., Feng, G. Y., Zhou, H., Mo, J., Sun, H. J., & Zhou, S. H. (2018). Ultra-broadband all-optical graphene modulator. *IEEE Photonics Technology Letters*, *30*(8), 661–664.

Lin, H., Song, Y., Huang, Y., Kita, D., Deckoff-Jones, S., Wang, K., Li, L., Li, J., Zheng, H., Luo, Z., & others. (2017). Chalcogenide glass-on-graphene photonics. *Nature Photonics*, *11*(12), 798–805.

Lin, J., Yan, K., Zhou, Y., Xu, L. X., Gu, C., & Zhan, Q. W. (2015). Tungsten disulphide based all fiber Q-switching cylindrical-vector beam generation. *Applied Physics Letters*, *107*(19), Article#191108.

Liu, F., Zhou, A., Chen, J., Zhang, H., Cao, J., Wang, L., & Hu, Q. (2016). Preparation and methane adsorption of two-dimensional carbide Ti_2C. *Adsorption*, *22*(7), 915–922.

Liu, H., Zheng, X.-W., Liu, M., Zhao, N., Luo, A.-P., Luo, Z.-C., Xu, W.-C., Zhang, H., Zhao, C.-J., & Wen, S.-C. (2014). Femtosecond pulse generation from a topological insulator mode-locked fiber laser. *Optics Express*, *22*(6), 6868–6873.

Lu, L., Wang, W., Wu, L., Jiang, X., Xiang, Y., Li, J., Fan, D., & Zhang, H. (2017). All-optical switching of two continuous waves in few layer bismuthene based on spatial cross-phase modulation. *Acs Photonics*, *4*(11), 2852–2861.

Luo, Z., Huang, Y., Zhong, M., Li, Y., Wu, J., Xu, B., ... & Weng, J. (2014). 1-, 1.5-, and 2-μm fiber lasers Q-switched by a broadband few-layer MoS_2 saturable absorber. *Journal of Lightwave Technology*, 32(24), 4077-4084.

Luo, Z., Zhou, M., Weng, J., Huang, G., Xu, H., Ye, C., & Cai, Z. (2010). Graphene-based passively Q-switched dual-wavelength erbium-doped fiber laser. *Optics letters*, 35(21), 3709-3711.

Maiman, T. H., & others. (1960). *Stimulated optical radiation in ruby*.

Mao, D., Cui, X., Gan, X., Li, M., Zhang, W., Lu, H., & Zhao, J. (2017). Passively Q-switched and mode-locked fiber laser based on an ReS_2 saturable absorber. *IEEE Journal of Selected Topics in Quantum Electronics*, 24(3), 1-6.

Martinez, A., & Sun, Z. (2013). Nanotube and graphene saturable absorbers for fibre lasers. *Nature Photonics*, 7(11), 842-845.

Martinez, A., Xu, B., & Yamashita, S. (2014). Nanotube based nonlinear fiber devices for fiber lasers. *IEEE Journal of Selected Topics in Quantum Electronics*, *20*(5), 89–98.

Mashtalir, O., Lukatskaya, M. R., Zhao, M.-Q., Barsoum, M. W., & Gogotsi, Y. (2015). Amine-assisted delamination of Nb_2C MXene for Li-ion energy storage devices. *Advanced Materials*, *27*(23), 3501–3506.

Mashtalir, O., Naguib, M., Dyatkin, B., Gogotsi, Y., & Barsoum, M. W. (2013). Kinetics of aluminum extraction from Ti_3AlC_2 in hydrofluoric acid. *Materials Chemistry and Physics*, *139*(1), 147–152.

Mashtalir, O., Naguib, M., Mochalin, V. N., Dall'Agnese, Y., Heon, M., Barsoum, M. W., & Gogotsi, Y. (2013). Intercalation and delamination of layered carbides and carbonitrides. *Nature Communications*, *4*(1), 1–7.

Mathlouthi, W., Rong, H., & Paniccia, M. (2008). Characterization of efficient wavelength conversion by four-wave mixing in sub-micron silicon waveguides. *Optics Express*, *16*(21), 16735–16745.

Meng, C., Yu, S.-L., Wang, H.-Q., Cao, Y., Tong, L.-M., Liu, W.-T., & Shen, Y.-R. (2015). Graphene-doped polymer nanofibers for low-threshold nonlinear optical waveguiding. *Light: Science & Applications*, *4*(11), e348--e348.

Meng, Y., Li, Y., Xu, Y., & Wang, F. (2017). Carbon nanotube mode-locked thulium fiber laser with 200 nm tuning range. *Scientific reports*, 7(1), 1-7.

Miao, L., Yi, J., Wang, Q., Feng, D., He, H., Lu, S., Zhao, C., Zhang, H., & Wen, S. (2016). Broadband third order nonlinear optical responses of bismuth telluride nanosheets. *Optical Materials Express*, *6*(7), 2244–2251.

Miniscalco, W. J. (2001). Optical and electronic properties of rare earth ions in glasses. *Optical Engineering-New York-Marcel Dekker Incorporated*, *71*, 17–112.

Mockuté, A., Lu, J., Moon, E. J., Yan, M., Anasori, B., May, S. J., Barsoum, M. W., & Rosén, J. (2015). Solid solubility and magnetism upon Mn incorporation in the bulk ternary carbides Cr_2AlC and Cr_2GaC. *Materials Research Letters*, *3*(1), 16–22.

Monerie, M., Georges, T., Francois, P. L., Allain, J. Y., & Neveux, D. (1990). Ground-state and excited-state absorption in rare-earth doped optical fibres. *Electronics Letters*, *26*(5), 320–321.

Morgner, U., Kärtner, F. X., Cho, S.-H., Chen, Y., Haus, H. A., Fujimoto, J. G., Ippen, E. P., Scheuer, V., Angelow, G., & Tschudi, T. (1999). Sub-two-cycle pulses from a Kerr-lens mode-locked Ti: sapphire laser. *Optics Letters*, *24*(6), 411–413.

Moulton, P. F., Rines, G. A., Slobodtchikov, E. V, Wall, K. F., Frith, G., Samson, B., & Carter, A. L. G. (2009). Tm-doped fiber lasers: fundamentals and power scaling. *IEEE Journal of Selected Topics in Quantum Electronics*, *15*(1), 85–92.

Mücke, O. D., Tritschler, T., Wegener, M., Morgner, U., & Kärtner, F. X. (2001). Signatures of carrier-wave Rabi flopping in GaAs. *Physical Review Letters*, *87*(5), Article#57401.

Naguib, M., Halim, J., Lu, J., Cook, K. M., Hultman, L., Gogotsi, Y., & Barsoum, M. W. (2013). New two-dimensional niobium and vanadium carbides as promising materials for Li-ion batteries. *Journal of the American Chemical Society*, *135*(43), 15966–15969.

Naguib, M., Kurtoglu, M., Presser, V., Lu, J., Niu, J., Heon, M., Hultman, L., Gogotsi, Y., & Barsoum, M. W. (2011a). Two-dimensional nanocrystals produced by exfoliation of Ti_3AlC_2. *Advanced Materials*, 23(37), 4248-4253.

Naguib, M., Kurtoglu, M., Presser, V., Lu, J., Niu, J., Heon, M., Hultman, L., Gogotsi, Y., & Barsoum, M. W. (2011b). Two-dimensional nanocrystals produced by exfoliation of Ti3AlC2. *Advanced Materials*, *23*(37), 4248–4253.

Naguib, M., Mashtalir, O., Carle, J., Presser, V., Lu, J., Hultman, L., Gogotsi, Y., & Barsoum, M. W. (2012). Two-dimensional transition metal carbides. *ACS Nano*, *6*(2), 1322–1331.

Nodop, D., Jauregui, C., Schimpf, D., Limpert, J., & Tünnermann, A. (2009). Efficient high-power generation of visible and mid-infrared light by degenerate four-wave-mixing in a large-mode-area photonic-crystal fiber. *Optics Letters*, *34*(22), 3499–3501.

Novoselov, K. S., Geim, A. K., Morozov, S. V, Jiang, D., Zhang, Y., Dubonos, S. V, Grigorieva, I. V, & Firsov, A. A. (2004). Electric field effect in atomically thin carbon films. *Science*, *306*(5696), 666–669.

O'Neill, W., Sparkes, M., Varnham, M., Horley, R., Birch, M., Woods, S., & Harker, A. (2004). High power high brightness industrial fiber laser technology. *International Congress on Applications of Lasers & Electro-Optics*, *2004*(1), Article#301.

Oyama, S. T., Schlatter, J. C., Metcalfe III, J. E., & Lambert Jr, J. M. (1988). Preparation and characterization of early transition metal carbides and nitrides. *Industrial \& Engineering Chemistry Research*, *27*(9), 1639–1648.

Partoens, B., & Peeters, F. M. (2006). From graphene to graphite: Electronic structure around the K point. *Physical Review B*, *74*(7), Article#75404.

Paschotta, R. (2008). Field guide to lasers (Vol. 12). Bellingham, WA: SPIE press.

Popov, S. (2008). Fiber laser overview and medical applications. *Tunable Laser Applications*, 197–226.

Powell, J., & Kaplan, A. F. H. (2012). A technical and commercial comparison of fiber laser and CO2 laser cutting. *International Congress on Applications of Lasers \& Electro-Optics*, *2012*(1), 277–281.

Ramachandran, R., Rajavel, K., Xuan, W., Lin, D., & Wang, F. (2018). Influence of $Ti_3C_2T_x$ (MXene) intercalation pseudocapacitance on electrochemical performance of Co-MOF binder-free electrode. *Ceramics International*, *44*(12), 14425–14431.

Ran, J., Gao, G., Li, F. T., Ma, T. Y., Du, A., & Qiao, S. Z. (2017). Ti_3C_2 MXene co-catalyst on metal sulfide photo-absorbers for enhanced visible-light photocatalytic hydrogen production. Nature communications, 8(1), 1-10.

Randin, J. P. (1981). Nonmetallic electrode materials. In Electrochemical Materials Science (pp. 473-537). Springer, Boston, MA.

Ren, J., Zheng, X., Tian, Z., Li, D., Wang, P., & Jia, B. (2016). Giant third-order nonlinearity from low-loss electrochemical graphene oxide film with a high power stability. *Applied Physics Letters*, *109*(22), Article#221105.

Ren, X., Rinke, P., Joas, C., & Scheffler, M. (2012). Random-phase approximation and its applications in computational chemistry and materials science. *Journal of Materials Science*, *47*(21), 7447–7471.

Richardson, D. J., Nilsson, J., & Clarkson, W. A. (2010). High power fiber lasers: current status and future perspectives. JOSA B, 27(11), B63-B92.

Aozasa, S., Sakamoto, T., Kanamori, T., Hoshino, K., & Shimizu, M. (2000). Gain-shifted thulium-doped fibre amplifiers employing novel high concentration doping technique. *Electronics Letters*, 36(5), 418-419.

Saidin, N., Zen, D. I. M., Ahmad, F., Haris, H., Ahmad, H., Dimyati, K., Harun, S. W., Halder, A., Paul, M. C., Pal, M., & others. (2016). Q-switched 2 μm thulium bismuth co-doped fiber laser with multi-walled carbon nanotubes saturable absorber. *Optics & Laser Technology*, *83*, 89–93.

Salcedo, J. R., Hendow, S., Guerreiro, P., Sousa, J., Berendt, M., & Romero, R. (2012, February). Dynamic pulsing of a MOPA pulsed fiber laser for optimized material processing. In Advances in Optical Materials (pp. JTh2A-31). *Optica Publishing Group.*

Salem, R., Foster, M. A., Turner, A. C., Geraghty, D. F., Lipson, M., & Gaeta, A. L. (2008). Signal regeneration using low-power four-wave mixing on silicon chip. *Nature Photonics*, *2*(1), 35–38.

Sang, X., Xie, Y., Lin, M.-W., Alhabeb, M., Van Aken, K. L., Gogotsi, Y., Kent, P. R. C., Xiao, K., & Unocic, R. R. (2016). Atomic defects in monolayer titanium carbide (Ti3C2T x) MXene. *ACS Nano*, *10*(10), 9193–9200.

Sarycheva, A., Polemi, A., Liu, Y., Dandekar, K., Anasori, B., & Gogotsi, Y. (2018). 2D titanium carbide (MXene) for wireless communication. *Science Advances*, *4*(9), Article#eaau0920.

Saynatjoki, A., Karvonen, L., Riikonen, J., Kim, W., Mehravar, S., Norwood, R. A., Peyghambarian, N., Lipsanen, H., & Kieu, K. (2013). Rapid large-area multiphoton microscopy for characterization of graphene. *ACS Nano*, *7*(10), 8441–8446.

Schnell, S., Ostroumov, V. G., Breguet, J., Luthy, W. A. R., Weber, H. P., & Shcherbakov, I. A. (1990). Acoustooptic Q-switching of erbium lasers. *IEEE Journal of Quantum Electronics*, *26*(6), 1111–1114.

Seh, Z. W., Fredrickson, K. D., Anasori, B., Kibsgaard, J., Strickler, A. L., Lukatskaya, M. R., Gogotsi, Y., Jaramillo, T. F., & Vojvodic, A. (2016). Two-dimensional molybdenum carbide (MXene) as an efficient electrocatalyst for hydrogen evolution. *ACS Energy Letters*, *1*(3), 589–594.

Sekhar, P., Mishra, A., & Pant, R. (2020). Characterization of Four-Wave Mixing in Specialty Silica Fibers at 2 μm Using Continuous-Wave Pumps. *IEEE Photonics Technology Letters*, *32*(9), 542–545.

Semnani, B., Majedi, A. H., & Safavi-Naeini, S. (2016). Nonlinear quantum optical properties of graphene. *Journal of Optics*, *18*(3), Article#35402.

Shcherbakov, E. A., Fomin, V. V., Abramov, A. A., Ferin, A. A., Mochalov, D. V., & Gapontsev, V. P. (2013, October). Industrial grade 100 kW power CW fiber laser. In Advanced Solid State Lasers (pp. ATh4A-2). *Optica Publishing Group*.

Shen, D. Y., Sahu, J. K., & Clarkson, W. A. (2006). High-power widely tunable Tm: fibre lasers pumped by an Er, Yb co-doped fibre laser at 1.6 μm. *Optics Express*, *14*(13), 6084–6090.

Shi, B., Miao, L., Wang, Q., Du, J., Tang, P., Liu, J., Zhao, C., & Wen, S. (2015). Broadband ultrafast spatial self-phase modulation for topological insulator Bi_2Te_3 dispersions. *Applied Physics Letters*, *107*(15), Article#151101.

Shirazi, M. R., Biglary, M., Harun, S. W., Thambiratnam, K., & Ahmad, H. (2008). Bidirectional multiwavelength Brillouin fiber laser generation in a ring cavity. Journal of Optics A: *Pure and Applied Optics*, 10(5), Article#055101.

Siegman, A. E. (1990). New developments in laser resonators. *Optical Resonators*, *1224*, 2–14.

Solodyankin, M. A., Obraztsova, E. D., Lobach, A. S., Chernov, A. I., Tausenev, A. V, Konov, V. I., & Dianov, E. M. (2008). Mode-locked 1.93 μm thulium fiber laser with a carbon nanotube absorber. *Optics Letters*, *33*(12), 1336–1338.

Song, D.-X., Du, Y.-Z., Ma, W.-G., & Zhang, X. (2021). High rate and capacity performances of functionalized MXene/graphene heterostructure anodes for magnesium-ion batteries. *International Journal of Energy Research*, *45*(2), 3421–3429.

Song, Y., Chen, Y., Jiang, X., Ge, Y., Wang, Y., You, K., Wang, K., Zheng, J., Ji, J., Zhang, Y., & others. (2019). Nonlinear few-layer MXene-assisted all-optical wavelength conversion at telecommunication band. *Advanced Optical Materials*, *7*(18), Article#1801777.

Song, Y., Chen, Y., Jiang, X., Liang, W., Wang, K., Liang, Z., Ge, Y., Zhang, F., Wu, L., Zheng, J., & others. (2018). Nonlinear few-layer antimonene-based all-optical signal processing: ultrafast optical switching and high-speed wavelength conversion. *Advanced Optical Materials*, *6*(13), Article#1701287.

Sotor, J., Sobon, G., Macherzynski, W., Paletko, P., & Abramski, K. M. (2015). Black phosphorus saturable absorber for ultrashort pulse generation. *Applied Physics Letters*, 107(5), Article#051108.

Sousa, J. M., Nilsson, J., Renaud, C. C., Alvarez-Chavez, J. A., Grudinin, A. B., & Minelly, J. D. (1999). Broad-band diode-pumped ytterbium-doped fiber amplifier with 34-dBm output power. *IEEE Photonics Technology Letters*, *11*(1), 39–41.

Sprangle, P., Hafizi, B., Ting, A., & Fischer, R. (2015). High-power lasers for directed-energy applications. *Applied Optics*, *54*(31), F201--F209.

Stankovich, S., Dikin, D. A., Dommett, G. H. B., Kohlhaas, K. M., Zimney, E. J., Stach, E. A., Piner, R. D., Nguyen, S. T., & Ruoff, R. S. (2006). Graphene-based composite materials. *Nature*, *442*(7100), 282–286.

Sun, D., Wu, Z.-K., Divin, C., Li, X., Berger, C., de Heer, W. A., First, P. N., & Norris, T. B. (2008). Ultrafast relaxation of excited Dirac fermions in epitaxial graphene using optical differential transmission spectroscopy. *Physical Review Letters*, *101*(15), Article#157402.

Sun, W., Shah, S. A., Chen, Y., Tan, Z., Gao, H., Habib, T., Radovic, M., & Green, M. J. (2017). Electrochemical etching of Ti_2AlC to Ti_2CT_x (MXene) in low-concentration hydrochloric acid solution. *Journal of Materials Chemistry A*, *5*(41), 21663–21668.

Szczepanek, J., Kardaś, T. M., Michalska, M., Radzewicz, C., & Stepanenko, Y. (2015). Simple all-PM-fiber laser mode-locked with a nonlinear loop mirror. *Optics letters*, 40(15), 3500-3503.

Szpulak, M., & Février, S. (2009). Chalcogenide As2S3 Suspended Core Fiber for Mid-IR Wavelength Conversion Based on Degenerate Four-Wave Mixing. *IEEE Photonics Technology Letters*, *21*(13), 884–886.

Tachibana, M., Laming, R. I., Morkel, P. R., & Payne, D. N. (1991). Erbium-doped fiber amplifier with flattened gain spectrum. *IEEE Photonics Technology Letters*, *3*(2), 118–120.

Takesue, H., & Inoue, K. (2004). Generation of polarization-entangled photon pairs and violation of Bell's inequality using spontaneous four-wave mixing in a fiber loop. *Physical Review A*, *70*(3), Article#31802.

Tao, W., Yang, Z., Chen, Y., Li, L., Jiang, Z., & Zhang, Y. (2013). Double-sided fiber laser beam welding process of T-joints for aluminum aircraft fuselage panels: Filler wire melting behavior, process stability, and their effects on porosity defects. *Optics \& Laser Technology*, *52*, 1–9.

Tian, Y., Yang, C., Que, W., Liu, X., Yin, X., & Kong, L. B. (2017). Flexible and free-standing 2D titanium carbide film decorated with manganese oxide nanoparticles as a high volumetric capacity electrode for supercapacitor. *Journal of Power Sources*, 359, 332-339.

Tian, Z., Wu, K., Kong, L., Yang, N., Wang, Y., Chen, R., Hu, W., Xu, J., & Tang, Y. (2015). Mode-locked thulium fiber laser with MoS_2. *Laser Physics Letters*, *12*(6), Article#65104.

Traxer, O., & Keller, E. X. (2019). Thulium fiber laser: the new player for kidney stone treatment A comparison with Holmium: YAG laser. *World Journal of Urology*, 1–12.

Tutt, L. W., & Boggess, T. F. (1993). A review of optical limiting mechanisms and devices using organics, fullerenes, semiconductors and other materials. *Progress in Quantum Electronics*, *17*(4), 299–338.

Urbankowski, P., Anasori, B., Makaryan, T., Er, D., Kota, S., Walsh, P. L., Zhao, M., Shenoy, V. B., Barsoum, M. W., & Gogotsi, Y. (2016). Synthesis of two-dimensional titanium nitride Ti_4N_3 (MXene). *Nanoscale*, *8*(22), 11385–11391.

Wang, C., Wang, Y. Z., Jiang, X. T., Song, Y. F., Zhang, F., Liu, J., & Zhang, H. (2019). Thermal stress-induced all-optical modulation in MXene-coated polarization maintaining fiber. *Laser Physics Letters*, *16*(6), Article#65107.

Wang, F., Torrisi, F., Jiang, Z., Popa, D., Hasan, T., Sun, Z., ... & Ferrari, A. C. (2012, May). Graphene passively Q-switched two-micron fiber lasers. In Quantum Electronics and Laser Science Conference (pp. JW2A-72). *Optica Publishing Group*.

Wang, G., Zhang, S., Zhang, X., Zhang, L., Cheng, Y., Fox, D., Zhang, H., Coleman, J. N., Blau, W. J., & Wang, J. (2015). Tunable nonlinear refractive index of two-dimensional MoS_2, WS_2, and $MoSe_2$ nanosheet dispersions. *Photonics Research*, *3*(2), A51--A55.

Wang, J., Lu, W., Li, J., Chen, H., Jiang, Z., Wang, J., Zhang, W., Zhang, M., Li, I. L., Xu, Z., & others. (2017). Ultrafast thulium-doped fiber laser mode locked by monolayer WSe_2. *IEEE Journal of Selected Topics in Quantum Electronics*, *24*(3), 1–6.

Wang, P., Wang, Y., & Tong, L. (2013). Functionalized polymer nanofibers: a versatile platform for manipulating light at the nanoscale. *Light: Science & Applications*, *2*(10), e102--e102.

Wang, Q., Chen, T., Zhang, B., Li, M., Lu, Y., & Chen, K. P. (2013). All-fiber passively mode-locked thulium-doped fiber ring laser using optically deposited graphene saturable absorbers. *Applied Physics Letters*, *102*(13), Article#131117.

Wang, X., Li, H., Li, H., Lin, S., Bai, J., Dai, J., ... & Dou, S. (2019). Heterostructures of Ni–Co–Al layered double hydroxide assembled on V_4C_3 MXene for high-energy hybrid supercapacitors. Journal of Materials Chemistry A, 7(5), 2291-2300.

Wang, Y., Huang, W., Wang, C., Guo, J., Zhang, F., Song, Y., Ge, Y., Wu, L., Liu, J., Li, J., & others. (2019). An all-optical, actively Q-switched fiber laser by an antimonene-based optical modulator. *Laser \& Photonics Reviews*, *13*(4), Article#1800313.

Wang, Y., Zhang, F., Tang, X., Chen, X., Chen, Y., Huang, W., Liang, Z., Wu, L., Ge, Y., Song, Y., & others. (2018). All-optical phosphorene phase modulator with enhanced stability under ambient conditions. *Laser \& Photonics Reviews*, *12*(6), Article#1800016.

Wang, Zhaolu, Liu, H., Huang, N., Sun, Q., & Wen, J. (2012). Efficient terahertz-wave generation via four-wave mixing in silicon membrane waveguides. *Optics Express*, *20*(8), 8920–8928.

Wang, Z., Wang, T., Ma, W., Jia, Q., Su, Q., & Zhang, P. (2017). Tunable multiwavelength Brillouin-Raman fiber laser in a linear cavity with spectrum reshaped by Rayleigh scattering. *Optical Fiber Technology*, 36, 327-333.

Wen, Y., Ma, C., Wei, Z., Zhu, X., & Li, Z. (2019). FeNC/MXene hybrid nanosheet as an efficient electrocatalyst for oxygen reduction reaction. *Rsc Advances*, *9*(24), 13424–13430.

Whitley, T. J. (1995). A review of recent system demonstrations incorporating 1.3 um praseodymium-doped fluoride fiber amplifiers. *Journal of Lightwave Technology*, *13*(5), 744–760.

Willner, A. E., Byer, R. L., Chang-Hasnain, C. J., Forrest, S. R., Kressel, H., Kogelnik, H., Tearney, G. J., Townes, C. H., & Zervas, M. N. (2012). Optics and photonics: Key enabling technologies. *Proceedings of the IEEE*, *100*(Special Centennial Issue), 1604–1643.

Woodward, R. I., Howe, R. C. T., Runcorn, T. H., Hu, G., Torrisi, F., Kelleher, E. J. R., & Hasan, T. (2015). Wideband saturable absorption in few-layer molybdenum diselenide (MoSe 2) for Q-switching Yb-, Er-and Tm-doped fiber lasers. *Optics express*, 23(15), 20051-20061.

Wooten, F. (1973). Optical properties of solids. *American Journal of Physics*, *41*(7), 939–940.

Wu, K., Guo, C., Wang, H., Zhang, X., Wang, J., & Chen, J. (2017). All-optical phase shifter and switch near 1550nm using tungsten disulfide (WS2) deposited tapered fiber. *Optics Express*, *25*(15), 17639–17649.

Wu, L., Jiang, X., Zhao, J., Liang, W., Li, Z., Huang, W., Lin, Z., Wang, Y., Zhang, F., Lu, S., & others. (2018). MXene-based nonlinear optical information converter for all-optical modulator and switcher. *Laser & Photonics Reviews*, *12*(12), Article#1800215.

Wu, M., Wang, B., Hu, Q., Wang, L., & Zhou, A. (2018). The synthesis process and thermal stability of V_2C MXene. *Materials*, *11*(11), Article#2112.

Wu, Y., Yao, B., Cheng, Y., Rao, Y., Gong, Y., Zhou, X., Wu, B., & Chiang, K. S. (2013). Four-wave mixing in a microfiber attached onto a graphene film. *IEEE Photonics Technology Letters*, *26*(3), 249–252.

Xiao, X., Wang, H., Urbankowski, P., & Gogotsi, Y. (2018). Topochemical synthesis of 2D materials. *Chemical Society Reviews*, *47*(23), 8744–8765.

Xu, B., Martinez, A., & Yamashita, S. (2012). Mechanically exfoliated graphene for four-wave-mixing-based wavelength conversion. *IEEE Photonics Technology Letters*, *24*(20), 1792–1794.

Xu, B., Omura, M., Takiguchi, M., Martinez, A., Ishigure, T., Yamashita, S., & Kuga, T. (2013). Carbon nanotube/polymer composite coated tapered fiber for four wave mixing based wavelength conversion. *Optics Express*, *21*(3), 3651–3657.

Yamamoto, T., Miyajima, Y., & Komukai, T. (1994). 1.9 um Tm-doped silica fibre laser pumped at 1.57 um. *Electronics Letters*, *30*(3), 220–221.

Yamashita, S. (2011a). A tutorial on nonlinear photonic applications of carbon nanotube and graphene. *Journal of Lightwave Technology*, *30*(4), 427–447.

Yamashita, S. (2011b). Carbon-nanotube and graphene photonics. *2011 Optical Fiber Communication Conference and Exposition and the National Fiber Optic Engineers Conference*, 1–51.

Yamashita, S., Martinez, A., & Xu, B. (2014). Short pulse fiber lasers mode-locked by carbon nanotubes and graphene. Optical Fiber Technology, 20(6), 702-713.

Yan, Z., Li, X., Tang, Y., Shum, P. P., Yu, X., Zhang, Y., & Wang, Q. J. (2015). Tunable and switchable dual-wavelength Tm-doped mode-locked fiber laser by nonlinear polarization evolution. *Optics Express*, *23*(4), 4369–4376.

Yang, H.-L., Wei, H.-Y., Li, Y., Ren, L.-B., Zhang, H.-Y., & others. (2014). Technique progress of high-precision gas absorption spectroscopy with femtosecond optical frequency comb. *Spectroscopy and Spectral Analysis*, *34*(2), 335–339.

Yang, H., Heo, J., Park, S., Song, H. J., Seo, D. H., Byun, K.-E., Kim, P., Yoo, I., Chung, H.-J., & Kim, K. (2012). Graphene barristor, a triode device with a gate-controlled Schottky barrier. *Science*, *336*(6085), 1140–1143.

Yang, J., Wang, Z., Wang, F., Xu, R., Tao, J., Zhang, S., Qin, Q., Luther-Davies, B., Jagadish, C., Yu, Z., & others. (2016). Atomically thin optical lenses and gratings. *Light: Science & Applications*, *5*(3), e16046--e16046.

Yang, S., Zhang, P., Wang, F., Ricciardulli, A. G., Lohe, M. R., Blom, P. W. M., & Feng, X. (2018). Fluoride-free synthesis of two-dimensional titanium carbide (MXene) using a binary aqueous system. *Angewandte Chemie International Edition*, *57*(47), 15491–15495.

Yang, T., Shu, C., & Lin, C. (2005). Depolarization technique for wavelength conversion using four-wave mixing in a dispersion-flattened photonic crystal fiber. *Optics Express*, *13*(14), 5409–5415.

Yang, Y., Wu, J., Xu, X., Liang, Y., Chu, S. T., Little, B. E., Morandotti, R., Jia, B., & Moss, D. J. (2018). Invited Article: Enhanced four-wave mixing in waveguides integrated with graphene oxide. *APL Photonics*, *3*(12), Article#120803.

Ying, G., Dillon, A. D., Fafarman, A. T., & Barsoum, M. W. (2017). Transparent, conductive solution processed spincast 2D Ti_2CT_x (MXene) films. *Materials Research Letters*, *5*(6), 391–398.

Yorulmaz, U., Özden, A., Perkgöz, N. K., Ay, F., & Sevik, C. (2016). Vibrational and mechanical properties of single layer MXene structures: a first-principles investigation. *Nanotechnology*, *27*(33), Article#335702.

Youngblood, N., Peng, R., Nemilentsau, A., Low, T., & Li, M. (2017). Layer-tunable third-harmonic generation in multilayer black phosphorus. *Acs Photonics*, *4*(1), 8–14.

Yu, S., Wu, X., Chen, K., Chen, B., Guo, X., Dai, D., Tong, L., Liu, W., & Shen, Y. R. (2016). All-optical graphene modulator based on optical Kerr phase shift. *Optica*, *3*(5), 541–544.

Yu, S., Wu, X., Wang, Y., Guo, X., & Tong, L. (2017). 2D materials for optical modulation: challenges and opportunities. *Advanced Materials*, *29*(14), Article#1606128.

Zawischa, I., Plamann, K., Fallnich, C., Welling, H., Zellmer, H., & Tünnermann, A. (1999). All-solid-state neodymium-based single-frequency master-oscillator fiber power-amplifier system emitting 5.5 W of radiation at 1064 nm. *Optics Letters*, *24*(7), 469–471.

Zhang, C. J., Pinilla, S., McEvoy, N., Cullen, C. P., Anasori, B., Long, E., Park, S.-H., Seral-Ascaso, A., Shmeliov, A., Krishnan, D., & others. (2017). Oxidation stability of colloidal two-dimensional titanium carbides (MXenes). *Chemistry of Materials*, *29*(11), 4848–4856.

Zhang, H., Virally, S., Bao, Q., Ping, L. K., Massar, S., Godbout, N., & Kockaert, P. (2012). Z-scan measurement of the nonlinear refractive index of graphene. *Optics Letters*, *37*(11), 1856–1858.

Zhang, J., Yu, X., Han, W., Lv, B., Li, X., Xiao, S., Gao, Y., & He, J. (2016). Broadband spatial self-phase modulation of black phosphorous. *Optics Letters*, *41*(8), 1704–1707.

Zhang, X., Ma, Z., Zhao, X., Tang, Q., & Zhou, Z. (2015). Computational studies on structural and electronic properties of functionalized MXene monolayers and nanotubes. *Journal of Materials Chemistry A*, *3*(9), 4960–4966.

Zhao, S., Zhao, J., Li, G., Yang, K., Sun, Y., Li, D., An, J., Wang, J., & Li, M. (2006). Doubly Q-switched laser with electric-optic modulator and GaAs saturable absorber. *Laser Physics Letters*, *3*(10), Article#471.

Zheng, J., Yang, Z., Si, C., Liang, Z., Chen, X., Cao, R., Guo, Z., Wang, K., Zhang, Y., Ji, J., & others. (2017). Black phosphorus based all-optical-signal-processing: toward high performances and enhanced stability. *Acs Photonics*, *4*(6), 1466–1476.

Zheng, X., Jia, B., Chen, X., & Gu, M. (2014). In situ third-order non-linear responses during laser reduction of graphene oxide thin films towards on-chip non-linear photonic devices. *Advanced Materials*, *26*(17), 2699–2703.

Zhong, Y., Xia, X., Shi, F., Zhan, J., Tu, J., & Fan, H. J. (2016). Transition metal carbides and nitrides in energy storage and conversion. *Advanced Science*, *3*(5), Article#1500286.

LIST OF PUBLICATIONS AND PAPERS PRESENTED

List of publications

1. Ahmad, H., Samion, M. Z., **Kamely, A. A.**, & Ismail, M. F. (2019). Mode-locked thulium doped fiber laser with zinc oxide saturable absorber for 2 μm operation. Infrared Physics & Technology, 97, 142-148.

2. Ahmad, H., Ahmed, M. H. M., Samion, M. Z., **Kamely, A. A.**, Ismail, M. F., Harun, S. W., & Thambiratnam, K. (2019). Generation of sub-nanosecond pulse in dual-wavelength praseodymium fluoride fibre laser. Laser Physics, 29(10), 105101.

3. Ahmad, H., **Kamely, A. A.**, & Samion, M. Z. (2019). A compact linear-cavity multi-wavelength Brillouin/thulium fiber laser in S/S^+-band. Optical Fiber Technology, 51, 25-30.

4. Ahmad, H., **Kamely, A. A.**, & Samion, M. Z. (2020). S/S^+-band tunable dual-wavelength thulium doped fluoride fiber laser. Infrared Physics & Technology, 105, 103168.

5. Ahmad, H., **Kamely, A. A.**, Yusoff, N., Bayang, L., & Samion, M. Z. (2020). Generation of Q-switched Pulses in Thulium-doped and Thulium/Holmium-co-doped Fiber Lasers using MAX phase (Ti_3AlC_2). Scientific reports, 10(1), 1-10.

6. Ahmad, H., Ramli, R., **Kamely, A. A.**, Samion, M. Z., Yusoff, N., Bayang, L., & Thambiratnam, K. (2020). GeSe Evanescent Field Saturable Absorber for Mode-Locking in a Thulium/Holmium Fiber Laser. IEEE Journal of Quantum Electronics, 56(5), 1-8.

7. Samion, M. Z., **Kamely, A. A.**, & Ahmad, H. (2020, July). A Compact Linear-Cavity Multi-wavelength Praseodymium Fiber Laser by Stimulated Brillouin Scattering. In Nonlinear Photonics (pp. NpW1D-5). Optical Society of America.

8. Ahmad, H., Samion, M. Z., **Kamely, A. A.**, Wang, S., Wang, Y., & Sahu, J. K. (2020). Multiwavelength Brillouin generation in Bismuth-doped fiber laser with single-and double-frequency spacing. Journal of Lightwave Technology, 38(24), 6886-6896.

9. Ahmad, H., Zaini, M. K. A., **Kamely, A. A.**, Samion, M. Z., Ismail, M. F., Lim, K. S., & Thambiratnam, K. (2021). Generation of four-wave mixing in molybdenum ditelluride ($MoTe_2$)-deposited side-polished fibre. Journal of Modern Optics, 68(8), 425-432.

10. Ahmad, H., **Kamely, A. A.**, Zaini, M. K. A., Samion, M. Z., Zamzuri, A. K., & Thambiratnam, K. (2021). 1.5 and 2.0 μm all-optical modulators based on niobium-carbide (Nb_2C)-PVA film. Laser Physics Letters, 18(8), 085103.

11. Ahmad, H., **Kamely, A. A.**, Zaini, M. K. A., Samion, M. Z., Chong, W. Y., Zamzuri, A. K., & Lim, K. S. (2022). Generation of four-wave mixing with nonlinear Vanadium-carbide (V_2C)-deposited side-polished fiber (SPF) in 1.5- and 2.0-μm wavelength operation. Optics & Laser Technology, 145, 107458.

12. Ahmad, H., **Kamely, A. A.**, Samion, M. Z., & Soo, Y. H. (2022). Ti_2C MXene for multi-wavelength enhancement in S-band Q-switched thulium doped fluoride fiber laser. Optical Fiber Technology, 68, 102790.

Papers presented

1. **A.A. Kamely**, M. Z. Samion and H. Ahmad, "A Compact Linear-Cavity Multi-wavelength Brillouin/Thulium Fiber Laser in S/S+ -Band", National Taiwan University – University of Malaya Joint Physics Seminar 2019, University Malaya, Kuala Lumpur, 5th – 6th August 2019.

2. **A.A. Kamely**, M. Z. Samion and H. Ahmad, "Ultrafast Mode-Locked Fiber Laser In 2 μm Using Zinc Oxide Film", National Technology Research in Engineering, Design and Social Science Conference 2019, Melaka, Malaysia, 29th – 30th August 2019.

3. **A.A. Kamely**, H. Ahmad, R. Ramli, M. Z. Samion, N. Yusoff, L. Bayang, S.N. Aidit and K. Thambiratnam, "Mode-locked GeSe-based Pulse Generation in Thulium/Holmium Fiber Laser", International Conference on Research Practice in Science, Technology and Social Sciences 2021 (I-CReST 2021), University Teknologi MARA (Kampus Dengkil), Malaysia, 26th June 2021.